Imperial College London

A Finite Element Model for Virtual Stent-graft Deployment in Aortic Dissection

Author: Xiaoxin Kan *Supervisor:* Prof. Xiao Yun Xu

Department of Chemical Engineering
Imperial College London
February 2022

A thesis submitted in fulfilment of the requirements for the degree of Doctor of Philosophy and Diploma of Imperial College London, 2022

Copyright

The copyright of this thesis rests with the author. Unless otherwise indicated, its contents are licensed under a Creative Commons Attribution-Non Commercial 4.0 International Licence (CC BY-NC). Under this licence, you may copy and redistribute the material in any medium or format. You may also create and distribute modified versions of the work. This is on the condition that: you credit the author and do not use it, or any derivative works, for a commercial purpose. When reusing or sharing this work, ensure you make the licence terms clear to others by naming the licence and linking to the licence text. Where a work has been adapted, you should indicate that the work has been changed and describe those changes. Please seek permission from the copyright holder for uses of this work that are not included in this licence or permitted under UK Copyright Law.

Declaration of originality

I hereby declare that this thesis and the work presented in it are my own as the result of my own investigation except where otherwise stated. This thesis has not been submitted in whole or in part to another university for the award of any other degree or professional qualification.

February 2022

Xiaoxin Kan

To my family…

Acknowledgement

First of all, I would first like to express my deepest gratitude to my supervisor Prof. Xiao Yun Xu for offering me the opportunity to start this doctoral degree which has changed my life. Thank you for your excellent guidance on my work, for offering opportunities to learn, collaborate and grow as a researcher. Thank you for your patience, encouragement and understanding in difficult times.

I would like to acknowledge the China Scholarship Council for providing my PhD scholarship and the Department of Chemical Engineering for hosting my PhD.

I would also like to thank my clinical collaborators: Prof. Zhihui Dong for your continuous support to both myself and the whole project, Prof. Christoph Nienaber for inspiring me in research and attending all my group meeting presentations before the pandemic, Dr. Tao Ma and Mr. Xun Yuan for collecting clinical data and sharing their invaluable clinical insights. A special thank you goes to Prof. Lu Wang, Dr. Jing Lin, Prof. James Moore, Prof. Thanos Athanasiou, Dr. Mohammad Salmasi and Dr. Sumesh Sasidharan for the collaborations on mechanical tests. A huge and special thank you to Prof. Shengzhang Wang, who led me to the world of biomechanics. I want to thank Rocky and Jack for answering me questions.

Thank you to all the members in 1M17B: Yu, Selene, Sam, George, Chloe, Emily, Boram, Kaihong, Howard, Wenbo, Moath, Nasrul, Claudia, Mei Yan, Zhongjie and Prof. Nigel Wood for making this path so enjoyable. A special thank you to Yu, Hanyu, Shuo and Rui for being great friends in these years.

Thank you to all my family, my mom, dad, parents-in-law, grandparents for your endless love and support. Special to my granddad, I hope you could be proud of me and may you rest in peace. To my cousin, thank you for your encouragement and help.

Finally, I would like to express my deepest thanks and love to my wife, Sixuan. We support and accompany each other all the way since we first met in 2013. Thank you for your love and encouragement. I love you.

Abstract

Aortic dissection is a catastrophic aortic disease initiated by a tear at the intima of aortic wall. It allows blood flow into the wall layers, leading to separation of the aorta into two lumens, i.e. the true and false lumen. As a minimally invasive procedure, thoracic endovascular aortic repair (TEVAR) has been accepted as a standard treatment approach for type B aortic dissection and a potential alternative treatment for type A aortic dissection in scenarios of prohibitive surgical risk. During TEVAR, a stent-graft (SG) is deployed to seal the proximal entry tear and restore blood flow in the true lumen, thereby minimising flow into the false lumen and promoting aortic remodelling.

Although TEVAR has been a great success with its advantage of being less invasive compared to open surgery, there are still unpredictable post-TEVAR complications, including stent-graft migration, stent induced new entry (SINE) and retrograde aortic dissection (RAD). These complications are associated with the SG deployment procedure and biomechanical changes induced by the SG. The underlying mechanical interaction between the SG and aorta can potentially determine the treatment outcome of TEVAR. However, detailed biomechanical conditions and post-TEVAR SG configuration are not available before the actual procedure. Clinicians usually choose the SG size and landing position based on anatomical measurements and guidelines provided by the manufacturer.

In the past decade, promising progress has been made towards developing finite element method (FEM) based simulation tools for biomechanical analysis of interactions between the aorta and medical implants. However, due to the complicated anatomical features of aortic dissection and the associated nonlinear contact problem, patient-specific simulation of SG deployment in aortic dissection is still challenging.

The aim of this study is to develop a FEM-based modelling framework for virtual SG deployment in aortic dissections suitable for patient-specific applications. The model incorporates purpose-built image segmentation for aortic dissection, detailed design features of commercially available SG, precise control of SG deployment, pre-stress in the aortic wall and change of loading conditions after TEVAR. The model is able to mimic the

dynamic interaction between SG and aortic wall, predict post-TEVAR SG configuration and biomechanical changes in the aortic wall induced by SG deployment.

The FEM-based simulation workflow is validated against in vivo data, demonstrating its capability of reproducing post-TEVAR SG configuration to a good degree of accuracy. The model has been successfully applied to a type A aortic dissection case, and the simulation results are used to understand the reason for stent-graft migration and whether changing the proximal landing position could potentially offer a different outcome. The simulation model has also been applied to a small selection of type B aortic dissection cases, in an initial attempt to identify potential biomechanical differences between patients with and without post-TEVAR SINE. Finally, the virtual SG deployment model is extended to investigate the impact of SG length and design on post-TEVAR biomechanical stresses in the aortic wall, demonstrating its potential to serve as a pre-surgical planning tool in the future.

Content

Copyright i
Declaration of originality ii
Acknowledgement iv
Abstract v
Content vii
List of Figures xiii
List of Tables xxi
Nomenclature xxiii
Abbreviations xxiii
Roman symbols xxv
Greek symbols xxviii
Chapter 1 Introduction 1
1.1 Background and motivation 1
1.2 Research objectives and thesis outline 3
Chapter 2 Literature review 6
2.1 Cardiovascular system and the aorta 6
2.1.1 Microstructure of the aortic wall 9
2.2 Aortic dissection 11
2.2.1 Overview of aortic dissection 12

2.2.2 Classifications and diagnosis of aortic dissection 13
2.2.3 Management and outcomes for aortic dissection 17
2.3 Thoracic endovascular aortic repair 20
2.3.1 Thoracic endovascular aortic repair procedure 20
2.3.2 Stent-graft for TEVAR 21
2.3.3 Post-TEVAR complications 23
2.3.4 Summary 25
2.4 Mechanics of the aorta and stent-graft 26
2.4.1 Pre-stress and residual stress in the aorta 26
2.4.2 Biomechanical properties of the aortic wall 27
2.4.3 Mechanics of stent-graft 31
2.5 Numerical models for virtual stent-graft deployment 32
2.5.1 Numerical approach to calculate prestress in aortic wall 32
2.5.2 Simulation of stent-graft and virtual stent-graft deployment in aorta 33
2.6 Summary and research objectives 35
Chapter 3 Mathematical models and numerical procedure 37
3.1 Basic concepts of continuum mechanics 37
3.1.1 Displacement and deformation 37
3.1.2 Strain and stress 40
3.1.3 Governing equations 43
3.2 Hyperelastic material model used for the aortic wall 44
3.3 Finite element modelling with Abaqus 45
3.4 Contact algorithm 47
3.5 Aorta geometry reconstruction and mesh generation 48
3.5.1 Image segmentation and geometry reconstruction 49

3.5.2 Mesh generation 53
3.6 Parametric model for stent-graft and mesh generation 54
3.7 Boundary conditions 58
3.7.1 Nodal specific displacement of the virtual sheath 58
3.7.2 Boundary conditions for the aorta 59
3.8 Numerical simulation procedure 60
3.8.1 Prestress of aortic dissection model 60
3.8.2 Virtual stent-graft deployment 61
3.8.3 Loading condition after stent-graft deployment 62
3.9 Summary 63
Chapter 4 Model evaluation and validation: Patient-specific simulation of stent-graft deployment in type B aortic dissection† 64
4.1 Model details 65
4.1.1 Patient information 65
4.1.2 Aortic dissection geometry and stent-graft modelling 65
4.1.3 Mechanical property of human type B aortic dissection 68
4.1.4 Virtual stent-graft deployment workflow and model variations 70
4.1.5 Quantitative description of stent-graft configuration after deployment 71
4.2 Results 73
4.2.1 Assessment of stent-graft configuration after virtual deployment 73
4.2.2 Material parameters for descending aortic wall in type B aortic dissection patients 74
4.2.3 Effect of different model settings 75
4.2.4 Effects of aortic wall and intimal flap mechanical properties 81
4.3 Discussion 86

4.4 Summary 89

Chapter 5 Application I: predicting procedural success of TEVAR in type A aortic dissection† 91

5.1 Methodology 92

5.1.1 Patient information 92

5.1.2 Aortic dissection geometry and stent-graft modelling 94

5.1.3 Aortic root motion measurement 95

5.1.4 Mechanical tensile test 96

5.1.5 Virtual stent-graft deployment workflow and selection of simulation scenarios 97

5.2 Results 99

5.2.1 Aortic root motion and mechanical properties of dissected ascending aorta 99

5.2.2 Stent-graft configuration assessment 100

5.2.3 Stress distribution 102

5.3 Discussion 104

5.4 Summary 106

Chapter 6 Application II: evaluating the risk for post-TEVAR distal stent-graft induced new entry (SINE) in type B aortic dissection 107

6.1 Introduction 107

6.2 Methodology 108

6.2.1 Patient information 108

6.2.2 Model geometry and material properties 110

6.2.3 Anatomical measurements 112

6.2.4 Computational model 114

6.3 Results 115

6.3.1 Anatomical features 115
6.3.2 Biomechanical analysis 117
6.4 Discussion 122
6.5 Summary 125
Chapter 7 Application III: simulation of stent-graft deployment for pre-surgical planning in aortic dissection† 126
7.1 Introduction 126
7.2 Methodology 127
7.2.1 Clinical background 127
7.2.2 Aortic dissection modelling 128
7.2.3 Stent-graft modelling and variations 131
7.2.4 Numerical simulation and model verification 135
7.3 Results 138
7.3.1 SG configuration 138
7.3.2 Stress distribution 139
7.3.3 Impact of stent-graft lengths 141
7.3.4 Impact of stent-graft designs 142
7.4 Discussion 144
7.5 Summary 148
Chapter 8 Conclusion and future work 149
8.1 Summary of main contributions 150
8.2 Limitations and future directions 152
8.2.1 Interaction with blood flow 152
8.2.2 Material property and thickness of aortic tissue 153
8.2.3 Motion of the aorta 154

8.2.4 Cohort size 155
8.3 Clinical implications 155
Bibliography 157
Apendix A Analysis of inter-observer error in image segmentation 168
Apendix B Mesh Sensitivity Test 170
B.1 Finite element mesh for the aortic wall 170
B.2 Finite element mesh for the stent-graft 172
Apendix C Publications and Conferences 174
C.1 Peer-Reviewed Publications 174
C.2 Conference abstracts 174
C.3 Presentations 175
Apendix D Copyright Permissions 176

List of Figures

Figure 2.1 The human circulatory system (Institute for Quality and Efficiency in Health Care, 2019)..... 7

Figure 2.2 The anatomical structure of aorta. (Cleveland Clinic, 2019)..... 9

Figure 2.3 Structure of the aortic wall (Holzapfel et al., 2000)..... 10

Figure 2.4 Aortic dissection is caused by a tear in the intima of aortic wall (Nienaber et al., 2016)..... 12

Figure 2.5 The anatomical classification of aortic dissection (Nienaber and Clough, 2015) 14

Figure 2.6 CTA image from a patient with Stanford Type B aortic dissection: a. A transverse view of the CTA scan; b. Reconstructed three-dimensional geometry of the dissected aorta. 16

Figure 2.7 Current management of aortic dissection 18

Figure 2.8 Medical interventions for aortic dissection: a. Open surgery procedure for the replacement of ascending aorta in treating type A aortic dissection (Johns Hopkins Medicine, 2021); b. Endovascular aortic repair in treating type B aortic dissection (Cook Medical, 2021a). 19

Figure 2.9 Commercial stent-graft products. a. Medtronic Valiant™ Thoracic Stent Graft (Medtronic, 2021); b. GORE® TAG® Conformable Thoracic Stent Graft (Gore Medical, 2021); c. Zenith® TX2® Dissection Endovascular Graft (Cook Medical, 2021b). 22

Figure 2.10 A series of computed tomography angiogram (CTA) for a patient who developed distal stent induced new entry (SINE) and retrograde type A aortic dissection (RTAD): a. Preoperative CTA image of the type B aortic dissection patient with partially thrombosed false lumen; b. Proximal endoleak and distal SINE (pointed by red arrows) were found at the

3-month follow-up; c. RTAD (pointed by red arrows) was found at the 18-month follow-up. Adopted from (Ma et al., 2017)..... 24

Figure 3.1 Configuration and motion of a continuum body. 38

Figure 3.2 Deformation of a continuum body. 39

Figure 3.3 Schematic illustration of traction and stress tensor: a. Traction vectors acting on an infinitesimal surface with unit normal **n**, b. Components of stress tensor..... 42

Figure 3.4 Discretisation (a) and enforcement (b) of contact formulation. 47

Figure 3.5 Workflow of image segmentation in Mimics. 49

Figure 3.6 Segmentation and reconstruction of the aortic dissection geometry from pre-TEVAR CTA scan of a patient without false lumen thrombus. a. Two segmentation masks for blood flow (mask A) and combined mask (mask B). b. Surface extrude and Boolean operations to create aortic dissection structure..... 51

Figure 3.7 Segmentation and reconstruction of the aortic dissection geometry from pre-TEVAR CTA scan of a patient with false lumen thrombus. a. Two segmentation masks for blood flow (mask A) and combined mask (mask B). b. Surfaces are extruded to create true lumen (TL) structure and aortic wall. c. Boolean operations are performed to create intimal flap and aortic dissection geometry..... 52

Figure 3.8 3D geometry and mesh of outer wall and intimal flap..... 54

Figure 3.9 Creation of parametric models for metallic stent scaffold of commercial stent-grafts: a. Medtronic Valliant stent-graft (Medtronic Vascular, Santa Rosa, California), b. GORE C-TAG Active Control stent-graft (W. L. Gore & Associates, Inc, Flagstaff, Ariz) and c. Zenith 2PT stent-graft (Cook Medical, Bloomington, Ind). 56

Figure 3.10 Model of Zenith 2PT stent-graft (Cook Medical, Bloomington, Ind). The proximal and distal struts are shown in dash line as they are sewn on the inside of the synthetic graft. The virtual sheath is created by using a tubular surface. 57

Figure 3.11 Illustration of nodes indexing direction of the initial and target positions for calculation of nodal specific displacement..... 59

Figure 3.12 Virtual stent-graft (SG) deployment steps. a. The SG is crimped, delivered and deployed at the target position in the true lumen. b. A curved tube is used to open up the local narrowing in the compressed true lumen. 62

Figure 4.1 Illustration of the segmentation and reconstruction of aortic dissection geometry from CTA scan. a. The transverse view of the descending aorta before TEVAR showed true lumen (TL), false lumen (FL), and the measurement of narrowed true lumen. b. The segmentation of mask A represented for blood flow domain and mask B represented for adventitia. c. the aortic wall was created by extrude the mask B outwardly by 1.5 mm. d. The segmentation of intimal flap was created by performing Boolean subtraction of mask A from mask B. e. The aortic wall and intimal flap part were combined and trimmed to make the pre-TEVAR aortic dissection geometry..... 66

Figure 4.2 Geometry of the 28-28-150 mm Medtronic Valiant stent-graft used in the TEVAR procedure and was covered by the virtual sheath. 67

Figure 4.3 Virtual stent-graft deployment simulation workflow and model variations. 71

Figure 4.4 Definitions of the parameters for quantitative assessment of stent-graft configuration and spatial position..... 72

Figure 4.5 Numbering of stent ends and the definition of landing sections. 74

Figure 4.6 Stress-stretch relationships for aortic tissue samples taken from type B aortic dissection patients..... 75

Figure 4.7 Deviations of the predicted stent-graft configuration from the simulations with three different settings. a. the local open area (LOA) deviation ($eLOA$). b. stent strut end centre points position difference (ec (mm)). 77

Figure 4.8 Comparison of local open area (LOA) at the stent strut ends measured from model A (a), model B (b) and model C (c) against to the corresponding value measured from the post-TEVAR follow-up CTA scan 78

Figure 4.9 The maximum principal stress maps on the aortic wall and intimal flap pre- and post-TEVAR obtained from model A(a), model B(b) and model C(c). The virtually deployed stent-graft is shown in the middle with the intimal flap being highlighted. 80

Figure 4.10 Effects of aortic wall and intimal flap mechanical properties on the prediction of post-TEVAR stent-graft configuration. a. deviation in local open area (LOA) from the baseline case for A1F2 and A2F1. b. stent strut end centre points position deviation (*ec* (mm)) relative to the post-TEVAR follow-up CT scan. 83

Figure 4.11 The maximum principal stress maps on the aortic wall and intimal flap pre- and post-TEVAR obtained from A1F2 (a) and A2F1 (b). The virtually deployed stent-graft is shown in the middle with the intimal flap being highlighted. 85

Figure 5.1 Illustration of the type A aortic dissection case. a. 3-dimentional reconstruction of a computed tomographic angiogram (CTA) with type A aortic dissection showing a single large entry tear. b. Digital subtraction angiogram (DSA) obtained immediately after full deployment of the device showing stent-graft migration. c. Post-intervention 3-dimentional CTA showing stent-graft migration and the proximal part of SG pushing into the false lumen. d. The ascending aorta cut during the open surgery along with the 45-100-mm GORE C-TAG Active Control SG 93

Figure 5.2 a. Reconstructed geometry of type A aortic dissection. b. 45-100-mm GORE C-TAG Active Control stent-graft. 94

Figure 5.3 Measurement of aortic root in-plane motion based on DSA. DSA images at two different time points, with the right and left coronary ostia chosen as anatomical landmarks. 96

Figure 5.4 Patient-specific finite element model analysis. a. Fluoroscopic view of stent-graft positioning in semi-open stage before launch. b. Simulated image of the stent-graft in the

ascending aorta with virtual adaptation to the aortic curvature. The orange circle marks the proximal landing position in scenario-I, which simulates the actual thoracic endovascular aortic repair procedure, whereas the green circle simulates the proximal position of stent-graft in scenario-II, which assumed a more proximal positioning by 10 mm. 98

Figure 5.5 Stress-stretch relationships for aortic wall and intimal flap samples obtained from the type A aortic dissection patient reported in this chapter. 100

Figure 5.6 Evolution of stent-graft configuration during the virtual deployment simulation, starting from initial contact to fully deployed stage after incorporating the aortic root motion. a. Simulation scenario I. b. Simulation scenario II. 101

Figure 5.7 Qualitative comparison of stent-graft (SG) configurations between medical images and simulation results within the same projection plane of DSA (left anterior oblique (LAO) angle of 45° and cranial (CRA) angle of 10°). a. Post-interventional DSA showing SG configuration immediately after release of SG from the sheath and the simulated fully deployed SG configuration without aortic root motion. b. Stent and aorta reconstructed from post-TEVAR CTA image 1 month after the intervention and the simulated SG configuration after implementing aortic root motion. 102

Figure 5.8 Distributions of maximum principal stress (MPS) on the intimal flap during the virtual SG deployment simulation. (a) Scenario I, (b) Scenario II. 103

Figure 6.1 Pre- and post-TEVAR geometries of the four patients. The distal-SINEs found in the follow-ups of patient 3 and patient 4 are indicated by an arrow. 110

Figure 6.2 Geometry of stent-graft (SG) used in TEVAR procedure for the four patients... 112

Figure 6.3 Illustration of the parameters measured to describe anatomical features. Distal landing zone (shown in insets) is defined as the region between the two cutting planes (red square) at 15 mm proximal to the distal landing border and 15 mm distal to the border (red circle). 114

Figure 6.4 Reconstructed post-TEVAR aortas for the four patients included in this study and predicted von Mises stress (VMS) on the intimal flap. a. Reconstruction based on follow-up CT scans, b. Von Mises stress maps on the intimal flap and c. Mean and maximum values of von Mises stress in the distal landing zone of intimal flap. 118

Figure 6.5 Maximum principal stress (MPS) on the intimal flap for the four patients included in this study. a. Maximum principal stress maps on the intimal flap and b. Mean and peak values of the maximum principal stress in the distal landing zone of intimal flap. 119

Figure 6.6 Maximum shear stress (MSS) on the intimal flap for the four patients included in this study. a. Maximum shear stress maps on the intimal flap and b. Mean and peak values of the maximum shear stress in the distal landing zone of intimal flap. 120

Figure 6.7 Displacement of the intimal flap. a. Maps of the displacement magnitude of the intimal flap after stent-graft deployment and b. Mean and maximum values of the displacement magnitude in the distal landing zone of the intimal flap. 121

Figure 7.1 Patient information. a. The patient was diagnosed with type B aortic dissection with one primary entry tear and a distal re-entry tear (marked by the black arrow), b. the distal stent-induced new entry (SINE) was found at the 3-month follow-up, and c. a newly formed proximal tear was found at the proximal landing zone at the 12-month follow-up. 128

Figure 7.2 Illustration of the steps in segmentation and reconstruction of the aortic dissection geometry from pre-TEVAR CTA scan. a. Transverse view of two segmentations, the true lumen (TL) surface represents the original blood flow channel, and the combined surface encloses true lumen, false lumen and intimal flap, b. the TL structure and outer wall structure were created by extruding the surfaces outwardly by 1.45 mm, c. the intimal flap was created by performing Boolean subtraction of outer wall from TL structure, d. the TL structure and outer wall were combined. e. the intimal flap and outer wall geometry were smoothed and trimmed to form the aortic dissection geometry. 130

Figure 7.3 Summary of the modelled stent-graft (SG) products. a. Cook Zenith TX2 PT tapered SG with different lengths (the proximal and distal strut are shown with dash line as they were sewed inside of the synthetic graft), b. 42-38-150 mm Medtronic Valiant Proximal Freeflo Tapered SG, c. 42-42-150-mm GORE C-TAG Active Control SG.....133

Figure 7.4 Summary of the workflow of FEM-based virtual stent-graft (SG) deployment and the quantitative assessment of SG configuration. a. the SG was crimped, delivered and deployed by controlling the virtual sheath, the intimal flap was subdivided into seven zones to analyse detailed stress distribution on the intimal flap and b. definitions of parameters for quantitative assessment of SG configuration, diameter difference (eD), spatial positioning deviation in longitudinal direction (eL) and transverse direction (eT).....137

Figure 7.5 Assessment of SG configuration. a. Superimposition of the SG from simulation result and 3-month follow-up scan, b. diameter difference (eD) at the stent strut ends, c. longitudinal positioning deviation (eL) at the stent strut ends, and d. transverse positioning deviation (eT) at the stent strut ends.....139

Figure 7.6 Stress distribution with Cook Zenith 42-38-150 mm stent-graft and reconstructions from clinical follow-ups. a. von Mises stress maps on the intimal flap. The distal landing zone was zoomed in to show the local stress distribution, b. 3-month follow-up geometry from the same view angle. The distal SINE is pointed by the black arrow, c. Distribution of von Mises stress on the aortic wall. High stress of 283.26 kPa was found at the location where a proximal tear was found at 12-month follow-up (d).....140

Figure 7.7 a. von Mises stress maps on the intimal flap with the medium-length Zenith SG, b. von Mises stress maps on the intimal flap with the long Zenith SG. The distal landing zones of the two scenarios were zoomed in to show the local stress distribution and c. comparison of the stress distribution in the landing zones.....141

Figure 7.8 a. Distribution of von Mises stress on the aortic wall after deploying Valiant SG virtually into the aorta. High stress of 263.97 kPa was found at the proximal landing zone, b. Distribution of von Mises stress on the aortic wall after deploying C-TAG SG virtually into the aorta. High stress of 196.56 kPa was found at the proximal landing zone.....143

Figure 7.9 a. von Mises stress maps on the intimal flap with Valiant SG, b. von Mises stress maps on the intimal flap with Valiant SG. The distal landing zones of the two scenarios were zoomed in to show the local stress distribution and c. Comparison of the stress distribution in the landing zones. 144

Figure 8.1 Possible timeline for management of type B aortic dissection with the virtual stent-graft deployment model serving as a pre-surgical planning tool. 156

Figure A.1 Inter-observer error in the segmentation on each slice of pre- and post-TEVAR CTA images from one type B aortic dissection patient 169

List of Tables

Table 2.1 Summary of mainstream stent-graft (SG) products. CB: connecting bar, PBS: proximal bare stent. 21

Table 4.1. Superelastic material parameters for Nitinol stent (Kleinstreuer et al., 2008) 68

Table 4.2 Local open area (LOA) deviations ($eLOA$) in three landing sections (mean, standard deviation and maximum values) 76

Table 4.3 Spatial position difference of stent strut end centre point (ec) in three landing sections (mean, standard deviation and maximum values). 77

Table 4.4 Maximum principal stress (kPa) in different landing sections obtained with models A, B and C (mean, 10th percentile and 90th percentile) pre- and post-TEVAR. 79

Table 4.5 Simulations to evaluate the effect of material parameters. 82

Table 4.6 Deviations in local open area from the baseline simulation in three landing sections (mean, standard deviation and maximum values) 83

Table 4.7 Spatial position deviation of stent strut end centre point (ec) relative to the follow-up CT scan in three landing sections (mean, standard deviation and maximum values). 84

Table 4.8 Maximum principal stress (kPa) in different landing sections obtained from A1F2 and A2F1 (mean, 10th percentile and 90th percentile) pre- and post-TEVAR (marked as grey lines) 86

Table 5.1 Comparison of maximum principal stress (MPS) (kPa) in the intimal flap between the two scenarios at different stages of the virtual deployment simulation (mean, 10th percentile and 90th percentile). 104

Table 6.1 Characteristics of patients enrolled in the study 109

Table 6.2 Anatomical measurements taken in the four patients pre-TEVAR and at 3-month post-TEVAR. 116

Table 6.3 Stress and displacement in the distal landing zone of intimal flap in the four patients 117

Table 7.1 Summary of the stent-graft (SG) materials 133

Table 7.2 Summary of material properties of 316L stainless steel, Nitinol, polyethylene terephthalate (PET) and expanded polytetrafluoroethylene (ePTFE) 134

Table B.1 Maximum element size and total element number for the five patient-specific type B aortic dissection meshes (M1-M5). 171

Table B.2 Maximum and mean values of von Mises stress (VMS) and the maximum principal logarithmic strain (MLE) obtained with the five aortic dissection meshes (M1-M5). 171

Table B.3 Quantitative comparison of the maximum and mean von Mises stress (VMS) and the maximum principal logarithmic strain (MLE) between M1/M2, M2/M3, M3/M4 and M4/M5 171

Table B.4 Maximum element size and total element number for the five stent-graft (SG) meshes (M1-M5). 172

Table B.5 Maximum and mean values of von Mises stress (VMS) and the maximum principal logarithmic strain (MLE) obtained with the five stent-graft (SG) meshes (M1-M5). 172

Table B.6 Quantitative comparison of the maximum and mean von Mises stress (VMS) and the maximum principal logarithmic strain (MLE) between M1/M2, M2/M3, M3/M4 and M4/M5 173

Table D.1 Figure copyright permissions. 177

Nomenclature

Abbreviations

BMT	Best medical therapy
ALLKE/ALLIE	Kinetic energy and internal strain energy ratio
CB	Connecting bar
CRA	Cranial (angle)
CT	Computed Tomography
CTA	Computed Tomography Angiogram
DSA	Digital Subtraction Angiography
ECG	Electrocardiograph
ECHO	Echocardiography
ePTFE	Expanded Polytetrafluoroethylene
FEM	Finite element method
SSFP	Steady-state free precession
HGO	Holzapfel-Grasser-Ogden (model)
ID	Inverse design
LAO	Left anterior oblique (angle)
LOA	Local open area
MPS	Maximum principal stress
MRA	Magnetic Resonance Angiography
MRI	Magnetic Resonance Imaging

MSS	Maximum shear stress
MULF	Modified updated Lagrangian formulation
NHS	the National Health Service
PBS	Proximal bare stent
PC-MRI	Phased-contrast magnetic resonance imaging
PET	Polyethylene terephthalate
RTAD	Retrograde type A dissection
SG	Stent-graft
SINE	Stent induced new entry
TEVAR	Thoracic endovascular aortic repair
TOE	Transoesophageal echo
TTE	Transthoracic echocardiography
VMS	von Mises tress

Roman symbols

$\mathbf{a}_i$	Orthogonal and normalised set of eigenvectors
$\boldsymbol{\mathcal{B}}$	Continuum body
$\mathbf{b}$	Body force
$\mathbf{C}$	Right Cauchy-Green tensor
c^d	Dilatational wave speed
c_{10}, c_{20}, c_{30}	Material parameters for Yeoh model (type B aortic dissection)
$c_{10}^{\mathrm{f}}, c_{20}^{\mathrm{f}}, c_{30}^{\mathrm{f}}$	Material parameters for the Yeoh model (intimal flap in type A aortic dissection)
$c_{10}^{w}, c_{20}^{w}, c_{30}^{w}$	Material parameters for the Yeoh model (aortic wall in type A aortic dissection)
D_d	Local diameter at the distal border of SG covered aorta segment
D_p	Local diameter at the proximal border of SG covered aorta segment
D_s	Diameter of SG at stress free state
d_l	Displacement parallel with the local vessel centreline
d_r	Displacement perpendicular to the local vessel centreline
$\mathbf{E}$	Green-Lagrange strain tensor
E	Yong's modulus
E_A	Austenite elastic modulus
E_{flap}	Young's modulus of intimal flap
$\mathbf{e}_1, \mathbf{e}_2, \mathbf{e}_3$	Orthonormal basis
e_c	Centre point difference
e_D	Differences in local diameter
e_L	Longitudinal deviation along the aorta centreline

e_{LOA}	Local open area (LOA) deviation
e_T	Transvers deviation at local cross-section
$\mathbf{F}$	Deformation gradient tensor
$\mathbf{f}$	Applied load vector
h	Slice thickness
h_{flap}	Thickness of intimal flap
h_{wall}	Thickness of aortic wall
$\mathbf{I}$	Unite tensor
$\mathbf{I_f}$	Internal force vector
I_1, I_2, I_3	Invariants of right Cauchy-Green tensor
J	Determinant of the deformation gradient
K	Kinematic energy
L	Length of an infinitesimal element in the reference configuration
L_0	Linear distance between the proximal and distal ends of the centreline
L_c	Length of the centreline in the SG covered aorta segment
L_d	Length of the local centreline in the distal landing zone
L_{d0}	Linear distance between the two ends of the centreline in the distal landing zone
l	Length of an infinitesimal element in the current configuration
l_c	Characteristic length of element
$\mathbf{M}$	Diagonal lumped mass matrix
$\mathbf{n}$	Unit normal vector
N	Total number of transverse slices
$\mathbf{P}$	The first Piola-Kirchhoff stress tensor

p	Contact pressure
p_1^i	Initial position
p_2^i	Target position
$\mathbf{R}$	Rotation tensor
R^2	Coefficient of determination
r	Aortic root rotation angle
$\boldsymbol{S}_0$	Pre-tress tensor
S_i	Corresponding cross-sectional area
$\mathbf{T}$	The first Piola-Kirchhoff traction vector
T	Reference temperature
$\mathbf{t}$	Cauchy traction vector
t	Time
Δt	Stable increment time
$\mathbf{U}$	Right stretch tensor
$\dot{\mathbf{u}}$	Velocity
$\ddot{\mathbf{u}}$	Acceleration
u_s^i	Unique displacement
V	Volume
W	Total potential energy
$W_{\boldsymbol{int}}$	Internal potential energy
W_{ext}	External potential energy
$\mathbf{X}$	Typical position in reference configuration
$\mathbf{x}$	Typical position in current configuration

Greek symbols

$\boldsymbol{\varepsilon}$	Small strain tensor
ε_T	Transformation strain
λ_i	Principal stretches
μ	Friction coefficient
ν	Poisson's ratio
ν_A	Austenite Poisson's ratio
ν_M	Martensite Poisson's ratio
ρ	Mass densities in current configuration
ρ_0	Mass densities in reference configuration
$\boldsymbol{\sigma}$	Cauchy stress tensor
$\sigma_1, \sigma_2, \sigma_3$	Principal normal stresses
σ_{MPS}	Maximum principal stress
σ_{VMS}	von Mises tress
σ_{CL}^S	Start of transformation stress in compress
σ_L^S	Start of transformation (Loading)
σ_L^E	End of transformation (Loading)
σ_U^S	Start of transformation (Unloading)
σ_U^E	End of transformation (Unloading)
σ_p^k	kth predicted Cauchy stress
σ_m^k	kth measured Cauchy stress
τ_{cirt}	Critical frictional stress
τ_{eq}	Equivalent frictional stress

τ_{MSS}	Maximum shear stress
$\boldsymbol{\chi}$	Motion
Ψ	Strain-energy density
Ω	Current configuration
Ω_0	Reference configuration
Ω_{CTA}	Configuration reconstructed from CTA
ω_{max}	Maximum element eigenvalue

Chapter 1

Introduction

1.1 Background and motivation

On 25th October 1760, King George II of England was found passed away at Kensington Palace. The personal physician of King George II, Frank Nicholls, was directed to open and embalm the royal body the next day. In his observation report, he wrote (Nicholls and Parker, 1761):

"… upon examining the heart, its pericardium was found distended, with a quantity of coagulated blood, nearly sufficient to fill a pint cup upon removing this blood, a round orifice appeared in the middle of the upper fide of the right ventricle of the heart, large enough to admit the extremity of the little finger. Through this orifice, all the blood brought to the right ventricle had been discharged into the cavity of the pericardium and by that extravasated blood, confined between the heart and pericardium, the whole heart was very soon compressed, as to prevent any blood contained in the veins from being forced into the auricles.

… and in the trunk of the aorta we found a transverse fissure on its inner side, about an inch and a half long, through which some blood had recently passed under its external coat and formed an elevated ecchymosis."

This report provided the very first description of aortic dissection and allowed the cause of the King's fatal cardiac tamponade, which led to his death, to be recognised as an acute type A aortic dissection in current understanding. In the same year, Morgagni, the father of

modern anatomical pathology, described an anonymous patient who developed a tear in the ascending aorta and underwent the same tragedy as the King (Morgagni, 1761).

Till nowadays in 2020s, aortic dissection is still one of the most critical medical conditions, which can affect the function of the whole aorta and lead to aortic rupture. Previous long-term clinical studies reported an incidence of 3 cases per 100,000 per year, but the incidence of aortic dissection increased to 6 cases per 100,000 per year in a recent UK population-based study (Olsson et al., 2006, Howard et al., 2013). Thoracic aortic endovascular repair (TEVAR), which is a minimally invasive procedure involving implantation of a stent-graft in the affected aorta, was first used to treat aortic dissection in 1999 (Nienaber et al., 1999, Dake et al., 1999). Since then, TEVAR has been widely accepted as the standard treatment for type B aortic dissection. During TEVAR procedure, a fabric coated metal stent, stent-graft (SG), is deployed in the aorta to restore blood flow in the true lumen and strengthen the dissected aorta. Based on the report from the International Registry of Acute Aortic Dissection (IRAD), endovascular treatments of type B aortic dissection increased from 7% to 31% (Pape et al., 2015) with a lower 5-year mortality rate when compared with traditional medical therapy (Fattori et al., 2013). More recently, TEVAR has also been used in selected cases of type A aortic dissections in scenarios of prohibitive surgical risk (Nienaber et al., 2017). Furthermore, advanced imaging techniques, especially high-resolution Computed Tomography Angiography (CTA) and Magnetic Resonance Imaging (MRI), have been frequently used in diagnosis and monitoring of aortic dissection patients.

Although TEVAR has achieved remarkable success so far in treating type B aortic dissection and shown its feasibility in treating type A aortic dissection, it has also been reported with several short and long-term complications, including stent-graft migration, stent induced new entry (SINE) and retrograde type A dissection (RTAD) (Dong et al., 2009, Huang et al., 2018, Yuan et al., 2021b). These complications are associated with the deployment procedure of SG and changes in biomechanical conditions induced by the SG. The excessive forces generated by SG are believed to have strong correlations with TEVAR prognosis (Dong et al., 2010, Nienaber et al., 2013). Mechanical interactions between the SG and aorta influence the post-TEVAR biomechanical environment and can potentially determine the

treatment outcome. However, neither the biomechanical interaction nor the post-TEVAR SG configuration is available to clinicians at the pre-TEVAR planning stage.

Finite element method (FEM) has been widely employed in the study of vascular diseases and the design of medical implants. It has been applied to the modelling of endovascular aortic repair in treating abdominal aortic aneurysms (Perrin et al., 2015a). Very recently, SG deployment simulations have been applied to more complex scenarios in the aortic arch and abdominal aorta, demonstrating good accuracy in predicting SG configuration (Derycke et al., 2019, Derycke et al., 2020). However, patient-specific simulation of SG deployment in aortic dissection poses additional challenges due to complicated morphological features of aortic dissection and nonlinear contact relationship between SG and aortic wall.

To the best of the author's knowledge, only one other group has reported FEM-based simulations of SG deployment in type B aortic dissection prior to the completion of research work presented in this thesis (Ma et al., 2018, Meng et al., 2020). However, these studies did not consider the effect of pre-stress in the aortic wall nor blood pressure. Furthermore, no other study on the simulation of SG deployment in type A aortic dissection has been reported so far. Little is known about how the intimal flap deforms during SG deployment in aortic dissection and SG-induced stresses within the intimal flap and aortic wall.

1.2 Research objectives and thesis outline

The aim of this study is to develop a finite element modelling framework for virtual SG deployment in aortic dissections suitable for patient-specific applications. The FEM-based model should be able to predict post-TEVAR SG configuration and biomechanical changes in the aortic wall induced by the deployment of SG. It would allow assessment of the choice of SG design and size, as well as landing locations. It is hoped that the finite element modelling framework developed in this thesis can help understand the role of biomechanical factors in post-TEVAR complications, serves as a tool for optimisation of SG design and assist clinicians in making pre-TEVAR planning in the future.

This thesis consists of eight chapters. In the next chapter, an overview of the cardiovascular system, the aorta and microstructure of the aortic wall is first given, which is followed by

clinical features, pathology, classification, diagnosis and current management of aortic dissection. Details of the TEVAR procedure, commercial SG products used for TEVAR and post-TEVAR complications are presented. Chapter 2 also includes a review of biomechanics of aortic tissue and SG, followed by relevant numerical studies up to date.

Chapter 3 starts with a description of the basic concepts of continuum mechanics used in this thesis, which is followed by a summary of hyperelastic constitutive models for aortic tissue and finite element method as well as the contact algorithm based on Abaqus explicit. Details of the FEM-based methodology for virtual SG deployment in aortic dissection is described, including a purpose-built image segmentation approach, parametric models for SG geometry, nodal specific displacement control of the virtual sheath and the overall simulation procedure.

In Chapter 4, the virtual SG deployment model is evaluated based on a type B aortic dissection patient case with different model settings and material properties. The simulation results are validated against the corresponding post-TEVAR CTA scan. Hyperelastic material parameters derived from uniaxial tensile testing of type B aortic dissection tissue samples are also presented.

In Chapter 5, the model is applied to a patient-specific type A aortic dissection where the TEVAR procedure failed due to immediate stent-graft migration. The simulation results are used to understand the reason for stent-graft migration and whether changing the proximal landing position could potentially offer a different outcome. Patient-specific aortic root motion is also incorporated in the finite element simulation and its influences on intimal flap deformation and SG movement are assessed.

In Chapter 6, the virtual SG deployment model is applied to a small selection of type B aortic dissection cases with and without post-TEVAR SINE. The aim of this chapter is to further test the robustness of the developed methodology for patient-specific applications, while making an initial attempt to identify potential biomechanical differences between patients with and without SINE.

Chapter 7 explores the potential of using the virtual SG deployment model as a pre-surgical planning tool by varying the SG length and design and evaluating their impact on post-TEVAR wall stress distributions.

Finally, conclusions, limitations and recommendations for future work are summarised in Chapter 8.

Chapter 2

Literature review

2.1 Cardiovascular system and the aorta

The cardiovascular system consists of the heart, blood vessels and blood. The heart is one of the critical organs of the human body, which can be subdivided into two pumps to supply blood in two separate circuits (Figure 2.1). The right atrium collects venous blood from the superior vena cava and the inferior vena cava before passing it into the right ventricle. The blood is then pumped into the pulmonary circuit and transformed into oxygenated blood in the lung. The left atrium collects oxygenated blood from the pulmonary veins and passes blood into the left ventricle via the bicuspid mitral valve. The left ventricle is the largest chamber of the heart with the thickest wall and it supplies blood for the perfusion of distal organs. The blood is ejected from the left ventricle through the aortic valve before entering the aorta, through which the blood is supplied to other main organs.

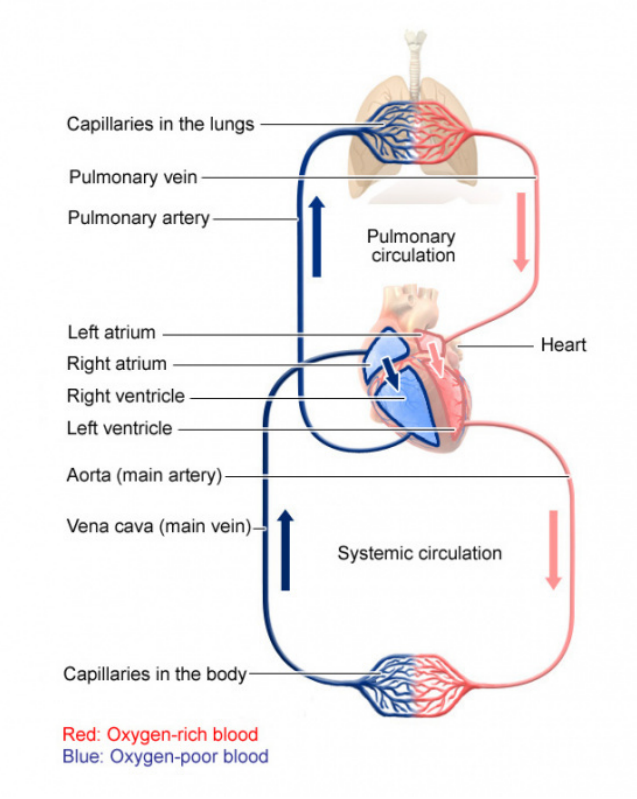


Figure 2.1 The human circulatory system (Institute for Quality and Efficiency in Health Care, 2019)

Blood flow inside the pulmonary (from the right ventricle to the left atrium) and systemic (from left ventricle to right atrium) circulations is driven by the pulsatile pressure gradient generated by the contraction of cardiac muscles. This cyclic contraction of cardiac muscle is also known as heartbeat. Under resting conditions, normal human hearts beat 60 to 80 times per minute. The time period of one heartbeat is defined as the cardiac cycle which can be divided into two phases: systole and diastole. Before the start of systolic phase, the two atria contact synchronously pumping blood into the ventricles. During the systolic phase, the heart contracts and pushes blood into the arterial trunks with a rapid increase in blood pressure to its maximum (normally 120 mmHg for the aorta). At the end of the systolic phase, cardiac muscles enter a relaxation phase; this causes the left ventricular blood pressure to decrease to a level below the arterial blood pressure, resulting in closure of the aortic valve. Then the heart enters its diastolic phase when the whole heart rests for the remaining

cardiac cycle. During this phase, the atria are passively filled and relaxed preparing for the next cycle.

Through the aorta, oxygenated blood is supplied to the whole body. The aorta originates from the left ventricle of the heart and takes off from the left ventricle, arches over the heart and descends toward the abdominal cavity (Figure 2.2). The aorta can be divided into two anatomical structures by the diaphragm, i.e. thoracic aorta and abdominal aorta.

The thoracic aorta, which is superior to the diaphragm, can be subdivided into three sections, ascending aorta, aortic arch and descending aorta. The ascending aorta starts from the aortic valve, in which blood travels upwards before making a U-turn in the aortic arch. The aortic arch is superior to the left pulmonary artery and contains three main branches: the brachiocephalic trunk, the left carotid artery and the left subclavian artery, which are responsible for supplying oxygenated blood to the neck and the head. The distal part of the thoracic aorta is called the descending aorta, which contains several small branches, including intercostal arteries and mediastinal arteries. These small branches provide additional constrains to the aorta, preventing it from large rigid body movement during cardiac cycles. The abdominal aorta, the part inferior to the diaphragm, has several main branches, which supply blood to the middle part of the body, before terminating with a bifurcation into the left and right common iliac arteries.

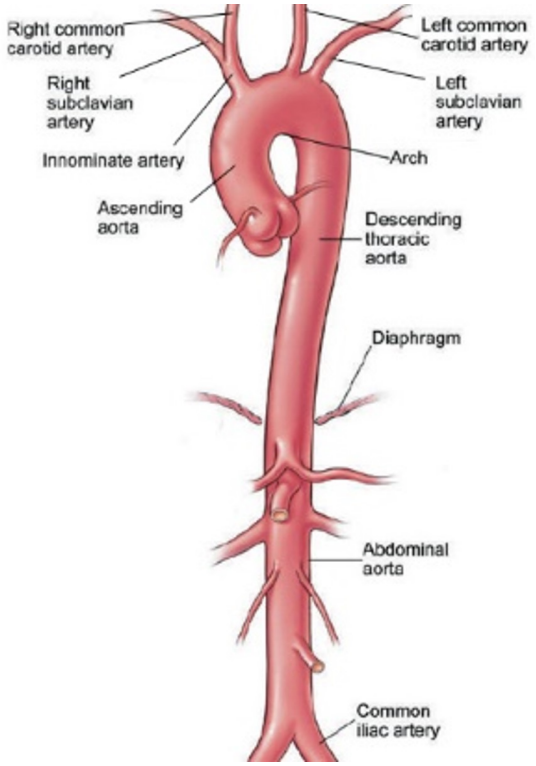


Figure 2.2 The anatomical structure of aorta. (Cleveland Clinic, 2019)

As the largest artery in human body, the diameter of the aorta decreases from proximal to distal with a mean value of 3.09 cm at the ascending aorta, 2.94 cm proximal to the innominate artery and 2.61 cm at the descending aorta (Hager et al., 2002). It is usually smaller in female than male and increases with age.

The thickness of aortic wall also decreases from proximal to distal aorta and varies with gender. For the ascending aorta, the mean wall thickness for female is 1.46 mm (5th–95th range: 1.15–1.88 mm) and 1.56 mm (1.22-1.99 mm) for male, while the mean wall thickness for the descending aorta is 1.26 mm (0.97-1.58 mm) in female and 1.36 mm (1.04-1.75 mm) in male (Mensel et al., 2014).

2.1.1 Microstructure of the aortic wall

The aortic wall is a complex constitutive tissue, which contains three main layers, i.e. the tunica intima, tunica media and tunica adventitia (Figure 2.3). This complex tissue is able to remodel and reorganise itself under the influence of external conditions, such as high blood

pressure (hypertension) and injuries. Therefore, understanding the microstructure of the aortic wall is important in the study of aortic diseases.

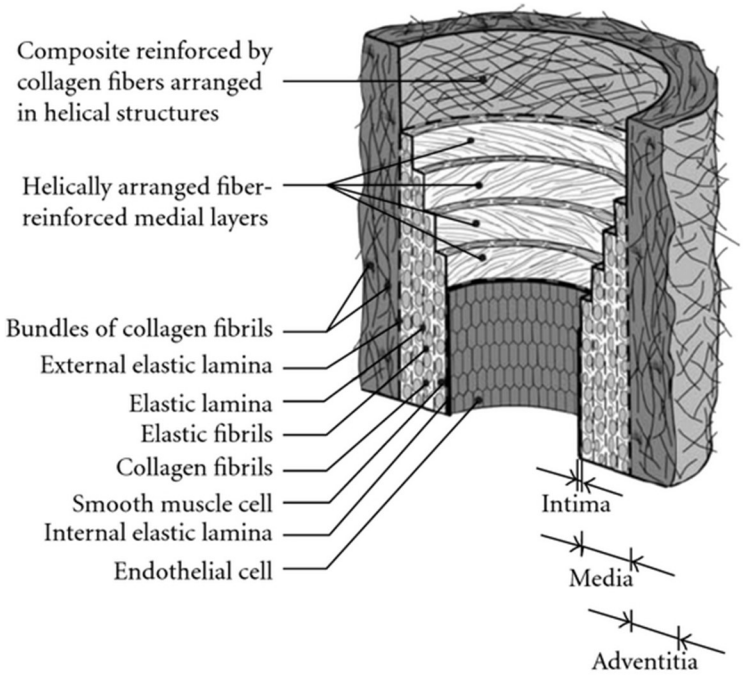


Figure 2.3 Structure of the aortic wall (Holzapfel et al., 2000)

The tunica intima, the most inner layer, is composed of a monolayer of endothelium, basal membrane and subendothelial connective tissue. The subendothelial connective tissue, which is directly in contact with the blood flow, varies in its thickness with age and disease (Holzapfel, 2000). Pathological changes of the intima, including thickening and stiffening of subendothelial tissue, are associated with atherosclerosis and contribute significantly to the change of biomechanical properties of the aortic wall.

The middle layer of the aortic wall, tunica media, is the thickest of the three layers (Holzapfel et al., 2007). The tunica media consists of a complex three-dimensional network of smooth muscle cells, elastin fibrils and collagen fibrils, and elastic laminae. These elastic fibrils and collagen fibrils orient regularly and interconnect with smooth muscles cells forming a continuous fibrous helix, which orients circumferentially and gives high strength and resilience to the aortic wall (Rhodin, 1980). The elastic laminae separates the tunica media

into a large number of transversely isotropic fibre-reinforced units, whose number decreases towards the distal end of arteries (Holzapfel et al., 2000). This microstructure enables the media layer to have high strength and compliance in both longitudinal and circumferential directions. In the biomechanical prospective, the media layer of the aortic wall makes the most significant contribution in determining the overall mechanical properties of the aortic wall.

The adventitia is the outmost layer and is mainly composed of collagen-rich connective tissues (helical structure of collagen fibrils) and fibrocytes (cells that produce collagen and elastin). The adventitia is less stiff under low loading conditions and increases its stiffness when collagen fibrils reach their straightened lengths under high loading conditions, which provides support to the aortic wall and prevents the aorta from overstretch.

Aging and hypertension are associated with microstructure changes in the aortic wall, either in the content or architecture of the elastin and collagen fibrils. The concentration of elastin decreases with age due to increases in collagen (Schlatmann and Becker, 1977), but the elastin contents remain unchanged.

Aortic diseases, including Marfan syndrome, aortic aneurysm and dissection are also associated with microstructural changes in the aortic wall. In diseased aortas with aneurysm or dissection, the elastin concentration decreases in the diseased segment with unchanged content, while the content of collagen increases with reduced concentration (Tsamis et al., 2013). In the aorta of patient with Marfan syndrome, the concentration of elastin decreases with a significant reduction in its content (50% less than healthy aorta), but no significant changes in collagen fibrils. The microstructure of tunica media has a strong influence on the mechanical properties of the aortic wall especially its stiffness and tensile strength, which are associated with the aortic disease initiation and progression (Perejda et al., 1985).

2.2 Aortic dissection

The first pathological description of aortic dissection was provided by Morgagni in 1761. A patient who developed a tear at the ascending aorta with subsequent rupture into the pericardial space was described in his report (Morgagni, 1761). In 1819, aortic dissection

was first defined as “anverisme dissquant” by Laennec (Laennec, 1819), but with confusion between thoracic aneurysm and dissection. However, due to the infrequency of aneurysmal dissection, the simple term “aortic dissection” has been adopted in recent decades (Miller et al., 1979).

2.2.1 Overview of aortic dissection

Aortic dissection begins with a tear in the intima of aorta, allowing blood flow into the medial layer of the aortic wall, which separates the intima from the adventitia (Figure 2.4). The split of the aortic wall propagates in an antegrade or retrograde manner under the load of blood pressure, causing the formation of a false lumen which is the newly formed flow channel. The original flow channel of the aorta is defined as the true lumen. The lamella, commonly referred to as an intimal flap, separates the false lumen from the true lumen. The progressive separation of aortic wall layers can also result in aortic rupture in case of adventitial disruption, or by re-entry back to the true lumen due to the disruption of intimal flap. This catastrophic disease can affect the normal function of the whole cardiovascular system. With the expansion of false lumen, the true lumen is compressed, and the aortic side branches may also be involved which can lead to malperfusion of the distal main organs (Nienaber and Clough, 2015).

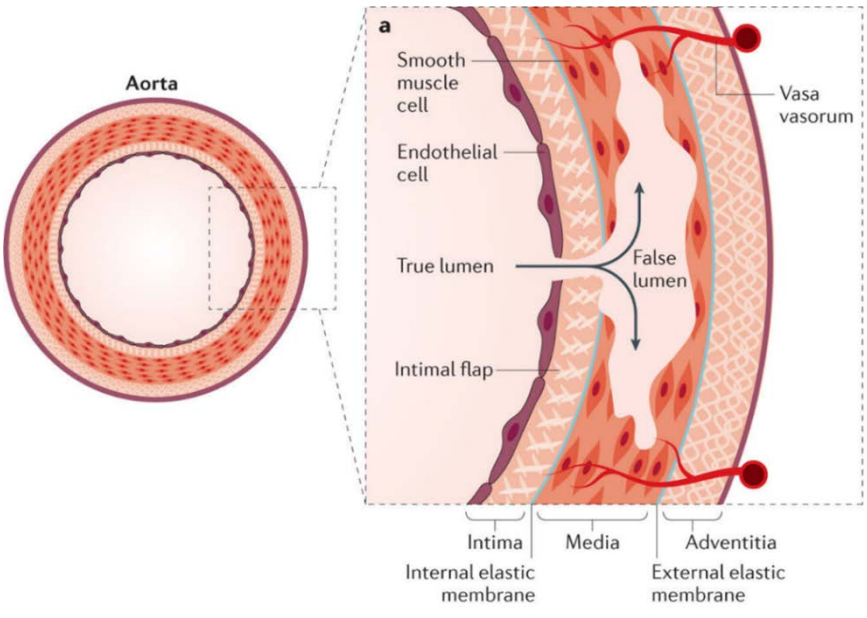


Figure 2.4 Aortic dissection is caused by a tear in the intima of aortic wall (Nienaber et al., 2016)

The development of aortic dissection is associated with several risk factors. Hypertension is the most prevalent risk factor, which is present in up to 75% of the reported cases (Baguet et al., 2012), followed by a history of atherosclerosis, smoke and use of drugs (cocaine and amphetamines) (Nienaber and Clough, 2015). Poor blood pressure control, inducing increased stiffness in the aortic wall and other pathophysiological mechanism, has been analysed and believed to have a significant correlation with the development of aortic dissection (Baguet et al., 2012). Deceleration trauma, caused by traffic accident or fall from height, is another contributor to aortic dissection or rupture (Richens et al., 2003). Genetic disorders, including Marfan syndrome, Turner's syndrome, smooth muscle cell contraction, make up 20% of the aortic dissection cases, due to the altered microstructure of aortic wall (Nienaber and Clough, 2015).

The overall incidence of aortic dissection varies, because data were derived from retrospective registries in different centres, and some might not include deaths before hospital admission. The ten-year population-based study in Oxfordshire, United Kingdom, reported an incidence of 6 cases per 100,000 (Howard et al., 2013). A Swedish population based study identified 4425 cases among 8.7 million people, giving an annual incidence of 3.4/100,000 (Olsson et al., 2006). A study from Mayo Clinic reported an annual incidence of 3.5/100,000 for aortic dissection based on the population data in Olmstead, USA (Clouse et al., 2004). The Swedish and USA studies excluded patients who died before hospital admission, which made their incidence rates lower than the UK study. Overall in-hospital mortality for aortic dissection was 27.4%, but differs among patients depending on anatomical and temporal features of the dissection (Hagan et al., 2000).

2.2.2 Classifications and diagnosis of aortic dissection

Classification systems have been introduced by clinicians according to time of onset and anatomical structure of the dissection. Aortic dissection is classified as acute phase within 2 weeks of symptom onset and chronic if longer than 2 weeks based on the survival estimate of patients treated in 1950s. This classification was revised by Booher et al., and has been widely accepted (Booher et al., 2013). Following the new classification system, the dissection

is classified into four time-domains: hyperacute (<24 h), acute (2-7 days), sub-acute (8-30 days), and chronic (>30 days).

Based on anatomical features of aortic dissection (e.g. position of entry tear and the part of aorta affected), two main streams of classification systems have been widely accepted, i.e. the Stanford system and DeBakey system.

The DeBakey system classifies aortic dissections into three types based on the position of entry tear and the propagation area (Figure 2.5). DeBakey Type I dissection patients present the first tear in the ascending aorta with dissection propagating distally to include at least the aortic arch and typically the descending aorta. When the false lumen zone is limited to the ascending aorta, the dissection is classified as Type II DeBakey aortic dissection. Dissections with an entry tear in the descending aorta and propagating distally are defined as Type III DeBakey aortic dissection. Type III DeBakey dissection is subdivided into two categories based on the dissection propagation, Type IIIa (dissection only in the descending aorta) and Type IIIb (dissection propagating below the diaphragm).

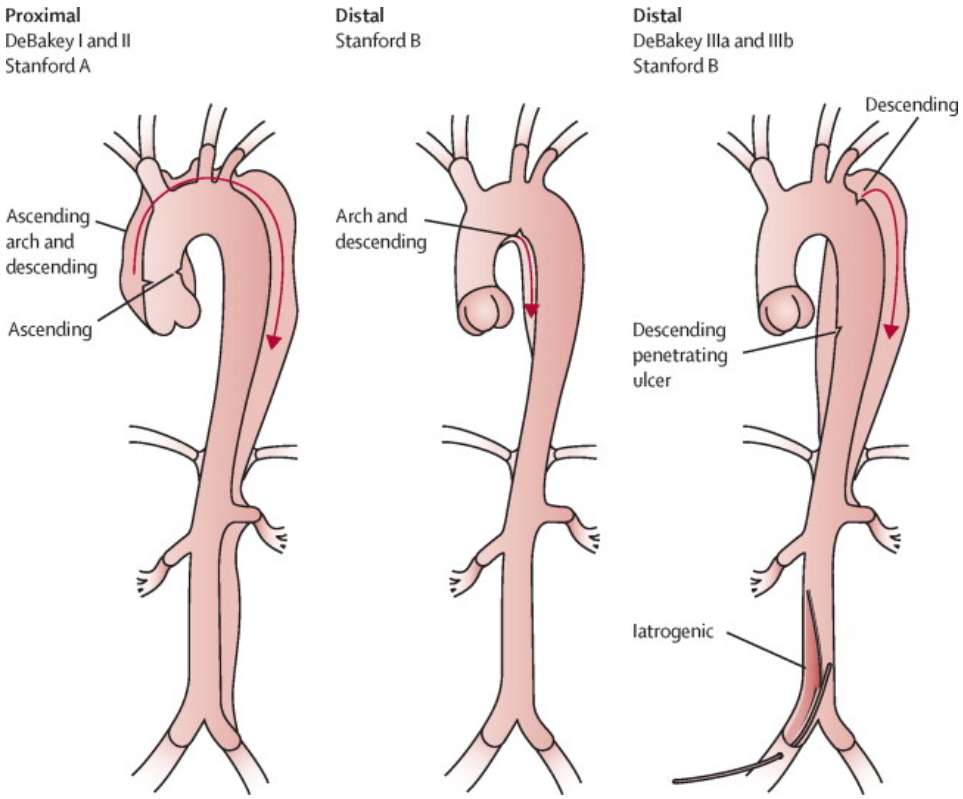


Figure 2.5 The anatomical classification of aortic dissection (Nienaber and Clough, 2015)

The Stanford classification system divides aortic dissections into two groups, Type A aortic dissection and Type B aortic dissection depending on whether the ascending aorta is involved. Type A dissection involves the ascending aorta and can propagate distally to the descending aorta. The dissection which only involves the descending aorta is defined as Type B aortic dissection. Dissections with the involvement of the aortic arch but not the ascending aorta also belong to Type B aortic dissection. Further classification of Type B dissection has been developed with the distinction between complicated and uncomplicated. Dissections with malperfusion, progression, extra-aortic blood collection (high risk in false lumen rupture), or rapid expansion are regarded as complicated dissection, whereas stable conditions are observed in uncomplicated dissection.

In 2013, a new mnemonic-based classification system, DISSECT, was proposed (Dake et al., 2013). This mnemonic classification provides fundamental anatomical and clinical features for the selection of treatment for aortic dissection. The classification system contains six elements: duration of dissection (D), intimal tear location (I), size of the aorta (S), segmental extent (SE), clinical complications (C) and thrombosis of false lumen (T). DISSECT includes more detailed prognostic characteristics of aortic dissection and shows the development of techniques in managing dissection patients.

The diagnosis of aortic dissection is challenging, as similar symptoms are shared with several medical conditions. Although patients usually present chest or back pain (85%), which might be described as sharp, progressive, migrating, or tearing, there is still about 10% who do not complain of pain (Golledge and Eagle, 2008). Imaging techniques are required for confirmation of diagnosis, classification of the dissection, localisation of the tears, and assessment of the urgency of aortic dissection before medical treatment. The mainstream imaging techniques include echocardiography (ECHO), Computed Tomography (CT) and Magnetic Resonance Imaging (MRI).

ECHO is a rapid imaging technique with the use of ultrasound waves to produce images of the vessel. Transthoracic echocardiography (TTE) is favoured because it's portable and fast. Access to patients is allowed during image acquisition which permits its usage under emergence conditions. However, TTE is highly user skill dependent and has limitations of a

narrow view field. Transoesophageal echo (TOE) is preferred for its improved image quality and resolution compared to TTE. Anatomical features, including entry tear and true lumen compression, and the dynamic movement of flap can be obtained by TOE, which provides a sensitivity of 98% and a specificity of 95% in the diagnosis of aortic dissection (Cantrill et al., 2015).

CT is a powerful imaging technique which involves the use of x-ray offering high quality images of patients. In conventional CT scanning, aortic dissection is diagnosed by the presence of two distinct lumens. Contrast-enhanced, Computed Tomography Angiogram (CTA) (Figure 2.6.a), is the most widely used imaging technique in the diagnosis of aortic dissection, due to its high efficiency and wide availability, based on the report from the International Registry of Acute Aortic Dissection (IRAD) (Pape et al., 2015). Before a CTA assessment, the iodinated contrast agents need to be injected to enhance the visibility of vasculature. The image acquisition of CTA is commonly triggered by electrocardiograph (ECG) gating, which enables the CTA to provide medical images at a specific time point during the cardiac cycle. ECG-gated CTA enables three-dimensional reconstruction of the aorta and its branches (Figure 2.6.b), which has enhanced the sensitivity and specificity of the diagnosis of aortic dissection to nearly 100%.

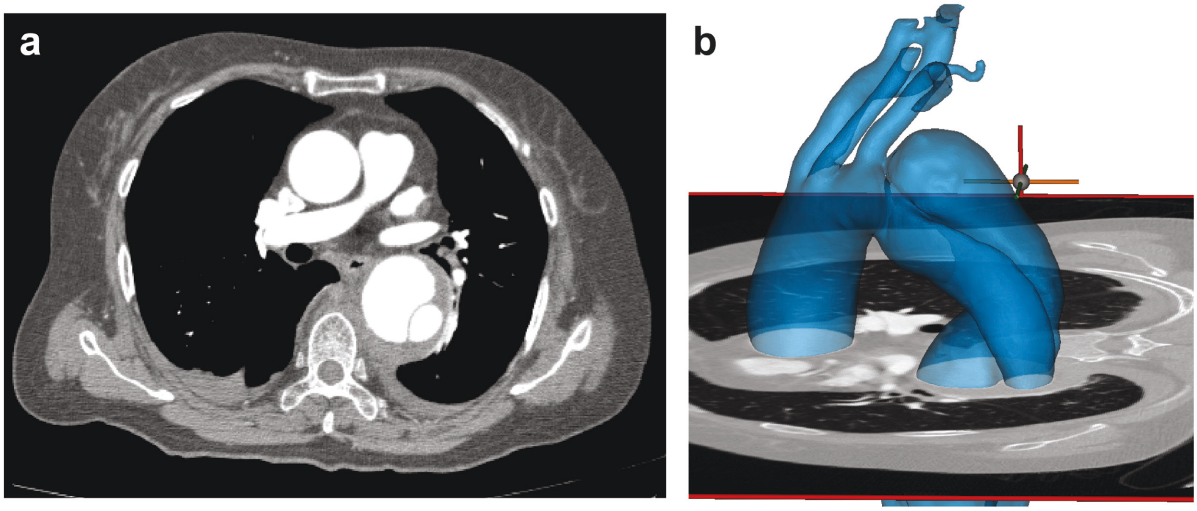


Figure 2.6 CTA image from a patient with Stanford Type B aortic dissection: a. A transverse view of the CTA scan; b. Reconstructed three-dimensional geometry of the dissected aorta.

MRI is considered a more comprehensive diagnostic technique in the assessment of aortic dissection by providing functional information (Nienaber et al., 2016). This technique is based on the use of a strong magnetic field and radio waves to produce highly detailed images of the inner structure of human body. Contrast-enhanced Magnetic Resonance angiography (MRA) is commonly used to evaluate the aorta before and after medical treatment with the injection of gadolinium-based contrast agents, which are preferred due to their less nephrotoxicity than the iodinated agents. Black blood MRI, using spin-echo sequences, can provide anatomical and morphological features of soft tissues, including the shape, size and the thickness of aortic wall. The steady-state free precession (SSFP) cine-MRI imaging provides high contrast between blood and tissue without the need for intravenous contrast administration. In addition to providing anatomical images, phased-contrast magnetic resonance imaging (PC-MRI), which is controlled by electrocardiograph gating, provides time-resolved haemodynamic data of blood flow. However, due to its limited availability and efficiency, MRI is still not the first method for the diagnosis of aortic dissection (Nienaber and Clough, 2015).

2.2.3 Management and outcomes for aortic dissection

The management of aortic dissection is highly dependent on its anatomical features. Initial management of acute aortic dissection aims to limit the propagation through controls of systolic blood pressure and heart rate with the use of drug (Nienaber and Clough, 2015). This practice can also reduce the risk of aortic rupture and maintain the perfusion of distal organs. The management of patients with aortic dissection is summarised in the flowchart shown in Figure 2.7.

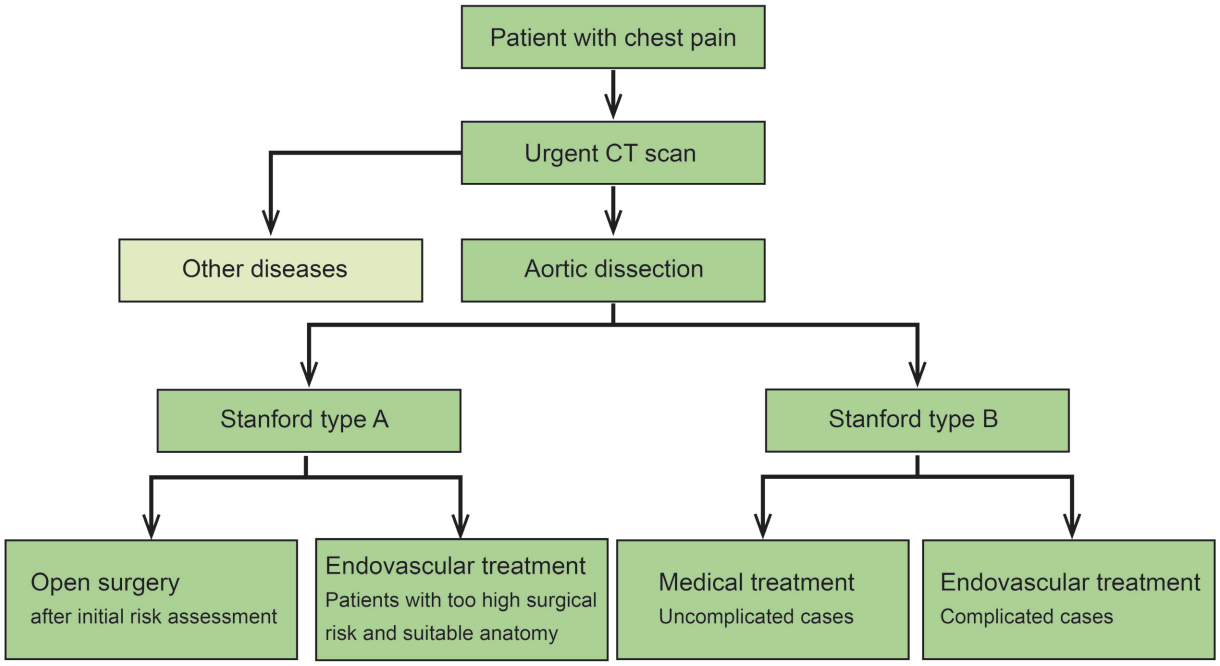


Figure 2.7 Current management of aortic dissection

After diagnosis and initial assessment based on imaging, surgical repair is a common practice for Stanford type A dissection, although in rare cases, hybrid approaches or endovascular therapy can be used. The surgical repair procedure involves reinforcement or replacement of the diseased ascending aorta with a synthetic (Dacron) vascular prosthesis (Figure 2.8.a). Over the last two decades, significant improvement has been made in patient management, image techniques and surgical procedure, which has reduced the in-hospital mortality rate of type A dissection from 31% to 22% ($P < 0.001$). However, surgical repairs of type A dissection which require single-lung ventilation, left heart bypass and cerebrospinal fluid drainage, still have a high mortality of up to 18% ($P < 0.001$) based on data from IRAD (Pape et al., 2015). Approximately 10-30% of the patients with acute type A aortic dissection are considered too high risk for surgical repair and would only receive medical treatment with associated high mortality of ~60% in the intermediate term (Nienaber et al., 2017). Therefore, endovascular repair has been adopted to treat type A aortic dissection patients with high surgical risk and suitable anatomy (Lu et al., 2013).

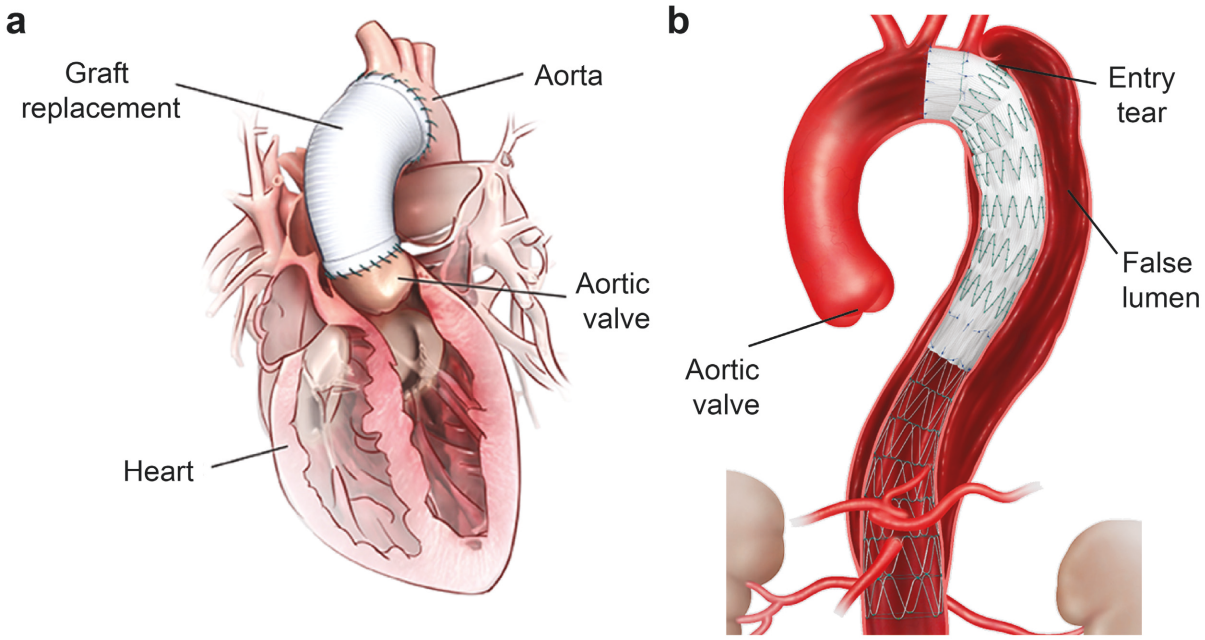


Figure 2.8 Medical interventions for aortic dissection: a. Open surgery procedure for the replacement of ascending aorta in treating type A aortic dissection (Johns Hopkins Medicine, 2021); b. Endovascular aortic repair in treating type B aortic dissection (Cook Medical, 2021a).

The management strategy for type B aortic dissection highly depends on the condition of the patient, including medical treatment, open surgery and endovascular repair. For patients with uncomplicated aortic dissection and stable condition, medical treatment (best medical therapy or BMT) with antihypertensive therapies is usually recommended, which aims to regulate aortic pressure thereby reducing the pressure load on aortic wall. Open surgery for type B aortic dissection is especially risky for patients with malperfusion and can lead to severe outcomes, including irreversible spinal cord injury and death (Nienaber et al., 2005, Nienaber and Clough, 2015). With an in-hospital mortality rate of 17%, open surgery has been widely replaced by endovascular treatment. Endovascular aortic repair (Figure 2.8.b) has now been accepted as the standard treatment for complicated type B aortic dissection with its lower mortality than open surgery (Nienaber and Clough, 2015).

In early studies, the 2-year data from INSTEAD (INvestigation of STEnt grafts in Aortic Dissection) trial showed no difference in mortality between patient treated with BMT plus endovascular repair and those treated with BMT alone (Nienaber et al., 2009). Research data

from the ADSORB (Acute Dissection: Stent graft OR Best medical therapy) trial suggested that BMT plus endovascular repair provided better mid-term outcomes compared to BMT alone (Hughes, 2015). With the improvement of endovascular repair technique and the development of better endografts, endovascular repair has been suggested as the first option to improve late outcomes for uncomplicated type B aortic dissection patients (Xiang et al., 2019).

2.3 Thoracic endovascular aortic repair

Thoracic endovascular aortic repair (TEVAR), which was firstly introduced in 1999 (Nienaber et al., 1999), has been increasingly employed in the treatment of type B aortic dissection (from 7% to 31% over 17 years) (Pape et al., 2015). Due to the less invasive nature of endovascular intervention, TEVAR has been accepted as a standard treatment for type B aortic dissection and a potential alternative treatment for type A aortic dissection in scenarios of prohibitive surgical risk (Nienaber and Clough, 2015).

2.3.1 Thoracic endovascular aortic repair procedure

The first step of a TEVAR procedure is to deliver a stent-graft (SG) proximally to the entry tear of the dissection in its crimped state. Then the position of SG is confirmed with the aid of Digital Subtraction Angiography (DSA) by injecting contrast agents through the delivery system. After the position is confirmed, the SG is released from the delivery system (sheath), and then expands by itself. The proximal entry tear of the dissection is covered by the SG, which reduces blood pressure in the false lumen and restores blood flow in the true lumen (Figure 2.8.b). The position of the deployed SG and blood perfusion are checked by DSA again to verify the outcome of the TEVAR procedure. With altered haemodynamic features in the false lumen, blood starts to thrombose, which helps to stabilise the dissection and is considered one of the desired outcomes post-TEVAR. Furthermore, recent clinical studies have shown positive results of TEVAR for the treatment of uncomplicated acute and chronic dissections. The 5-year outcome from the INSTEAD trial has shown that TEVAR procedure was associated with SG induced false lumen thrombosis in 90.6% of the 140 cases and reduced the aorta-specific mortality rate (Nienaber et al., 2013). The report from IRAD has

shown reduced rate in aortic growth/new aneurysm after TEVAR (62.7%) when compared with medical therapy (73.3%) (Fattori et al., 2013).

2.3.2 Stent-graft for TEVAR

Commercial SG products have been developed by a number of medical device manufacturers in the past decade with several generations of products (Table 2.1). The cover length of commercial products ranges from 40 mm to 250 mm to meet the requirements under complicated clinical conditions. The diameter of SG ranges from 20 mm to 46 mm to satisfy anatomical features of the affected aorta.

Table 2.1 Summary of mainstream stent-graft (SG) products. CB: connecting bar, PBS: proximal bare stent.

Product	Length (mm)	Diameter (mm)	Stent material	Graft material	CB	PBS
Valiant Medtronic Vascular, Santa Rosa, USA	100, 150, 200	22- 46	Nitinol	PET	No	Yes
Talent Medtronic Vascular, Santa Rosa, USA	110- 200	22- 46	Nitinol	PET	Yes	Yes
C-TAG W. L. Gore & Associates, Inc, Flagstaff, USA	100, 150, 200	21- 45	Nitinol	ePTFE	No	No
Zenith TX2 Cook Medical, Bloomington, USA	115- 216	22- 42	Stainless steel	PET	No	No
Relay Bolton Medical, Sunrise, USA	100- 250	22- 46	Nitinol	PET	Yes	No
Ankura Lifetech, Shenzhen, China	40- 200	24- 44	Nitinol	ePTFE	Yes	Yes

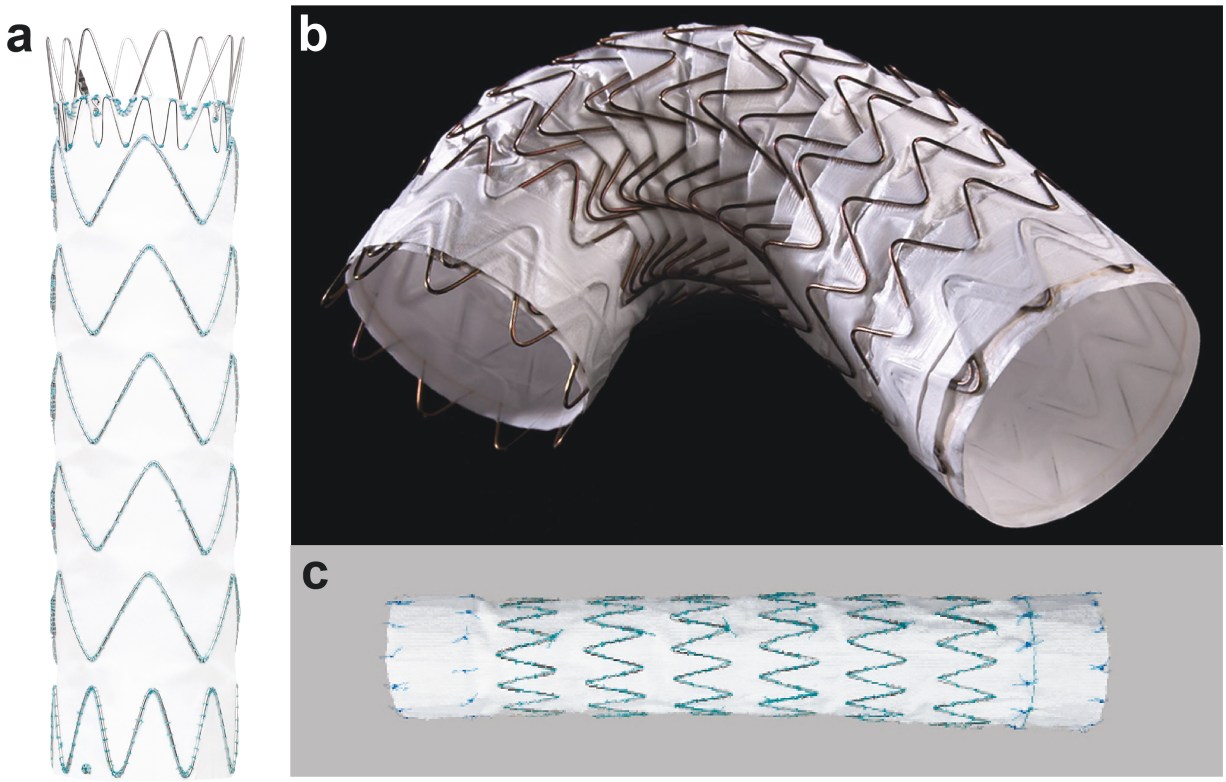


Figure 2.9 Commercial stent-graft products. a. Medtronic Valiant™ Thoracic Stent Graft (Medtronic, 2021); b. GORE® TAG® Conformable Thoracic Stent Graft (Gore Medical, 2021); c. Zenith® TX2® Dissection Endovascular Graft (Cook Medical, 2021b).

SGs are assembled by two main components: metal scaffold and synthetic graft. The woven metal scaffold provides a radial force which enables the SG to expand by itself, prevents its migration under pulsatile blood flow and provides sufficient sealing to the tears with the synthetic graft. The metal scaffold is composed of a series of struts with different patterns or a single helical metal wire (Figure 2.9). The material of the metallic stent is carefully chosen with the consideration of mechanical performance and biocompatibility. Nickel-titanium alloy (Nitinol) is the most commonly used stent material for aortic SG devices, while some products use stainless steel (Demanget et al., 2013). The synthetic graft is commonly made of polyethylene, including Polyethylene terephthalate (PET) fibric and expanded Polytetrafluoroethylene (ePTFE) membrane. The metal struts are sewn or glued to the synthetic graft manually during the manufacture process to complete the product assembly.

In the early generations of commercial SG for TEVAR, a connecting bar (CB) is included which serves the purpose of connecting all the stent struts together to prevent excessive twist of the SG. Some products contain proximal bare stent (PBS) to facilitate the release of SG in the aortic arch and perfusion of the left subclavian artery. In several SG products, a separate stent strut made from a thinner metal wire is sewn to the proximal end of the synthetic graft. This is known as sealing stent strut which is designed to provide extra radial support, to prevent the synthetic graft from folding inward and to guarantee sealing efficiency of the SG (e.g. Valiant SG (Medtronic Vascular, Santa Rosa, USA)). Considering the natural tapering of the aorta along its length, tapered SG product has also been developed (e.g. Valiant SG and Zenith SG (Cook Medical, Bloomington, Ind)). Moreover, in the latest generation of SG devices, special designs allow clinicians to adjust the SG proximal end curvature during TEVAR and open the SG halfway to determine the deployment location (e.g. C-TAG SG (W. L. Gore & Associates, Inc, Flagstaff, USA)) (Farber et al., 2013). These special designs have improved the accuracy in deploying the SG to the targeted locations (Böckler et al., 2021).

2.3.3 Post-TEVAR complications

Although considerable improvement has been made in commercial stent-graft devices along with their clinical applications, treating aortic dissection with TEVAR still has several drawbacks. TEVAR complications, including endoleak, stent induced new entry (SINE) and retrograde type A dissection (RTAD), are associated with the interaction between SG and aortic wall under pulsatile blood pressure. Some of the complications are believed to be strongly correlated with stent-induced biomechanical changes in the aortic wall (Dong et al., 2009).

SINE, an iatrogenic new entry caused by the SG itself excluding those arising from natural dissection progression (Figure 2.10), is associated with Marfan syndrome, proximal bare stent, curved aorta and distal oversizing (Dong et al., 2009, Dong et al., 2010). Dong et al. suggested the spring-back force as a predominant factor in the formation of proximal SINE due to all 16 cases of proximal SINE occurred at the greater curve. Distal SINE cases, occurring at the intimal flap, are associated with the radial force induced by oversized stent-graft. In a previous study, SINE was reported with 3% incidence and a mortality rate of 26%,

calling for an urgent investigation of such complication (Dong et al., 2010). A recent study also suggested a strong correlation between the incidence of SINE and SG oversizing ratio, and SG length (Ma et al., 2017). Based on a more recent review of 1415 cases from seven articles, distal SINE has an incidence of 7.9% and also correlates with distal oversizing (Canaud et al., 2019).

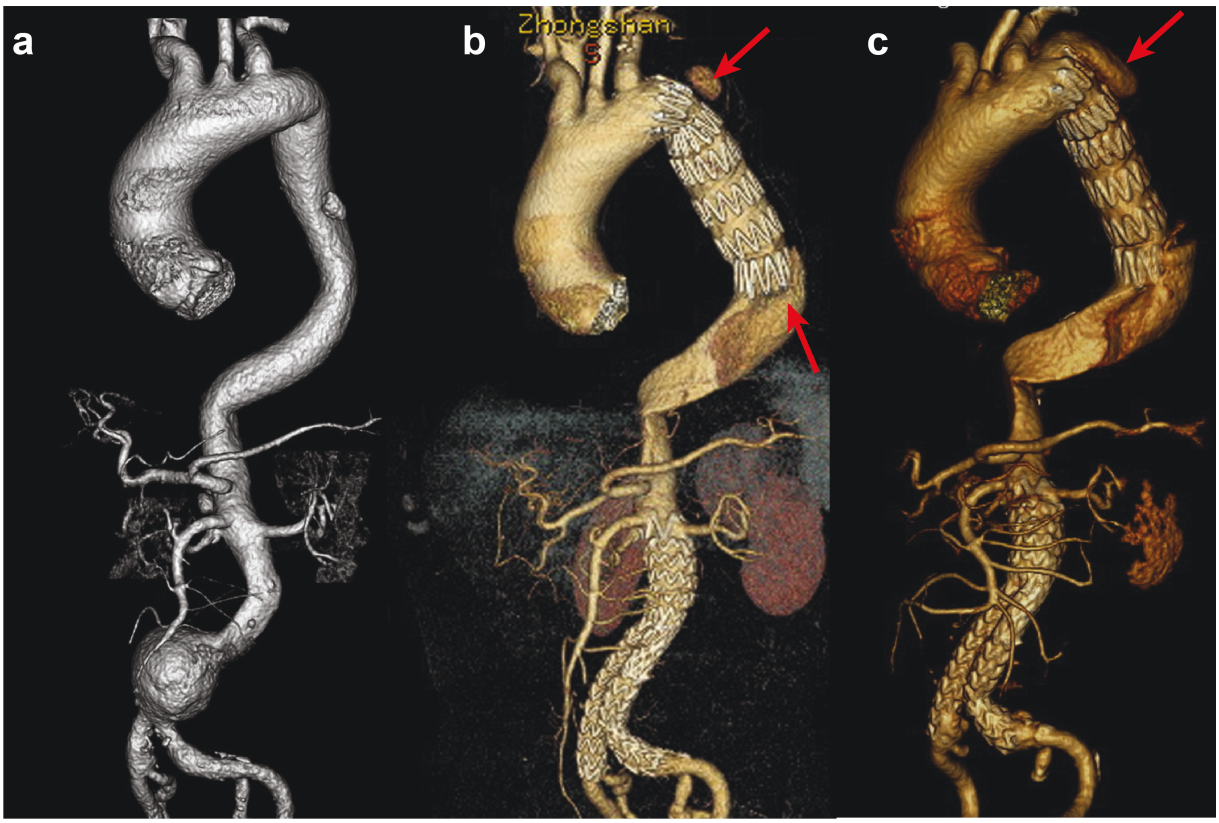


Figure 2.10 A series of computed tomography angiogram (CTA) for a patient who developed distal stent induced new entry (SINE) and retrograde type A aortic dissection (RTAD): a. Preoperative CTA image of the type B aortic dissection patient with partially thrombosed false lumen; b. Proximal endoleak and distal SINE (pointed by red arrows) were found at the 3-month follow-up; c. RTAD (pointed by red arrows) was found at the 18-month follow-up. Adopted from (Ma et al., 2017).

RTAD is caused by a new tear formed as a result of endovascular manipulation which propagates proximally to the aortic arch and ascending aorta, resulting in aortic dissection (Figure 2.10). RTAD was reported as a significantly lethal complication of TEVAR with an incidence of 2% to 16% and mortality ranging from 20% to 57% (Nauta et al., 2015). The location of RTAD is commonly seen in the SG proximal landing zone, which led to attentions

being paid to the proximal end design of SGs, i.e. PBS and non-PBS. However, clinical studies have shown no significant difference in the incidence of RTAD between the PBS and non-PBS patient groups (Ma et al., 2017).

False lumen thrombosis and morphological change of the true lumen are associated with both short- and long-term outcomes of the treatment. Type B aortic dissection cases with partial thrombosis of the false lumen are reported with subsequent false lumen expansion and a higher mortality rate (Kim et al., 2011). The haemodynamic conditions in the false lumen have a strong influence on false lumen thrombosis. Incompatibility between SG and aorta or lack of radial force of the SG can lead to the bird beak effect, which is caused by a gap between the aorta and the proximal end of the SG. This SG malapposition after TEVAR can lead to insufficient sealing, resulting in increased risk of stent-graft migration, endoleak or SG collapse (Ueda et al., 2010).

2.3.4 Summary

The complications of TEVAR for type B aortic dissection, including distal SINE, RTAD, bird beak effect, malapposition, stent-graft migration and endoleak, can lead to catastrophic outcomes and call for improvement of pre-surgical planning, patient selection and design of SG. Considerable efforts have been made to find the risk factors responsible for these complications based on clinical observations. Risk factors, including short SG, excessive distal oversizing ratio and insufficient radial force have been flagged up in clinical studies reported so far (Canaud et al., 2019, Li et al., 2015, Dong et al., 2009, Ma et al., 2017). However, selecting the most appropriate SG size, design and landing position in pre-surgical planning can still be very challenging. Risk levels estimated based on clinical guidelines alone can sometimes be contradictory or very hard to balance: short SG is associated with the occurrence of SINE (Ma et al., 2017), but longer SG may block blood supply to more intercostal arteries, potentially affecting spinal cord perfusion and increasing the risk for paraplegia (Nienaber et al., 2007); large oversizing ratio can guarantee the sealing sufficiency and prevent stent-graft migration, but may increase the risk of SINE (Ma et al., 2017).

From the biomechanical perspective, SG induced forces, including spring-back force and radial force, will lead to stress concentration on the aortic wall and intimal flap. These biomechanical changes can also alter the microstructure of the aortic wall, which may lead to degradation of collagen and elastin fibrils. However, current medical imaging techniques can only provide clinicians with anatomical and haemodynamic information which is insufficient for the evaluation of biomechanical interactions between the stent-graft and the aortic wall. Further biomechanical studies and analyses are required to make in-depth investigation and prediction of post-TEVAR complications in aortic dissection patients.

2.4 Mechanics of the aorta and stent-graft

In the past decades, numerous research studies have been performed aiming to gain insight into the mechanics of both aorta and stent-graft. These research studies played fundamental roles in the biomechanical analysis and simulation of the aortic diseases.

2.4.1 Pre-stress and residual stress in the aorta

The aorta is constantly subjected to complicated in vivo biomechanical conditions. When medical images acquired from an individual patient are used to build 3-dimensional geometry of the aorta, the reconstructed aorta represents its state under the loading from internal blood pressure and interaction with surrounding tissues. As stresses already exist in the aortic wall, this configuration cannot be treated as a zero-stress state in numerical simulations and biomechanical analyses.

Haemodynamics plays a dominate role in determine the aortic configuration, structure, biomechanics and function (Humphrey et al., 2009). The stresses induced by the blood flow and pressure, including wall shear stress, intramural circumferential and axial stress, dominate the primary geometric features of the aortic wall: luminal diameter, wall thickness and the axial length. With its compliant characteristics, when the internal blood pressure load (typical 80-120 mmHg) is removed, the aorta recoils in its luminal diameter and axial length. Apart from the stress induced by blood flow, stresses within the aortic wall are also influenced by its interaction with the surrounding organs and soft tissues.

In the 1960s, in vivo observations suggested that arteries experience less longitudinal deformation than radial deformation (Tickner and Sacks, 1967). During open surgery, arteries showed retraction in the longitudinal direction when cut off, suggesting the existence of longitudinal/axial pre-stretch (Dobrin et al., 1975). The source of axial pre-stretch was subsequently studied by selectively removing structural components from the aortic wall, showing that nearly all the axial pre-stretch in healthy aortic wall is caused by the presence of elastin instead of collagen (Dobrin et al., 1990). The configuration of aorta after being isolated from intraluminal blood pressure and longitudinal pre-stretch is however still not in a zero-stress state (Delfino et al., 1997).

The stress and strain that remain in the aorta when the in vivo load is removed are defined as residual stress and strain. In 1983, observations by Fung confirmed the existence of residual stress in arteries, which was believed to correlate with the growth and remodelling process within the arterial wall (Fung, 1984). The residual stress and strain within arteries was revealed by the famous opening angle experiment, by cutting a segment of unloaded artery along an axial plane (Fung and Liu, 1989). The arterial wall was found to spring open after being cut and reached an asymptotic steady state and zero-stress state in about 15 minutes. In the remarkable study by Fung in 1991, the residual stress within arteries was suggested to make stress distribution more uniform in the wall (Fung, 1991). More recent study has suggested that a radially-cut, unloaded artery only reaches a completely zero-stress state when the tissue material is assumed as homogenous (Taber and Humphrey, 2001). Hence, in the modern viewpoint, this isolated and radially cut configuration should be regarded as nearly zero-stress configuration (Cardamone et al., 2009).

As described above, there are two key mechanical factors that contribute to the in vivo stress state of aorta: the pre-stress induced by normal state of loadings, including intraluminal blood pressure and longitudinal pre-stretch: the residual stress which is independent from the applied external loading.

2.4.2 Biomechanical properties of the aortic wall

Numerous experimental studies can be found in the literature on investigating and describing detailed biomechanical characteristics of the human aortic wall. These

experimental studies typically involve the following steps: harvesting tissue samples, sample storage, cutting samples into desired shapes, preconditioning tissue samples, and performing mechanical tests. Load and stretch data obtained from tensile tests can then be fitted to a constitutive model (strain energy function) to describe the tissue behaviour. To quantify mechanical properties of the aortic wall, both uniaxial and biaxial tensile tests have been reported. Uniaxial tensile testing only measures the tissue behaviour in one direction, while biaxial tensile testing allows simultaneous tensile testing in two directions which circumvent the limitation of non-physiological traction-free boundary conditions inherent in uniaxial tensile testing.

2.2.4.1 Biomechanical characteristics of the human aorta

Uniaxial tensile testing of human aortic tissues was first performed with the homogenous, isotropic material assumption and revealed the hyperelastic behaviour of human aortic wall (Kas'yanov, 1974). A subsequent study found the aortic wall exhibited anisotropic behaviour with higher tensile strength in the circumferential direction than the longitudinal direction (Mohan and Melvin, 1982). Further studies also found differences in stiffness in the longitudinal and the circumferential direction and confirmed anisotropic behaviour of the aortic wall (Raghavan and Vorp, 2000, Vorp et al., 2003). The three layers of aortic wall also exhibit different biomechanical behaviours owing to their microstructural differences (Holzapfel et al., 2000). The influence of other factors on biomechanical behaviour of the aortic wall has also been investigated, including age (Groenink et al., 1999, Guinea et al., 2010), gender (Vande Geest et al., 2006, Tong et al., 2013), and aortic diseases (Sokolis et al., 2012b, Amabili et al., 2020).

In summary, aortic wall is a composite material with anisotropic hyperelastic behaviour, whose biomechanical properties vary among the three layers which have different microstructures. Changes in microstructure of the aortic wall can lead to differences in its biomechanical behaviour. Therefore, finding a suitable constitutive model to describe the complex biomechanical behaviour of aortic tissue is a challenging task.

2.2.4.2 Constitutive models

Aortic tissues show a hyperelastic strain-stress response under tensile load with a typical (exponential) stiffening effect at high strain along with negligible compressibility (Holzapfel et al., 2000). This response is similar to the mechanical behaviour of rubber like materials. Therefore, a series of rubber like constitutive models were proposed in literature and used to represent the strain stiffening behaviour of aortic wall (Chagnon et al., 2015). Polynomial constitutive models, including neo-Hookean model, Mooney-Rivlin model, Ogden model and Yeoh model, were adopted to characterise the nonlinear elastic behaviour of aortic wall with an isotropic assumption (Treloar, 1943, Mooney, 1940, Rivlin, 1948, Ogden, 1972, Yeoh, 1993).

Further constitutive models were developed to capture the anisotropic mechanical behaviour of the aortic wall. One of the general strain energy functions was the Fung's strain energy function which was firstly proposed in 1993 and further developed by Humphrey into a more generic model (Fung, 1993, Humphrey, 1995). Another anisotropic constitutive formulation based on the neo-Hookean model was proposed by Holzapfel et al., known as Holzapfel-Grasser-Ogden (HGO) model which has been widely adopted in the biomechanics community (Holzapfel et al., 2000). The HGO model was further modified to address layer-specific features and to incorporate fibre orientation in recent years (Holzapfel, 2006). This model was further refined by incorporating the fibre damage process to describe discontinuous softening in aortic tissues (Weisbecker et al., 2012). More recently, constitutive models accounting for the dispersion of compressed collagen fibres have been proposed (Holzapfel and Ogden, 2015, Holzapfel et al., 2019).

2.2.4.3 Material parameters for aortic tissues

A series of study adopted the second order Yeoh model to quantify the hyperelastic behaviour of aortic tissues harvested from abdominal and thoracic aortas (Raghavan and Vorp, 2000, Vorp et al., 2003). A layer-specific constitutive model, which was based on neo-Hookean strain energy function, was applied to fit the uniaxial tensile data. Layer-specific and direction-specific material properties for abdominal aortic aneurysms were also

obtained by fitting uniaxial tensile testing results to a modified Mooney-Rivlin strain energy function with an isotropic material assumption (Teng et al., 2015, Wang et al., 2019).

In 2010s, uniaxial tensile tests were still widely employed by researchers to fit the material parameters based on Fung's type material model or HGO material model. Uniaxial tensile testing data obtained in the longitudinal and circumferential directions were fitted into Fung's type material to describe the composite mechanical property of the entire aortic wall and stiffening of aortic tissue during the remodelling of ascending aortic aneurysm (Sokolis et al., 2012a). Similar composite material properties of the descending aortic wall were also obtained by fitting experimental data to the HGO model (Garcia-Herrera et al., 2012). Layer-specific material properties of the thoracic and abdominal aortas were then obtained by fitting the experimental data using the refined HGO model (Weisbecker et al., 2012). Similar layer-specific tensile tests were performed by focusing on the mechanical characteristics of abdominal aortic aneurysm (Sassani et al., 2015a), ascending thoracic aortic aneurysm (Sassani et al., 2015b) and descending thoracic aorta (Amabili et al., 2019). In addition, the mechanical behaviour of aortic wall with type A aortic dissection was quantified (Deplano et al., 2019).

Furthermore, layer-specific collagen fibre orientation was measured by biaxial tensile experiment (Schriefl et al., 2012). Thoracic aorta tissue specimens were tested under both uniaxial tensile and shear loads with detailed material properties for normal, aneurysmal and dissected aortas aiming to determine both the anisotropic mechanical behaviour under tension and material failure criterion of the aortic wall (Sommer et al., 2016). Pealing test of the aortic tissue was also performed aiming to reveal the mechanism and factors contributing to the initiation and propagation of aortic dissection (Tong et al., 2016).

However, very limited experimental work has been carried out so far on tissues obtained from type B aortic dissection patients. Detailed mechanical testing on dissected aortic wall and intimal flap will be needed to obtain their material parameters required for finite element analysis.

2.4.3 Mechanics of stent-graft

As described in section 2.3.2, SGs are commonly assembled by a metallic stent and synthetic graft. As shown in Table 2.1, the metallic stent is commonly made from Nitinol or 316L stainless steel, while the synthetic graft is commonly made from PET fabric or ePTFE membrane. Their mechanical properties are essential parameters required for finite element based biomechanical simulation and analysis of TEVAR.

Nitinol has been increasingly utilised in biomedical applications with its unique shape memory characteristics, surperelasticity, biocompatibility, durability and fatigue resistance (Duerig et al., 1999). When cooled under 5 °C, nitinol alloy fully transforms into martensite phase and becomes highly deformable and easily crimped into the delivery sheath. After the stent is released from the delivery sheath and at a typical body temperature of 37 °C, nitinol recovers to the austenite phase and its originally determined shape with a larger diameter (Kleinstreuer et al., 2008). Nitinol is also recognised for its superelastic behaviour, with which the material is in the austenite phase under no loading conditions and starts to transform into the martensite phase beyond a certain stress. Another commonly used metallic material in SGs is 316L stainless steel, which shows an isotropic linear elasticity before the yield point, undergoes plastic deformation after the yield stress point and fails when the ultimate stress is reached. When 316L stainless steel is used in SGs, unlike its application in balloon-expandable stents, the yield stress should never be reached under normal storage conditions and medical practice.

Mechanical properties of the PET fabric graft are highly dependent on the woven pattern of fibric, which can display anisotropic and orthotropic behaviour under tension loads (Bustos et al., 2016, Demanget et al., 2012). The ePTFE membrane can be considered as an isotropic linear elastic material with a homogenous microstructure (Kleinstreuer et al., 2008). In addition, experimental and numerical studies have been performed to investigate the friction coefficient between SGs and local aorta (Vad et al., 2010, Altnji et al., 2015).

2.5 Numerical models for virtual stent-graft deployment

Fundamental experimental studies provide information on the structure and properties of aortic tissues and how aorta gives rise to its in vivo functions. On the other hand, in-silico studies aim to predict the physiological behaviour of aorta or the interaction between aorta and SGs using material properties measured in-vitro. Numerical models have demonstrated their capability in simulating biological conditions and biomechanical behaviour of the aorta with complex geometry, nonhomogeneous boundary conditions and nonlinear constitutive models (Vorp, 2007). The common numerical practice for these complicated problems is to discretise the field equations into a finite number of unknowns and solve these equations using numerical approximation. Finite element method (FEM) is the common algorithm employed in structure analyses. FEM-based biomechanical models have been developed to simulate a variety of aortic diseases and related medical devices aimed to predict stresses in the aorta under in vivo conditions and to verify the performance of endografts.

2.5.1 Numerical approach to calculate prestress in aortic wall

As discussed in section 2.4.1, the 3D geometry of aorta reconstructed directly from medical imaging represents a configuration under in vivo load, such as blood pressure. Among prestress, longitudinal pre-stretch and residual stress, prestress induced by blood pressure plays a dominate role in determining the stress distribution within the aortic wall (Humphrey et al., 2009). It is also known that the aortic tissue displays nonlinear elasticity when undergoing large strain. Hence, prestress induced by blood pressure cannot be neglected in FEM-based simulations of the aorta. It is necessary to evaluate the stress-state within the aortic wall that corresponds to a given spatial configuration under a known intraluminal blood pressure load.

One of the numerical methods to obtain such a prestressed state is to first determine a reference configuration without internal blood pressure load by inverse design (ID) analysis (Schield, 1967, Lu et al., 2007). An ID analysis calculates the unloaded configuration as unknowns of a nonlinear algebraic system by using the weak form of virtual work principle

(Gee et al., 2010), allowing not only the unloaded configuration but also the strains and stresses associated with a known loading to be obtained. However, since an ID analysis involves both backward and forward simulations, this method is weak in its robustness when applied to complex patient-specific geometry. Gee et al. proposed another method, known as modified updated Lagrangian formulation (MULF) (Gee et al., 2009, Gee et al., 2010). Different from an ID analysis, MULF does not yield an unloaded configuration and only approximates the prestressed state with a forward simulation based on a multiplicative split of the deformation gradient. The MULF method offers improved robustness with physically meaningful results for complex patient-specific geometry.

In addition to the two methods described above, Votta et al. proposed a different method based on forward calculation of prestress tensor directly, which is easy to implement in existing finite element solvers (Votta et al., 2017). Similar to the MULF method, direct calculation of prestress tensor does not require the unloaded configuration and the prestressed configuration is determined as a reference configuration for the forward simulation. The prestress tensor is applied onto the reference configuration to achieve approximate equilibrium with the internal blood pressure. The robustness and high efficiency of this method has been demonstrated in simulations of patient-specific aortic root and aortic coarctation (Votta et al., 2017, Caimi et al., 2020).

2.5.2 Simulation of stent-graft and virtual stent-graft deployment in aorta

Several computational models have been developed to simulate SG and cardiovascular diseases with varying focuses, including the study and optimisation of SG and virtual deployment strategy based on FEM simulations.

During the development of SG, numerical models are usually employed in the optimisation of the design (Abad et al., 2012). Simulations of SG are performed with specific aims, including predicting structural failures and evaluating product performances. Structural failures, including fatigue and fracture, can be estimated with the penalty algorithm based on strain distributions on the metal stent struts (Pelton et al., 2008). Kleinstreuer et al. were the first to formulate a numerical model of SG by incorporating detailed morphological and

mechanical characteristics of nitinol wire and the synthetic graft (Kleinstreuer et al., 2008). Numerical simulations of commercial SG products were performed with their unique geometry and material features to evaluate and compare their bending behaviour and flexibility (Demanget et al., 2012, Demanget et al., 2013). The simulation model can be simplified by reducing the model overall size based on geometric symmetry and adjusting the boundary conditions to improve simulation efficiency (Ghriallais and Bruzzi, 2014). Finite element modelling was also used to optimise detailed SG design in order to improve its fatigue resistance and radial strength (Zhou et al., 2019).

Several FEM-based numerical simulation studies have been published focusing on virtual SG deployment in the aorta. In 2012, De Bock et al. reported their SG deployment simulation in an realistic abdominal aortic aneurysm model, demonstrating a good agreement with the corresponding in-vitro stenting experiment (De Bock et al., 2012). Auricchio et al. were the first to report simulations of SG deployment in a patient-specific ascending aorta with a rigid wall assumption for the aortic wall (Auricchio et al., 2013). The deployment of SG in an abdominal aortic aneurysm model was extended to a compliant artic wall by Perrin et al. who developed a robust morphing methodology to deploy a tubular SG into an idealised geometry (Perrin et al., 2015b) and a double-branched SG into complex patient-specific geometry (Perrin et al., 2015a, Perrin et al., 2016). Other numerical studies further extended the SG deployment simulation in patient-specific aortic aneurysm to more complex scenarios, such as the SG deployment process and the influence of blood flow (Romarowski et al., 2018, Romarowski et al., 2019). Recently, FEM-based simulation of SG deployment has been extended to more complex SG devices and validated in more patient cases showing excellent quantitative agreement with reconstructions from post-intervention CT scans (Derycke et al., 2019, Derycke et al., 2020).

Despite the aforementioned progress in the development and application of FEM-based simulation model for SG deployment in the aorta, virtual SG deployment simulation in aortic dissection is lacking, owing to the complex morphology of aortic dissection and nonlinearity in the simulation of SG deployment. Other than the author's own work, only two other studies employing FEM-based virtual SG deployment in type B aortic dissection have been reported so far (Ma et al., 2018, Meng et al., 2020). These studies were designed to examine

potential correlations between stress concentration and RTAD found in post-TEVAR follow-ups. However, their models neglected prestress in the aorta and intraluminal blood pressure load, making the predicted values of stresses in the aortic wall unrealistic. Up to date, only Hemmler et al. incorporated prestress and the action of blood pressure in their simulations of SG deployment in abdominal aortic aneurysms (Hemmler et al., 2019a, Hemmler et al., 2019b).

Additionally, Chen et al. reported a virtual stenting algorithm based on simplex deformable mesh method and identified a correlation between large stent-induced deformation and distal SINE (Chen et al., 2018). However, their models were built based on post-TEVAR CT scans, making this method unsuitable for pre-surgical planning when only pre-TEVAR CT scans are available.

2.6 Summary and research objectives

In this chapter, an overview of the cardiovascular system was presented with a special focus on aortic dissection. As a critical medical condition, aortic dissection is associated with high mortality and morbidity rates. TEVAR has been widely accepted as the standard treatment for type B aortic dissection and increasingly used in treating selective type A aortic dissection. Although TEVAR has been a huge success so far, its associated complications, including SINE, RTAD and stent-graft migration, are still not negligible and can lead to catastrophic outcomes. Clinical observations suggest that anatomical and biomechanical factors play an important role in the development of TEVAR-induced complications.

In the past two decades, significant progress has been made in understanding the biomechanics of human aorta and computational modelling of the mechanical behaviour of aortic wall. With advances in computational algorithms and computer hardware, FEM-based models have been increasingly used for patient-specific biomechanical analysis of the aorta and its interactions with medical implants, but a comprehensive model for virtual SG deployment in aortic dissections is lacking.

The aim of this PhD project is to develop a finite element modelling framework for virtual SG deployment in aortic dissections suitable for patient-specific applications. This virtual SG

deployment model will not only help to understand the role of biomechanical factors in post-TEVAR complications, but also serve as a pre-surgical planning tool to assist clinicians in selecting the most appropriate SG for individual patient.

Chapter 3

Mathematical models and numerical procedure

3.1 Basic concepts of continuum mechanics

3.1.1 Displacement and deformation

The (fixed) reference configuration (undeformed configuration) of a continuum body $\boldsymbol{\mathcal{B}}$ is defined as Ω_0 with a typical position $\mathbf{X}$ corresponding to the fixed reference time, i.e. $\mathbf{X} \in \Omega_0$ (Figure 3.1). The motion $\boldsymbol{\chi}$ is assumed to be uniquely invertible which transforms $\mathbf{X}$ to a position:

$$\mathbf{x} = \boldsymbol{\chi}(\mathbf{X}, t) \in \Omega \tag{3.1}$$

The new region Ω is defined as the current configuration (deformed configuration). The displacement field of a typical point relating to its position $\mathbf{X}$ at time t can be expressed as

$$\mathbf{u}(\mathbf{X}, \mathrm{t}) = \boldsymbol{\chi}(\mathbf{X}, t) - \mathbf{X} \tag{3.2}$$

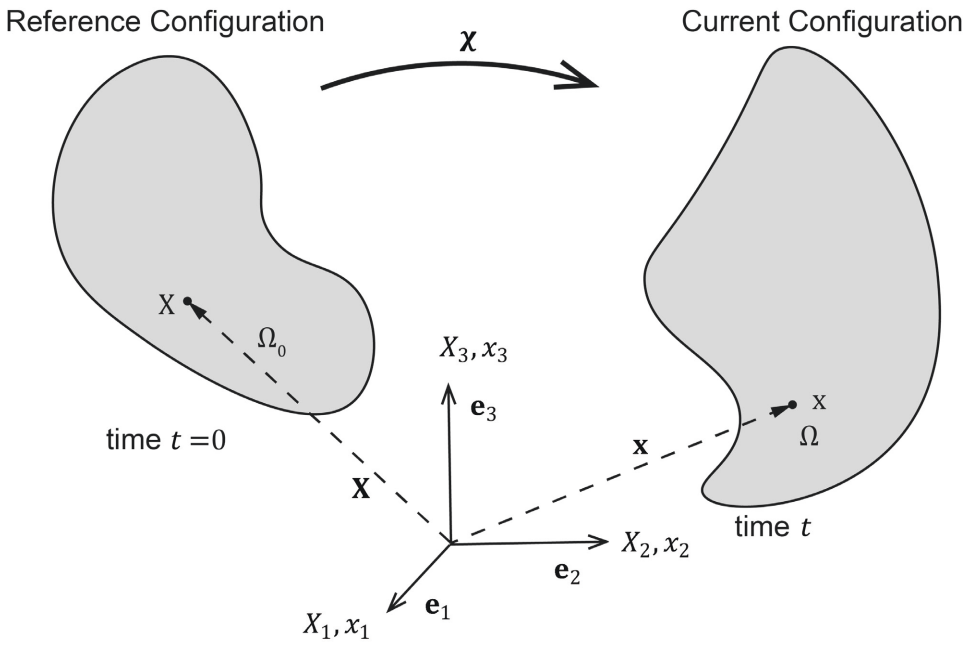


Figure 3.1 Configuration and motion of a continuum body.

Consider two neighbouring points, located at $\mathbf{X}$ and $\mathbf{X} + d\mathbf{X}$ in the reference configuration (Figure 3.2), in the current configuration we have

$$d\mathbf{x} = \boldsymbol{\chi}(\mathbf{X} + d\mathbf{X}, t) - \boldsymbol{\chi}(\mathbf{X}, t) \tag{3.3}$$

For an infinitesimal element $d\mathbf{X}$ and assuming continuity in the displacement field, performing first-order Taylor expansion of $\boldsymbol{\chi}(\mathbf{X}, t)$ near $\mathbf{X}$ at time t gives,

$$\boldsymbol{\chi}(\mathbf{X} + d\mathbf{X}, t) = \boldsymbol{\chi}(\mathbf{X}, t) + \nabla_{\mathbf{X}} \boldsymbol{\chi}(\mathbf{X}, t) d\mathbf{X} \tag{3.4}$$

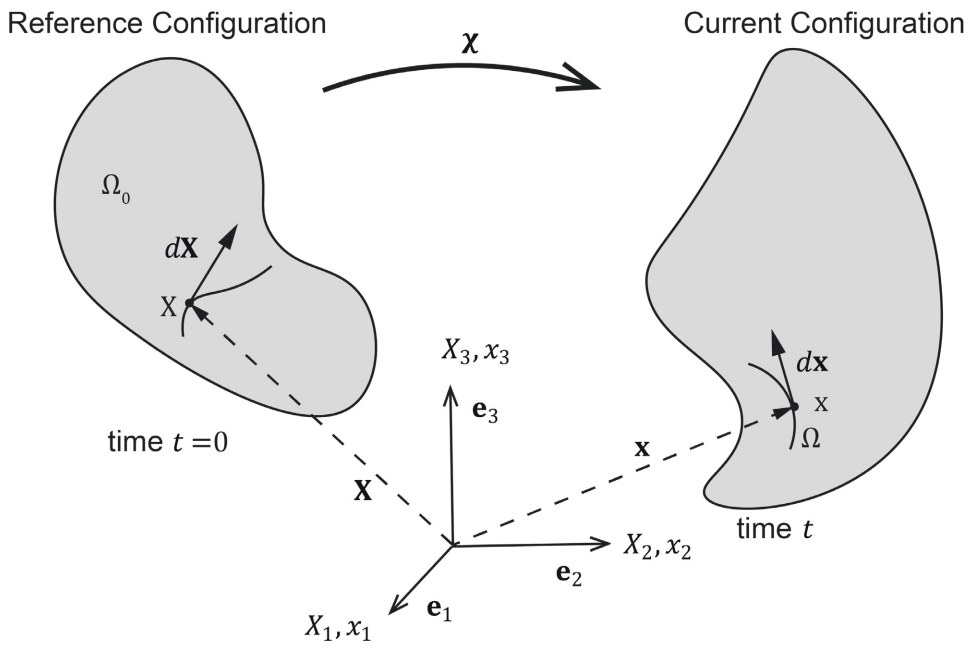


Figure 3.2 Deformation of a continuum body.

Equation (3.3) can be rewritten as

$$d\mathbf{x} = \nabla_{\mathbf{X}} \boldsymbol{\chi}(\mathbf{X}, t) d\mathbf{X} = \mathbf{F}(\mathbf{X},\mathrm{t}) d\mathbf{X} \tag{3.5}$$

$$\mathbf{F}(\mathbf{X},\mathrm{t}) = \frac{\partial \boldsymbol{\chi}(\mathbf{X},t)}{\partial \mathbf{X}} \tag{3.6}$$

where $\mathbf{F}$ is called the deformation gradient tensor and characterises the map from $d\mathbf{X}$ in reference configuration to $d\mathbf{x}$ in current configuration. J is the determinant of gradient $\mathbf{F}$

$$J=\det(\mathbf{F}) \tag{3.7}$$

which is known as the volume ratio and must be satisfied under the incompressible assumption. The deformation gradient $\mathbf{F}$ can be decomposed into a pure stretch and a pure rotation as

$$\mathbf{F} = \mathbf{R}\mathbf{U} \tag{3.8}$$

$$\mathbf{R}^{\mathrm{T}}\mathbf{R} = \mathbf{I}, \quad \mathbf{U} = \mathbf{U}^{\mathrm{T}} \tag{3.9}$$

where $\mathbf{U}$ is the right stretch tensor, $\mathbf{R}$ is the rotation tensor and $\mathbf{I}$ denotes the unit tensor.

3.1.2 Strain and stress

Strain is used to measure the deformation in terms of a given arbitrary transform of the continuum body $\boldsymbol{\mathcal{B}}$ by vanishing the rigid body motion. Consider an infinitesimal element in the reference configuration, the length can be measured as

$$dL^2 = d\mathbf{X} \cdot d\mathbf{X} \tag{3.10}$$

In the current configuration, the length is

$$dl^2 = d\mathbf{x} \cdot d\mathbf{x} = \mathbf{F}d\mathbf{X} \cdot \mathbf{F}d\mathbf{X} = d\mathbf{X}\mathbf{F}^{\mathrm{T}}\mathbf{F}d\mathbf{X} = d\mathbf{X} \cdot \mathbf{C} \cdot d\mathbf{X} \tag{3.11}$$

where $\mathbf{C}$ is the right Cauchy-Green tensor, defined by

$$\mathbf{C} = \mathbf{F}^{\mathbf{T}}\mathbf{F} \tag{3.12}$$

Introducing the mutually orthogonal and normalised set of eigenvectors $\mathbf{a}_i$ (i = 1,2,3) (also known as principal referential directions) and the corresponding eigenvalues λ_i^2 (i = 1,2,3) (λ_i is also known as principal stretches) of the right stretch tensor $\mathbf{U}$, a spectral decomposition can be performed over $\mathbf{C}$:

$$\mathbf{C} = \sum_{i=1}^{3} \lambda_i^2 \mathbf{a}_i \otimes \mathbf{a}_i \tag{3.13}$$

Invariants of $\mathbf{C}$ are expressed as

$$I_1 = \mathrm{tr}(\mathbf{C}) = \lambda_1^2 + \lambda_2^2 + \lambda_3^2 \tag{3.14}$$

$$I_2 = \frac{1}{2}[\mathrm{tr}(\mathbf{C})^2 - \mathrm{tr}(\mathbf{C}^2)] = \lambda_1^2\lambda_2^2 + \lambda_2^2\lambda_3^2 + \lambda_3^2\lambda_1^2 \tag{3.15}$$

$$I_3 = \det(\mathbf{C}) = \lambda_1^2\lambda_2^2\lambda_3^2 = J^2 \tag{3.16}$$

The Green-Lagrange strain tensor is introduced as $\mathbf{E}$, defined by

$$dl^2 - dL^2 = 2d\mathbf{X} \cdot \mathbf{E} \cdot d\mathbf{X} \tag{3.17}$$

$$\mathbf{E} = \tfrac{1}{2}(\mathbf{C} - \mathbf{I}) \tag{3.18}$$

which measures the difference of the square of the length of an infinitesimal element in the reference and current configuration. The Green-Lagrange strain tensor **E** can also be expressed in terms of displacement gradient by

$$\mathbf{E} = \frac{1}{2}((\nabla \mathbf{u})^{\mathrm{T}} + \nabla \mathbf{u} + (\nabla \mathbf{u})^{\mathrm{T}} \cdot \nabla \mathbf{u}),\ E_{ij} = \frac{1}{2}\left(\frac{\partial u_i}{\partial X_j} + \frac{\partial u_j}{\partial X_i} + \frac{\partial u_i}{\partial X_j}\frac{\partial u_j}{\partial X_i}\right) \tag{3.19}$$

The aortic tissue often undergoes large deformation under in vivo loading conditions. However, it is also vital to note the strain under small deformation, which is fundamental in nonlinear analysis. Under the small deformation assumption, the quadratic term $(\nabla \mathbf{u})^{\mathrm{T}} \cdot \nabla \mathbf{u}$ can be neglected in Equation 3.19, and the Green-Lagrange strain tensor **E** can be simplified to the small strain tensor **ε**:

$$\boldsymbol{\varepsilon} = \frac{1}{2}((\nabla \mathbf{u})^{\mathrm{T}} + \nabla \mathbf{u}), \varepsilon_{ij} = \frac{1}{2}\left(\frac{\partial u_i}{\partial X_j} + \frac{\partial u_j}{\partial X_i}\right) \tag{3.20}$$

Stresses measure the internal forces between neighbouring particles within a continuum body when an arbitrary force acts on the body. Arbitrary forces acting on the external boundary surface of a given body is defined as external forces. Then let the body be cut by a plane at a given point **X**, where the local normal direction of the infinitesimal surface element $ds \in \partial\Omega$ is marked by the unit vector **n** (Figure 3.3.a). The force acting at the surface element can be defined by

$$d\mathbf{f} = \mathbf{t}ds = \mathbf{T}dS \tag{3.21}$$

where **t** represents the Cauchy traction vector (force measured per unit surface area in the current configuration), and **T** represents the first Piola-Kirchhoff traction vector (forces measured per unit surface area in the reference configuration).

According to the Cauchy's stress theorem, there exist unique tensor fields **σ** and **P** such that

$$\mathbf{t} = \boldsymbol{\sigma} \cdot \mathbf{n} \tag{3.22}$$

$$\mathbf{T} = \mathbf{P} \cdot \mathbf{N} \tag{3.23}$$

where **σ** denotes a symmetric spatial tensor called Cauchy stress tensor, while **P** is known as the first Piola-Kirchhoff stress tensor.

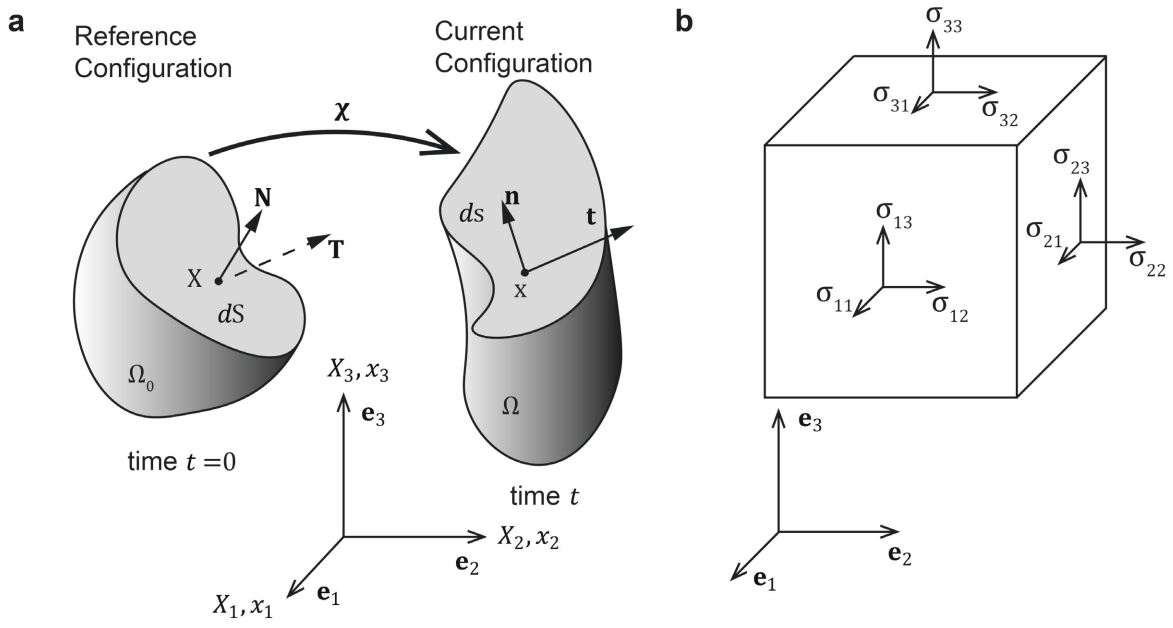


Figure 3.3 Schematic illustration of traction and stress tensor: a. Traction vectors acting on an infinitesimal surface with unit normal **n**, b. Components of stress tensor.

In biomechanical analysis, the distribution of Cauchy stress tensor **σ** within the aortic wall can be very complex to describe. The Cauchy stress tensor **σ** can be projected along an orthonormal basis $[\mathbf{e}_1, \mathbf{e}_2, \mathbf{e}_3]$ and expressed by matrix representation in nine components σ_{ij} $(i, j = 1,2,3)$ (Figure 3.3.b):

$$[\boldsymbol{\sigma}] = \begin{bmatrix} \sigma_{11} & \sigma_{12} & \sigma_{13} \\ \sigma_{21} & \sigma_{22} & \sigma_{23} \\ \sigma_{31} & \sigma_{32} & \sigma_{33} \end{bmatrix} \tag{3.24}$$

By solving the eigenvalue equation, three principal normal stresses σ_i $(i = 1,2,3)$ can be derived from the stress tensor **σ** in corresponding principal directions $\mathbf{a}_i$ $(i = 1,2,3)$:

$$\mathbf{a} \cdot \boldsymbol{\sigma} = \sigma \mathbf{a} \tag{3.25}$$

Three stress terms calculated from the principal stresses, maximum principal stress (MPS) σ_{MPS}, von Mises tress (also known as effective stress) (VMS) σ_{VMS} and maximum shear stress (MSS) τ_{MSS}, will be employed to describe stress levels within the aortic wall in the following chapters, which are defined as:

$$\sigma_{MPS} = \max\{\sigma_1, \sigma_2, \sigma_3\} \tag{3.26}$$

$$\sigma_{VMS} = \sqrt{\frac{1}{2}[(\sigma_1 - \sigma_2)^2 + (\sigma_2 - \sigma_3)^2 + (\sigma_3 - \sigma_1)^2]} \tag{3.27}$$

$$\tau_{MSS} = \max\left\{\frac{\sigma_1 - \sigma_2}{2}, \frac{\sigma_2 - \sigma_3}{2}, \frac{\sigma_1 - \sigma_3}{2}\right\} \tag{3.28}$$

3.1.3 Governing equations

The fundamental balance principles, including the mass conservation, the momentum balance principle and energy conservation, are valid in all branches of continuum mechanics.

Assuming V is the volume of a continuum body $\boldsymbol{\mathcal{B}}$, the mass conservation of a closing system should follow:

$$\rho_0(\mathbf{X}) = \rho(\boldsymbol{\chi}(\mathbf{X}, t), t)J(\mathbf{X}, t) \tag{3.29}$$

where ρ_0 and ρ are the mass densities of the reference and current configuration respectively. For aortic tissues, which are usually assumed to be incompressible, ρ_0 should be equal to ρ.

The momentum balance of a continuum body is described using Cauchy's first equation of motion with body force **b** and displacement field **u**:

$$\nabla\boldsymbol{\sigma} + \mathbf{b} = \rho\ddot{\mathbf{u}} \tag{3.30}$$

If the acceleration $\ddot{\mathbf{u}}$ is assumed to be zero for all $\mathbf{x} \in \Omega$, the problem can be considered as quasi-static, and the equation becomes:

$$\begin{gathered} \nabla\boldsymbol{\sigma} + \mathbf{b} = \mathbf{0} \\ \mathbf{u} = \bar{\mathbf{u}} \ \text{ on } \partial\Omega_{\mathrm{u}} \\ \mathbf{t} = \boldsymbol{\sigma} \cdot \mathbf{n} \ \text{ on } \partial\Omega_{\sigma} \end{gathered} \tag{3.31}$$

which is referred as Cauchy's equation of equilibrium, where $\bar{\mathbf{u}}$ and **t** are the prescribed displacement and traction on the boundary surface $\partial\Omega_{\mathrm{u}}$ and $\partial\Omega_{\sigma}$ respectively.

Let the scalar functions W_{ext} and $W_{\boldsymbol{int}}$ be the potential energy of external loading (external potential energy) and the total strain energy (internal potential energy) respectively, the total potential energy can be expressed as:

$$W = W_{ext} + W_{\boldsymbol{int}} \tag{3.32}$$

For a dynamic process of a continuum solid, the sum of total potential energy and kinematic energy K is conserved:

$$W_{int} - W_{\boldsymbol{ext}} + K = \text{const with } W_{\boldsymbol{int}} = \int_{\Omega} \Psi \, dV \tag{3.33}$$

where Ψ denotes the strain-energy density function and will be further discussed in the next section.

3.2 Hyperelastic material model used for the aortic wall

A constitutive law is used to describe the inherent material property by using the relationship between strain/stretch and stress/forces. As described in Chapter 2 (section 2.4.2), aortic tissues display anisotropic hyperelastic behaviour due to their complex microstructure. In this study, the aortic wall is assumed as an incompressible, isotropic hyperelastic material. The anisotropic mechanical behaviour of the aortic wall is ignored because anisotropic material parameters for dissected aortic tissues are lacking, while uniaxial testing data on multiple aortic dissection tissue samples were provided by our collaborators. The Yeoh hyperelastic model (also known as reduced polynomial model) is adopted, which is commonly used to describe rubber like materials, and has also been employed to describe the mechanical behaviour of aortic wall (Vorp et al., 2003). The strain energy function of the Yeoh model can be expressed as

$$\Psi = c_{10}(\bar{I}_1 - 3) + c_{20}(\bar{I}_1 - 3)^2 + c_{30}(\bar{I}_1 - 3)^3 \tag{3.34}$$

where c_{10}, c_{20}, c_{30} are material parameters, $\bar{I}_1$ is the first deviatoric invariant defined as

$$\bar{I}_1 = \bar{\lambda}_1^2 + \bar{\lambda}_2^2 + \bar{\lambda}_3^2 \tag{3.35}$$

where the deviatoric stretch ratios $\bar{\lambda}_i = J^{-\frac{1}{3}}\lambda_i$, $i = 1,2,3$, with J being the total volume ratio and λ_i the principal stretches.

Under the isothermal and incompressible assumption, $J = 1$, we can have

$$\lambda_1\lambda_2\lambda_3 = 1 \tag{3.36}$$

Under uniaxial loading conditions,

$$\lambda_1 = \lambda\,, \qquad \lambda_2 = \lambda_3 = \frac{1}{\sqrt{\lambda}} \tag{3.37}$$

the principal stress can be derived from the strain energy function by:

$$\sigma_i = \lambda_i \frac{\partial \Psi}{\partial \lambda_i} = \lambda_i \frac{\partial \Psi}{\partial I_1}\frac{I_1}{\lambda_i} \tag{3.38}$$

Therefore, with uniaxial tensile loading, the principal stress σ along the tensile direction can be expressed by

$$\sigma = 2\left(\lambda^2 - \frac{1}{\lambda}\right)\sum_{i=1}^{3} i c_{i0}\left(\lambda^2 + \frac{2}{\lambda} - 3\right)^{i-1} \tag{3.39}$$

where λ is the stretch ratio. The Cauchy stress σ and the stretch ratio λ can be calculated from the measured loading force and the distance between the grips in the uniaxial tensile experiment. The material parameters that describe the mechanical behaviour of the tissue, c_{10}, c_{20}, c_{30}, can be fitted by using the least square fitting method based on experimental data points. In Chapter 4 and Chapter 5, this method was employed to produce material parameters for type B aortic wall tissues, type A aortic wall tissue and the intimal flap.

3.3 Finite element modelling with Abaqus

Finite element method (FEM) has been widely used to solve nonlinear structural mechanics problems, including biomechanical behaviour of the aorta with complex geometry and physiological boundary conditions. Several proprietary finite element structural analysis software packages are available; among these Abaqus (Dassault Systèmes, France) has been a popular choice in the biomechanics research community. Because of its outstanding

robustness in tackling non-linear contact problems, Abaqus Explicit is adopted to build the virtual SG deployment simulation framework in this thesis.

In FEM simulations, the continuum body is discretised into finite elements which are interconnected at nodal points on element boundaries. Abaqus Explicit is based on the implementation of an explicit integration rule along with the use of a diagonal mass matrix, where acceleration terms can be calculated as:

$$\ddot{\mathbf{u}}^{(i)} = \mathbf{M}^{-1}\left(\mathbf{f}^{(i)} - \mathbf{I}_{\mathbf{f}}^{(i)}\right) \tag{3.40}$$

where $\mathbf{M}$ is the diagonal lumped mass matrix, $\mathbf{f}$ is the applied load vector, and $\mathbf{I_f}$ is the internal force vector. The superscript i refers to the increment number.

By adopting a central difference explicit time integration algorithm, the solution can be expressed as:

$$\dot{\mathbf{u}}^{\left(i+\frac{1}{2}\right)} = \dot{\mathbf{u}}^{\left(i-\frac{1}{2}\right)} + \frac{\Delta t^{(i+1)} + \Delta t^{(i)}}{2}\ddot{\mathbf{u}}^{(i)} \tag{3.41}$$

$$\mathbf{u}^{(i+1)} = \mathbf{u}^{(i)} + \Delta t^{(i+1)}\dot{\mathbf{u}}^{\left(i+\frac{1}{2}\right)} \tag{3.42}$$

where $\dot{\mathbf{u}}$ is velocity, $\ddot{\mathbf{u}}$ is acceleration, Δt is stable increment time and $i - \frac{1}{2}$ and $i + \frac{1}{2}$ refer to the midincrement values. The central difference integration scheme is explicit in that the kinematic state can be advanced using known values of $\dot{\mathbf{u}}^{\left(i-\frac{1}{2}\right)}$ and $\ddot{\mathbf{u}}^{(i)}$ from the previous increment. Then the element strain increments $d\varepsilon$ can be calculated and the stresses at increment $i + 1$ can be calculated from constitutive equations.

The explicit integration operator is conditionally stable, so that the time increment must satisfy

$$\Delta t \leq \frac{2}{\omega_{max}} \tag{3.43}$$

where ω_{max} is the maximum element eigenvalue. A conservative estimate of the stable time increment is given by the minimum value for all elements in the model. The above stability limit can be written as:

$$\Delta t = \min\left(\frac{l_c}{c^d}\right) \tag{3.44}$$

where l_c is a characteristic length of element and c^d is the dilatational wave speed of the material.

3.4 Contact algorithm

The process of deploying SG in a targeted aorta involves complicated interactions among multiple objects. Contacts between objects are modelled using the general contact formulation with penalty method in Abaqus Explicit. After the modelled objects are meshed into finite elements, the surfaces of the objects under contact relation can be represented by contact surfaces. Under the surface-to-surface contact discretisation, one master and one slave surface are defined, and the contact formulation is enforced in an average sense over regions nearby the slave nodes (Figure 3.4.a). The averaging regions are approximately centred on slave nodes, so each contact constraint will predominantly involve one slave node but will also involve adjacent slave nodes (Abaqus User's Manual, 2019).

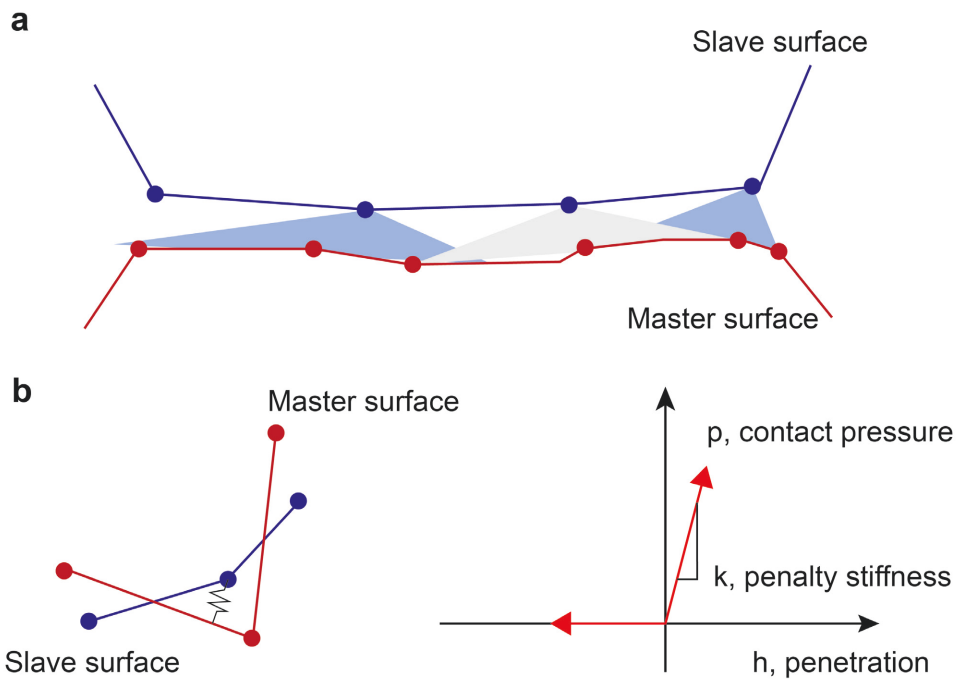


Figure 3.4 Discretisation (a) and enforcement (b) of contact formulation.

The contact formulation is enforced by a penalty method to approximate hard contacts. The penalty method works like a spring to bring back the penetrating node to the surface (Figure 3.4.b). The "spring" stiffness that relates the contact force to the penetration distance is chosen automatically by Abaqus Explicit, such that the effect on the time increment is minimal yet the allowed penetration is not significant in most analyses. Then the finite sliding formulation is adopted in terms of contact evolution upon sliding between contact surfaces, which allows for arbitrary separation, sliding, and rotation of the surfaces. In the finite sliding formulation, points under contact interaction on the master surface are updated using true representations of the master surface (Abaqus User's Manual, 2019). The friction between contact surfaces is modelled by using the Coulomb friction model, under which no relative motion occurs if the equivalent frictional stress,

$$\tau_{eq} = \sqrt{\tau_1^2 + \tau_2^2} \tag{3.45}$$

is less than the critical frictional stress τ_{cirt}. The critical stress is proportional to the contact pressure given by,

$$\tau_{cirt} = \mu p \tag{3.46}$$

where μ is the friction coefficient. The friction coefficient can vanish when a 'smooth friction' is defined between contact surfaces and can become infinite when a 'rough friction' is defined to restrict sliding between contact surfaces. In the simulations presented in this thesis, the friction coefficient between the SG and inner surface of the aorta is defined as 0.1 unless specified (Vad et al., 2010). This value was obtained based on the pull out force and radial force recorded in an experimental study where commercial self-expanding SGs were deployed and pulled out from polymeric cylinders (Vad et al., 2010).

3.5 Aorta geometry reconstruction and mesh generation

All patient-specific geometries used in this thesis have been reconstructed from CTA scans by using the commercial medical image processing software Mimics (Materialise, Leuven), which provides a set of powerful functions for image segmentation, reconstruction,

smoothing and anatomical measurements. Different from traditional segmentation workflow reported by previous studies based on patient-specific geometry of aortic dissections, a purpose-built segmentation and reconstruction workflow has been developed in this study which allows the intimal flap to be segmented as a separate component from the aortic wall.

3.5.1 Image segmentation and geometry reconstruction

After the CTA images are imported into Mimics, a greyscale threshold is set to create a raw segmentation mask including the aorta and other regions which are within the same threshold range (Figure 3.5). Then the region of aorta can be separated from the raw mask by using mask cropping, mask splitting, region growing and manual operations. Since manual operations are involved in the segmentation process, inter-observer errors have been evaluated by comparing the segmentation mask areas on each image slice obtained by two independent observers. The results show that the difference between two observers was 1.92 ± 1.26% for pre-TEVAR segmentation and 0.93 ± 1.31% for post-TEVAR segmentation based on one patient. Detailed results on the analysis of inter-observer errors can be found in Appendix A.

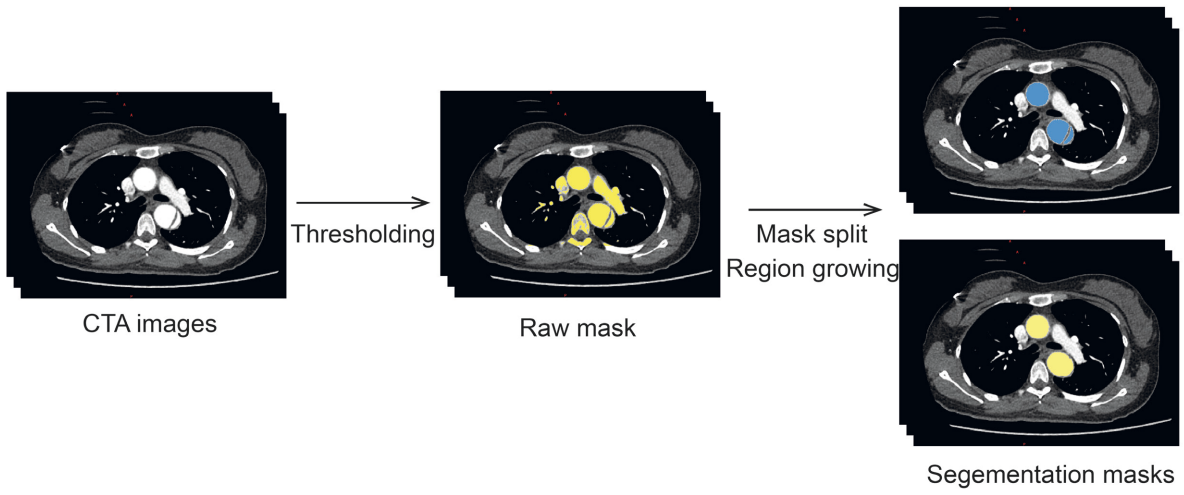


Figure 3.5 Workflow of image segmentation in Mimics.

Two segmentation masks are defined on the pre-TEVAR CTA images: segmentation mask A represents the blood flow lumen, while mask B represents the 'outer surface of aortic wall' by enclosing true lumen, false lumen and the intimal flap. Details of Boolean calculations to create the intimal flap and outer wall structure differ depending on whether the false lumen is thrombosed or not. If it is not thrombosed, the false lumen can be enhanced by contrast agent in CTA image which allows clear visualisation of the intimal flap (the gap between true and false lumen) (Figure 3.6.a). Boolean calculation is first performed by subtracting mask A from mask B to obtain the segmentation of intimal flap. The aortic wall is then created from mask B which is extruded outwardly by a uniform thickness. The two components, intimal flap and aortic wall, are combined to produce the geometric structure of aortic dissection (Figure 3.6.b).

If the false lumen is fully or partially thrombosed, blood perfusion would be limited making the false lumen difficult to be distinguished from intimal flap (Figure 3.7.a). Therefore, mask A which represents the blood flow domain only includes the true lumen, while mask B still includes the true lumen, false lumen and intimal flap. The first step is to extrude the mask A surface outwardly by a uniform thickness to create a TL structure. Then the combined surface is offset outwardly by a uniformed thickness, resulting in the aortic wall structure (Figure 3.7.b). Boolean operation is performed by subtracting the outer wall structure from the TL structure to obtain the intimal flap structure (Figure 3.7.c), which is followed by the combination of the aortic wall and intimal flap to finishing the creation of aortic dissection geometry.

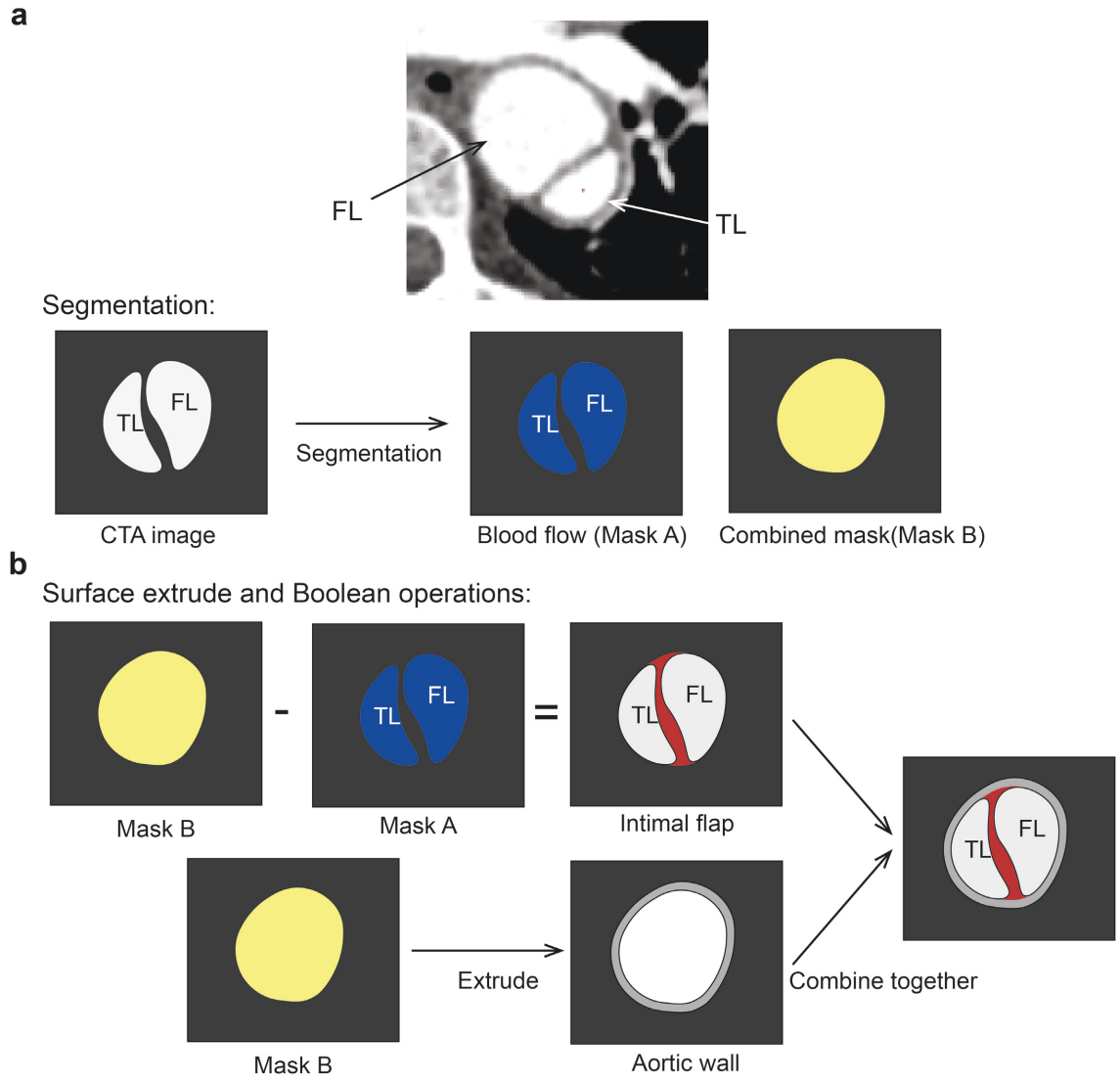


Figure 3.6 Segmentation and reconstruction of the aortic dissection geometry from pre-TEVAR CTA scan of a patient without false lumen thrombus. a. Two segmentation masks for blood flow (mask A) and combined mask (mask B). b. Surface extrude and Boolean operations to create aortic dissection structure.

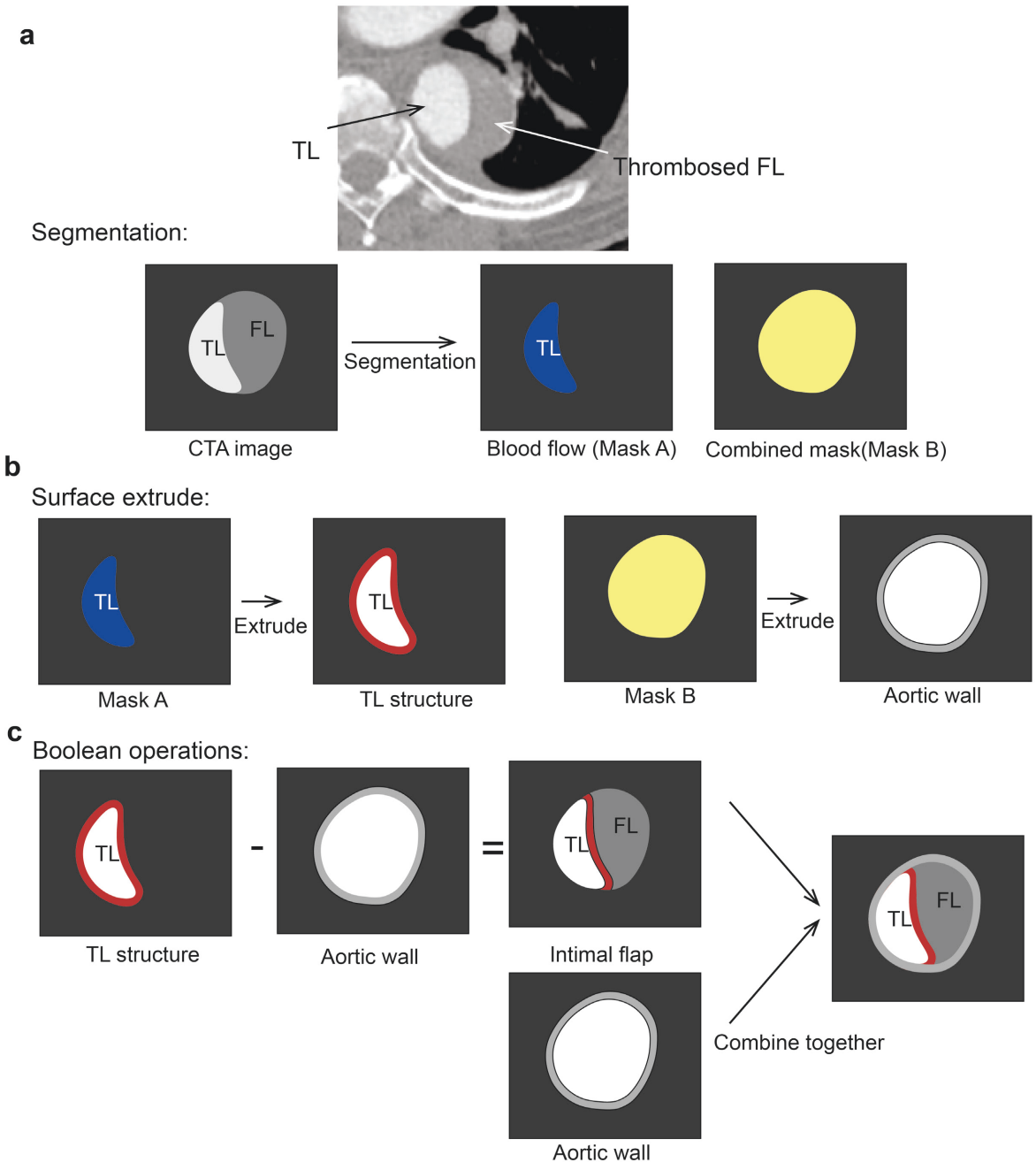


Figure 3.7 Segmentation and reconstruction of the aortic dissection geometry from pre-TEVAR CTA scan of a patient with false lumen thrombus. a. Two segmentation masks for blood flow (mask A) and combined mask (mask B). b. Surfaces are extruded to create true lumen (TL) structure and aortic wall. c. Boolean operations are performed to create intimal flap and aortic dissection geometry.

The segmentation masks are reconstructed into 3D surfaces and are exported in STL format for further processing. This involves smoothing and cutting of the 3D surface geometries performed by using Meshmixer (Autodesk, Inc., San Rafael, CA, USA), which is an open-source geometry processing software. The geometry smoothing is performed by using the in-built 'robust smooth' option in Meshmixer with the smoothing strength been set as 30 to ensure consistency when processing different geometric models. The outer wall and intimal flap are trimmed by placing a transverse plane in the proximal ascending aorta and cutting planes perpendicular to the local centreline in the supra-aortic branches and in the abdominal aorta above the aortic bifurcation.

3.5.2 Mesh generation

Computational meshes for the aortic wall and intimal flap are generated by using ANSYS ICEM CFD (ANSYS Inc., Canonsburg, PA). Compared to aortic aneurysms, aortic dissections pose additional geometry complexity, such as the presence of an intimal flap separating the true and false lumen, multiple tears on the intimal flap, narrowed true lumen and highly tortuous aorta. All these presents a significant challenge for mesh generation. In this study, an unstructured tetrahedra mesh is adopted, with the quality index of the mesh being monitored and kept above 0.4 through ANSYS ICEM during the mesh generation. Mesh size is determined by performing a sensitivity analysis of the aortic dissection to guarantee mesh-independent results (Appendix B). Final meshes of the aortic wall and intimal flap contain a total of 0.8 - 1.3 million tetrahedral elements and are exported to Abaqus (Dassault Systèmes, France) as C3D4 elements (Figure 3.8).

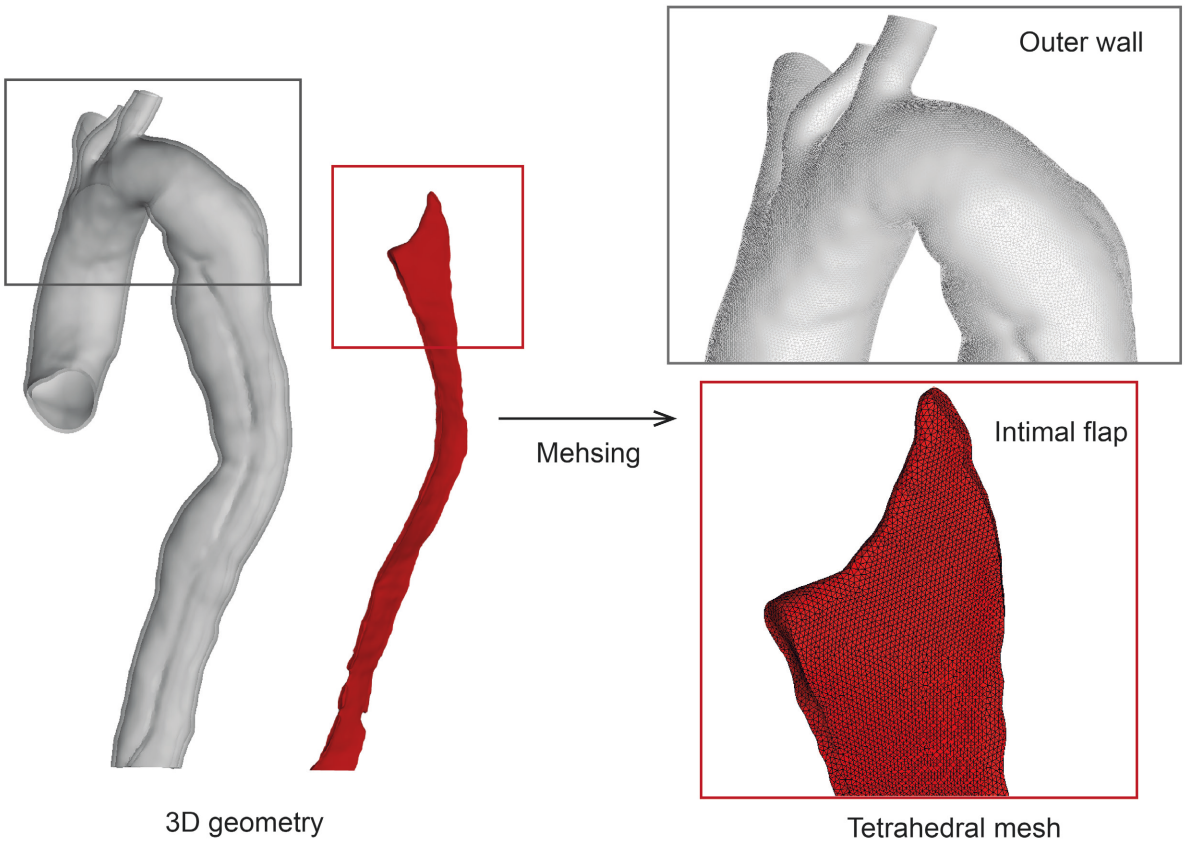


Figure 3.8 3D geometry and mesh of outer wall and intimal flap.

3.6 Parametric model for stent-graft and mesh generation

As described in Chapter 2 (Section 2.3.2), the SG consists of two parts: metallic stent and synthetic graft. In this thesis, parametric models of three commercial SG products are created; these include Medtronic Valliant SG (Medtronic Vascular, Santa Rosa, California), GORE C-TAG Active Control SG (W. L. Gore & Associates, Inc, Flagstaff, Ariz) and Zenith TX2 PT SG (Cook Medical, Bloomington, Ind).

The metallic stent scaffolds are described by using mathematical equations in SolidWorks (Dassault Systèmes, France), where geometric dimensions can be easily adjusted by changing the parameters in these equations. The key to creating a parametric model for SG

is to identify the minimum repetitive unit for each SG design. As shown in Figure 3.9, the repetitive unit is described in the reference plane first, which is then projected onto a cylindrical surface with the diameter of SG to create the reference line for the minimum repetitive unit. The length of stent limbs and radius of the stent apex can be measured directly from product sample or obtained from the manufacturer's documentation. The minimum repetitive unit of metal wire is created by sweeping a circle along the reference line from one end to the other. The diameter of the metal wire can be measured from product sample. The geometry of stent strut is then generated by rotating the minimum repetitive unit wire along the longitudinal axis of the SG. Different from the Valiant SG and the Zenith SG, metallic scaffold of the C-TAG SG is assembled by a single nitinol ring, which is created by performing helical rotation of the minimum repetitive unit (Figure 3.9.b). Assembly of the entire stent scaffold is completed by linear replication of the stent strut and connection of all the stent struts included in the SG product.

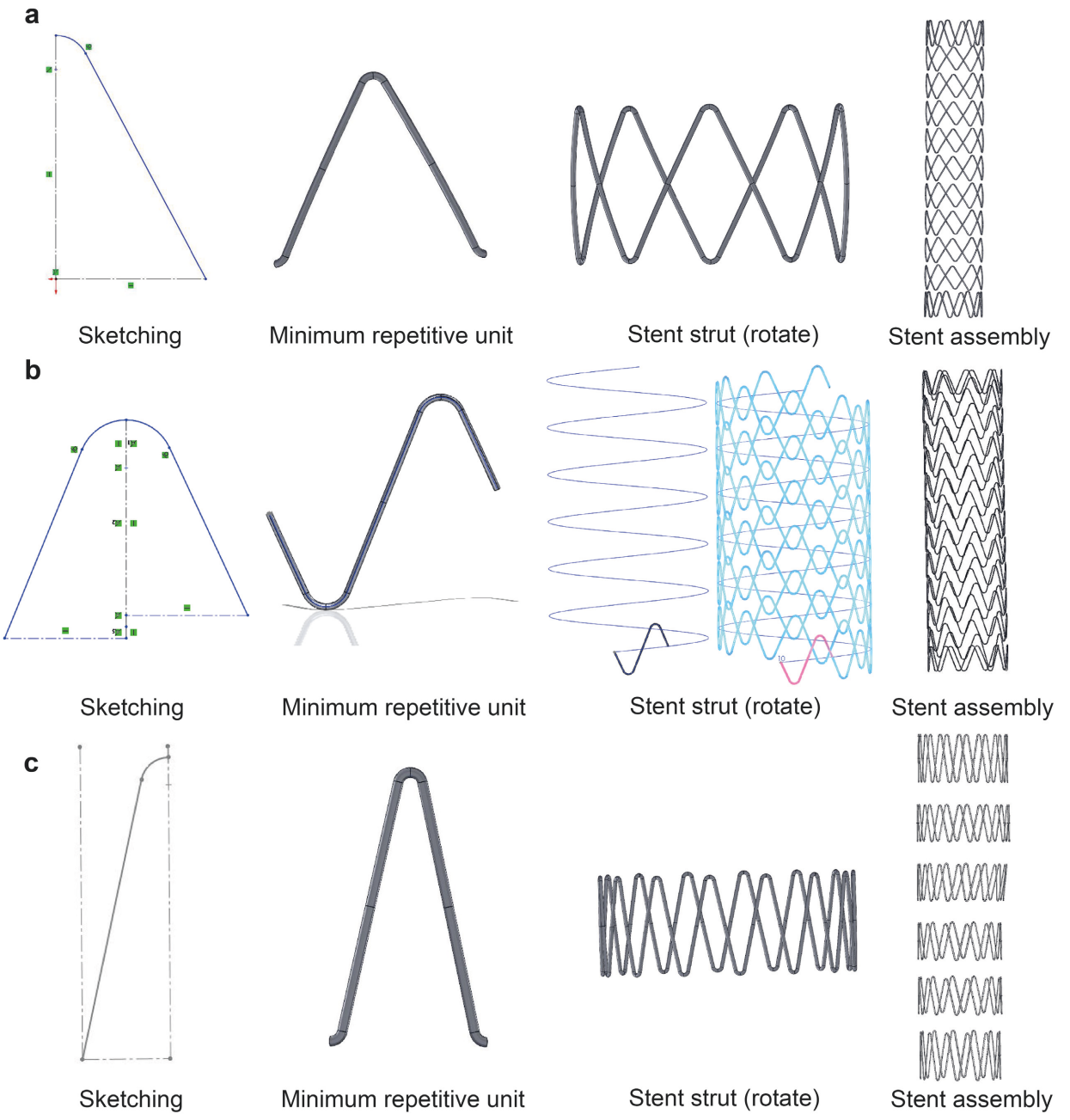


Figure 3.9 Creation of parametric models for metallic stent scaffold of commercial stent-grafts: a. Medtronic Valliant stent-graft (Medtronic Vascular, Santa Rosa, California), b. GORE C-TAG Active Control stent-graft (W. L. Gore & Associates, Inc, Flagstaff, Ariz) and c. Zenith 2PT stent-graft (Cook Medical, Bloomington, Ind).

The synthetic graft is modelled as a tube with the same diameter and length as the corresponding SG. The metallic stent scaffold and synthetic graft are assembled together by

using the tie constrains in Abaqus, which prevents separation or relative sliding between the two components (Figure 3.10). For Zenith and Valiant SG devices, the stent struts are fully attached to the synthetic graft. The C-TAG SG device is different in that the metallic scaffold is partially attached to the synthetic graft, which will be described in detail in Chapter 5 (Section 5.1.2).

A virtual sheath is created by using a tubular surface which is 1 mm larger in diameter and 40 mm longer in length than the actual SG device to ensure full coverage and control of the SG during the process of crimping, delivery and deployment. As shown in Figure 3.10, this virtual sheath serves two purposes during a SG deployment simulation: (i) as a crimping tool to crimp the SG from its stress-free state to a crimped state within the delivery system, and (ii) as a delivery sheath when delivering and deploying the SG into the dissected aorta.

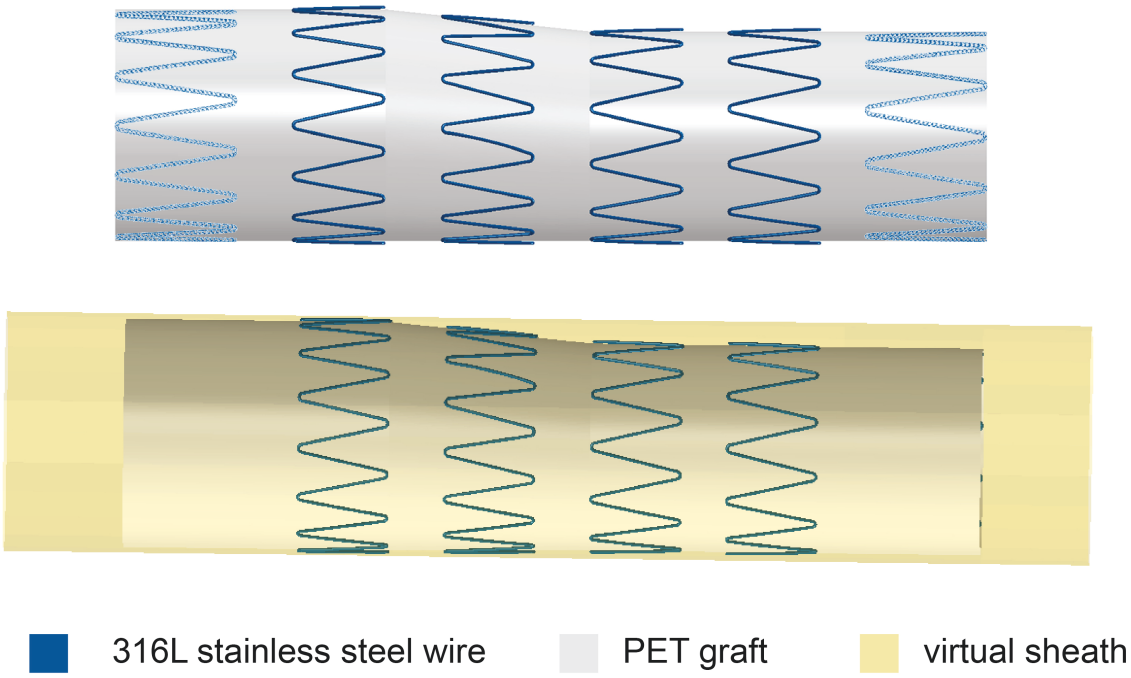


Figure 3.10 Model of Zenith 2PT stent-graft (Cook Medical, Bloomington, Ind). The proximal and distal struts are shown in dash line as they are sewn on the inside of the synthetic graft. The virtual sheath is created by using a tubular surface.

The metallic scaffolds of the three commercial SG devices are meshed into linear hexahedral elements with reduced integration (C3D8R), while the synthetic graft is meshed into

membrane elements with reduced integration (M3D4R) in Abaqus. Mesh sensitivity analysis has been performed by crimping a fully assembled SG, and a suitable mesh density is chosen to ensure that differences in the average maximum principal strain between two successive meshes are less than 2.5% (Desyatova et al., 2020). Details of the mesh sensitivity analysis results can be found in Appendix B. The virtual sheath is meshed into surface elements (SMF3D4R) with a uniform element size of 5 mm, which has been tested and shown to be sufficient for precise control of the displacement and deformation of the sheath during the simulation.

3.7 Boundary conditions

3.7.1 Nodal specific displacement of the virtual sheath

To guarantee precise control of the crimping, delivery and deployment of the SG, a nodal specific displacement boundary condition is applied on the virtual sheath during the simulation. Nodal specific displacements are determined in a simple and robust way by using the initial position and target position of the virtual sheath. Initial positions of the nodes of the first simulation step are the positions of nodes on the virtual sheath, while the target positions are also prescribed using a tubular surface which shares the same node number and node index order as the virtual sheath. Mesh nodes on the virtual sheath and the target position surface are indexed in anticlockwise and bottom to top direction, which ensures one-to-one mapping between nodes on the two surfaces (Figure 3.11). The position of the ith node can then be obtained from the initial position mesh $p_1^i(x, y. z)$ and target position mesh $p_2^i(x, y. z)$. The nodal specific displacement can be calculated by following:

$$u_s^i(x, y, z) = p_2^i(x, y, z) - p_1^i(x, y. z) \tag{3.47}$$

where $u_s^i(x, y, z)$ is the unique displacement for the node indexed by i.

Simulation of virtual SG deployment involves multiple steps. Tubular surfaces corresponding to the initial position and a target position are created for each step, which allows the nodal displacements within the current simulation step to be calculated. As the simulation proceeds to the next step, the target position from the previous simulation step is defined as the initial position, while another new target is created. By using this nodal specific

displacement condition, the displacement of virtual sheath can be controlled precisely while ensuring continuity.

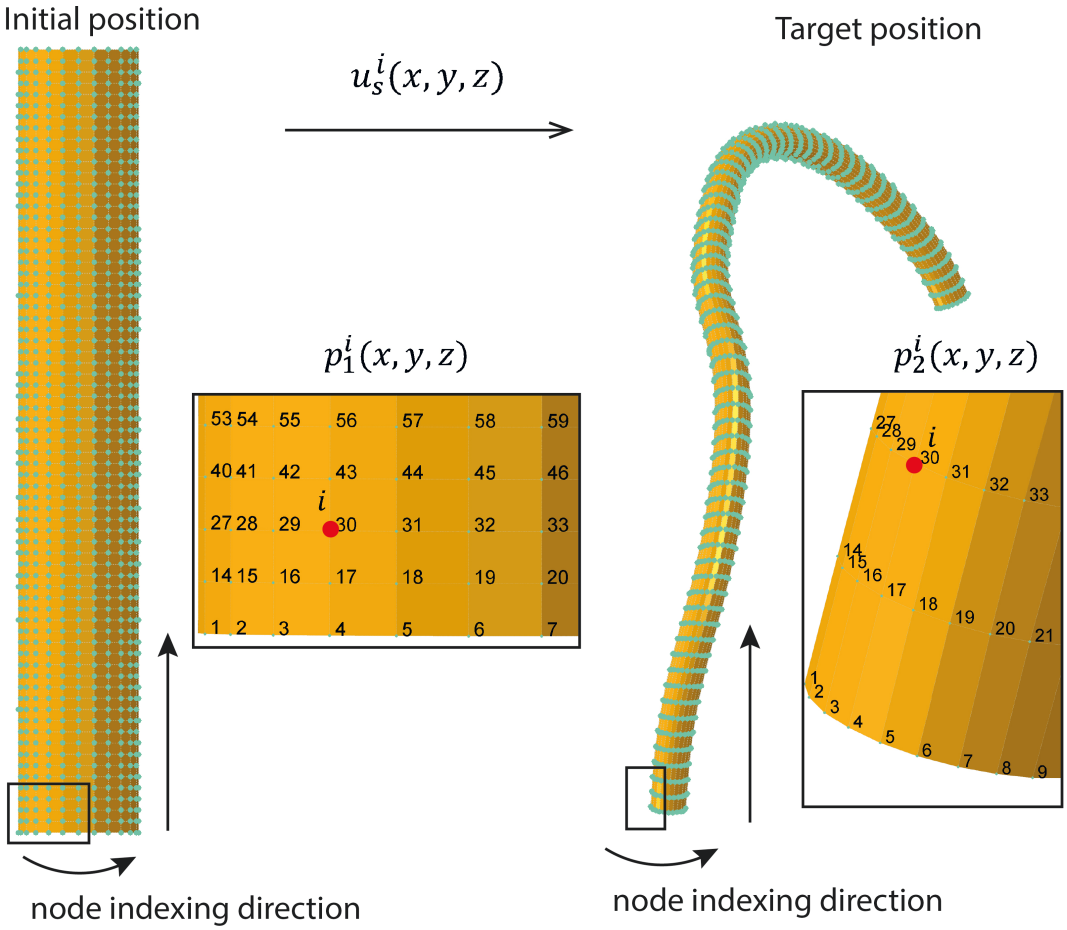


Figure 3.11 Illustration of nodes indexing direction of the initial and target positions for calculation of nodal specific displacement.

3.7.2 Boundary conditions for the aorta

Several assumptions are made when defining boundary conditions for the aorta. In all the simulations presented in this thesis, the intraluminal blood pressure is assumed to be constant at 80 mmHg (typical diastolic pressure) and uniform in both the true lumen and false lumen. A typical diastolic pressure is applied, as the ECG-grated CTA scan is taken at the diastolic phase. The motion of the aortic root is neglected, except for the type A aortic

dissection case presented in Chapter 5 where patient-specific aortic root motion is applied. All the proximal and distal ends of the aorta are clamped with zero displacement in all directions. To account for tethering of the aorta to its surrounding biological tissues and organs, Rayleigh damping is applied to prevent the aorta from excessive vibration. The attachment of the descending aorta to the spine is modelled by specifying four pairs of fixed spots along the descending aorta representing the intercostal arteries, effectively preventing any excessive rigid body movement.

3.8 Numerical simulation procedure

3.8.1 Prestress of aortic dissection model

Pre-stress conditions in the aorta are calculated by following the method reported by Votta et al. (Votta et al., 2017). By using a predefined Cauchy stress tensor as the initial condition in Abaqus, this method involves the following steps:

1. The aorta geometry configuration reconstructed from the pre-TEVAR CTA scan is defined as Ω_{CTA}. A uniform internal pressure normal to the internal surface of the aorta is applied, which is gradually increased from 0 to 80 mmHg, resulting in a deformed configuration Ω_1 and stress tensor $\boldsymbol{S}_1$.
2. After the first end-diastolic stress field is obtained, the initial stress tensor is updated with $\boldsymbol{S}_0 = \boldsymbol{S}_1$and n = 1. This is followed by an iterative loop with the same internal pressure loading to produce updated configuration and stress tensor, $\Omega_{\mathrm{n+1}}$ and $\boldsymbol{S}_{n+1}$ respectively. The iteration continues until the difference between the deformed configuration under 80 mmHg pressure loading ($\Omega_{\mathrm{n+1}}$) and the true geometry reconstructed from the CTA scan (Ω_{CTA}) is less than 0.5 mm.
3. Set the converged stress tensor $\boldsymbol{S}_{n+1}$ as $\boldsymbol{S}_0$ which is mapped directly onto Ω_{CTA} .

By following this approach, the pre-stress tensor field $\boldsymbol{S}_0$ corresponding to the diastolic pressure can be obtained. This is then applied as the initial stress in the virtual SG deployment simulation.

3.8.2 Virtual stent-graft deployment

Simulation of SG deployment including SG crimping, delivery and release, is performed within the reconstructed pre-TEVAR aorta geometry by applying a nodal specific displacement boundary condition on the virtual sheath. The centreline of the true lumen in the pre-TEVAR geometry is extracted and the guide wire is assumed to follow the centreline, allowing determination of the proximal landing and distal positions during SG implantation.

As shown in Figure 3.12, the first step involves assembly of the SG at stress-free state, the pre-TEVAR aorta model and the virtual delivery sheath while neglecting any contact relations between the SG and the aorta. This is followed by shrinking a tubular virtual sheath, which has an initial diameter 1 mm larger than the actual SG (29 – 46 mm), to the diameter of a real sheath for the SG product (7 mm) to simulate the SG delivery system. The SG within this virtual sheath is then compressed from its stress-free state to crimped state (Figure 3.12.a).

In some type B aortic dissection cases, the true lumen can be excessively compressed by the enlarged false lumen making the diameter of true lumen smaller than the diameter of the crimped SG. In such a case, a curved tube following the centreline of the pre-TEVAR aorta is placed inside the true lumen and expanded in radial direction to open up the compressed true lumen to allow the delivery sheath to pass through the local narrowing for SG deployment (Figure 3.12.b). It is assumed that there is no friction between the curved tube and the aorta internal surface to avoid creating additional tangential force.

The next step is to select the proximal landing position based on the post-TEVAR CTA scan. The target position of the virtual sheath is then created through another virtual tube with a diameter of 7 mm along the centreline. The SG is delivered into the true lumen by deforming the virtual sheath to the target position with the use of nodal specific displacement in three sub-steps (Figure 3.12.a). No sliding between the SG and virtual sheath is permitted during this process. Finally, with the crimped SG in the true lumen, the sliding restriction between the SG and virtual sheath is lifted, while the contact between the SG and inner surface of the aorta is activated with a friction coefficient of 0.1 (Vad et al., 2010). The SG is deployed by expanding the virtual sheath radially to a diameter larger than the local diameter of the aorta

(Figure 3.12.a). The entire SG deployment simulation is completed when the SG is fully in contact with the aorta and reaches mechanical equilibrium. The kinetic energy and internal strain energy ratio (ALLKE/ALLIE) is monitored and kept within 10% to ensure the simulation as a quasi-static analysis.

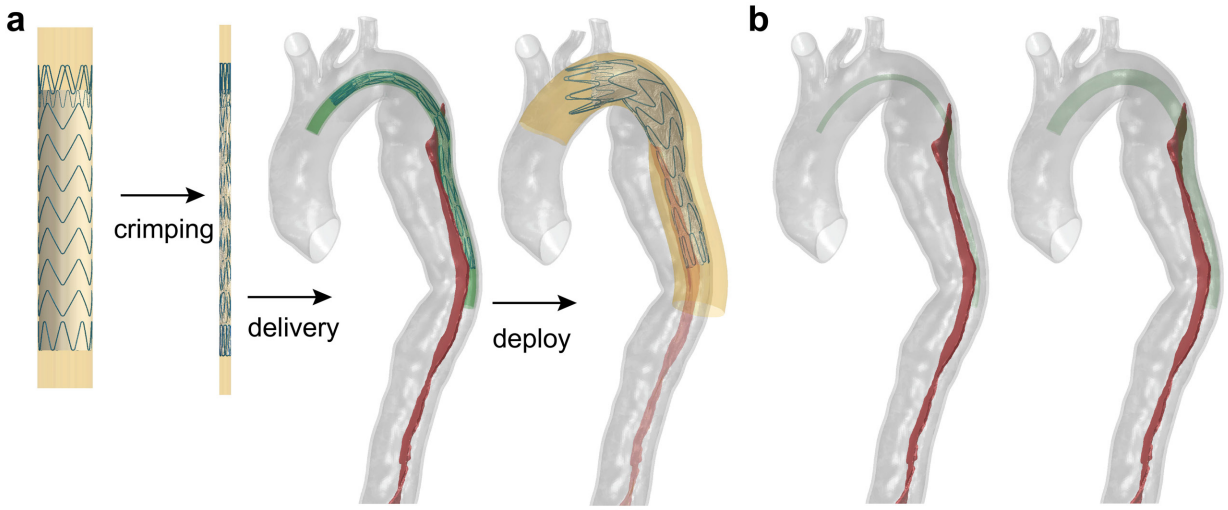


Figure 3.12 Virtual stent-graft (SG) deployment steps. a. The SG is crimped, delivered and deployed at the target position in the true lumen. b. A curved tube is used to open up the local narrowing in the compressed true lumen.

3.8.3 Loading condition after stent-graft deployment

After the SG is deployed into the true lumen, the primary entry tear is sealed, and blood flow is restored through the conduit formed by the SG. In the stented segment, the graft fabric and metallic stent wires shield the aortic wall and initial flap from the pulsating blood pressure. This requires a change in loading condition so that the blood pressure acting on the inner surface of the aortic wall is reduced from 80 mmHg to 0, while the graft internal pressure is increased from 0 to 80 mmHg. If blood pressure inside the graft is neglected, the graft fabric would tend to fold inwards leaving small gaps between the graft fabric and local aortic wall after SG deployment.

3.9 Summary

In this chapter, the basic concept of continuum mechanics and governing equations of solid mechanics that are relevant to this study are described. The Yeoh constitutive model is adopted to describe the hyperelastic mechanical property of the aortic wall which is assumed as an isotropic material. The explicit FEM procedure and contact algorithm in Abaqus are then introduced.

The main focus of this chapter is to present the key components developed for the virtual SG deployment simulation framework; these include: (i) a purpose-built segmentation approach, allowing the intimal flap to be treated as a different material from the aortic wall; (ii) parametric models for three market-leading SG products: Medtronic Valliant SG, GORE C-TAG Active Control SG and Zenith TX2 PT SG, offering the freedom to choose SG design, diameter and length in the simulation model, (iii) a nodal specific displacement boundary condition for accurate control of the virtual sheath and the SG, and (iv) the overall numerical simulation procedure, including pre-stress of the aortic dissection model, virtual deployment of SG and the change of loading conditions after SG deployment.

Chapter 4

Model evaluation and validation: Patient-specific simulation of stent-graft deployment in type B aortic dissection†

It has been highlighted in previous chapters that there is a need for a patient-specific virtual stent-graft deployment model that is capable of mimicking the biomechanical interactions between aorta and stent-graft during and after TEVAR and predicting the post-TEVAR stent-graft configuration. In this chapter, the virtual stent-graft deployment model described in Chapter 3 is applied to a complicated type B aortic dissection patient case with different model settings. Simulation results are analysed to obtain a better understanding of the impact of model complexity levels on predicting post-TEVAR stent-graft configuration and stress distribution. Mechanical tensile test data obtained on dissected aortic tissues are fitted to a hyperelastic model which is employed in the virtual stent-graft deployment simulation in type B aortic dissection. The accuracy of model prediction is evaluated by comparing simulated post-TEVAR stent-graft configuration to the actual stent-graft configuration

† The author of this dissertation carried out all the work described in this chapter unless specified otherwise. The material test was performed by Dr Jing Lin from Key Laboratory of Textile Science and Technology of Ministry of Education, College of Textiles, Donghua University, Shanghai, China. The test specimen was collected by Prof Zhihui Dong from Department of Vascular Surgery, Zhongshan Hospital, Fudan University, Shanghai, China. The main content of this chapter was adapted from Kan, X., Ma, T., Lin, J., Wang, L., Dong, Z. and Xu, X.Y., 2021. Patient-specific simulation of stent-graft deployment in type B aortic dissection: Model development and validation. *Biomechanics and Modeling in Mechanobiology*, *20*(6), pp.2247-2258.

reconstructed from CTA scans. In addition, material parameter sensitivity tests are performed to evaluate the impact of tissue mechanical property on the simulation results.

4.1 Model details

4.1.1 Patient information

A 44-year-old female type B aortic dissection patient from Zhongshan hospital, Shanghai, China was included in this study. The patient gave informed consent, and the study was approved by the local ethics committee. The patient underwent TEVAR intervention at sub-acute phase and remained stable with false lumen thrombosis at 3-months follow-up. CTA scans of the patient were acquired before TEVAR and 3 months after TEVAR. CTA scans were performed with Aquilion ONE (Toshiba Medical Systems, Otawara, Japan) scanner (1.0 mm slice thickness and 0.68 mm × 0.68 mm pixel size). The pre-TEVAR aorta was found with extremely compressed true lumen had a local diameter of 6.5 mm at the narrowest section and aneurysmal dilatation at the proximal primary entry tear to the false lumen (Figure 4.1.a).

4.1.2 Aortic dissection geometry and stent-graft modelling

Pre- and post-TEVAR CTA images were processed in Mimics 22.0 (Materialise, Leuven) software by using special segmentation workflow described in Chapter 3 (Section 3.5.1). Two segmentation masks were segmented from the pre-TEVAR CTA scan: the segmentation mask A represented the domain of blood flow by including the true and false lumen, while the segmentation mask B represented the adventitia by including the true and false lumen and the intimal flap (Figure 4.1.b). The aortic wall was created from mask B which was extruded outwardly by a uniform thickness of 1.5 mm (Figure 4.1.c). Boolean calculation was then performed by subtracting mask A from mask B to obtain the segmentation of intimal flap (Figure 4.1.d). Therefore, the distance between the true and false lumen in mask A represented the local thickness of the intimal flap which was in the range of 0.6 - 1.6 mm in this patient. The geometry of the aortic wall and intimal flap were smoothed and combined using Meshmixer (Autodesk, Inc.). The proximal and distal ends of the dissection model were trimmed by placing cutting planes perpendicular to the local centreline in the proximal

ascending aorta, distal segments of the supra-aortic branches and in the abdominal aorta above the aortic bifurcation (Figure 4.1.e). The intimal flap and the aortic wall were then meshed into tetrahedra elements (C3D4 in Abaqus (Dassault Systèmes, France)).

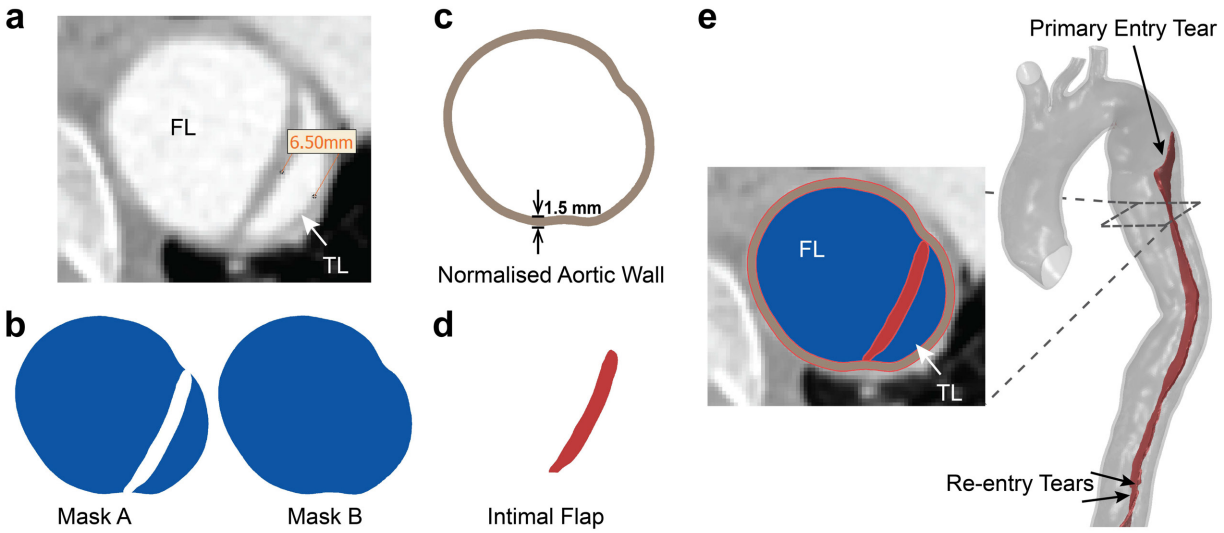


Figure 4.1 Illustration of the segmentation and reconstruction of aortic dissection geometry from CTA scan. a. The transverse view of the descending aorta before TEVAR showed true lumen (TL), false lumen (FL), and the measurement of narrowed true lumen. b. The segmentation of mask A represented for blood flow domain and mask B represented for adventitia. c. the aortic wall was created by extrude the mask B outwardly by 1.5 mm. d. The segmentation of intimal flap was created by performing Boolean subtraction of mask A from mask B. e. The aortic wall and intimal flap part were combined and trimmed to make the pre-TEVAR aortic dissection geometry.

During the TEVAR procedure, a 28-28-150 mm Medtronic Valiant SG (Medtronic Vascular, Santa Rosa, California) with proximal bare metal stent was deployed into the true lumen of the aorta. The diameter and length of the SG were used as the inputs of the parametric model of Valiant SG, which described in Chapter 3, to generate the SG geometry sharing all the design and dimension feature with the SG used in the TEVAR procedure (Figure 4.2). The SG consists of a Nitinol alloy stent scaffold and PET fabric graft. The Nitinol stent was meshed into linear hexahedral elements with reduced integration (C3D8R) in Abaqus. A superelastic material behaviour of Nitinol alloy was defined by adopting the material parameters shown in Table 4.1. The PET fabric graft was modelled by using a tube with 0.1 mm thickness and meshed into membrane elements with reduced integration (M3D4R) in Abaqus. The

material property of the PET graft was simplified by defining it a isotropic elastic material with the Young's modulus of 1.84 MPa and Poisson's ratio of 0.35 (Kleinstreuer et al., 2008).

The two main components of the SG, Nitinol stent and the PET fabric graft, were assembled together by the tie constraint in Abaqus, which prevents separation or relative sliding between the two components. Then a virtual sheath which defined by using a tubular surface with a diameter of 29 mm was created outside of the SG and meshed into surface elements (SMF3D4R) (Figure 4.2). This virtual sheath represented the crimping tool to crimp the SG and the delivery sheath when deliver and deploy the SG into the aortic dissection in the simulation model.

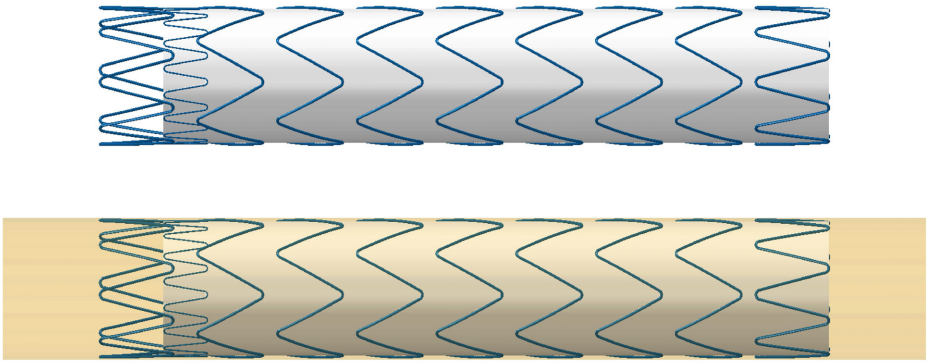


Figure 4.2 Geometry of the 28-28-150 mm Medtronic Valiant stent-graft used in the TEVAR procedure and was covered by the virtual sheath.

Table 4.1. Superelastic material parameters for Nitinol stent (Kleinstreuer et al., 2008)

Austenite elastic modulus E_A, MPa	51,700
Austenite Poisson's ratio ν_A	0.3
Martensite elastic modulus E_M, MPa	47,800
Martensite Poisson's ratio ν_M	0.3
Transformation strain ε_T	0.063
Start of transformation (Loading) σ_L^S, MPa	600
End of transformation (Loading) σ_L^E, MPa	670
Start of transformation (Unloading) σ_U^S, MPa	288
End of transformation (Unloading) σ_U^E, MPa	254
Start of transformation stress in compress σ_{CL}^S, MPa	900
Reference temperature T, ℃	37
Density ρ, g/cm^3	6.5

4.1.3 Mechanical property of human type B aortic dissection

In order to obtain mechanical property of aortic wall tissue from type B aortic dissection patients, stress-strain curves from uniaxial tests of 12 descending aorta samples were included in this part of study. The 12 dissected descending aorta samples were collected from 6 type B aortic dissection patients during open surgical repair from Zhongshan Hospital, Shanghai, China. The tissue samples were cut into strips (40 mm × 10 mm) along the circumferential direction (perpendicular to the direction of blood flow) and stored, refrigerated at 4 ℃ in saline solution and tested within 72h after the surgery. The protocol was approved by the local ethics committee and written informed consent was obtained from the patients.

The uniaxial tensile tests were carried out by our collaborators from the Key Laboratory of Textile Science and Technology of Ministry of Education, College of Textiles, Donghua University, Shanghai, China by using the YG(B)026G-500 Electronic Tensile Testing System (Darong Textile Instrument Co., Ltd, Wenzhou, China). The position resolution of the stepper motor was 1 μm; the accuracy of the load cell accuracy was 0.01N. The tissue strips were

clapped at both ends by the two grips, while the initial distances between the grips l_0 was set as 25 mm with preconditioning load of 0.05 N. The samples were left as free of load in the other direction.

As described in Chapter 3 (Section 3.2), the Yeoh strain energy function was used to characterise the mechanical behaviour of the tissue samples (Yeoh, 1993). Recall the Equation (3.39), with uniaxial tensile load, the Cauchy stress σ along the tensile direction can be expressed by

$$\sigma = 2\left(\lambda^2 - \frac{1}{\lambda}\right)\sum_{i=1}^{3} i c_{i0}\left(\lambda^2 + \frac{2}{\lambda} - 3\right)^{i-1} \tag{4.1}$$

where λ is the stretch ratio. The Cauchy stress σ can be calculated from the measured loading force by using sample thickness, the width of the sample and the stretch ratio with the assumption of incompressibility.

Each stress-stretch curve of the test was fitted from zero stretch to the material failure point by using an inhouse MATLAB code (MathWorks, Inc., Natick, USA). The material parameters in Equation 4.1 for each sample were determined by using the least square fitting method, through which the local minimum of the following objective function was found with the initial guess of $(c_{10}^0, c_{20}^0, c_{30}^0)$,

$$F(c_{10}, c_{20}, c_{30}) = \sum_{k=1}^{N}\left[\sigma_p^k - \sigma_m^k\right]^2 \tag{4.2}$$

where N is the number of measured data points, σ_p^k and σ_m^k are the kth predicted and measured Cauchy stresses. The material parameters were constrained to be positive to avoid physical unrealistic behaviour. The fitting quality was assessed by using the coefficient of determination calculated R^2 by

$$R^2 = 1 - \frac{\sum_{k=1}^{N}\left(\sigma_p^k - \sigma_m^k\right)^2}{\sum_{k=1}^{N}(\sigma_m^k - \bar{\sigma}_m)^2} \tag{4.3}$$

Then the values of material parameters obtained from all tissue samples were averaged and the mean value of the material parameters, c_{10}, c_{20}, c_{30}, were employed to describe the incompressible isotropic mechanical behaviour of the aortic wall in the simulation model.

As the aortic dissection progresses from acute phase to chronic phase, the histopathology of the intimal flap changes, leading to significant difference in its mechanical behaviour (Peterss et al., 2016). However, very few studies have reported the mechanical property of intimal flap in different phases of the dissection. Based on a recent study, the intimal flap exhibits linear elastic response rather than nonlinear hyperelastic behaviour seen in complete aortic wall under small deformations (Deplano et al., 2019). Therefore, the intimal flap was assumed to have a linear elastic material property with Young's modulus E_{flap} = 277 kPa (Deplano et al., 2019). The intimal flap tissue was assumed as nearly incompressible by defining the Poisson's ratio as 0.49 (Holzapfel, 2000).

There is considerable variability in material parameters for the aortic wall as reported in previous studies (Vorp et al., 2003, Deplano et al., 2019). Furthermore, the mechanical behaviour of intimal flap also changes as the dissection progressing from acute to chronic phase (Pape et al., 2015). For these reasons, the sensitivity of the simulation results to the choice of material parameters should be investigated. To this end, another set of Yeoh hyperelastic material parameters was derived by decomposing the anisotropic material model of aortic wall reported by Daplano et al. to obtain parameters in the circumferential direction (Deplano et al., 2019). In order to test the model sensitivity to different combinations of material parameters, a stiffer intimal flap was also modelled with E_{flap} = 350 kPa.

4.1.4 Virtual stent-graft deployment workflow and model variations

The virtual SG deployment simulation in patient-specific aortic dissection including SG crimping, delivery and deploy, was performed by following the framework described in Chapter 3. The SG crimping, delivery and deployment was achieved by employing a nodal specific displacement boundary condition on the virtual sheath (Figure 3.12.a). Another virtual tube was placed in the true lumen and expanded from 6 mm to 8 mm in diameter to open up the local narrowing which simulated the process of delivery sheath passing through this local narrowing (Figure 3.12.b). The contacts between objects were modelled by using the general contract formulation with penalty method in Abaqus Explicit. The ratio of kinetic

energy and internal strain energy (ALLKE/ALLIE) was monitored and kept under 10% to ensure the simulation as a quasi-static analysis.

In order to quantify the effects of pre-stress in the aortic wall and the action of blood pressure, three models with different levels of complexity were simulated by using the virtual SG deployment framework described in Chapter 3 (Figure 4.3). In model A, the effect of pre-stress in the aortic wall was neglected, and the SG was not loaded with internal blood pressure after SG deployment. In model B, the pre-stress tensor $\boldsymbol{S}_0$ was calculated and applied as the initial stress field in the aorta before deploying the SG into the true lumen, but the action of blood pressure on SG was not included. In model C, both the effect of pre-stress tensor and the action of internal pressure on SG were considered.

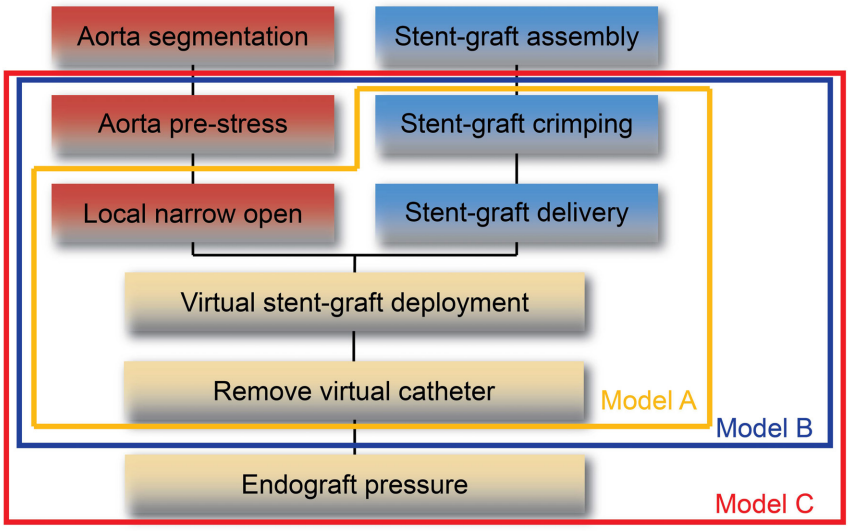


Figure 4.3 Virtual stent-graft deployment simulation workflow and model variations.

4.1.5 Quantitative description of stent-graft configuration after deployment

The pre-TEVAR and post-TEVAR scans were registered into the same coordinate system by using the anatomical landmarks on the T4 and T11 thoracic vertebrae in Mimics 22.0. Hence, the SG configuration obtained from simulation based on pre-TEVAR image scan shared the same coordinate system as the SG configuration reconstructed from the post-TEVAR scan.

To evaluate the simulation accuracy and the impact of model variation as well as the choice of material parameters, quantitative assessment of the SG configuration and spatial position was performed by using two parameters, local open area (LOA) and the centre point difference (e_c).

Due to the narrowed true lumen in this simulation case, the SG was compressed to a non-cylindrical configuration which cannot be directly assessed by adopting the cylinder fitting approach used in a previous publication (Derycke et al., 2019). Instead, a spline was created through the apexes at each end of the stent strut in SpaceClaim (ANSYS Inc., Pittsburgh, PA) (Figure 4.4). The spline enclosed area was defined as the LOA at the stent strut end. The distance between the centre points of each virtually deployed stent strut end and follow-up stent strut end was used to assess the stent strut spatial position difference (e_c) (Figure 4.4).

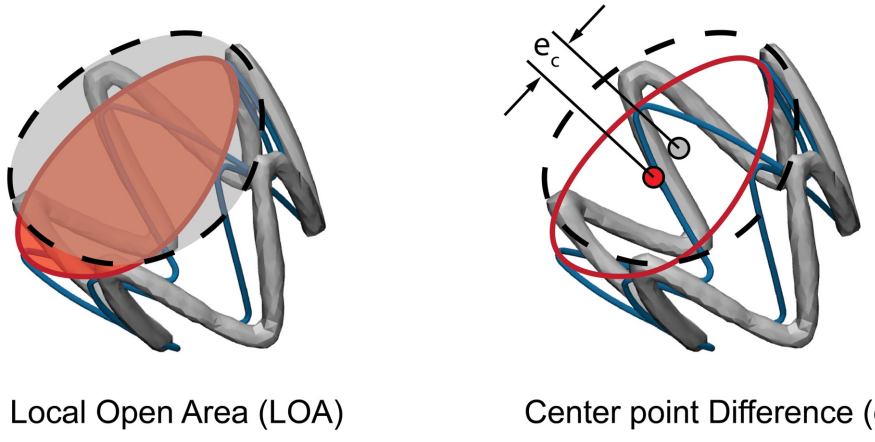


Figure 4.4 Definitions of the parameters for quantitative assessment of stent-graft configuration and spatial position.

4.2 Results

The SG was successfully deployed into the narrowed true lumen in all simulation models with different model settings and material parameters. The isotropic hyperelastic material parameters for describing the mechanical behaviour of the aortic wall were obtained by fitting to the uniaxial tensile testing data on the aortic wall tissue from type B aortic dissection patients. The predicted SG configuration and the aortic wall biomechanics were assessed and analysed. The effect of the choice of material parameters was evaluated by comparing the SG configurations based on the Model C setting.

4.2.1 Assessment of stent-graft configuration after virtual deployment

After delivery of the SG into the true lumen of the dissection, SG configuration obtained by the simulation was compared to the SG configuration based on the post-TEVAR follow-up. As shown in Figure 4.5, the stent struts were numbered from 1 to 9 (proximal to distal), with each stent strut having a proximal end (marked as P) and a distal end (marked as D). The nine stent struts landed in three landing zones based on the surrounding anatomical structure. Struts 1 and 2 and the proximal end of strut 3 (P3) landed in the healthy aorta which was not involved in the dissection. The distal end of strut 3 (D3), strut 4 and the proximal end of strut 5 (P5) landed in the primary entry tear region, while the distal end of strut 5 and the rest of the SG (D5 to D9) landed in the narrowed true lumen.

Based on the observation and measurement of the SG configuration reconstructed from the post-TEVAR CTA scan, the stent strut ends landed in the entry tear section (D3 to P5) have much larger LOA (468.0 ± 37.7 mm^2) than the LOA measured at the stent strut ends landed in other two sections. The local narrowing of true lumen has contributed to the smaller LOA (137.3 ± 31.1 mm^2) measured at the stent strut ends landed in this section. There were dramatic changes of LOA on the section borders, e.g. LOA at P3 was 173.6 mm^2 smaller than that at D3 while LOA difference between P5 and D5 was 204.1 mm^2.

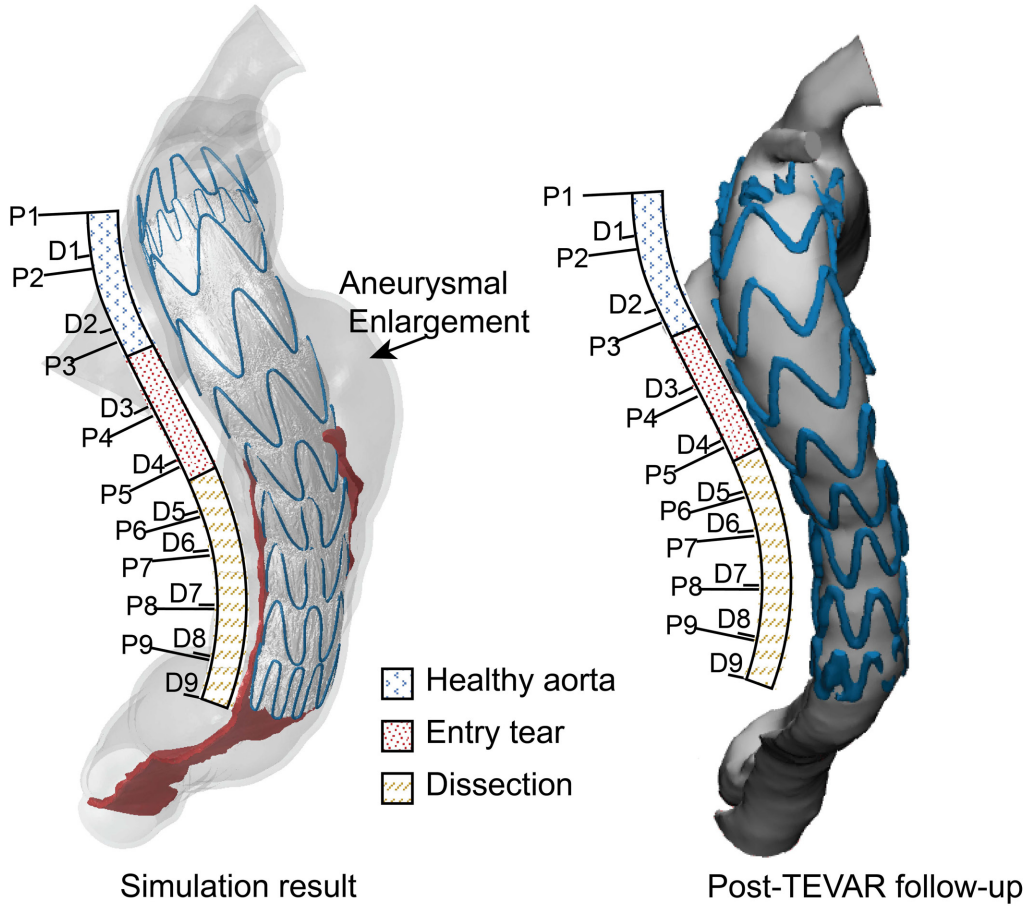


Figure 4.5 Numbering of stent ends and the definition of landing sections.

4.2.2 Material parameters for descending aortic wall in type B aortic dissection patients

Stress-stretch curves from 12 tissue samples obtained from 6 type B aortic dissection patients were analysed by using the in-house MATLAB code based on least square fitting. The coefficient of determination R^2 of each fitting curve was calculated to assess the quality of fitting, and its mean value was 0.996. The averaged Yeoh material parameters from the 12 samples were calculated as c_{10} = 17.5 KPa, c_{20} = 58.9 KPa, c_{30} = 116.1 KPa which were used in the simulations. The stress-stretch curves of the tissue samples, along with the averaged fitting curve are shown in Figure 4.6.

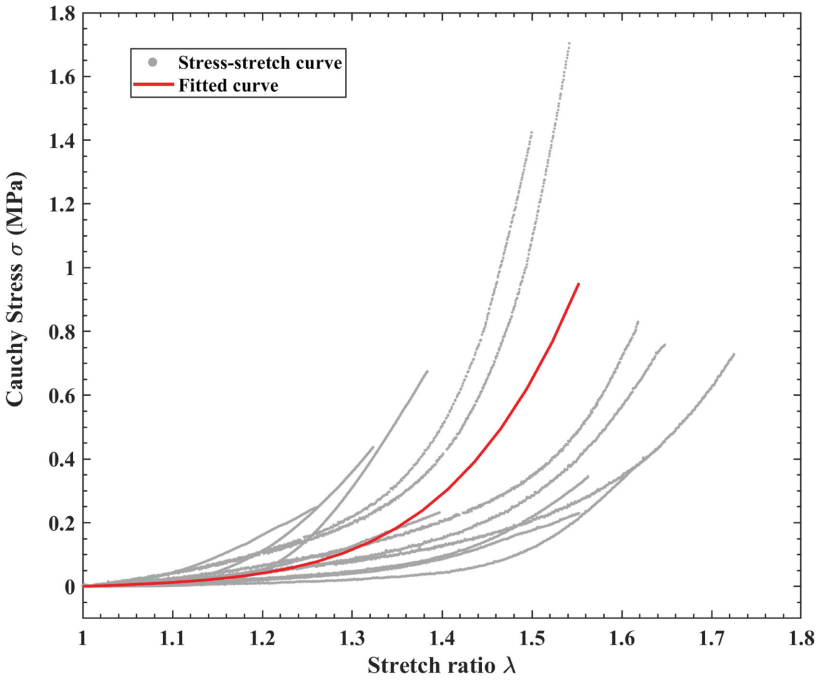


Figure 4.6 Stress-stretch relationships for aortic tissue samples taken from type B aortic dissection patients.

4.2.3 Effect of different model settings

4.2.3.1 Stent-graft configuration

The predicted SG configurations with models A, B and C settings were compared to the SG configuration reconstructed from the follow-up CTA scan in terms of LOA and spatial position of the centre point at each stent strut end.

As shown in Table 4.2, model A overpredicted LOA by an average of 14.5% in the healthy aorta section and 38.7% in the dissection section, with a minor deviation of 3.2% in the entry tear section. Regarding the detailed LOA deviation measured at the stent strut ends, stent struts landed in the narrowed true lumen had 24.0~50.8% larger LOA than those measured from the follow-up CTA scan (Table 4.2 and Figure 4.7.a). The dramatic change in LOA for stent strut landed on the section borders was partially captured by model A, with P3 to D3 LOA difference being 112.1 mm^2 and P5 to D5 LOA difference being 189.9 mm^2 (Figure 4.8.a). As shown in Table 4.3, the spatial position of the centre point of the stent strut end deviated

from the post-TEVAR CTA scan by an average of 10.8 mm, 11.6 mm and 7.1 mm in the three sections respectively with the maximum difference of 13.8 mm at P2 (Figure 4.7.b).

By incorporating the pre-stress tensor $\boldsymbol{S}_0$ as the initial stress of the simulation but neglecting the action of blood pressure on the SG inner surface, model B underpredicted LOA in all three sections with a mean deviation of -23.4 % in healthy aorta section, -38.3% in entry tear section and -15.3% in dissection section with narrowed true lumen (Table 4.2 and Figure 4.7.a). The largest deviation of LOA was observed at P5 with -50.2% underprediction, but reduced deviation was observed at the dissection section (Figure 4.7.a and Figure 4.8.b). The LOA difference at the section borders was 54.1 mm^2 for P3 to D3 and 74.3 mm^2 for P5 to D5, which were significantly lower than the corresponding LOA difference measured from the follow-up CTA scan. Model B provided slightly better predictions of the stent strut spatial positions difference with mean values of 11.0 mm, 10.4 mm and 5.7 mm for the three landing sections (Figure 4.7.b and Table 4.3).

After incorporating the pre-stress tensor $\boldsymbol{S}_0$ as the initial stress in the aorta and the action of internal blood pressure on SG, model C produced the best results by capturing the main features of the SG configuration. The mean LOA deviations were less than 6% for all three sections (Table 4.2 and Figure 4.7.a). The dramatic changes of LOA for the stent struts landed on the section borders (strut 3 and strut 5) were also well captured by model C with differences of 163.4 mm^2 for P3 to D3 and 195.5 mm^2 for P5 to D5 (Figure 4.8.c). The local LOA for the stent struts landed in the dissection section with narrowed true lumen was also well captured. In addition, model C produced the best prediction of stent strut positions with an average difference of up to 4.6 mm for all regions.

Table 4.2 Local open area (LOA) deviations (e_{LOA}) in three landing sections (mean, standard deviation and maximum values)

Landing sections	Model A e_{LOA} (%)	Model B e_{LOA} (%)	Model C e_{LOA} (%)
Healthy aorta	14.5 ± 13.2 [-6.2, 28.8]	-23.4 ± 10 [-35.3, -8.7]	-5.8 ± 10.8 [-22.8, 4.7]
Entry tear	3.2 ± 6.7 [-6.1, 9.6]	-38.3 ± 8.5 [-50.2, -30]	-3.2 ± 3.8 [-6.7, 1]
Dissection	38.7 ± 9.3 [24, 50.8]	-15.3 ± 9.6 [-37, -5.3]	-1.7 ± 3.1 [-9.2, 1.3]

Table 4.3 Spatial position difference of stent strut end centre point (e_c) in three landing sections (mean, standard deviation and maximum values).

Landing sections	Model A e_c (mm)	Model B e_c (mm)	Model C e_c (mm)
Healthy aorta	10.8 ± 1.9 [8.8, 13.8]	11.0 ± 1.9 [8.8, 14]	3.0 ± 1.9 [0.5, 5.5]
Entry tear	11.6 ± 0.5 [10.9, 12]	10.4 ± 1 [9.4, 11.7]	3.8 ± 1.2 [2.8, 5.3]
Dissection	7.1 ± 1.3 [5.5, 9]	5.7 ± 1.4 [4.2, 7.9]	4.6 ± 1.2 [2.3, 5.8]

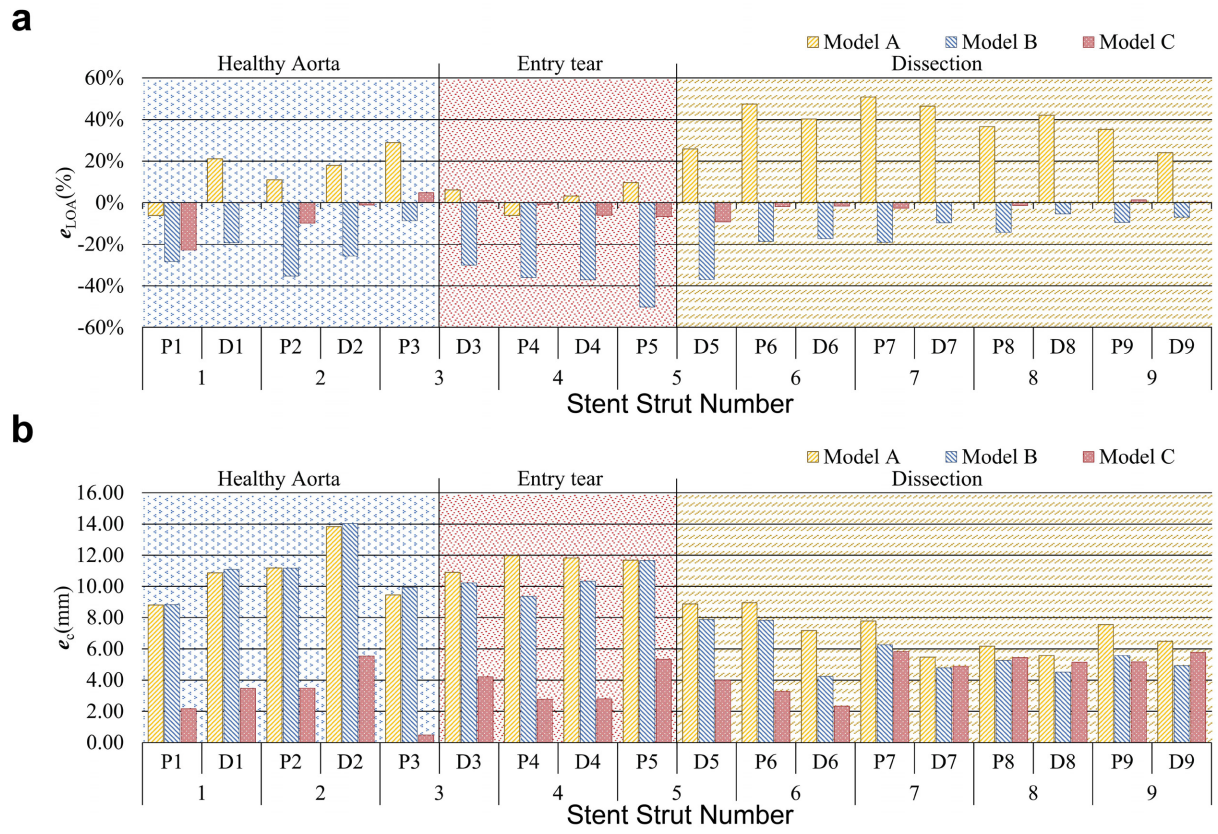


Figure 4.7 Deviations of the predicted stent-graft configuration from the simulations with three different settings. a. the local open area (LOA) deviation (e_{LOA}). b. stent strut end centre points position difference (e_c (mm)).

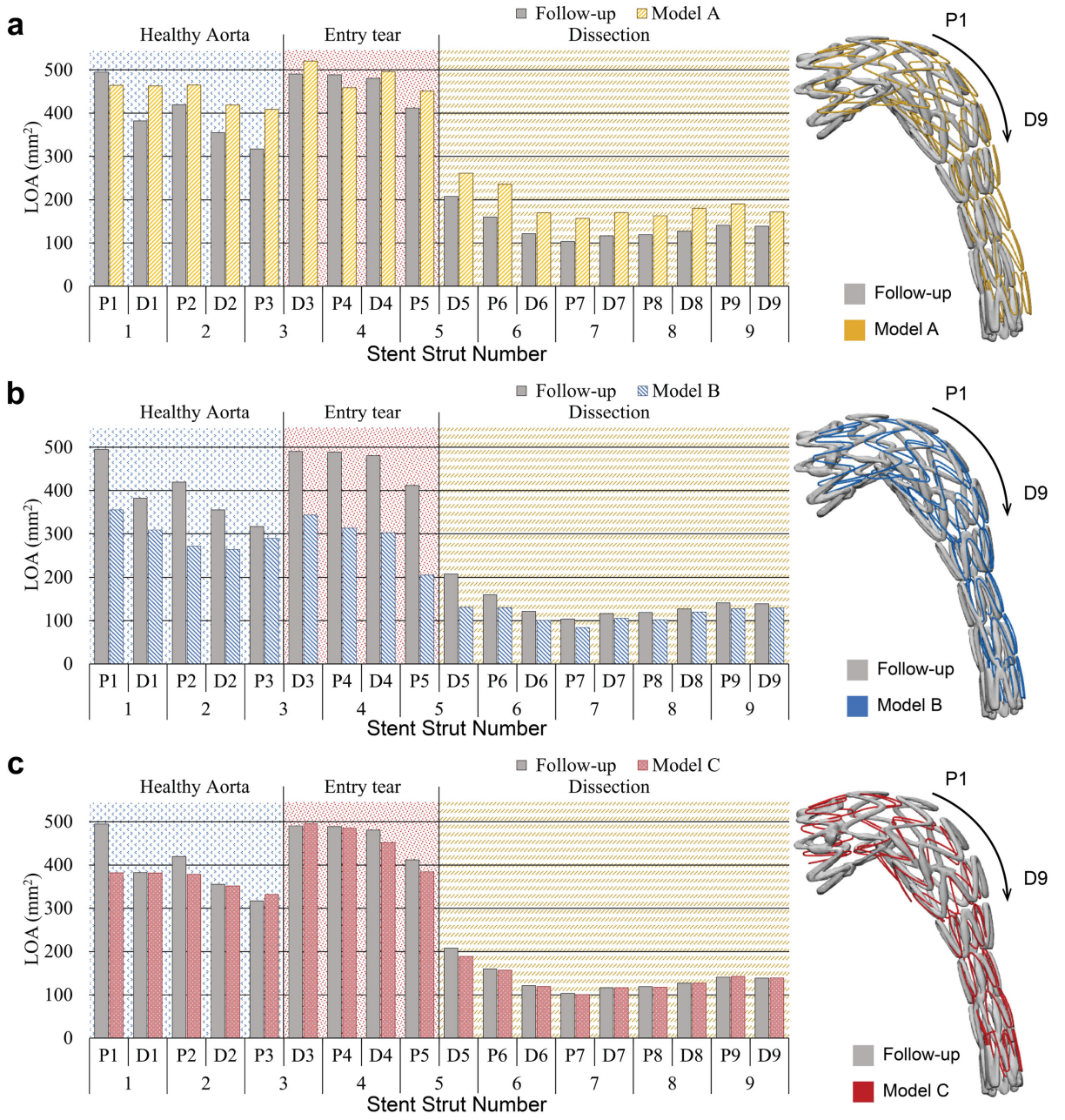


Figure 4.8 Comparison of local open area (LOA) at the stent strut ends measured from model A (a), model B (b) and model C (c) against to the corresponding value measured from the post-TEVAR follow-up CTA scan

4.2.3.2 Stress distribution

Table 4.4 shows the detailed quantitative comparison of the maximum principal stress in the three landing sections in pre- and post-TEVAR state based on the three models. Due to the absence of internal pressure load and the pre-stress tensor $\boldsymbol{S}_0$, there was no stress in model A before the SG deployment - this is also clear from the pre-TEVAR stress maps shown in Figure 4.9.a. After the SG was deployed into the true lumen, noticeable stress was introduced by the interaction between the aorta and SG with mean values of 63.31 kPa and 55.50 kPa for the aortic wall and intimal flap in the dissection section, respectively, but stress levels in the other two sections were very low (Table 4.4 and Figure 4.9.a).

Table 4.4 Maximum principal stress (kPa) in different landing sections obtained with models A, B and C (mean, 10th percentile and 90th percentile) pre- and post-TEVAR.

landing Sections			Model A	Model B	Model C
Healthy aorta		Pre-TEVAR	0 [0, 0]	103.09 [43.53, 179.43]	103.09 [43.53, 179.43]
		Post-TEVAR	15.38 [6.44, 26.06]	110.76 [49.78, 192.24]	86.83 [34.17, 155.74]
Entry tear		Pre-TEVAR	0 [0, 0]	105.55 [69.09, 142.46]	105.55 [69.09, 142.46]
		Post-TEVAR	11.53 [5.57, 17.31]	108.50 [73.05, 148.37]	81.49 [49.41, 117.96]
Dissection	Aortic wall	Pre-TEVAR	0 [0, 0]	83.65 [43.38, 129.77]	83.65 [43.38, 129.77]
		Post-TEVAR	63.31 [26.61, 104.79]	138.52 [77.17, 210.61]	122.02 [65.61, 188.80]
	Intimal flap	Pre-TEVAR	0 [0, 0]	54.63 [14.97, 93.26]	54.63 [14.97, 93.26]
		Post-TEVAR	55.50 [-6.16, 132.57]	74.89 [15.80, 131.00]	71.78 [14.45, 123.2]

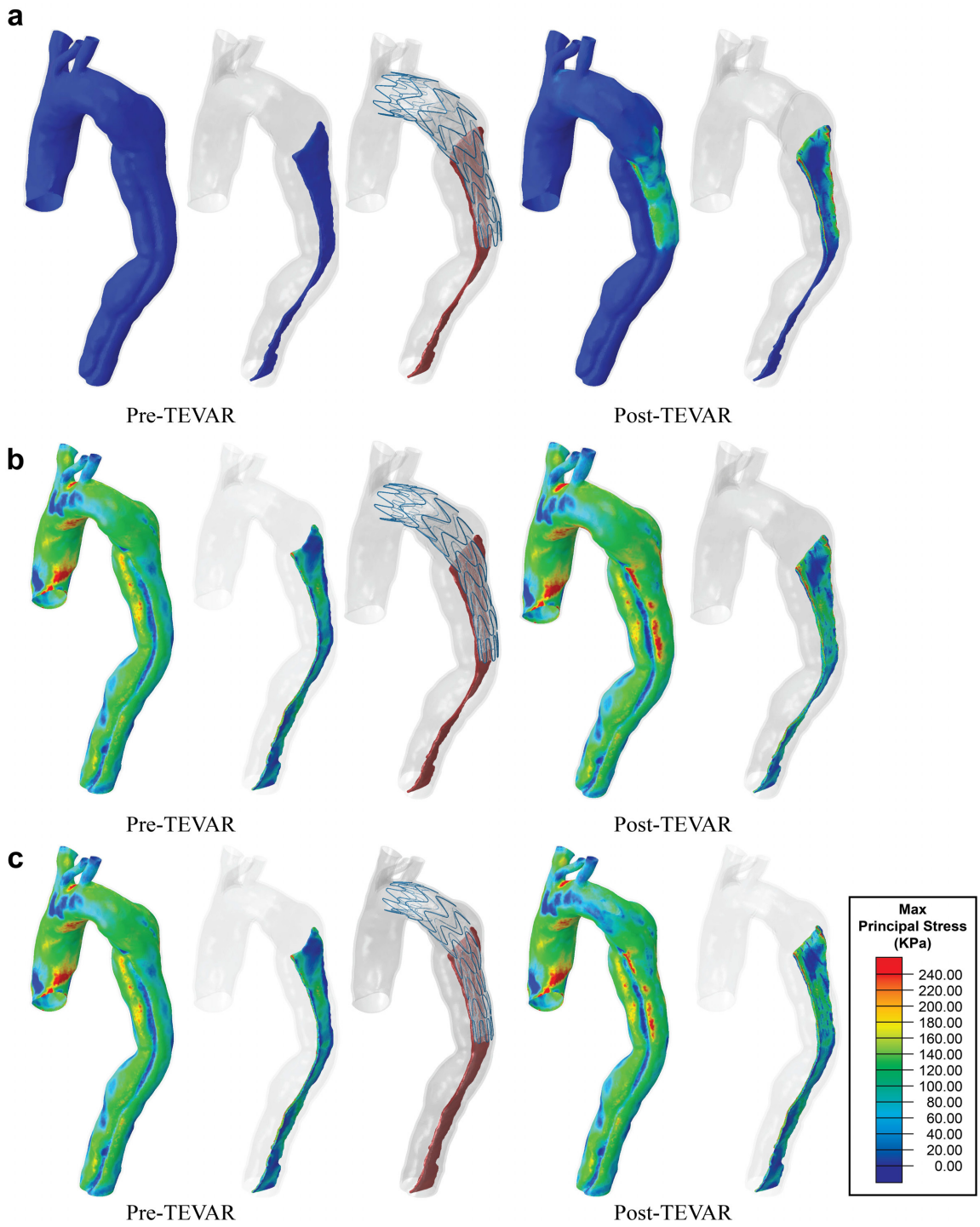


Figure 4.9 The maximum principal stress maps on the aortic wall and intimal flap pre- and post-TEVAR obtained from model A(a), model B(b) and model C(c). The virtually deployed stent-graft is shown in the middle with the intimal flap being highlighted.

After defining the pre-stress tensor $\boldsymbol{S}_0$ as the initial stress field in the aorta, the pre-TEVAR maximum principal stress map was calculated using model B (Figure 4.9.b). By comparing the pre- and post-TEVAR stress distribution, the SG slightly enlarged the high stress area between the left common carotid artery and the left subclavian artery. SG also introduced extra stress concentration in the dissection section (Figure 4.9). Quantitative comparisons of the pre- and post-TEVAR maximum principal stresses suggested that SG deployment slightly increased the maximum stress in the healthy aorta and entry tear section, but there was a significant increase of 65% on the aortic wall and 37% on the intimal flap in the dissection section (Table 4.4).

Since the pre-stress tensor $\boldsymbol{S}_0$ was employed as the initial stress for both model B and model C, the pre-TEVAR stress distribution and magnitude obtained from model C was the same as the results from model B (Figure 4.9b-c). Comparison of the pre- and post-TEVAR stress maps also suggested the same increase in high stress area in the proximal bare metal stent landing area where the stent apexes touched the aortic wall between the left subclavian artery and the left common carotid artery. The maximum principal stress in the healthy aorta and entry tear section was reduced by 16% and 23% respective after the SG deployment (Table 4.4). Following the TEVAR procedure, stress concentration was also introduced by the SG (Figure 4.9.c) and the maximum principal stress in the dissection was increased by 46% on the aortic wall and 31% in the intimal flap.

4.2.4 Effects of aortic wall and intimal flap mechanical properties

The effects of mechanical properties for the aorta and intimal flap on the SG configuration and stress distribution were assessed by using model C. The original settings in model C with the hyperelastic material parameters fitted from the type B aortic tissue for aortic wall and linear elastic Young's modulus of 277 kPa for the intimal flap provided the baseline case (A1F1) for this sensitivity test. As summarised in Table 4.5, two additional simulations were performed: one had the same aortic wall properties as in the baseline case but a stiffer intimal flap (E_{flap} = 350 kPa) (A1F2); and another (A2F1) using a different set of Yeoh

hyperelastic parameters (c_{10} = 37.1 kPa, c_{20} = 503.9 kPa and c_{30} = 721.4 kPa) which was derived from the anisotropic material model reported by Daplano et al. (Deplano et al., 2019).

Table 4.5 Simulations to evaluate the effect of material parameters.

Simulation	Aortic wall			Intimal flap
	c_{10} (kPa)	c_{20} (kPa)	c_{30} (kPa)	E_{flap} (kPa)
A1F1	17.5	58.9	116.1	277
A1F2	17.5	58.9	116.1	350
A2F1	37.1	503.9	721.4	277

4.2.4.1 Stent-graft configuration

To evaluate the sensitivity of the results to material parameters for the aortic wall and intimal flap, differences in LOA from the baseline case were calculated at each stent strut end and results for A2F1 and A1F2 are shown in Figure 4.10.a. Increasing the Young's modulus of the intimal flap (A1F2) only introduced minor differences in LOA in the healthy aorta (-0.1%) and entry tear (-0.2%) section, while relatively large difference of -9.4% was introduced in the dissection section (Table 4.6). When evaluating the spatial position of the centre point of the stent strut end in comparison with the post-TEVAR CTA, A1F2 showed averaged deviations of 3.1 mm, 3.9 mm and 4.8 mm in the three landing sections (Table 4.7).

Using a different set of material parameters for the aortic wall (A2F1), mean differences in LOA were -3.3%, -4.9% and -5.6% in the three landing sections when compared with the LOA measured from the baseline simulation (Table 4.6). The spatial position deviation between the simulation result and follow-up scan at the stent strut end was significantly increased at P1, D1 and P3, while the deviation was reduced at D5 when compared to the results from the A1F1 and A1F2 simulations (Figure 4.10.b). The mean values of centre point spatial deviation were 4.5 mm, 3.6 mm and 4.6 mm in the three landing sections (Table 4.7).

Table 4.6 Deviations in local open area from the baseline simulation in three landing sections (mean, standard deviation and maximum values)

Landing sections	LOA difference A1F2 (%)	LOA difference A2F1 (%)
Healthy aorta	-0.1 ± 2.6 [-3.5, 3.4]	-3.3 ± 4.1 [-10.2, 0.8]
Entry tear	-0.2 ± 3.7 [-2.8, 5.3]	-4.9 ± 5.2 [-8.9, 2.8]
Dissection	-9.4 ± 3.3 [-13.6, -3.2]	-5.6 ± 4.4 [-12.8, 1.2]

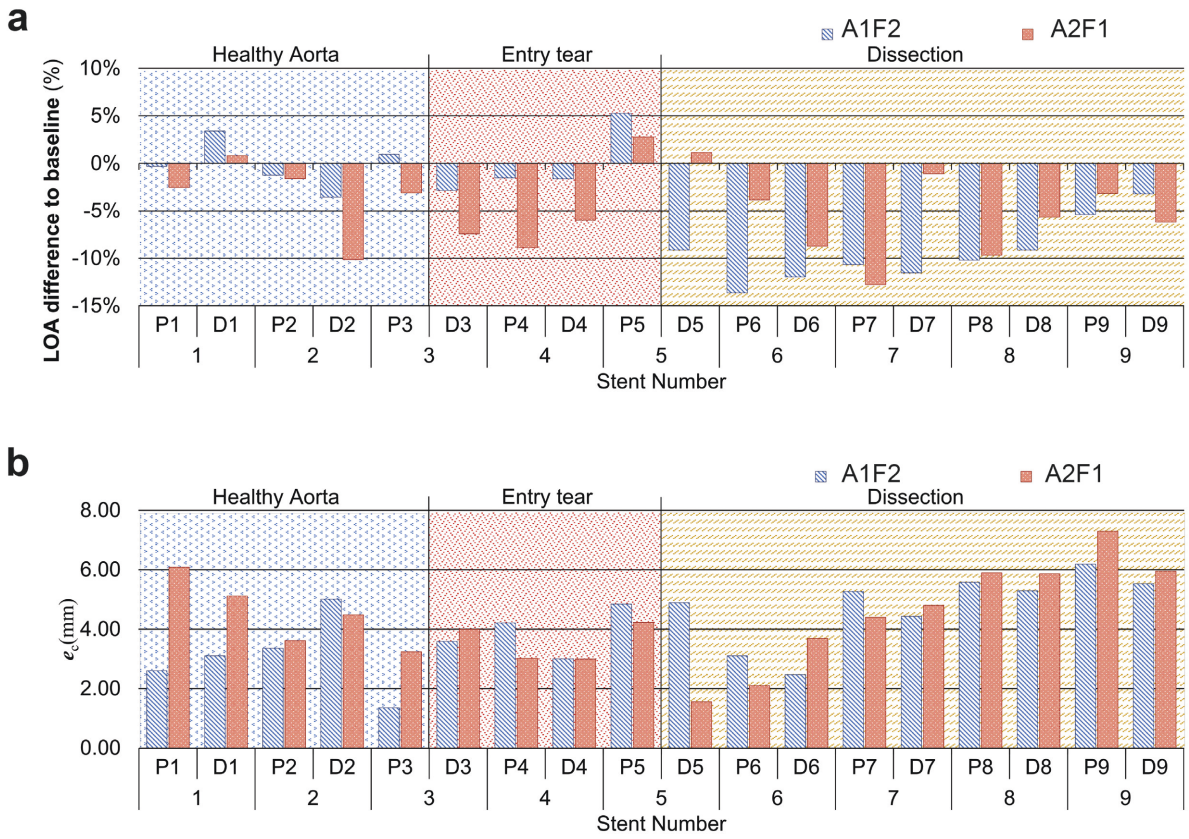


Figure 4.10 Effects of aortic wall and intimal flap mechanical properties on the prediction of post-TEVAR stent-graft configuration. a. deviation in local open area (LOA) from the baseline case for A1F2 and A2F1. b. stent strut end centre points position deviation (e_c (mm)) relative to the post-TEVAR follow-up CT scan.

Table 4.7 Spatial position deviation of stent strut end centre point (e_c) relative to the follow-up CT scan in three landing sections (mean, standard deviation and maximum values).

Landing sections	e_c A1F2 (mm)	e_c A2F1 (mm)
Healthy aorta	3.1 ± 1.3 [1.4, 5]	4.5 ± 1.1 [3.2, 6.1]
Entry tear	3.9 ± 0.8 [3, 4.8]	3.6 ± 0.6 [3, 4.2]
Dissection	4.8 ± 1.2 [2.5, 6.2]	4.6 ± 1.9 [1.6, 7.3]

4.2.4.2 Stress distribution

Figure 4.11 shows the maximum principal stress distribution in the aortic wall and intimal flap for the pre-TEVAR and post-TEVAR based on the two simulations, A1F2 and A2F1. Similar to the trend observed in the baseline simulation A1F1 (Figure 4.9.c), SG enlarged high stress area between the left common carotid artery and the left subclavian artery, introduced extra stress concentration at the dissection section, but reduced the maximum principal stress in the healthy aorta and entry tear section.

By comparing the pre-TEVAR and post-TEVAR stress in the A1F2 simulation quantitatively, the maximum principal stress in the healthy aorta and entry tear section was reduced by 13% and 27% respectively, while there was an increase of 47% on the aortic wall and 72% on the intimal flap in the dissection section (Table 4.8). In the A2F1 simulation, following the virtual SG deployment the maximum principal stress was reduced by 8% in the healthy aorta, but had a larger reduction by 38% in the entry tear section (Table 4.8). In the dissection section, the virtual SG deployment of SG into the narrowed true lumen caused the maximum principal stress to increase by 38% on the aortic wall and 10% on the intimal flap in A1F2 simulation.

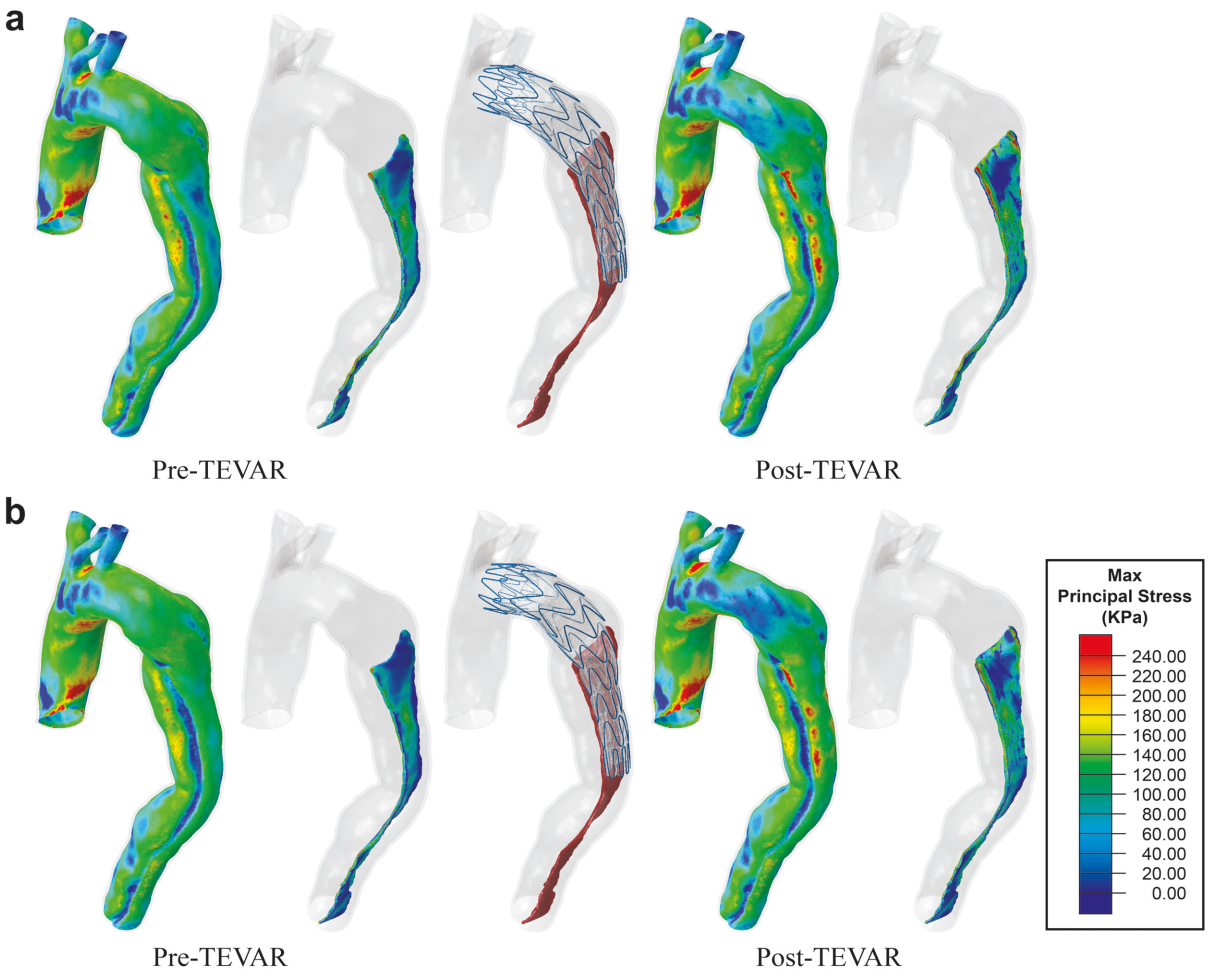


Figure 4.11 The maximum principal stress maps on the aortic wall and intimal flap pre- and post-TEVAR obtained from A1F2 (a) and A2F1 (b). The virtually deployed stent-graft is shown in the middle with the intimal flap being highlighted.

Table 4.8 Maximum principal stress (kPa) in different landing sections obtained from A1F2 and A2F1 (mean, 10th percentile and 90th percentile) pre- and post-TEVAR (marked as grey lines).

landing Sections			A1F2	A2F1
Healthy aorta		Pre-TEVAR	102.60 [44.24, 175.99]	103.81 [51.24, 171.03]
		Post-TEVAR	89.31 [34.67, 169.39]	95.68 [35.72, 186.09]
Entry tear		Pre-TEVAR	105.23 [69.47, 141.51]	107.69 [75.91, 142.85]
		Post-TEVAR	76.93 [46.2, 116.61]	66.68 [35.09, 104.11]
Dissection	Aortic wall	Pre-TEVAR	81.61 [41.11, 129.71]	91.71 [50.74, 132.45]
		Post-TEVAR	119.79 [58.34, 193.3]	126.12 [72.4, 186.95]
	Intimal flap	Pre-TEVAR	55.16 [14.23, 98.67]	40.39 [8.25, 74.8]
		Post-TEVAR	94.76 [15.96, 85.78]	44.46 [7.31, 86.64]

4.3 Discussion

Patient-specific virtual SG deployment in aortic dissection is challenging owing to the anatomic complexity and mechanical nonlinearity. Unlike aortic aneurysms or coarctation, aortic dissection usually involves multiple lumens and communications (entry and re-entry tears). This is further complicated by the hyperelastic behaviour of aortic wall, different material properties between the aortic wall and the intimal flap, superelastic mechanical behaviour of the metallic stent and contact nonlinearity introduced by the membrane-like synthetic graft. All these factors contribute to the complexity in simulating the interaction between SG and the local aorta. Although solid-solid interactions between the aorta and SG in patient-specific type B aortic dissection have been investigated by Ma et al. and Meng et al. (Ma et al., 2018, Meng et al., 2020), these studies ignored pre-stress conditions of the aorta,

the material difference between intimal flap and aortic wall and changes in pressure after TEVAR.

The model evaluated in this chapter offers multiple advances over the existing published methods. First, non-uniform thickness of the intimal flap was incorporated in the model geometry. This was achieved by employing a purpose-built segmentation approach which also allowed the intimal flap to be treated as a different material from the aortic wall. Therefore, the effect of material properties for the aortic wall and intimal flap can be evaluated independently. This feature is important when simulating acute and chronic stages of the pathology in the future (Peterss et al., 2016). Second, the crimping, delivery and deployment of the virtual SG was achieved via a virtual sheath which was controlled by the nodal specific displacement boundary condition. This enabled the model to deploy the SG virtually into very complicated type B aortic dissection anatomy with unusual curvature or local narrowing. Thirdly, the model incorporated the pre-stress tensor $\boldsymbol{S}_0$ and accounted for the intraluminal blood pressure load on the internal surface of graft. By adding layers of complexity to the model gradually, it was also possible to examine the influence of model settings and assumptions on improving the simulation accuracy.

In the evaluation of the effect of different model settings, qualitative and quantitative assessment of the simulation results was performed by comparing the SG configuration obtained from the simulation to the actual SG configuration reconstructed from post-TEVAR CTA scan. Due to the absence of pre-stress in the hyperelastic aortic wall, model A overpredicted the LOA at most stent strut ends. Although model B incorporated pre-stress in the aortic wall, it still underpredicted the LOA throughout the stent struts due to the absence of graft internal pressure. Model C produced the best prediction of SG configuration in all landing sections and well captured the LOA shift on the borders of landing sections. Regarding the spatial position of the SG, model C also achieved the best agreement with the post-TEVAR follow-up scan.

Another key factor, the choice of the mechanical properties for the intimal flap and the aortic wall, was also evaluated in terms of LOA and spatial positioning deviation. Simulations with material properties differing from the baseline simulation (A1F1) were performed based on

model C settings. When the Young's modulus for the intimal flap was increased from 277 to 350 kPa while keeping the same aortic wall property (A1F2), there was a 4.8% reduction in the LOA. When using a much stiffer (approximately twofold) set of parameters for the aortic wall (A2F1), the LOA was reduced by 4.8% compared to the baseline simulation. The predicted spatial positions of the stent struts were found to be less sensitivity to the choice of mechanical properties for the intimal flap and the aortic wall, with mean differences of 4.00 mm in A1F1 simulation, 4.10 mm in A1F2 simulation and 4.35 mm in A2F1 simulation.

Along with the model settings and choice of material properties, other factors also had influences when making quantitative assessment of the simulation accuracy. The CTA scan used to reconstruct the post-TEVAR SG configuration was performed 3 months after the TEVAR procedure. Since remodelling of the aorta starts immediately after the TEVAR procedure along with the expansion of true lumen and shrinkage of false lumen, it would be reasonable to expect that the LOA extracted from the 3-month post-TEVAR CTA scan was slightly larger than the LOA immediately after the intervention (Canaud et al., 2014). The virtual SG deployment model only captured the SG configuration during and immediately after TEVAR. This might explain why model C slightly underpredicted LOA at most of the stent strut ends than the follow-up CTA scan.

When compared with other virtual SG deployment models reported in the literature, the model presented in this chapter also showed its distinct advantages. Auricchio et al. performed a SG deployment simulation in patient-specific ascending aorta geometry with a rigid wall assumption and achieved high accuracy with deviation of <1.5 mm in the cross-sectional radius of the graft (Auricchio et al., 2013). A more recent study by Derycke et al. presented simulation of a double-branched SG in an aortic arch aneurysm and achieved a good agreement between the simulation result and the post-intervention CTA scan with a deviation of 3.2 ± 4.0% in the SG diameter (Derycke et al., 2019). Another simulation study of SG deployment in abdominal aortic aneurysms of 51 patients achieved very high accuracy with a mean equivalent spatial positioning difference of 1.28 ± 1.36 mm (Derycke et al., 2020). However, both studies employed the 'morphing' procedure instead of simulating the whole SG crimping, delivery and deploy procedure. The A1F1 simulation of virtual SG deployment in a patient-specific type B aortic dissection achieved LOA deviation less than

6.0% (equivalent to ~ 3% deviation in diameter) and spatial positioning deviation of 4.6 ± 1.2 mm, which are comparable to the results reported by Derycke et al. on the deployment of a double-branched SG in arch aneurysm (Derycke et al., 2019).

With regards to the influence of model settings on stress distribution in the aorta after TEVAR, both model B and model C showed the expansion of high stress area between the left carotid artery and left subclavian artery, where the proximal bare mental stent landed (Figure 4.9). This finding is consistent with the results presented in the literature (Ma et al., 2018, Meng et al., 2020). Including the pre-stress tensor altered the distribution of the maximum principal stress (MPS) both in the aortic wall and intimal flap (Figure 4.9). Model B produced much higher level of MPS than model A in the intimal flap and aortic wall in the three landing sections (Table 4.4). When comparing the results between model B and model C, the MPS reduced by 16% in the heathy aorta section and 23% in the entry tear section where an aneurysmal enlargement was present in model C result, instead of an increase of MPS in all sections with model B. After the deployment of SG, blood flow was diverted to flow through the SG instead of directly interacting with the aortic wall, which could be regarded as the pressure shielding effect of SG. Considering this shielding effect, the stress reduction in model C, especially in the entry tear section with aneurysmal enlargement, was reasonable and was similar to the findings for abdominal aortic aneurysms (Hemmler et al., 2019a).

Regarding the effect of material properties on the MPS, increasing the Young's modulus for the intimal flap by 26% or the aortic wall stiffness by twofold did not alter the qualitative distribution of MPS, nor did this affect the changing trend of MPS pre- and post-TEVAR. However, MPS in the dissection section appeared to be more sensitive to the intimal flap stiffness, whereas making the aorta stiffer caused further reduction of MPS in the entry tear section but did not have a notable impact on the stress level in other landing sections.

4.4 Summary

In this chapter, the virtual SG deployment model described in Chapter 3 was validated against the post-TEVAR CTA scan of a type B aortic dissection patient. The feasibility of the model was demonstrated by simulating the virtual deployment of SG into a complicated patient-specific aortic dissection with an extremely narowed true lumen. The model

incorporated patient-specific anatomical information based on pre-TEVAR CTA scan, details of the SG design, and the superelastic mechanical behaviour of the metal stent. Hyperelastic material parameters for the aortic wall were determined by the uniaxial tensile testing performed on the aortic wall tissue samples obtained from type B aortic dissection patients.

The effects of pre-stress condition of aortic wall and the SG internal pressure were assessed by comparing the simulation results with the post-TEVAR CTA scan. Simulation models without applying the pre-stress tensor and the SG internal pressure were proved to be inaccurate in predicting the SG configuration. The absence of pre-stress condition of the aortic wall produced unphysical stress distribution, while incorporating the SG internal pressure altered the quantitative stress changes between pre- and post-TEVAR. These findings confirmed the need to include both effects for patient-specific simulation of virtual SG deployment in type B aortic dissection. The effect of mechanical properties for the aortic wall and intimal flap was also assessed by increasing their stiffness, which showed very limited influence in predicting the SG configuration.

Results from model C by incorporating pre-stress condition in the aortic wall and the SG internal pressure presented in this chapter show good quantitative agreement with the post-TEVAR follow-up CTA scan. This highlighted the potential applicability of virtual SG deployment to clinically relevant studies. Further applications of the validated virtual SG deployment model will be presented in the following chapters.

Chapter 5

Application I: predicting procedural success of TEVAR in type A aortic dissection†

Although TEVAR has been recognised as a default treatment for type B aortic dissections (Nienaber and Clough, 2015), acute type A aortic dissection usually requires emergency open surgery to replace the dissected aorta with a synthetic graft. It has recently been reported that selected type A dissection cases may qualify for TEVAR in scenarios of prohibitive surgical risks and straight ascending aorta morphology (Nienaber et al., 2017).

As presented in Chapter 4, the FEM-based virtual SG deployment simulation method has shown its capability in reproducing post-TEVAR SG configuration in type B aortic dissection, along with wall stress distribution closer to the in vivo biomechanical environment by incorporating pre-stress condition of the aortic wall and SG internal blood pressure. This chapter extends the application of the method to a failed TEVAR in type A aortic dissection caused by immediate migration following SG deployment. In addition to the method adopted in Chapter 4, it also incorporates the aortic root motion obtained by digital subtraction angiogram (DSA) prior to the TEVAR procedure and hyperelastic material parameters derived from tensile testing on the patient's ascending aortic tissue samples. The aim was to

---

† The author of this dissertation carried out all the work described in this chapter unless specified otherwise. The preparation of aortic tissue samples was conducted by Dr M. Yousuf Salmasi from Department of Surgery and Cancer, Imperial College London, UK. Mechanical testing of the tissue samples was performed by Dr Sumesh Sasidharan from Department of Bioengineering, Imperial College London, UK. The content of this chapter was partially adapted from Yuan, X.*, Kan, X.*, Xu, X.Y. and Nienaber, C.A., 2020. Finite element modeling to predict procedural success of thoracic endovascular aortic repair in type A aortic dissection. *JTCVS Techniques*, 4, pp.40-47.

test if the virtual SG deployment model could reproduce the immediate stent-graft migration occurred in this case, which may help to understand why the procedure failed. An alternative deployment scenario was also simulated to explore possibilities of avoiding the immediate stent-graft migration in the ascending aorta of this patient.

5.1 Methodology

5.1.1 Patient information

An 80-year-old man was admitted with sudden onset of severe chest pain radiating to neck and jaw lasting for 13 hours after presenting to the emergency department of a district general hospital. A diagnostic CT angiogram revealed a type A aortic dissection, prompting transfer to intensive care unit and further on to a tertiary care aortic centre for open surgery (Figure 5.1.a). However, the open surgery for replacing ascending aorta was postponed twice due to the comorbidities and age of the patient. A follow-up ECG-gated contrast-enhanced CTA showed stability of the confined type A aortic dissection with no signs of progression, the presence of a single entry tear and no aortic valve dysfunction or abnormal coronary perfusion. Subsequent multidisciplinary team decision recommended TEVAR with a suitable compliant stent-graft to cover the single entry, as the distance between coronaries and the brachiocephalic branch was sufficient to accommodate a 45-100-mm GORE C-TAG Active Control stent-graft (W. L. Gore & Associates, Inc, Flagstaff, Ariz).

During the interventional procedure, DSA was performed to obtain the motion of the aortic root. Using femoral access and a 22F DrySeal introducer, a 45x100mm GORE® C-TAG® Active Control stent-graft (SG) was positioned in the ascending aorta guided by fluoroscopy and transoesophageal echocardiography to cover the tear. A special design feature of the C-TAG SG allows clinicians to further adjust the landing position while keeping the device in a semi-opened state. After confirmation of the landing position under fluoroscopy, stent-graft was fully launched from the delivery system. However, the device was found to have migrated seconds after deployment with its distal end being dislodged into the false lumen (Figure 5.1.b). Although hemodynamically stable, no second stent was placed in the absence of any landing zone left.

Another ECG-gated contrast-enhanced CTA was performed to identify the SG configuration (Figure 5.1.c) and prepare for the open surgery. One month later successful surgery was performed by removing the SG under conditions of 28 °C hypothermia and antegrade brain perfusion and replacing the ascending aorta/hemiarch with a 32mm Gelweave® graft with sidearm. During the open surgery, the dissected ascending aorta of the patient was also removed along with the SG (Figure 5.1.d) and the tissue was then restored in saline solution at 4 °C for further mechanical tests. The postoperative course was complicated by both temporary respiratory and kidney failure requiring prolonged ventilation and intermittent renal replacement therapy, eventually leading to full recovery.

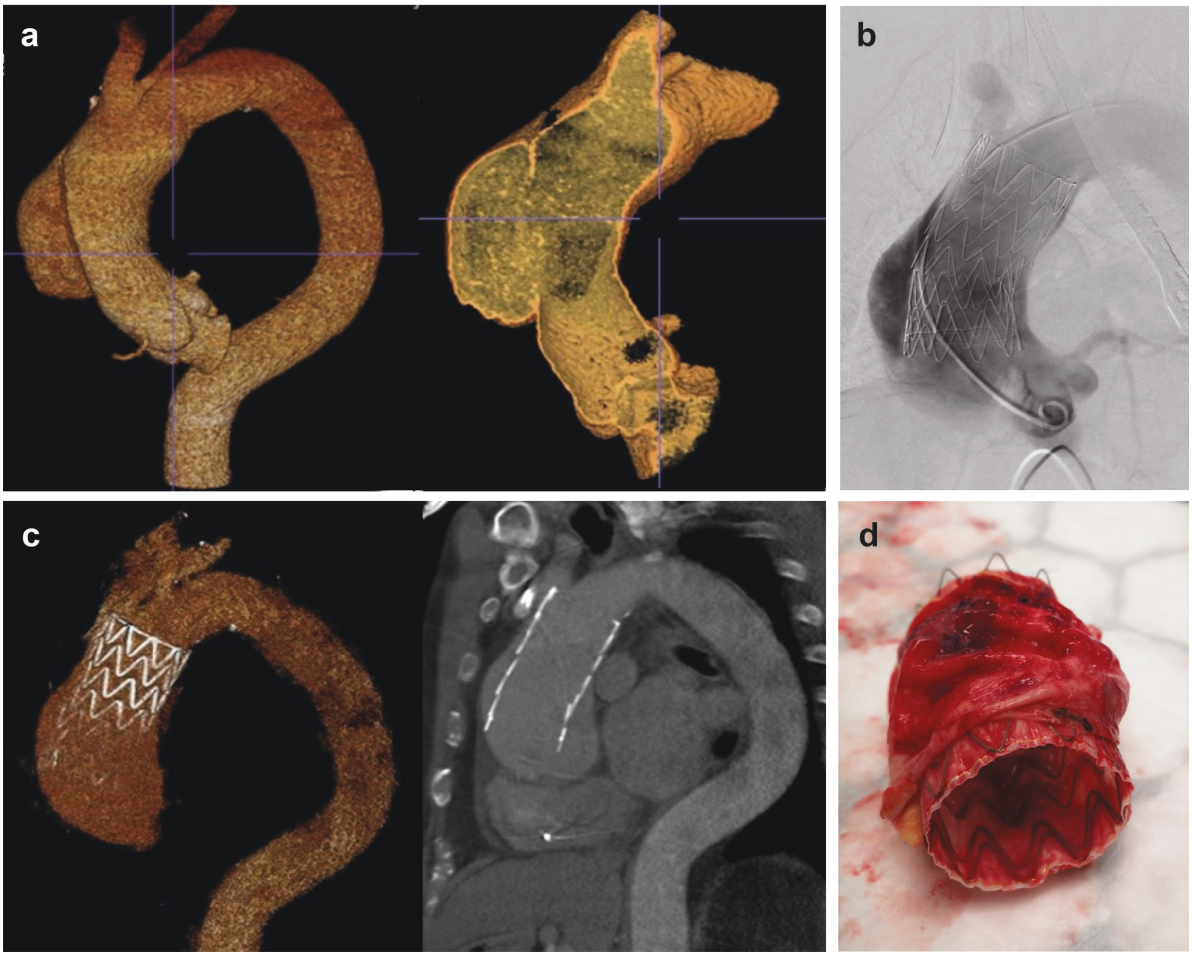


Figure 5.1 Illustration of the type A aortic dissection case. a. 3-dimentional reconstruction of a computed tomographic angiogram (CTA) with type A aortic dissection showing a single large entry tear. b. Digital subtraction angiogram (DSA) obtained immediately after full deployment of the device showing stent-graft migration. c. Post-intervention 3-dimentional CTA showing stent-graft migration and the proximal part of SG pushing into the false lumen. d. The ascending aorta cut during the open surgery along with the 45-100-mm GORE C-TAG Active Control SG.

5.1.2 Aortic dissection geometry and stent-graft modelling

The pre-intervention CTA images were obtained from Cardiology and Aortic Centre, Royal Brompton & Harefield NHS Foundation Trust and processed to reconstruct the 3-dimensional patient-specific aortic geometry and the intimal flap by following the same special segmentation workflow described in Chapter 4 (Section 4.1.2). Ethical approval was obtained from the local Ethics Committee, and written consent was given by the patient. The aortic wall was assumed to have a uniform thickness of 1.5 mm, while the intimal flap had non-uniform thickness determined by the local distance between the true and false lumen on CTA images. The geometry of aortic wall and intimal flap were combined together (Figure 5.2a) and meshed into tetrahedra elements (C3D4 in Abaqus (Dassault Systèmes, France)).

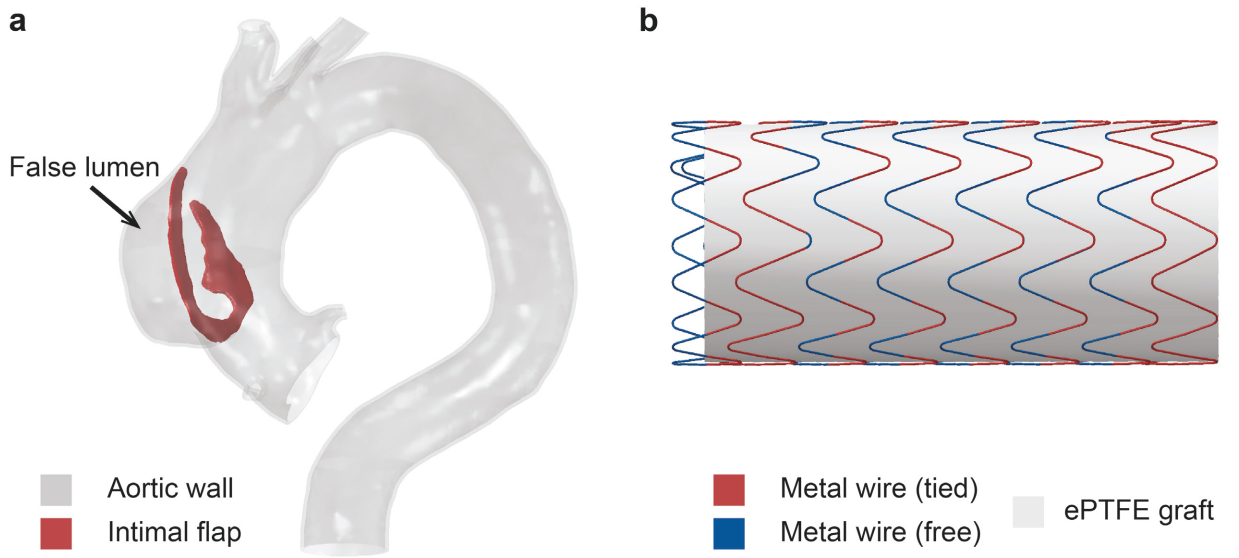


Figure 5.2 a. Reconstructed geometry of type A aortic dissection. b. 45-100-mm GORE C-TAG Active Control stent-graft.

During the intervention, a 45-100-mm GORE C-TAG Active Control stent-graft (W. L. Gore & Associates, Inc, Flagstaff, Ariz) was launched into the dissected ascending aorta. The diameter (45 mm) and length (100 mm) of the SG were used as inputs for the parametric model of C-TAG SG, which is described in Chapter 3. The expanded polytetrafluoroethylene (ePTFE) graft was modelled as a cylindrical tube with a thickness of 0.1 mm. Different from the Valiant SG described in Chapter 4, metallic scaffold of the C-TAG SG was only assembled

by a single nitinol ring and was partially attached to the ePTFE synthetic graft. This special design in the attachment prevents the metallic stent from sliding along the graft, while also allowing the SG to retain its curved configuration when deployed into the curved ascending aorta or aortic arch (Figure 5.2b).

The nitinol stent scaffold was meshed into reduced integration linear hexahedral elements (C3D8R) in Abaqus and modelled as a superelastic material using the same parameters given in Table 4.1. The ePTFE graft was meshed into reduced integrated membrane elements (M3D4R) in Abaqus and modelled as an isotropic linear elastic material with a Young's modulus of 55.2 MPa and Poisson's ratio of 0.46 (Desyatova et al., 2020).

5.1.3 Aortic root motion measurement

The motion of aortic root is non-trivial and should not be neglected when performing finite element analysis of the ascending aorta (Singh et al., 2016). To determine the motion of aortic root, the DSA acquired during the TEVAR procedure prior to the positioning of SG was used which allows measurement of the root motion within the image plane. The DSA image plane was marked by following the angular system of fluoroscope with a left anterior oblique (LAO) angle of 45° and cranial (CRA) angle of 10°.

For each frame of the DSA image (Figure 5.3), the left and right coronary ostia were chosen as anatomical landmarks to track the in-plane motion of the aortic root. The midpoint between the right and left ostia landmarks was defined as the governing point of this motion. The in-plane motion of aortic root was decomposed into 3 degrees of freedoms and transformed into the local coordinate system: the displacement parallel with the local vessel centreline d_l with positive direction from the midpoint toward the aortic root, the displacement perpendicular to the local vessel centreline d_r with the positive direction from the midpoint toward the left coronary ostium and the rotation angle r with the rotation axis defined as shown in Figure 5.3. The rotation angle is needed here because the local vessel axis varies with time (i.e. from frame to frame). The obtained motion data were imposed as the boundary condition at the midpoint of the aortic root in the simulation model.

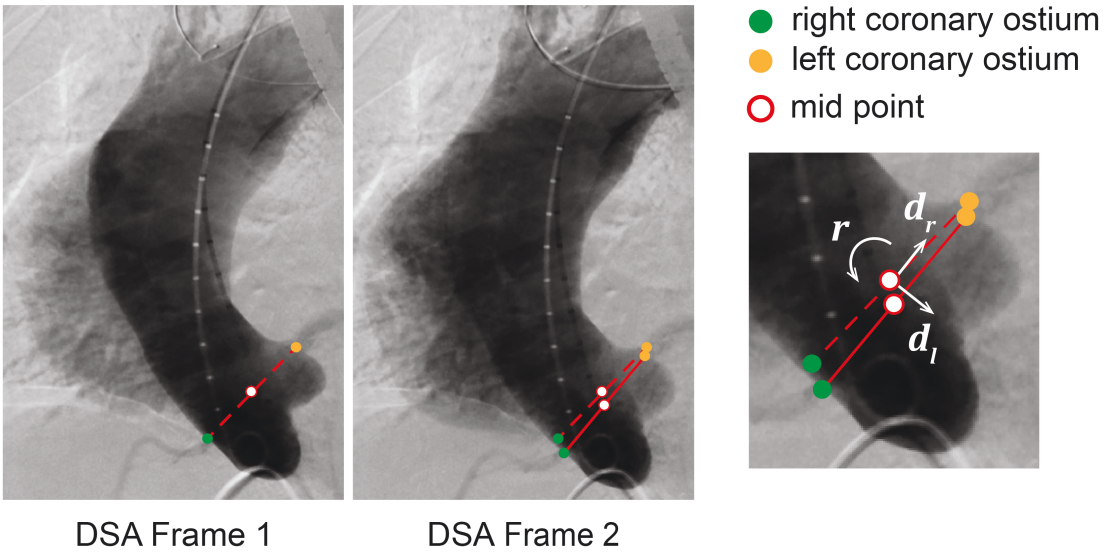


Figure 5.3 Measurement of aortic root in-plane motion based on DSA. DSA images at two different time points, with the right and left coronary ostia chosen as anatomical landmarks.

5.1.4 Mechanical tensile test

The specimen preparation and mechanical testing of the ascending aortic tissue from the patient were performed by our collaborators from the Department of Surgery and Cancer and the Department of Bioengineering, Imperial College London, by following the standard workflow for mechanical testing of human ascending aorta which has been described elsewhere (Salmasi et al., 2021). The tubular portion of the ascending aorta from the patient was collected during the open surgery and sent for mechanical testing within 48h after the surgery.

For completeness, a brief summary of the experimental procedure is given here following the work reported by Salmasi et al. (2021). After equilibration at the room temperature, the surrounding connective tissues were first removed from the ascending aorta specimen. Then the tubular tissue was cut along the longitudinal direction at the anterior side of the tissue producing a flat 'butterfly' shaped tissue specimen. A dog-bone shaped sharp stencil was used to cut the samples for uniaxial tensile test. 11 tissue samples with effective length of 10 mm and width of 5 mm were collected from the aortic wall without dissection, while 3 samples were collected from the intimal flap. Mechanical testing was performed by using a

purpose-built system fitted with a Test Resources R-Series Controller with a 44 N loading cell. All tensile tests were conducted at a constant temperature of 37 °C.

Each stress-stretch curve of the test was fitted from zero stretch to the material failure point by using an in-house MATLAB code (MathWorks, Inc., Natick, USA) as described in Chapter 4 (Section 4.1.3). The material parameters for the Yeoh hyperelastic model obtained from the 11 aortic tissue samples were averaged and the mean value of the material parameters, c_{10}^{w}, c_{20}^{w}, c_{30}^{w}, were employed to describe the incompressible isotropic mechanical behaviour of the aortic wall in the simulation model. Likewise, the mechanical behaviour of the intimal flap was described by another set of material parameters c_{10}^{f}, c_{20}^{f}, c_{30}^{f} fitted to the tensile test data obtained from the three intimal flap tissue samples.

5.1.5 Virtual stent-graft deployment workflow and selection of simulation scenarios

The initial geometric configuration used in the computational simulation was based on the pre-interventional CTA, while positioning of the SG was based on the angiographic image acquired during the TEVAR procedure. The workflow of virtual SG deployment followed that for model C in Chapter 4 by incorporating pre-stress of the aortic wall and the action of internal pressure on SG. Similarly, virtual SG deployment was controlled by the deformation of a virtual sheath; the SG was crimped from its stress-free state to the diameter of the delivery sheath. The proximal landing position was selected and assumed curvature of the SG were simulated before removing the virtual sheath. The SG landing position was determined based on the fluoroscopic image acquired at semi-open stage before TEVAR launch, as shown in Figure 5.4.a. Then the virtual sheath was removed to fully launch the SG at the targeted location. Finally, the motion of aortic root was applied after the SG was fully deployed.

Two different landing positions were simulated. Scenario I corresponded to the position adopted in the actual procedure, in order to reproduce the real TEVAR process and to find out possible reasons for the immediate stent-graft migration observed in this patient. To understand the influence of SG proximal landing position on its biomechanical performance, scenario II was simulated where the landing position was moved toward the aortic root by

10 mm as shown in Figure 5.4.b. Simulation results were verified by comparing the simulated SG position with the real SG position shown in the DSA acquired immediately after SG launch and the post-TEVAR CTA images.

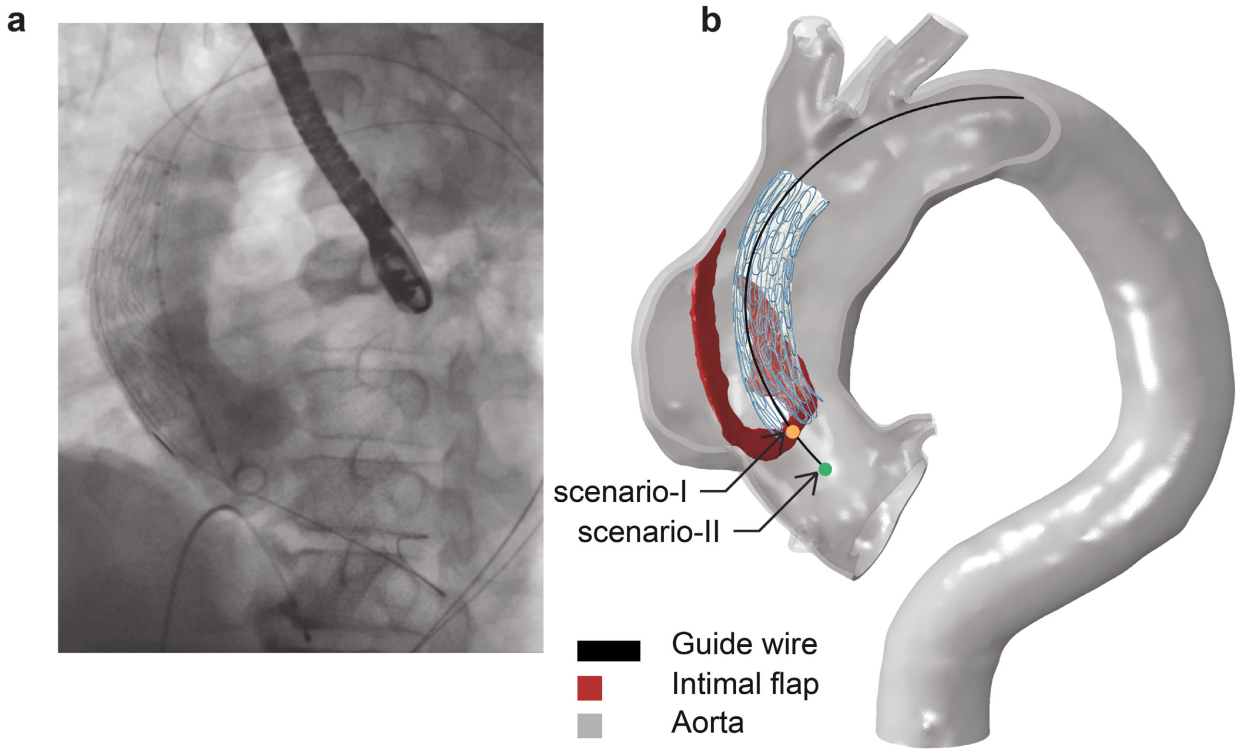


Figure 5.4 Patient-specific finite element model analysis. a. Fluoroscopic view of stent-graft positioning in semi-open stage before launch. b. Simulated image of the stent-graft in the ascending aorta with virtual adaptation to the aortic curvature. The orange circle marks the proximal landing position in scenario-I, which simulates the actual thoracic endovascular aortic repair procedure, whereas the green circle simulates the proximal position of stent-graft in scenario-II, which assumed a more proximal positioning by 10 mm.

The virtual SG deployment simulations were performed with Abaqus explicit solver (Dassault Systèmes, France). All contacts were modelled by using the general penalty contact with a friction coefficient of 0.2 under the Coulomb friction law (Desyatova et al., 2020). The ratio of the kinetic energy and internal energy (ALLKE/ALLIE) was kept below 10% to ensure that the simulation was quasi-static.

5.2 Results

In this section, data on the aortic root motion measured from the DSA images and the patient-specific mechanical properties of the aortic wall and intimal flap are presented first. This is followed by an assessment of the simulated SG configuration and comparisons of simulation results for the two landing positions.

5.2.1 Aortic root motion and mechanical properties of dissected ascending aorta

Due to the low frame rate of the DSA image (only 4 frames per second), it was not possible to generate a continuous motion trace of the aortic root within one cardiac cycle. The maximum motion of the aortic root was measured instead and the values for d_l, d_r and r were 4.14 mm, -3.5 mm and 3.24° respectively. The longitudinal motion measured in this patient was significantly restricted by the enlarged false lumen in the ascending aorta when compared with the averaged root motion in normal aorta (9.10±2.38 mm) (Yuan et al., 2021a).

Stress-stretch curves from 11 tissue samples obtained from the ascending aortic wall without dissection and 3 tissue samples from the intimal flap were analysed by using the MATLAB code described in Chapter 4 (Section 4.1.3). The coefficient of determination R^2 of each fitting curve was calculated to assess the quality of fitting, and mean values were 0.995 for the aortic wall tissue samples and 0.996 for the intimal flap samples. The average Yeoh model parameters for the aortic tissue were calculated at c_{10}^{w}= 5.95 kPa, c_{20}^{w}= 153.88 kPa, c_{30}^{w}= 17.72 kPa. These represented a lower stiffness (approximately 50%) when compared with data reported on another type A aortic dissection patient (Deplano et al., 2019). The intimal flap also showed nonlinear elastic behaviour, with the Yeoh parameters c_{10}^{f} = 9.3 kPa, c_{20}^{f}= 47.9 kPa, c_{30}^{f}= 0.0 kPa. The stretch-stress curves of the tissue samples from the aortic wall and intimal flap, along with the averaged fitting curves for the two tissue sample families are shown in Figure 5.5.

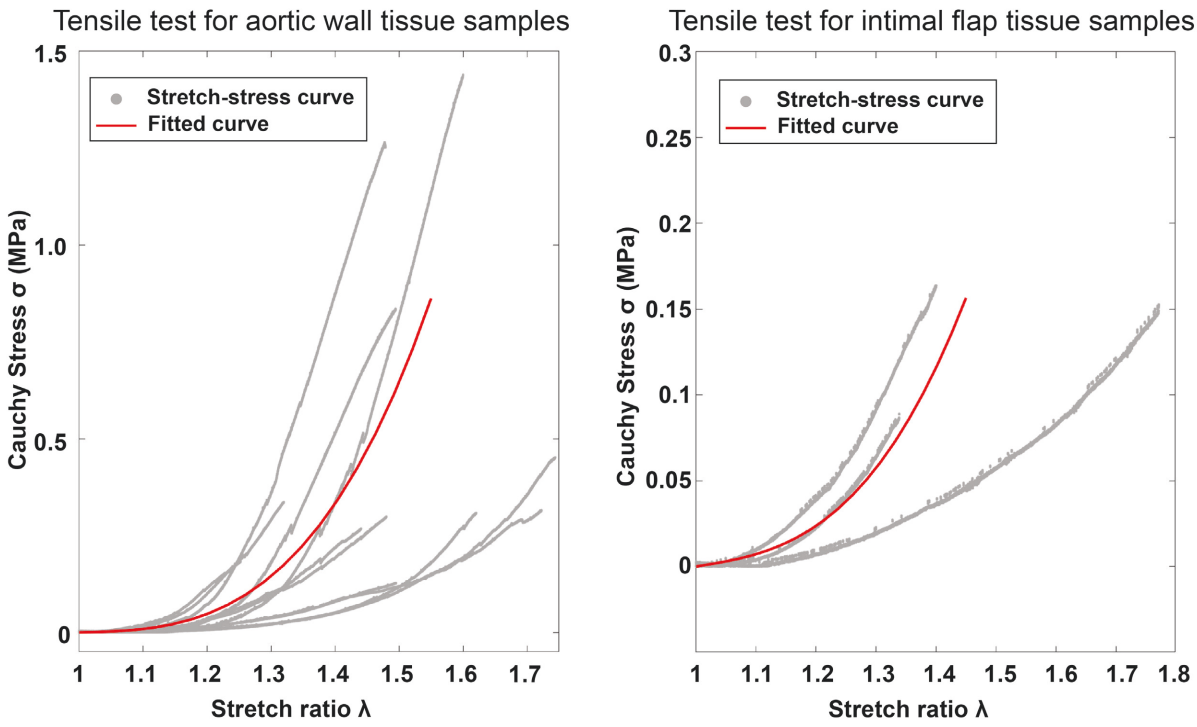


Figure 5.5 Stress-stretch relationships for aortic wall and intimal flap samples obtained from the type A aortic dissection patient reported in this chapter.

5.2.2 Stent-graft configuration assessment

The simulated SG configuration and its variation during the virtual deployment simulation are shown in Figure 5.6. It can be seen that in simulation scenario I, the proximal bare metal stent apex landed onto the intimal flap directly, causing the intimal flap to deform toward the false lumen side. This local deformation allowed the proximal bare mental stent to push further into the false lumen and migrated along the intimal flap in semi-open stage. The fully deployed SG configuration was compared with the DSA acquired immediately after stent-graft deployment during the intervention, demonstrating good congruence as shown in Figure 5.7.a. Minor discrepancies can be observed at the distal end of SG, possibly caused by further stent-graft migration as a result of aortic root motion and blood flow. This is confirmed by Figure 5.6.a where the simulated SG straightened and pushed further into the false lumen after incorporating patient-specific aortic root motion. It is reassuring to note that the post-TEVAR CTA scan acquired 1 month after the intervention (included in Figure

5.7.b) also revealed a straightened SG configuration, which agreed well with the simulation result.

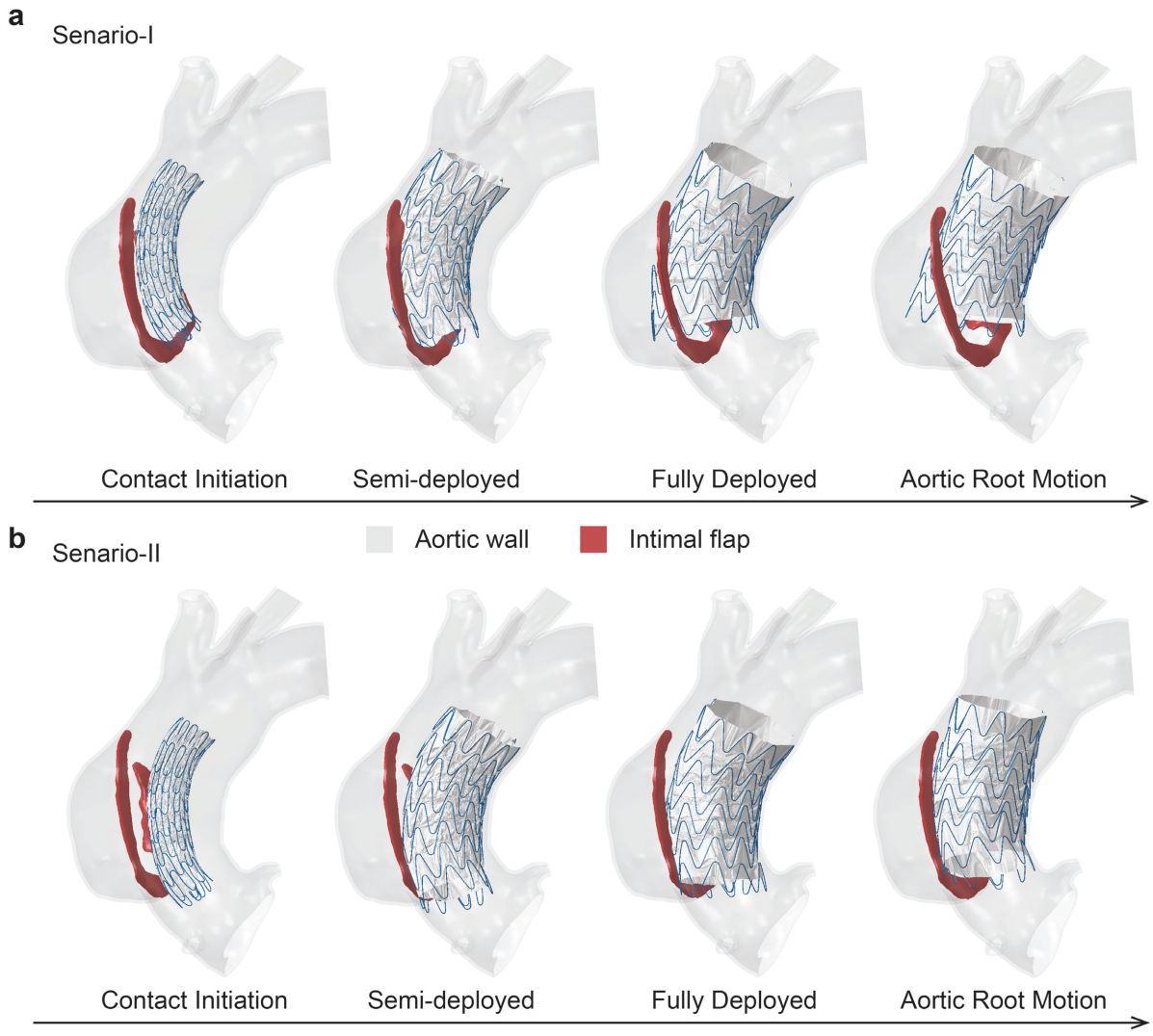


Figure 5.6 Evolution of stent-graft configuration during the virtual deployment simulation, starting from initial contact to fully deployed stage after incorporating the aortic root motion. a. Simulation scenario I. b. Simulation scenario II.

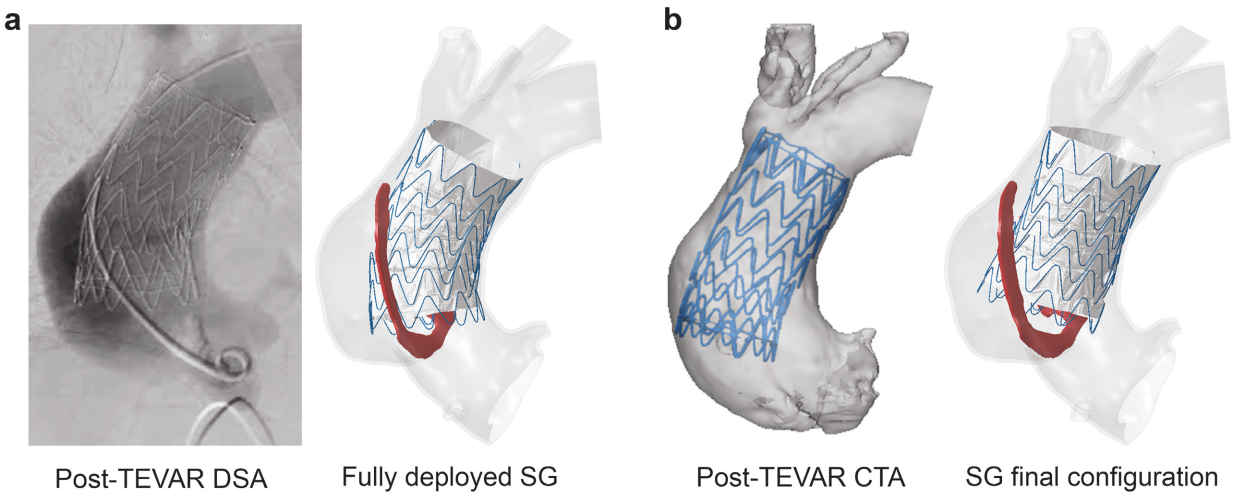


Figure 5.7 Qualitative comparison of stent-graft (SG) configurations between medical images and simulation results within the same projection plane of DSA (left anterior oblique (LAO) angle of 45° and cranial (CRA) angle of 10°). a. Post-interventional DSA showing SG configuration immediately after release of SG from the sheath and the simulated fully deployed SG configuration without aortic root motion. b. Stent and aorta reconstructed from post-TEVAR CTA image 1 month after the intervention and the simulated SG configuration after implementing aortic root motion.

Comparison of the simulation results between the two scenarios showed that there was less SG deformation toward the false lumen in scenario II and that the proximal end of the SG stayed within the true lumen. In simulation scenario II, the proximal bare metal stent apex landed onto the aortic wall instead of the highly deformable intimal flap (Figure 5.6.b). The intimal flap experienced less deformation toward the false lumen side. Consequently, the SG remained stable within the ascending aorta with a very small migration. After incorporating the aortic root motion into the simulation, the SG straightened but the proximal end of the SG hardly moved.

5.2.3 Stress distribution

Figure 5.8 Shows variations of stress on the intimal flap at different stages of the virtual deployment simulation. Quantitative comparison of the maximum principal stress (MPS) between the two simulated scenarios are given in Table 5.1.

In simulation scenario I, higher MPS at the mean value of 76.88 kPa was introduced by the stent-graft during stent-graft migration along the intimal flap in semi-deployed stage. The

mean value of MPS was reduced to 72.11 kPa after the stent-graft was fully deployed and migrated into the false lumen. Negative MPS was introduced at the proximal end of the intimal flap during stent-graft migration. After implementing the aortic root motion, MPS on the intimal flap was increased by 6.4 % (Table 5.1).

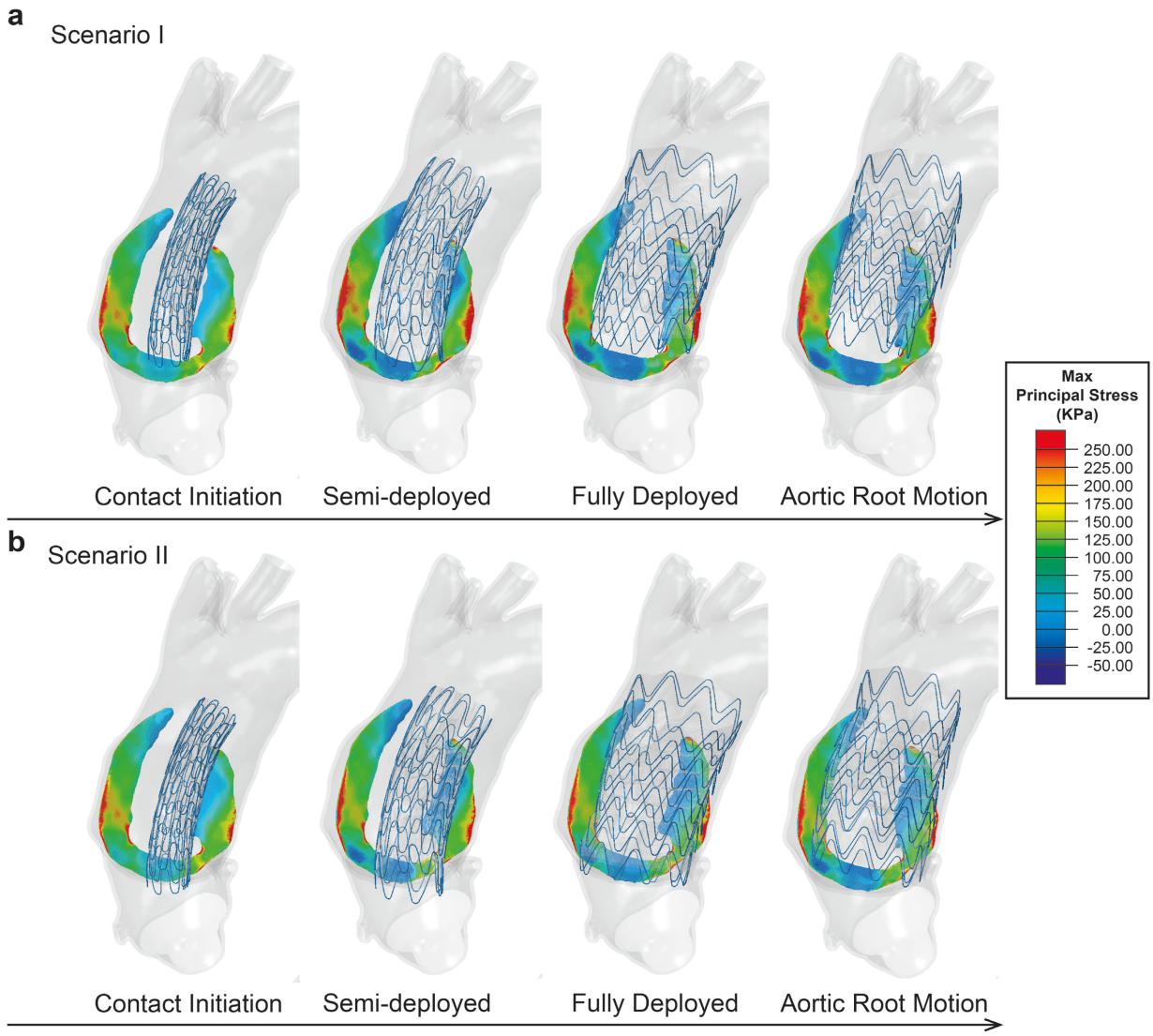


Figure 5.8 Distributions of maximum principal stress (MPS) on the intimal flap during the virtual SG deployment simulation. (a) Scenario I, (b) Scenario II.

Table 5.1 Comparison of maximum principal stress (MPS) (kPa) in the intimal flap between the two scenarios at different stages of the virtual deployment simulation (mean, 10th percentile and 90th percentile).

	Contact initiation	Semi-deployed	Fully deployed	Aortic root motion
Scenario I	69.13 [-8.47, 201.77]	76.88 [-9.16, 251.87]	72.11 [-9.69, 238.48]	76.78 [-9.72, 250.54]
Scenario II	69.13 [-8.47, 201.76]	71.29 [-9.38, 209.76]	69.68 [-8.73, 206.83]	71.83 [-9.4, 211.44]

In simulation scenario II, the results followed the same trend in that the mean MPS on the intimal flap reduced slightly after the stent-graft was fully deployed, and that applying the aortic root motion resulted in a small increase in MPS. Compared with the results from simulation scenario I, mean values of MPS were slightly lower but there was a significant reduction in the peak MPS with the 90th percentile values being reduced by up to 42 kPa.

5.3 Discussion

Although endovascular procedures have recently been applied with some success to the ascending aorta in various chronic scenarios (Nienaber et al., 2017), the technology appears not ready for prime time for a number of reasons: first, there are no dedicated endovascular devices available for specific use in the ascending aorta addressing the challenges of the anatomy and the 3-dimensional motion of the ascending aorta; second, current devices should precisely fit between coronary ostia and the brachycephalic trunk, and third the delivery of such device must be controlled and precise in order to avoid major problems.

In this highly selective case such pre-conditions seem to be fairly well met given the contraindication for open surgery, the suitable anatomy for a flexible device (GORE® C-TAG® 45-100mm Active Control) and the modern automatic release mechanisms supported by rapid right ventricular pacing and low blood pressure for precise placement. Nevertheless, the procedure failed as shown in Figure 5.7.a. The important questions are to understand the reasons for the failure and whether this could have been predicted.

This is why finite element modelling of the interaction between an endovascular device and surrounding anatomy was brought in. Based on pre-intervention CT angiogram images, virtual stent-graft deployment simulations were performed offline and the results revealed interesting findings. The crown, proximal bare metal stent was found to push against the intimal flap at the level of the proximal landing zone (Figure 5.6.a) with extra stresses in the tissue. High compression stress and localised deformation of the proximal portion of intimal flap induced by radial force of the stent-graft caused stent-graft migration during the semi-deployed stage (Figure 5.8.a). The deformation of intimal flap further reduced local contact pressure and friction between the stent-graft and the intimal flap allowing the stent-graft to slide on the intimal flap. After imposing the aortic root motion, the moving aortic root and ascending aorta facilitated the stent-graft to straighten after deployment, which was consistent with observations made by comparing the DSA acquired during the intervention and the follow-up CT angiogram at 1 month after the procedure (Figure 5.7). Results obtained for simulation scenario I suggested that the proximal landing zone was too close to the tear and the tissue too vulnerable to support the radial force of a self-expanding stent-graft.

By moving the proximal landing position about 10 mm towards the aortic valve as simulated in scenario II, the predicted peak MPS in the intimal flap was much lower (Table 5.1), avoiding over-stretching the intimal flap and stent-graft migration as predicted by the scenario I simulation. Simulation of scenario II suggested that the new proximal landing position could be a better strategy to prevent stent-graft migration. Localised deformation and stress concentration were reduced which would have avoided migration and dislocation of the stent into the false lumen.

Furthermore, this case study was unique in the following aspects: rare stent-graft migration during the TEVAR intervention; availability of very comprehensive clinical data, including patient-specific aortic root motion data and patient-specific aortic tissue mechanical property, making it a good lesson to learn from during the progression of introducing TEVAR in treating selective type A aortic dissection patients. The aortic root motion data and material parameters derived from the mechanical tests provided additional patient-specific data for the virtual stent-graft deployment simulation. The remarkable agreement between

the simulation results of scenario I and the clinical outcome is very promising and suggests that our virtual stent-graft deployment simulation method has the potential to not only predict changes in biomechanical conditions induced by TEVAR, but also improve planning of TEVAR procedure in the future.

5.4 Summary

Biomechanical interactions between stent-graft and native aorta play a vital role in determining the immediate result of stent-graft deployment. These interactions cannot be directly evaluated from anatomic dimensions. The virtual stent-graft deployment model has provided new insights into the stent-graft behaviour within dissected aorta and successfully reproduced the immediate outcome of TEVAR as observed in vivo; the model indicated that TEVAR-induced changes in local biomechanical conditions were responsible for stent-graft migration during the launching phase. A modified deployment position was simulated showing a lower risk of migration with improvement in the local biomechanical environment. The potential value of virtual stent-graft deployment simulation has been well illustrated by this case study demonstrating that slight differences in stent-graft landing position can determine the outcome of a given procedure.

Chapter 6

Application II: evaluating the risk for post-TEVAR distal stent-graft induced new entry (SINE) in type B aortic dissection

6.1 Introduction

TEVAR has become a standard treatment for type B aortic dissection (Nienaber et al., 2016). Despite the great success attained by TEVAR, there are still severe complications related to this procedure, one of which is SINE (Dong et al., 2010). SINE is defined as a new tear on the aortic wall caused by SG itself. Recent clinical studies have identified that distal oversizing ratio, length of SG and stent morphology are important factors influencing the formation of distal SINE (Ma et al., 2017). All these factors are associated with biomechanical changes in the aortic wall after TEVAR which are highly dependent on SG choice and mechanical interactions between the SG and aorta. SG configuration and SG/aorta mechanical interaction are crucial to the post-TEVAR biomechanical behaviour and consequential clinical results. However, current pre-surgical planning and SG selection are based more on anatomical geometries and clinical guidelines, but less on quantitative biomechanical analysis and risk assessment (Pape et al., 2015). Neither biomechanical forces, such as SG induced spring-back force and radial force, nor the SG final configuration are available to clinicians when making pre-surgical decisions.

To the best of the author's knowledge, only two FEM-based simulations of SG deployment in type B aortic dissection have been reported so far (Ma et al., 2018, Meng et al., 2020). These studies focused on stress concentrations at the proximal end and their correlation with RTAD, but they did not consider the effect of pre-stress in the aortic wall nor blood pressure. Beside the FEM-based virtual deployment of SG simulations, a simplified FEM model showed a potential link between stress concentration in the distal landing zone and distal SINE (Menichini et al., 2018). By employing a simplex deformable mesh method, Chen et al. identified a correlation between large stent-induced displacement and distal SINE (Chen et al., 2018).

In this chapter, patient-specific virtual SG deployment model was adopted to reproduce the TEVAR procedure by following the exact clinical practice in four type B aortic dissection patients. The simulation model incorporated the effect of pre-stress in the aortic wall and change of intraluminal blood pressure after TEVAR. Simulation results were analysed to provide some insight into the stent-graft-induced biomechanical changes in an attempt to search for potential causes for distal-SINE.

6.2 Methodology

6.2.1 Patient information

Four complicated type B aortic dissection patients who underwent TEVAR procedure in sub-acute phase at the Zhongshan Hospital, Shanghai, China, were enrolled in this study. The patients gave informed consent, and this study was approved by the local ethics committee. CTA scans of the four patients were acquired before TEVAR and after TEVAR. CTA scans were performed with Aquilion ONE (Toshiba Medical Systems, Otawara, Japan) scanner (1.0 mm slice thickness and 0.68 mm × 0.68 mm pixel size).

The clinical information of the patients is summarised in Table 6.1. All four patients underwent successful TEVAR procedures and were treated with Medtronic Valiant SG (Medtronic Vascular, Santa Rosa, California). Patient 1 and patient 2 remained stable after their TEVAR procedures, without any post-TEVAR complications found at follow-ups. In the 3-month post-TEVAR routine follow-up, formation of a distal SINE was observed in patient

3 near the distal end of the SG, which led to aneurysmal enlargement allowing the SG to push into the original false lumen (Figure 6.1). Patient 4 remained stable at the 3-month follow-up, along with true lumen remodelling and false lumen thrombosis. However, a SINE was found near the distal end of SG at the 14-month follow-up (Figure 6.1).

Table 6.1 Characteristics of patients enrolled in the study

	Patient 1	Patient 2	Patient 3	Patient 4
Age (years)	44	62	50	59
Gender	Female	Male	Male	Male
Dissection stage at TEVAR	Sub-acute	Sub-acute	Sub-acute	Sub-acute
SG product	Medtronic Valiant	Medtronic Valiant	Medtronic Valiant	Medtronic Valiant
SG size (mm)	28-28-150	38-38-200	32-32-200	32-32-200
Post-TEVAR complications	None	None	Distal SINE	Distal SINE

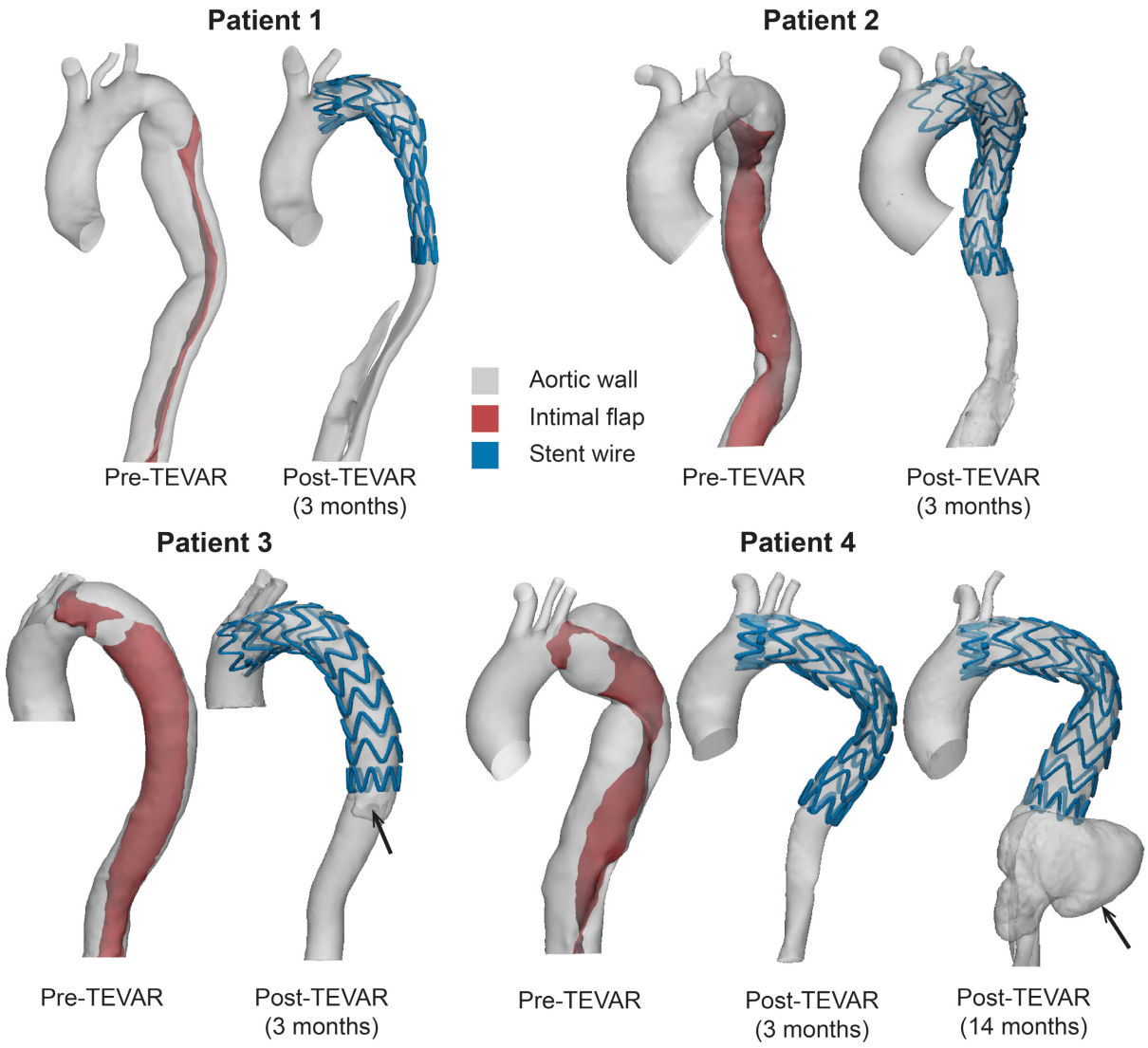


Figure 6.1 Pre- and post-TEVAR geometries of the four patients. The distal-SINEs found in the follow-ups of patient 3 and patient 4 are indicated by an arrow.

6.2.2 Model geometry and material properties

All the pre- and post-TEVAR patient-specific geometries were reconstructed from the corresponding CTA scans in Mimics 22.0 (Materialise, Leuven) software by using special segmentation workflow based on a semi-automated threshold-based algorithm. Pre-TEVAR CTA scans were segmented by the purpose-built approach described in Chapter 3 (Section 3.5.1) which allows the intimal flap to be treated as a different material from the aortic wall (Figure 6.1).

The aortic wall was assumed as an isotropic hyperelastic material by using the Yeoh model and the material parameters described in Chapter 4, with c_{10} = 17.5 KPa, c_{20} = 58.9 KPa, c_{30} = 116.1 KPa. The intimal flap was approximated as a linear elastic material with Young's modulus E_{flap} = 277 kPa. The aortic wall and intimal flap were assumed as nearly incompressible by defining the Poisson's ratio as 0.49.

By using the parametric model of Valiant SG described in Chapter 3, all the design features and dimensions of the real SG products used in the TEVAR procedure for each patient were faithfully reproduced (Figure 6.2). Then the stent and graft were tied together and meshed by following the protocol presented in Chapter 4 (Section 4.1.2). A virtual sheath comprised of a tubular surface was created and meshed into surface elements (SMF3D4R). The Valiant SG consists of a Nitinol alloy stent scaffold and PET fabric graft. Parameters describing the surperelastic behaviour of Nitinol and the mechanical behaviour of PET graft were kept consistent with those summarised in Chapter 4 (Section 4.1.2).

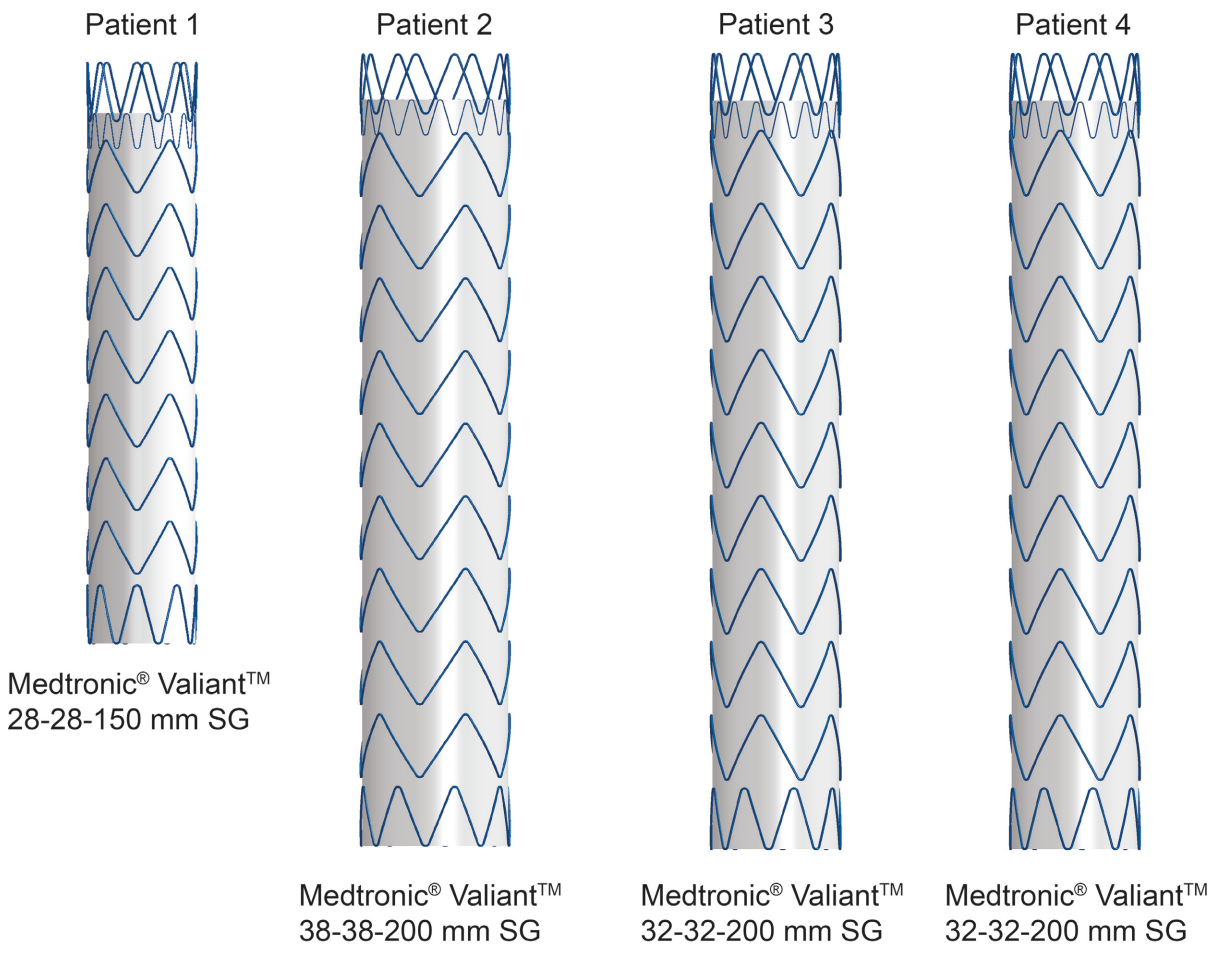


Figure 6.2 Geometry of stent-graft (SG) used in TEVAR procedure for the four patients.

6.2.3 Anatomical measurements

In order to assess morphological changes of the aorta induced by TEVAR intervention, key geometric parameters were measured in Mimics based on pre- and first post-TEVAR (3-month follow-up) CTA scans. These included true lumen and false lumen volumes, tortuosity of SG covered aorta segment, tapered ratio of SG covered aorta segment, distal oversizing ratio, and tortuosity of distal landing zone. Volumes of the true lumen and false lumen were calculated by using the following equations:

$$Vol_{TL/FL} = \sum_{i=1}^{N} \frac{(S_i + S_{i+1}) \cdot h}{2} \tag{6.1}$$

where S_i is the corresponding cross-sectional area of the true lumen or false lumen at the ith transvers slice, h is slice thickness and N is the total number of transverse slices. Volumes of the true lumen and false lumen were measured from the root of the left subclavian artery to the celiac artery.

Two anatomical parameters of the SG covered segment of aorta were calculated. The tortuosity of SG covered aorta segment was calculated as L_c/L_0, where L_c is the length of the centreline in the SG covered aorta segment, and L_0 is the linear distance between the proximal and distal ends of the centreline (Figure 6.3). The tapered ratio of SG covered aorta segment was defined as

$$Tapered\ ratio = \left(1 - \frac{D_p}{D_d}\right) \times 100\% \tag{6.2}$$

where D_p is the local diameter at the proximal border of SG covered aorta segment, and D_d is the local diameter at the distal border of SG covered aorta segment (Figure 6.3).

Another two anatomical parameters describing morphological features at the distal end were also calculated. Distal oversizing ratio was defined as

$$Distal\ oversizing\ ratio = \left(\frac{D_s}{D_d} - 1\right) \times 100\% \tag{6.3}$$

where D_s is the diameter of SG at stress free state, and D_d is the local diameter at the distal border of the SG covered aorta segment. The distal landing zone was defined as the aorta region starting from 15 mm proximal to the distal landing border to 15 mm distal to the border. Tortuosity of the distal landing zone was calculated as L_d/L_{d0}, where L_d is the length of the local centreline in the distal landing zone (which is 30 mm), and L_{d0} is the linear distance between the two ends of the centreline in the distal landing zone (Figure 6.3).

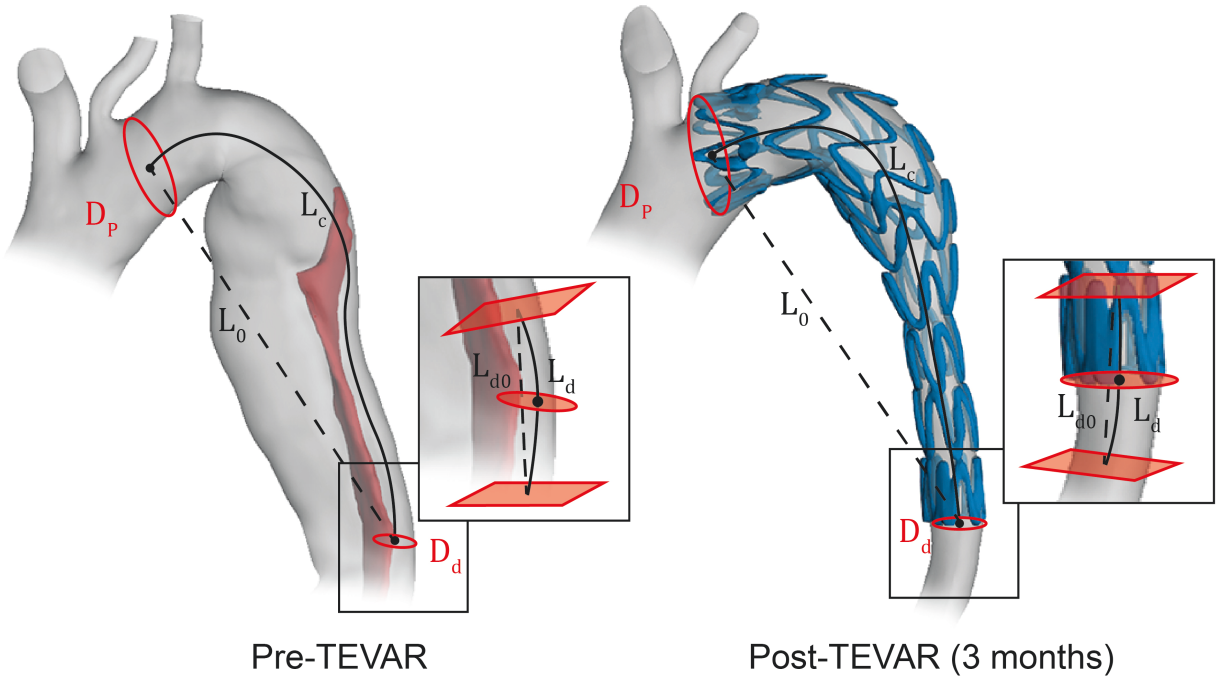


Figure 6.3 Illustration of the parameters measured to describe anatomical features. Distal landing zone (shown in insets) is defined as the region between the two cutting planes (red square) at 15 mm proximal to the distal landing border and 15 mm distal to the border (red circle).

6.2.4 Computational model

The four virtual SG deployment simulations performed in this chapter followed the framework described in Chapter 3 by adopting a nodal specific displacement boundary condition of the virtual sheath to crimp, deliver and deploy the SG to its targeted location. The simulation model also incorporated pre-stress in the aortic wall before TEVAR and change in internal blood pressure after TEVAR. Other simulation assumptions and boundary conditions were also kept consistent with the virtual SG deployment model C described in Chapter 4.

The motion of the aortic root and ascending aorta was neglected in this study. Therefore, the nodes at all model ends in the proximal ascending aorta, supra-aortic branches and distal descending aorta were fixed with zero displacement. Rayleigh damping was applied to the aorta to account for the viscoelastic tissue support on the outer arterial wall. As the descending aorta is tethered to the spine by paired intercostal arteries, this attachment was

modelled by defining four pairs of fixed spots along the descending aorta, effectively preventing any excessive rigid body movement. The contacts between objects were modelled by using the general contact formulation with penalty method in Abaqus Explicit. The ratio of kinetic energy and internal strain energy (ALLKE/ALLIE) was monitored and kept under 10% to ensure the simulation was run as a quasi-static analysis.

During clinical follow-ups, distal SINEs were observed in patients 3 and 4 but not in patients 1 and 2. To analyse the difference between the SINE and non-SINE patients, distributions of four biomechanical parameters, namely von Mises stress, maximum principal stress, maximum shear stress and the displacement magnitude, on the intimal flap were evaluated and compared. The same definition of the distal landing zone as illustrated in Figure 6.3 was also applied to the intimal flap.

6.3 Results

6.3.1 Anatomical features

All the anatomical measurements of the four patients are summarised in Table 6.2. Comparing the true lumen and false lumen volumes before and after TEVAR, it is clear that true lumen remodelling and false lumen thrombosis occurred in all 4 patients. The extent of true lumen remodelling varied substantially among patients, with a 154% increase in true lumen volume in patient 3 compared to a 21% increase in patient 2. Significant false lumen thrombosis was achieved in all patients where reduction in false lumen volume varied between 79% and 100%. Patients 1, 3 and 4 had similar pre-TEVAR tapered ratios within a narrow range of 47% to 50%, while patient 2 showed a lower tapered ratio at 40%. Patient 2 also showed an increase in tapered ratio after TEVAR, while all other patients had a reduction with patient 3 displaying the most significant reduction in tapered ratio, Likewise, after TEVAR the distal oversizing ratio was increased in patient 2 but reduced by varying amount in the other three patients. Tortuosity of the SG covered segment did not change after TEVAR, except for patient 2 where a 10% reduction was found. Tortuosity of the distal landing zone was similar for all patients with little change after TEVAR.

Table 6.2 Anatomical measurements taken in the four patients pre-TEVAR and at 3-month post-TEVAR.

Patient 1	Pre-TEVAR	Post-TEVAR	% Change
True Lumen Volume (mm^3)	35399	51788	46%
False Lumen Volume (mm^3)	94878	15743	-83%
Tapered Ratio	47%	40%	-14%
Tortuosity of Stent-graft Covered Segment	1.30	1.28	-1%
Distal Oversizing Ratio	116%	76%	-35%
Tortuosity of the Distal Landing Zone	1.007	1.007	0.07%
Patient 2	Pre-TEVAR	Post-TEVAR	% Change
True Lumen Volume (mm^3)	99487	120319	21%
False Lumen Volume (mm^3)	95699	19690	-79%
Tapered Ratio	40%	48%	18%
Tortuosity of Stent-graft Covered Segment	1.43	1.28	-10%
Distal Oversizing Ratio	118%	136%	15%
Tortuosity of the Distal Landing Zone	1.009	1.007	-0.19%
Patient 3	Pre-TEVAR	Post-TEVAR	% Change
True Lumen Volume (mm^3)	56532	143605	154%
False Lumen Volume (mm^3)	137745	2233	-98%
Tapered Ratio	50%	2%	-95%
Tortuosity of Stent-graft Covered Segment	1.37	1.37	0%
Distal Oversizing Ratio	107%	8%	-92%
Tortuosity of the Distal Landing Zone	1.004	1.006	0.21%
Patient 4	Pre-TEVAR	Post-TEVAR	% Change
True Lumen Volume (mm^3)	50229	76716	53%
False Lumen Volume (mm^3)	240830	0	-100%
Tapered Ratio	48%	41%	-16%
Tortuosity of Stent-graft Covered Segment	1.49	1.50	-0.6%
Distal Oversizing Ratio	102%	78%	-24%
Tortuosity of the Distal Landing Zone	1.017	1.011	-1%

6.3.2 Biomechanical analysis

The SGs used in the TEVAR procedure were successfully deployed into the true lumen in all patients. After completing the virtual deployment simulations, distributions of von Mises stress, maximum principal stress, maximum shear stress and displacement of the intimal flap resulting from SG deployment were analysed and compared.

Figure 6.4 shows the predicted von Mises stress distributions on the intimal flap for the four patients. High von Mises stresses (>150 kPa) were observed near the primary entry tear in all patients. For patient 3 and patient 4, regions of high von Mises stress were also found in the distal landing zone of the intimal flap (Figure 6.4.b), where distal SINEs were observed on post-TEVAR follow-up scans (Figure 6.4.a). In order to make a quantitative comparison, the mean and maximum values of von Mises stress in the distal landing zone of the intimal flap were evaluated. As shown in Figure 6.4.c, it is obvious that patient 3 and patient 4 had much higher maximum von Mises stresses than patient 1 and patient 2. Moreover, patients 3 and 4 also had higher mean values of von Mises stress in the distal landing zone compared to patients 1 and 2 (Table 6.3).

Table 6.3 Stress and displacement in the distal landing zone of intimal flap in the four patients

		Patient 1	Patient 2	Patient 3	Patient 4
von Mises stress (kPa)	max.	122.36	142.98	196.29	198.62
	mean	49.02	33.15	80.07	70.87
Maximum principal stress (kPa)	Max.	329.74	297.88	409.46	489.56
	Mean	45.34	26.16	72.91	76.26
Maximum shear stress (kPa)	Max.	141.09	164.25	225.86	228.69
	Mean	55.40	37.42	90.42	81.03
Displacement magnitude (mm)	Max.	3.88	4.32	6.19	4.14
	Mean	2.05	2.60	2.64	2.61

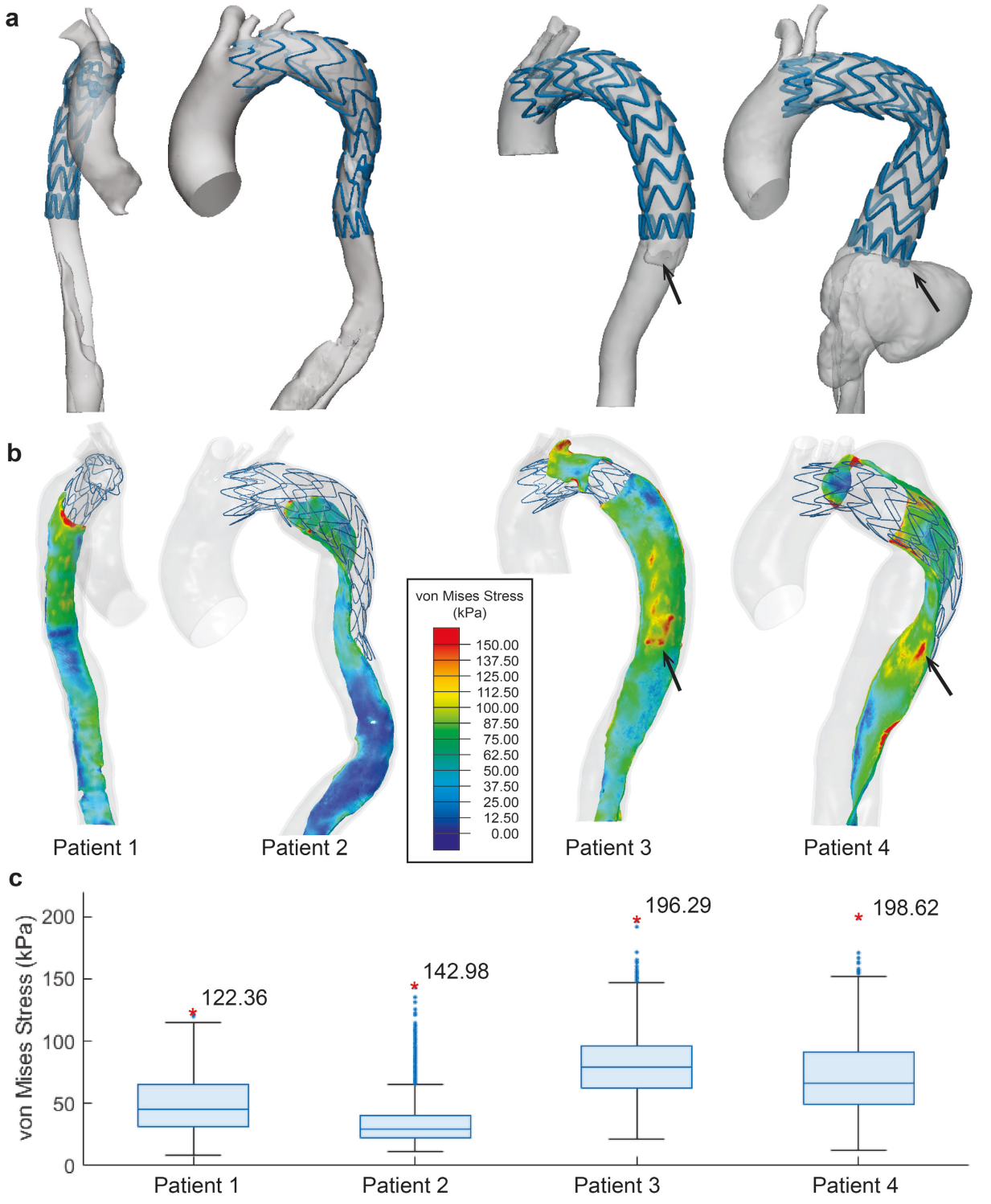


Figure 6.4 Reconstructed post-TEVAR aortas for the four patients included in this study and predicted von Mises stress (VMS) on the intimal flap. a. Reconstruction based on follow-up CT scans, b. Von Mises stress maps on the intimal flap and c. Mean and maximum values of von Mises stress in the distal landing zone of intimal flap.

Distributions of maximum principal stress on the intimal flap for the four patients are presented in Figure 6.5. Similar to the trend observed in the distribution of von Mises stress, there were high maximum principal stresses in the distal landing zone of intimal flap in patient 3 and patient 4, while high maximum principal stress was only observed near the primary entry tear in patient 1 and patient 2 (Figure 6.5.a). Within the distal landing zone of the intimal flap, peak and mean values of the maximum principal stress were much higher for patients 3 and 4 compared to patients 1 and 2 (Figure 6.5.b and Table 6.3).

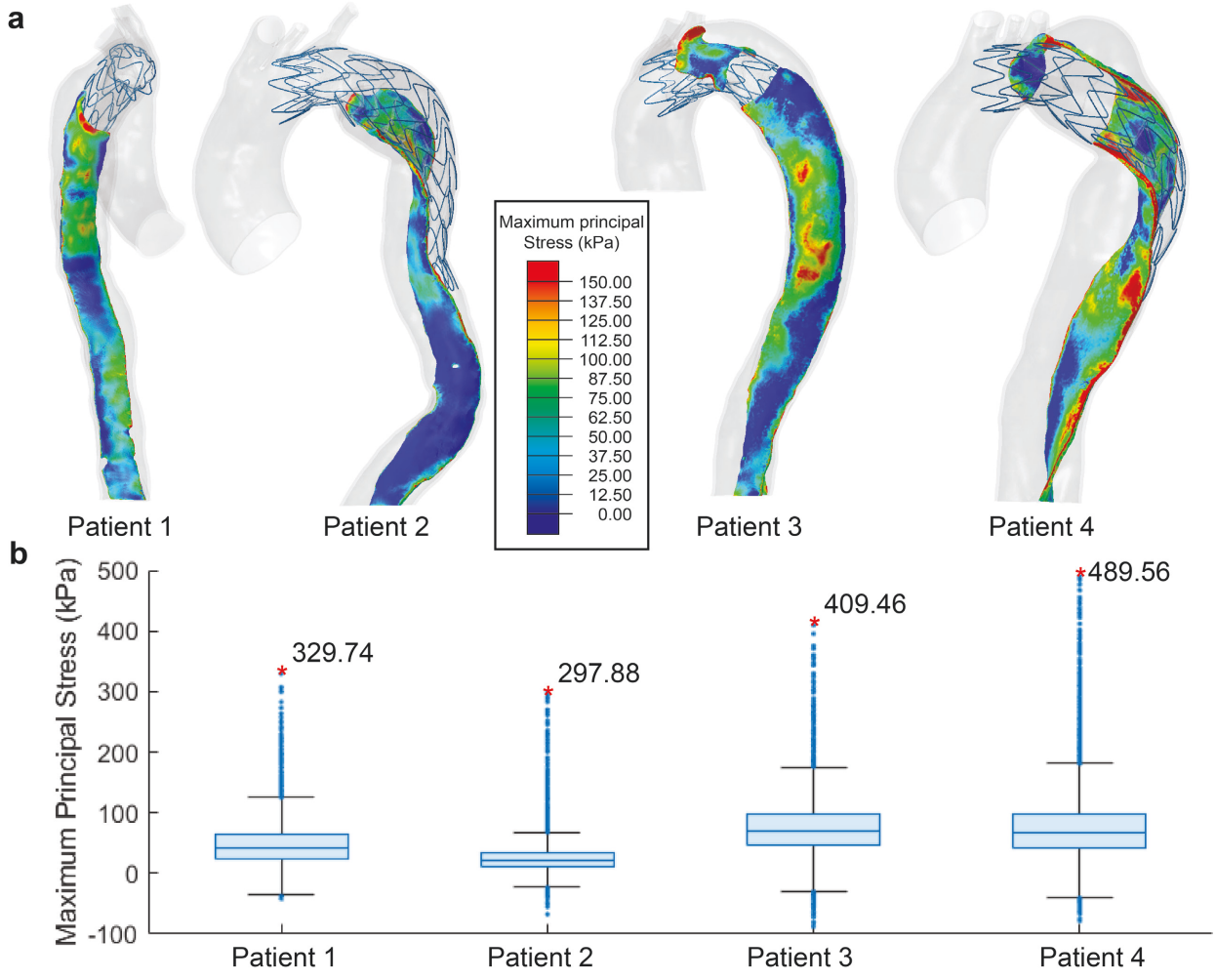


Figure 6.5 Maximum principal stress (MPS) on the intimal flap for the four patients included in this study. a. Maximum principal stress maps on the intimal flap and b. Mean and peak values of the maximum principal stress in the distal landing zone of intimal flap.

Figure 6.6 shows distributions of maximum shear stress on the intimal flap. Similarly, high shear stress can be found near the primary entry tear in all four patients (Figure 6.6.a). In patient 3 and patient 4, higher shear stress was also found in the distal landing zone with peak values exceeding 225 kPa, whereas patient 1 and patient 2 did not have high shear stress in the distal landing zone (Figure 6.6.b). Similarly, patients 3 and 4 also showed higher mean values of the maximum shear stress within the distal landing zone than patients 1 and 2 (Table 6.3).

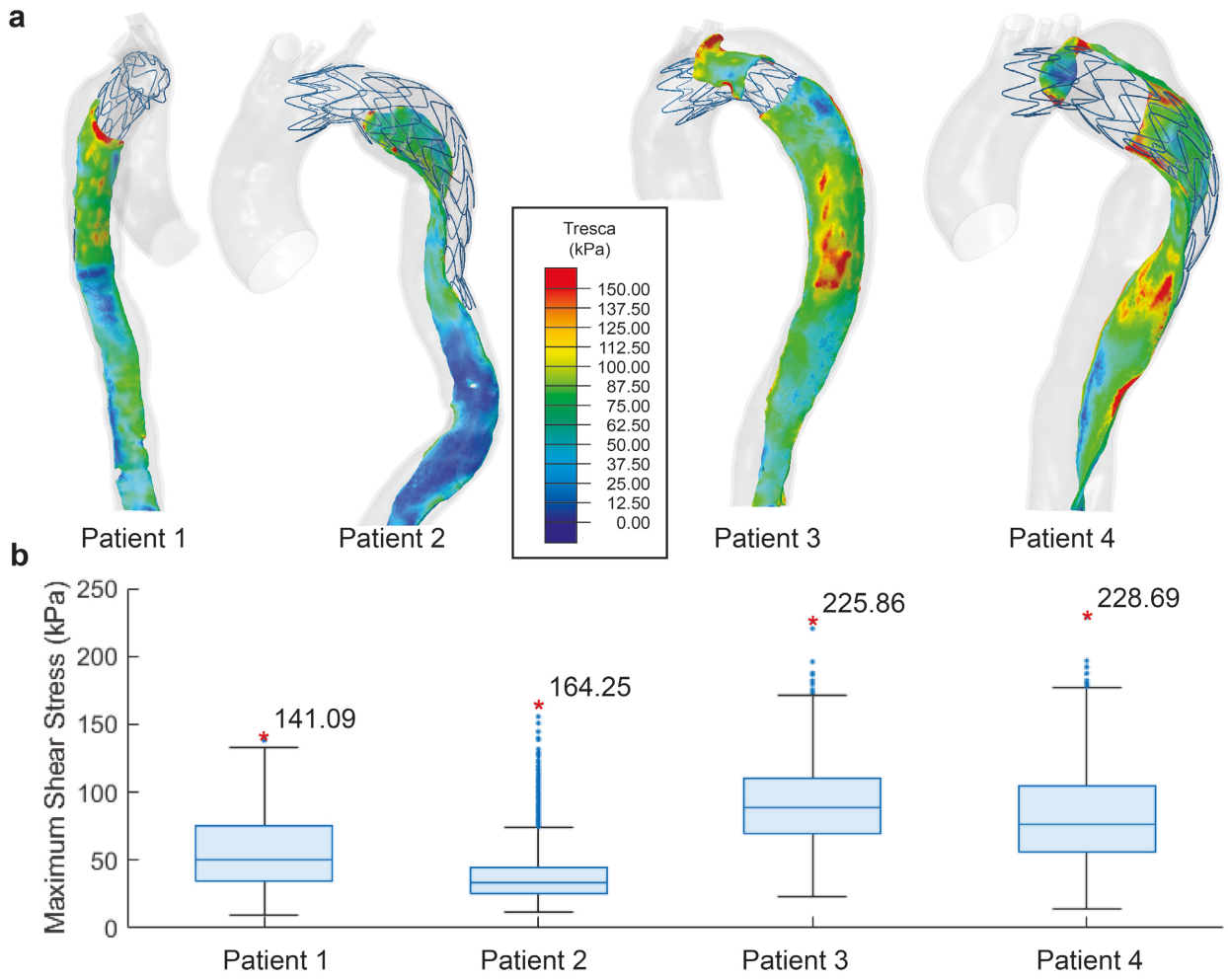


Figure 6.6 Maximum shear stress (MSS) on the intimal flap for the four patients included in this study. a. Maximum shear stress maps on the intimal flap and b. Mean and peak values of the maximum shear stress in the distal landing zone of intimal flap.

Contours of displacement magnitude of the intimal flap are shown in Figure 6.7. After SG deployment, large displacements were found near the primary entry tear, especially in patients 2 and 4 where larger areas of the proximal intimal flap experienced displacements greater than 7.5 mm (Figure 6.7.a). In the distal landing zone of the intimal flap, patient 3 showed the largest displacement among the four patients with a maximum displacement of 6.19 mm (Figure 6.7.b). The mean displacements of the intimal flap in the distal landing zone were similar for the four patients, with values within the range of 2.05 - 2.64 mm (Table 6.3).

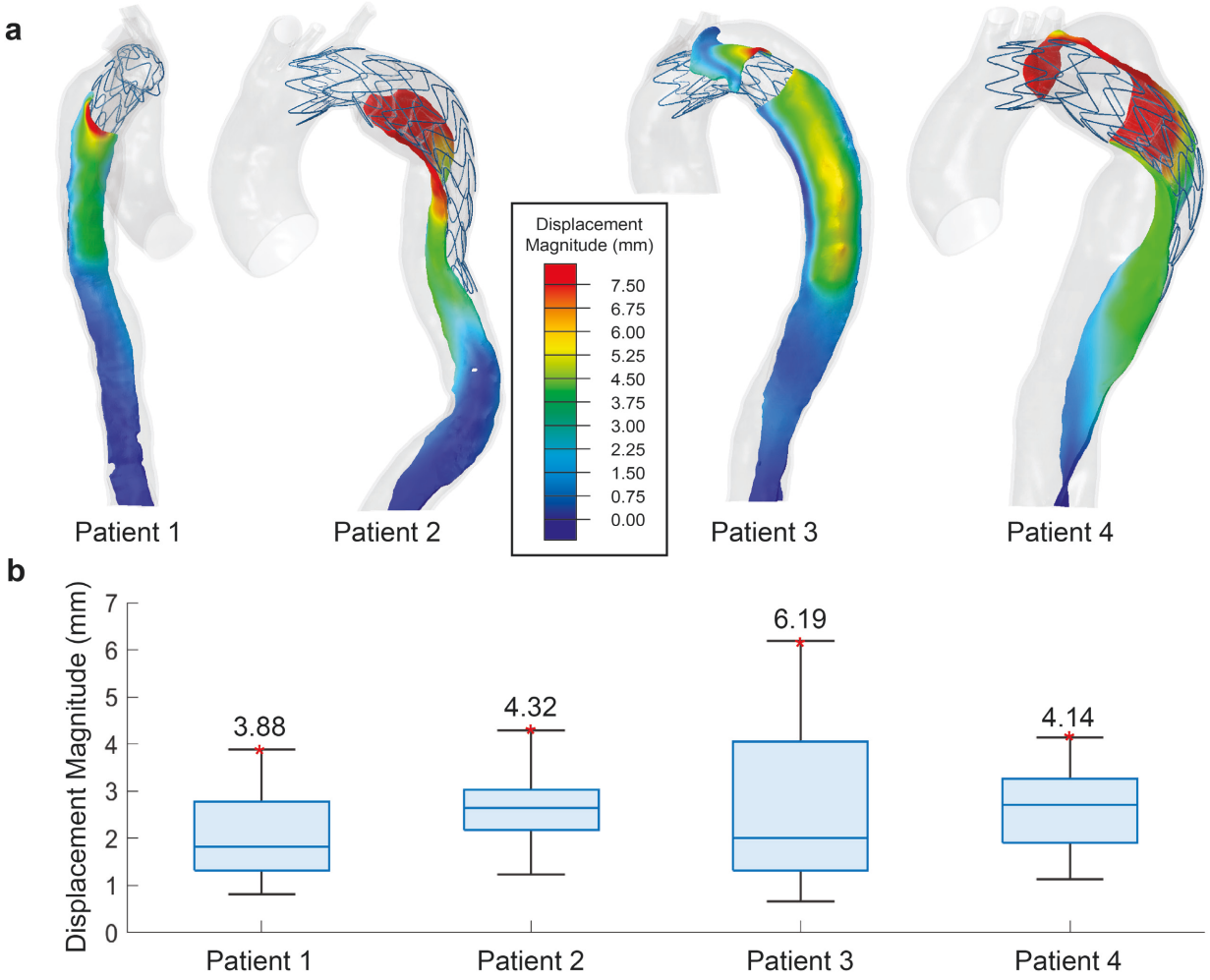


Figure 6.7 Displacement of the intimal flap. a. Maps of the displacement magnitude of the intimal flap after stent-graft deployment and b. Mean and maximum values of the displacement magnitude in the distal landing zone of the intimal flap.

6.4 Discussion

As one of the post-TEVAR complications, SINE is non-frequent (incidence of 3.8 – 6.1%) but fatal (Ma et al., 2017, Li et al., 2019, Czerny et al., 2020). Since it was first reported in 2010, SINE has been studied by clinicians and multi-disciplinary research groups in the past decade (Dong et al., 2009, Ma et al., 2017, Chen et al., 2018, Menichini et al., 2018, Canaud et al., 2019). With wider acceptance of TEVAR as a default treatment of type B aortic dissection (Canaud et al., 2014), more data on SINE are now available.

Clinical studies have been carried out and aimed to identify potential risk factors based on anatomical measurements taken from SINE and non-SINE patients. Anatomical features, including distal oversizing ratio, tapered ratio of SG covered segment and tortuosity, have been highlighted as potential factors influencing the occurrence of distal SINE (Canaud et al., 2019). Although these factors showed statistical differences between patients with and without distal SINE, their threshold values vary among the clinical studies (Jang et al., 2017, Canaud et al., 2019). Moreover, there is no clear guideline for estimating the risk level of distal SINE for individual patients.

Considering the anatomical measurement results presented in this chapter, patient 1 (non-SINE) showed tapered ratio of 47% and high distal oversizing ratio of 116% which are close to the threshold values (48% for tapered ratio and 109% for distal oversizing ratio) reported in a previous study (Jang et al., 2017). Interestingly, patient 2 (non-SINE), who had the highest distal oversizing ratio at 118% along with a high tortuosity of the SG covered segment, should have been considered to have a high risk for developing distal SINE but remained stable at follow-ups. Patient 3 (SINE) was found to have significant reduction in tapered ratio and distal oversizing ratio before and after TEVAR, resulting from the already formed distal SINE at the first post-TEVAR follow-up. In this case, the distal end of SG caused a new tear on the intimal flap and pushed into the original false lumen side as observed on the CT scan at 3-month follow-up. There were no warning signs based on the pre-TEVAR measurements that patient 3 might potentially develop distal SINE shortly after TEVAR. Patient 4 (SINE) who had the highest tortuosity of the SG covered segment among the four patients, remained stable at 3-month follow-up and was found to have developed distal SINE

at 14-month follow-up. This potential link between high tortuosity of the SG covered segment supports the findings reported in previous studies (Menichini et al., 2018, Tan et al., 2021). However, when comparing tortuosity of the SG covered segment between patient 4 and patient 2, patient 4 only showed 4% higher tortuosity than patient 2. By only focusing on the pre-TEVAR anatomical measurements which is currently employed in making pre-surgical planning, there is no significant difference between the SINE and non-SINE patients in most measured features other than the distal oversizing ratio. However, the two non-SINE patients had even higher distal oversizing ratio (117% on average) than the two SINE patients (104.5% on average), which challenges the use of high distal oversizing ratio as a measure to assess the risk of a patient for post-TEVAR SINE (Canaud et al., 2019). Taking all these into consideration, a reliable assessment of the risk level for distal SINE cannot be made based on patient-specific pre-TEVAR anatomical measurement alone.

Along with the aforementioned anatomical features, short SG length and Marfan syndrome have also been identified in previous studies as risk factors for SINE (Ma et al., 2017). Marfan syndrome can cause microstructure defect of the aortic wall and reduce the ultimate tensile strength of the aortic tissue (Sulejmani et al., 2017). Short SG can lead to high 'spring-back' force (like a spring, SG has an inherent tendency to retain its initial straight configuration when deployed into a tortuous aorta) and induce high stress in the aortic wall which might cause fracture of the wall or intimal flap, eventually causing SINE (Dong et al., 2009, Ma et al., 2017). All these risk factors are associated with biomechanical changes in the aortic wall induced by TEVAR which are highly dependent on SG choice and mechanical interactions between the SG and aorta.

Patient-specific virtual SG deployment can offer insights into the biomechanical changes introduced by TEVAR and identify potential link between biomechanical factors and distal SINE. Higher peak and mean values of all stress measures, including von Mises stress, maximum principal stress and maximum shear stress, were found in the distal landing zone of intimal flap in the two SINE patients, while the two non-SINE patients had much lower stress levels in the distal landing zone (Table 6.3). Similar to the findings reported by Ma et al. on retrograde type A aortic dissection (RTAD), high von Mises stress co-located with the region where the new entry tear was found, although this occurred in the distal landing zone

in the present study rather than in the proximal landing zone in (Ma et al., 2018). Unlike the finding from the study by Chen et al., the two SINE patients did not show high TEVAR induced intimal flap displacement at the distal landing zone (Figure 6.7) (Chen et al., 2018).

Von Mises stress (VMS) is a measure often used in structural failure analysis. Simulation results for the four patients showed considerably higher VMS in the distal landing zone of the two SINE patients compared to the two non-SINE patients. The averaged value of peak VMS in the two SINE patients was 48.8% higher than that of the two non-SINE patients. Similar trend was also found in the maximum principal stress (MPS) and maximum shear stress (MSS), with the two SINE patients showing 43.2% (MPS) and 48.9% (MSS) higher averaged peak values than the two non-SINE patients. MPS and MSS measure the highest principal stress and highest shear stress based on the principal stresses respectively, and have been used to evaluate the failure of aortic tissues (Sommer et al., 2016, Canchi et al., 2018).

The results presented in this chapter highlight the limitation of relying on anatomical measurements alone to assess the risk of SINE, and the need for detailed stress analysis. The virtual SG deployment simulation model developed in this thesis is capable of predicting post-TEVAR stress distribution based on pre-TEVAR CT scan, allowing any high stress hot spots to be identified before intervention. Although there were significant differences in all stress measures (VMS, MPS and MSS) between the two SINE and two non-SINE patients, it is too early to draw a firm conclusion regarding the predictive power of these parameters. On the other hand, more experimental studies are needed to determine the mechanical properties of dissection intimal flap and its failure strength. This poses a significant challenge as TEVAR is becoming widely adopted in treating type B aortic dissections, hence less patients are treated by open surgery making it harder to obtain relevant tissue samples. The initiation of SINE and intimal flap material failure mechanism are still unclear, which will require more fundamental studies of intimal flap and aortic wall from type B aortic dissection patients in the future.

6.5 Summary

In this chapter, data obtained from two distal SINE patients and two non-SINE patients were used for detailed analysis of anatomical features and structural mechanics by performing virtual SG deployment. Based on the anatomical measurements, there was no clear difference between the two SINE patients and the two non-SINE patients. The virtual SG deployment simulations revealed substantial differences in all stress measures, especially in the distal landing zone where the peak von Mises stress was 48.8% higher in the SINE patients than the two non-SINE patients. Similar trend was also shown in the maximum principal stress and maximum shear stress, with their respectively peak values being 43.2% and 48.9% higher in the two SINE patients. No apparent difference in TEVAR-induced flap displacement was noted between the SINE and non-SINE patients. The finding of higher wall stress in the distal landing zone of the SINE patients is promising and the potential link between high structural stress and SINE is worth further investigation in the future.

Chapter 7

Application III: simulation of stent-graft deployment for pre-surgical planning in aortic dissection†

7.1 Introduction

It has been demonstrated in previous chapters that patient-specific simulations of SG deployment in aortic dissections can potentially predict the outcome of TEVAR. There is also evidence suggesting that post-TEVAR complications (e.g. SINE and RTAD) may be associated with the choice of SG product and size, as well as proximal and distal landing positions. In the current practice, clinicians choose the SG product and length based on anatomical measurements and guidelines provided by the manufacturer. There is no reliable methods to determine the optimal SG design or size to achieve the best outcome for a given patient. In this chapter, by using the virtual SG deployment model, the impact of SG design and length on post-TEVAR biomechanical conditions will be evaluated in a patient-specific type B aortic dissection. This chapter aims to demonstrate the capability and potential of the virtual SG deployment model as a pre-surgical planning tool by providing both the configuration after SG deployment and the biomechanical changes introduced by SGs.

---

† The author of this dissertation carried out all the work described in this chapter unless specified otherwise. The content of this chapter was partially adapted from Kan, X., Ma, T., Dong, Z. and Xu, X.Y., 2021. Patient-Specific Virtual Stent-Graft Deployment for Type B Aortic Dissection: A Pilot Study of the Impact of Stent-Graft Length. *Frontiers in Physiology*, 12.

7.2 Methodology

7.2.1 Clinical background

A 66-year-old male patient was admitted to Zhongshan Hospital, Fudan University, Shanghai with persistent back pain. The patient underwent CTA scan using Aquilion ONE (Toshiba Medical Systems, Otawara, Japan; 1.0 mm slice thickness and 0.72 mm × 0.72 mm pixel size) and was diagnosed with type B aortic dissection (Figure 7.1.a). Three days later, the patient underwent TEVAR intervention, during which a tapered self-expandable 42-38-158 mm Zenith TX2 PT SG (Cook Medical, Bloomington, Ind) was deployed into the true lumen and sealed the primary entry tear. Follow-up CTA scans were performed at 3-month and 12-month post-TEVAR. A distal SINE was found at the 3-month follow-up. The new tear occurred on the intimal flap at the distal end of SG which partially pushed into the FL side (Figure 7.1.b). On the 12-month follow-up CTA scan, the SG was found to have perforated the aortic intima and caused a minor tear at the proximal end (Figure 7.1.c). All medical data included in this study complied with the Declaration of Helsinki and were approved by the local Ethics Committee. The patient provided written informed consent for participation.

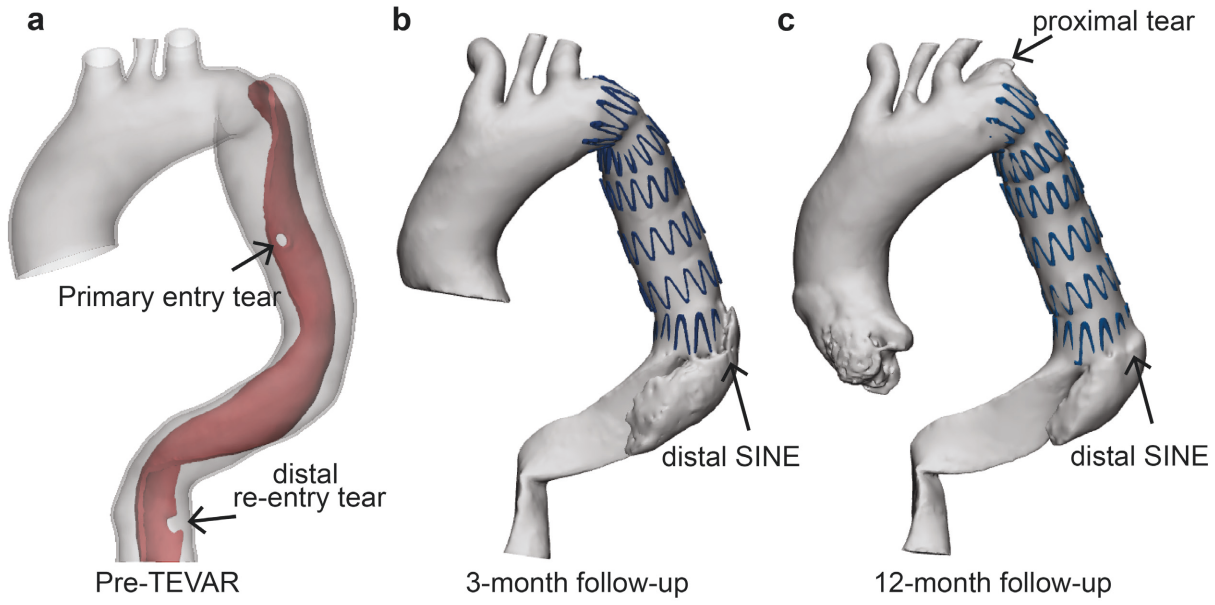


Figure 7.1 Patient information. a. The patient was diagnosed with type B aortic dissection with one primary entry tear and a distal re-entry tear (marked by the black arrow), b. the distal stent-induced new entry (SINE) was found at the 3-month follow-up, and c. a newly formed proximal tear was found at the proximal landing zone at the 12-month follow-up.

7.2.2 Aortic dissection modelling

All CTA scans were processed using Mimics 23.0 (Materialise, Leuven). Since the false lumen was partially thrombosed with very limited blood perfusion, the 'gap' between true and false lumen, which was used to determine the intimal flap thickness in Chapters 4 and 5, was not clear enough for segmentation on the pre-TEVAR CTA scan. As descripted in Chapter 3 (Section 3.5.1), a modified segmentation approach was employed in this simulation model to create the intimal flap geometry with a uniform thickness by following the segmentation approach presented by Bäumler et al (Baumler et al., 2020). The pre-TEVAR CTA scan was segmented and reconstructed into two separate surface models: a surface model of the true lumen and a combined surface model representing the 'outer surface of aortic wall' by enclosing true lumen, false lumen and the intimal flap (Figure 7.2.a). The solid domain of aortic dissection was created by Boolean operation in Meshmixer (Autodesk, Inc.).

The first step was to extrude the true lumen surface outwardly by a uniform thickness equivalent to the thickness of intimal flap (h_{flap}), resulting in the true lumen structure. This

was followed by extruding the combined surface outwardly by a uniformed thickness of h_{wall}, resulting in the outer wall structure (Figure 7.2.b). Boolean operation was then performed by subtracting the outer wall structure from the true lumen structure to obtain the intimal flap structure (Figure 7.2.c). The lumen enveloped by the outer wall was separated into true lumen and false lumen by the intimal flap (Figure 7.2.d). To reduce the influence of local wall thickness while focusing on analysing the impact of SG length on local aortic wall stress, both wall thickness parameters h_{flap} and h_{wall} were assumed to be constant at 1.45 mm, which corresponds to the average descending aortic wall thickness in the same gender and age group as that of the patient (Mensel et al., 2014). Following the same approach described in Chapter 3 (Section 3.5.1), the outer wall and intimal flap were further smoothed and trimmed by placing a transverse plane in the proximal ascending aorta, and cutting planes perpendicular to the local centreline in the distal segments of the supra-aortic branches and in the abdominal aorta above the aortic bifurcation (Figure 7.2.e). The outer wall and intimal flap were meshed with tetrahedral elements (C3D4 in Abaqus (Dassault Systèmes, France)) and combined to form the aortic dissection model.

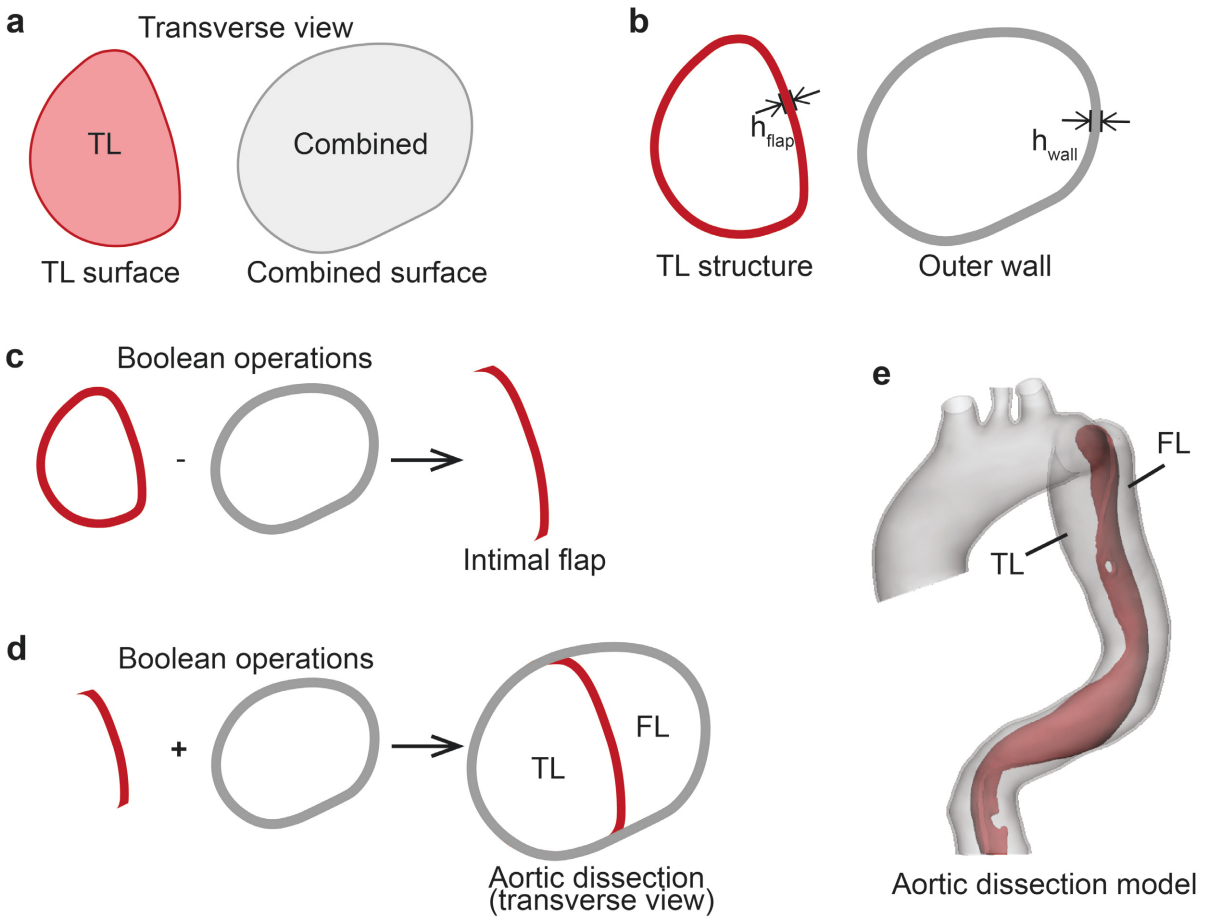


Figure 7.2 Illustration of the steps in segmentation and reconstruction of the aortic dissection geometry from pre-TEVAR CTA scan. a. Transverse view of two segmentations, the true lumen (TL) surface represents the original blood flow channel, and the combined surface encloses true lumen, false lumen and intimal flap, b. the TL structure and outer wall structure were created by extruding the surfaces outwardly by 1.45 mm, c. the intimal flap was created by performing Boolean subtraction of outer wall from TL structure, d. the TL structure and outer wall were combined. e. the intimal flap and outer wall geometry were smoothed and trimmed to form the aortic dissection geometry.

The outer wall was modelled as an isotropic, homogenous and hyperelastic material described by the second order reduced polynomial strain energy function:

$$W = c_{10}(\bar{I}_1 - 3) + c_{20}(\bar{I}_1 - 3)^2 \tag{7.1}$$

where c_{10} and c_{20} are material parameters, $\bar{I}_1$ is the first deviatoric invariant defined as

$$\bar{I}_1 = \bar{\lambda}_1^2 + \bar{\lambda}_2^2 + \bar{\lambda}_3^2 \tag{7.2}$$

where the deviatoric stretch ratios $\bar{\lambda}_i = J^{-1/3}\lambda_i$, $i = 1,2,3$, with J being the total volume ratio and λ_i the principal stretches. The material parameters were set to c_{10} = 150 kPa and c_{20} = 40 kPa based on data for healthy aorta from a previous study (Vorp et al., 2003). The intimal flap was found to behave more like a linear elastic material compared to the nonlinear elastic behaviour seen in healthy aorta (Deplano et al., 2019). Hence, the dissection flap was assumed as an isotropic, homogenous and linear elastic material with a Young's modulus of 277 kPa and Poisson's ratio of 0.49 (Deplano et al., 2019).

7.2.3 Stent-graft modelling and variations

The geometry of 42-38-158 mm Zenith TX2 PT SG (the device used to treat the patient during TEVAR), consisting of 6 stent struts, was created in Solidworks (Dassault Systèmes, France) by following the dimension and specification of SG from the manufacturer's open access database (Cook Medical, 2019). The next available SG length from the Zenith product library is 42-38-208 mm with 8 stent struts and was created by following the design details in the same database (Figure 7.3.a). In order to gain more insights into the impact of SG length, another medium-length SG (42-38-183 mm) with 7 stent struts was artificially created by following the design features of Zenith TX2 PT product (Figure 7.3.a). These three SG models with lengths of 158 mm (short length), 183 mm (medium length) and 208 mm (long length) were included in the virtual SG deployment simulation.

Apart from the three SG models with different lengths from the Cook Zenith SG product family, two additional SG models from different manufacturers were also included in the virtual SG deployment simulation, one was 42-38-150 mm Medtronic Valiant Proximal Freeflo Tapered SG (Medtronic Vascular, Santa Rosa, California) (Figure 7.3.b) and the other one was 42-42-150-mm GORE C-TAG Active Control SG (W. L. Gore & Associates, Inc, Flagstaff, Ariz) (Figure 7.3). Due to the fact that only straight SG was provided in the C-TAG SG product line, the 42-42-150 mm C-TAG SG was selected to guarantee sufficient sealing at the proximal end. The diameter and length of the SG were used as inputs to the parametric models of Valiant SG and C-TAG described in Chapter 3, in order to replicate the design and dimension features of the commercial products.

All SG models were assembled by metallic stent strut and synthetic graft. The metallic stent struts were fully attached to the synthetic graft for Zenith and Valiant SG, while the metallic scaffold of the C-TAG SG was partially attached to the synthetic graft as described in Chapter 5 (Section 5.1.2). The metallic struts were meshed into linear hexahedral elements with reduced integration (C3D8R) in Abaqus, while the synthetic graft was meshed into membrane elements with reduced integration (M3D4R). Referring to information provided in Table 2.1, materials of metallic stent and synthetic graft of the three commercial stent-graft are summarised in Table 7.1. Material parameters to determine the mechanical behaviour of the 316L stainless steel, Nitinol, polyethylene terephthalate (PET) and expanded polytetrafluoroethylene (ePTFE) in the simulation models are listed in Table 7.2. Mechanical behaviour of Nitinol was defined by the same superelastic material model used in previous chapters. The choice for a simplified linear elastic model for the 316L stainless steel metallic struts was made because self-expandable SG opens automatically within the elastic deformation phase after the delivery sheath is removed. Based on a previous study (Demangent et al., 2013), the yield stress was never reached during SG bending.

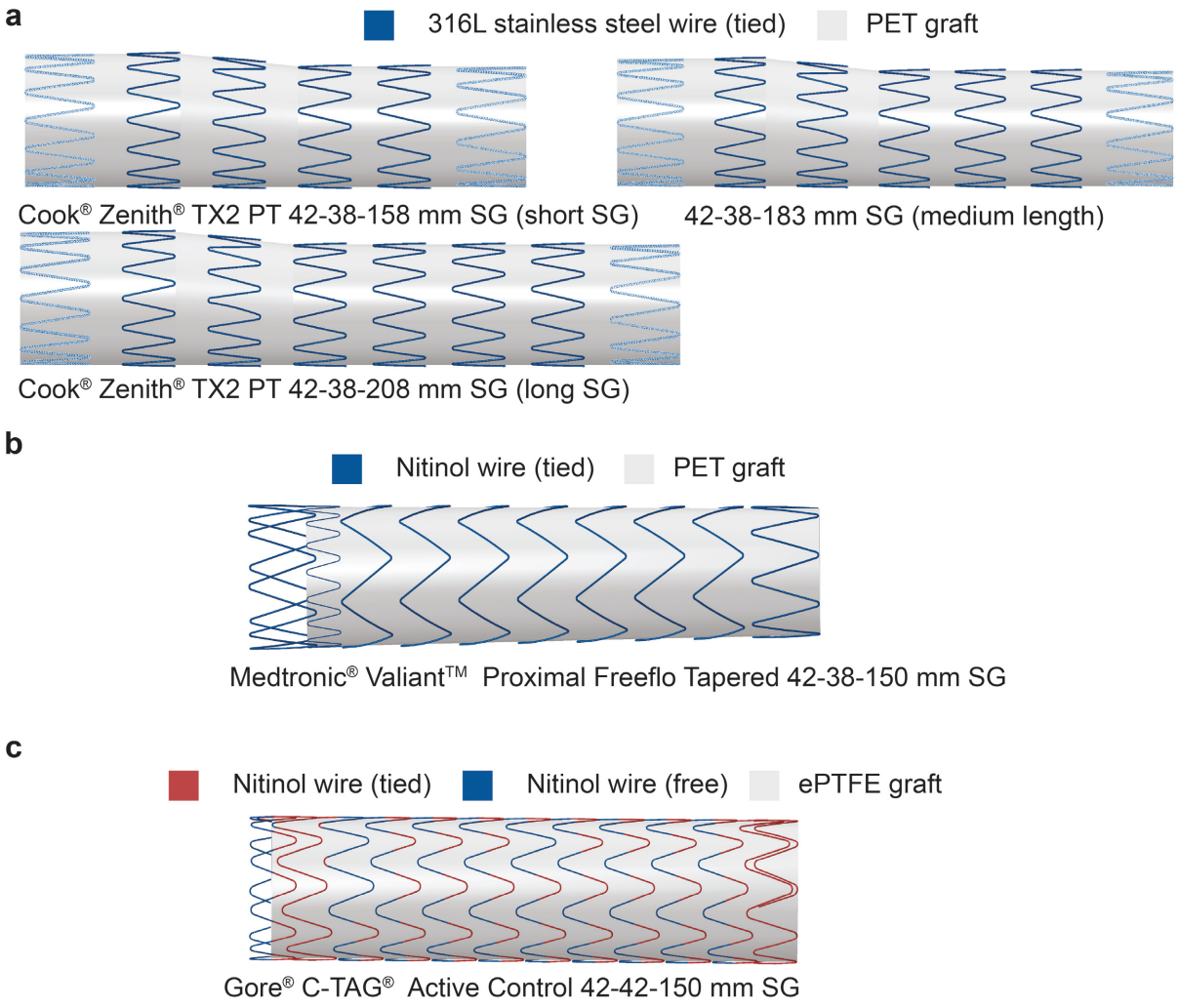


Figure 7.3 Summary of the modelled stent-graft (SG) products. a. Cook Zenith TX2 PT tapered SG with different lengths (the proximal and distal strut are shown with dash line as they were sewed inside of the synthetic graft), b. 42-38-150 mm Medtronic Valiant Proximal Freeflo Tapered SG, c. 42-42-150-mm GORE C-TAG Active Control SG.

Table 7.1 Summary of the stent-graft (SG) materials

Product	Metallic stent material	Synthetic graft material
Zenith TX2 Cook Medical, Bloomington, Ind	316L stainless steel	PET
Valiant Medtronic Vascular, Santa Rosa, Calif	Nitinol	PET
C-TAG W. L. Gore & Associates, Inc, Flagstaff, Ariz	Nitinol	ePTFE

Table 7.2 Summary of material properties of 316L stainless steel, Nitinol, polyethylene terephthalate (PET) and expanded polytetrafluoroethylene (ePTFE)

316L Stainless steel	
Yong's modulus E, MPa	210000
Poisson's ratio ν	0.3
Nitinol (Kleinstreuer et al., 2008)	
Austenite elastic modulus E_A, MPa	51,700
Austenite Poisson's ratio ν_A	0.3
Martensite elastic modulus E_M, MPa	47,800
Martensite Poisson's ratio ν_M	0.3
Transformation strain	0.063
Start of transformation (Loading) σ_L^S, MPa	600
End of transformation (Loading) σ_L^E, MPa	670
Start of transformation (Unloading) σ_U^S, MPa	288
End of transformation (Unloading) σ_U^E, MPa	254
Start of transformation stress in compress σ_{CL}^S, MPa	900
Reference temperature T, ℃	37
Density ρ, g/cm^3	6.5
Polyethylene terephthalate (PET) (Kleinstreuer et al., 2008)	
Yong's modulus E, MPa	1.84
Poisson's ratio ν	0.35
Expanded polytetrafluoroethylene (ePTFE) (Demanget et al., 2013)	
Yong's modulus E, MPa	55.2
Poisson's ratio ν	0.46

7.2.4 Numerical simulation and model verification

Numerical simulations were performed in two steps: pre-stress of the aortic dissection model and virtual deployment of SG. Several assumptions and constraints were adopted in the simulation.

i. Kinetics and constraints: The motion of the aortic root and ascending aorta was neglected in this study. Therefore, the nodes at the proximal ascending aorta, supra-aortic branches and distal descending aorta were fixed with zero displacement. Rayleigh damping was applied to the aorta to account for the viscoelastic tissue support on the outer arterial wall. As the descending aorta is tethered to the spine by paired intercostal arteries, this attachment was modelled by defining four pairs of fixed spots along the descending aorta, effectively preventing any excessive rigid body movement.

ii. Pre-stress of the aortic dissection model: The pre-TEVAR aortic dissection geometry was obtained at mid-diastole and could not be assumed as stress-free due to the intraluminal blood pressure. The calculation of pre-stress of aortic dissection was performed by modifying the method reported by Votta *et al*. (Votta et al., 2017). The intraluminal blood pressure was assumed to be constant at 80 mmHg and distributed uniformly in the true and false lumen. The aortic dissection model was first pressurised by increasing the internal pressure from 0 to 80 mmHg. Then the Cauchy stress tensor calculated from the previous simulation was defined as the initial condition for the next simulation in Abaqus. The pre-stress iteration looped until the deformation of the geometry was less than 0.72 mm (the pixel resolution of pre-TEVAR CTA scan) under the 80 mmHg intraluminal pressure loading. After the iteration loop stopped, the pre-stress tensor corresponding to the mid-diastolic phase was obtained and then applied in the following virtual SG deployment simulation.

iii. Virtual SG deployment: The virtual SG deployment was performed within the pre-TEVAR aortic dissection geometry with the pre-stress tensor as the initial condition. The virtual SG deployment, including crimp, delivery and release of SG, was attained by applying nodal specific displacement boundary conditions on the virtual sheath. In the first step, the diameter of the tubular virtual sheath was reduced from 44 mm to 8.5 mm (the diameter of introducer sheath from the manufacturers database), therefore, the SG within was

compressed from its stress-free state to the crimped state (Figure 7.4.a). The contact between SG and virtual sheath was modelled by using Abaqus Explicit general contact algorithm with penalty formulation. Then the SG was bended to follow the local centreline extracted from the true lumen of pre-TEVAR geometry and delivered to the target landing position selected on the centreline by referring to the 3-month follow-up scan. Finally, the contact between SG and aorta was activated with the friction coefficient of 0.1 (Vad et al., 2010), and followed by the deployment of SG by expanding the virtual sheath radially to a diameter wider than the local aorta (Figure 7.4.a). The virtual SG deployment simulation continued until mechanical equilibrium was reached. Simulations of the SG with three different lengths were performed separately with the targeting SG proximal landing position being fixed at the same location.

To analyse detailed stress distribution on the intimal flap, the intimal flap was subdivided into seven zones (Figure 7.4.a), by using the cutting planes perpendicular to the local centrelines. The distance between the cutting planes was adjusted to 25 mm to ensure that each zone represents the surrounding intimal flap of one stent strut of Cook Zenith SG. Therefore, the short-length stent-grafts, including Cook Zenith SG, Medtronic Valiant SG and Gore C-TAG SG, only cover zone 1 - 5, while the medium-length Zenith SG covers zone 1 - 6 and long-Zenith SG covers zone 1 - 7.

To verify the simulation results, the SG configuration obtained from the simulation with the real SG length (short SG) was compared against the reconstructed geometry from the 3-month follow-up CTA scan by following the approach reported in a previous study (Derycke et al., 2019). The pre-TEVAR scan and 3-month follow-up scan were mapped onto the same coordinate system by using the global registration algorithm in Mimics 23.0. A circle was then fitted into each stent strut end to represent the local diameter, while the centre point of the fitted circle was used to measure the spatial position of the stent strut end (Figure 7.4.b). Differences in local diameter (e_D) between the simulation and follow-up CTA scan were calculated at each stent strut end (Figure 7.4.b), while differences in spatial positioning of stent struts were quantified by measuring the longitudinal deviation along the aorta centreline (e_L) and transvers deviation at local cross-section (e_T) (Figure 7.4.b).

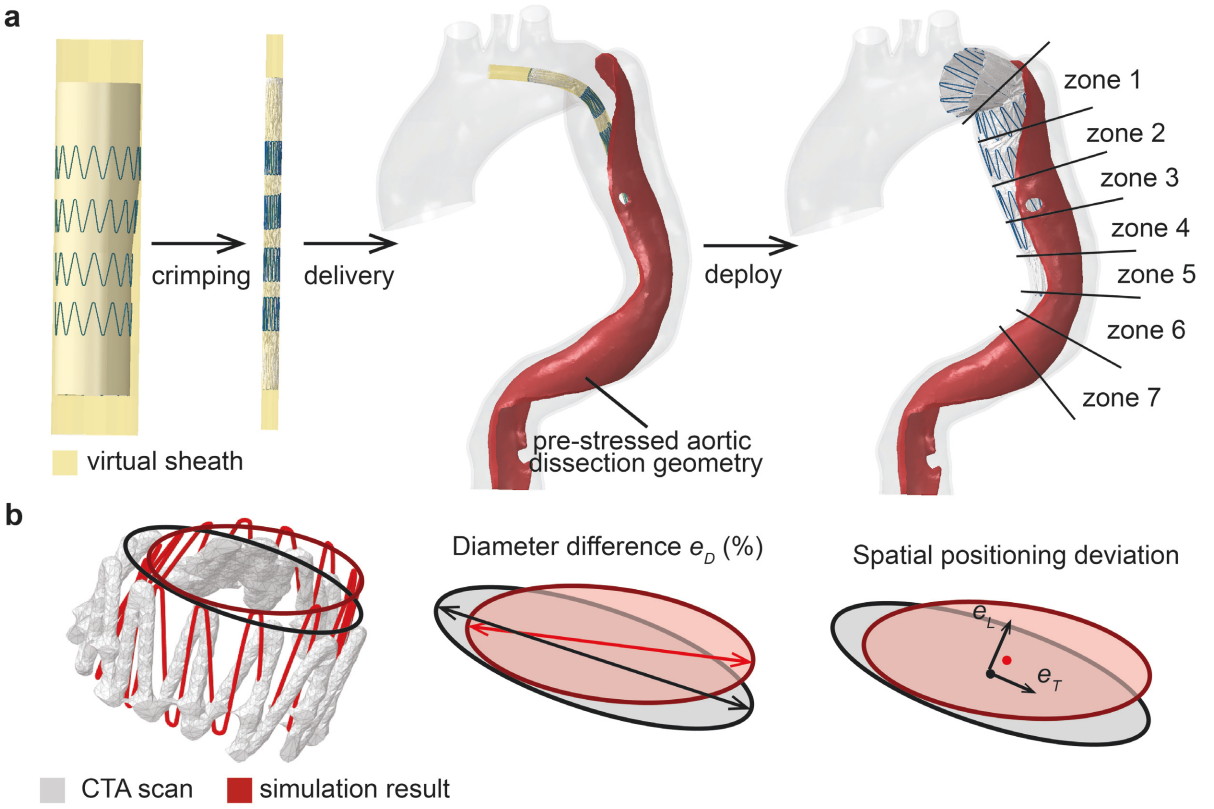


Figure 7.4 Summary of the workflow of FEM-based virtual stent-graft (SG) deployment and the quantitative assessment of SG configuration. a. the SG was crimped, delivered and deployed by controlling the virtual sheath, the intimal flap was subdivided into seven zones to analyse detailed stress distribution on the intimal flap and b. definitions of parameters for quantitative assessment of SG configuration, diameter difference (e_D), spatial positioning deviation in longitudinal direction (e_L) and transverse direction (e_T).

7.3 Results

The Zenith SG with three different lengths, short (158 mm), medium (183 mm), long (208 mm), 42-38-150 mm Valiant SG and C-TAG 42-42-150 mm SG were successfully deployed into the true lumen in five independent simulations. After completing the virtual deployment simulations, the five SGs landed at the same proximal location, but their distal ends were at different locations. The predicted configuration of the short Zenith SG was compared against the 3-month follow-up CTA scan to verify the simulation results. Distributions of von Mises stress on the intimal flap and aortic wall were analysed and compared. Von Mises stress was chosen here as it is a measure used in material failure analysis.

7.3.1 SG configuration

Qualitative evaluation was firstly performed by superimposing the simulated SG configuration on top of the geometry reconstructed from 3-month post-TEVAR CTA scan (Figure 7.5a). The stent struts are numbered from 1 (proximal) to 6 (distal), with each strut having a proximal end (marked as P) and a distal end (marked as D). Visual inspections suggested a good agreement in the stent strut spatial position. Moreover, the opening area of the proximal SG (strut 1 to strut 3) was well reproduced by the model, but the distal segment (strut 4 to strut 6) appeared to be narrower compared to the follow-up CTA scan.

Quantitative evaluation was made by calculating e_D, e_L and e_T as shown in Figure 7.5b-d or each stent strut end. Diameter difference was -7.01 ± 9.00% for all stent strut ends (1P to 6D). Relatively small e_D (< 10%) was found for the proximal struts, but the distal strut ends (4D to 6D) had larger deviations in diameter with the model under-predicting the opening diameter by 10 - 25% (Figure 7.5b). For the spatial position of stent struts, a very good agreement was achieved in longitudinal position with e_L being 1.62 ± 1.10 mm (Figure 7.5c), while the transverse spatial deviation was measured at 3.53 ± 2.09 mm (Figure 7.5d).

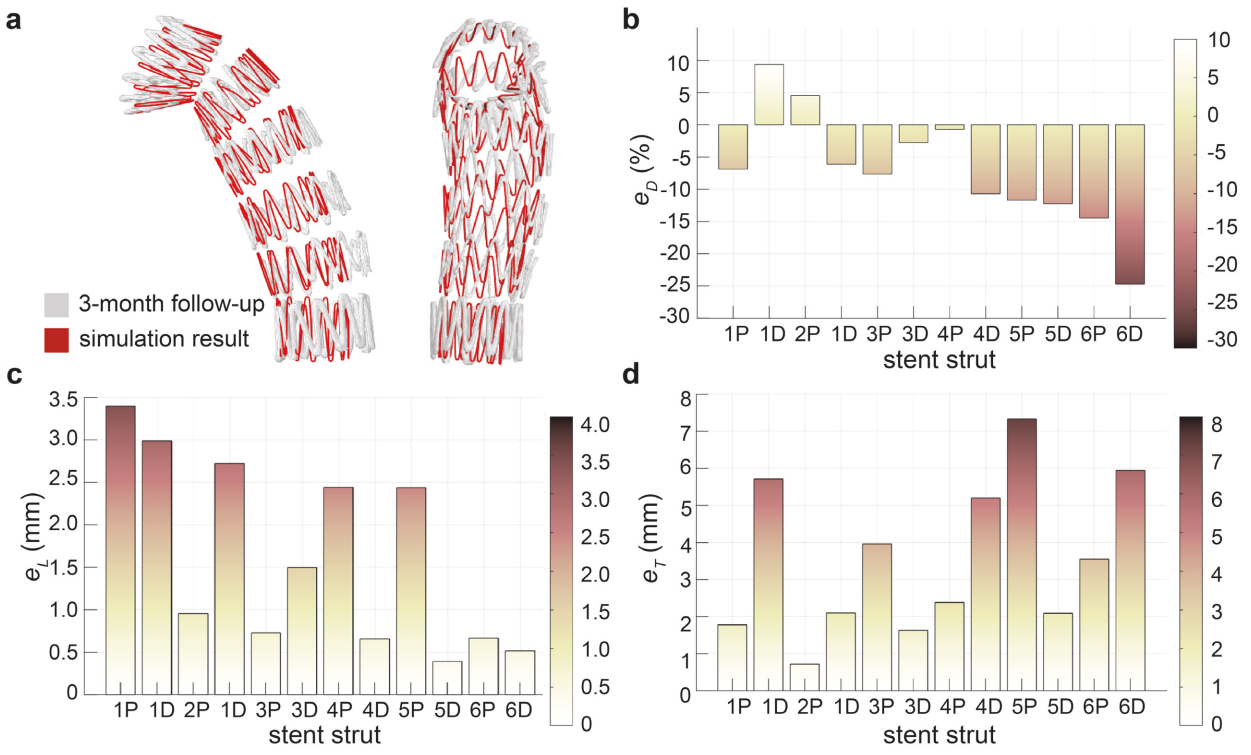


Figure 7.5 Assessment of SG configuration. a. Superimposition of the SG from simulation result and 3-month follow-up scan, b. diameter difference (e_D) at the stent strut ends, c. longitudinal positioning deviation (e_L) at the stent strut ends, and d. transverse positioning deviation (e_T) at the stent strut ends.

7.3.2 Stress distribution

Figure 7.6 shows the predicted von Mises stress distributions on the intimal flap for different Zenith SG lengths. High stresses can be observed at the proximal entry tear, edge of the intimal flap and the spots where the stent strut apexes landed on. Due to local geometric discontinuity and material mismatch induced by the SG, significant difference in von Mises stress distribution can be seen in the distal area (Figure 7.6.a).

The simulation results for the short Zenith SG (mimicking the SG used in the TEVAR procedure for the patient) revealed that the maximum stress on the intimal flap was 238.89 kPa (Figure 7.6.a), which was located at the left posterior side on the distal landing zone (zone 5) where the distal SINE was found on the 3-months follow-up scan (Figure 7.6.b). Moreover, a high stress spot with a maximum value of 283.26 kPa was found on the aortic

wall at the proximal landing zone (Figure 7.6.c) where the proximal entry tear was found at 12-month follow-up (Figure 7.6.d).

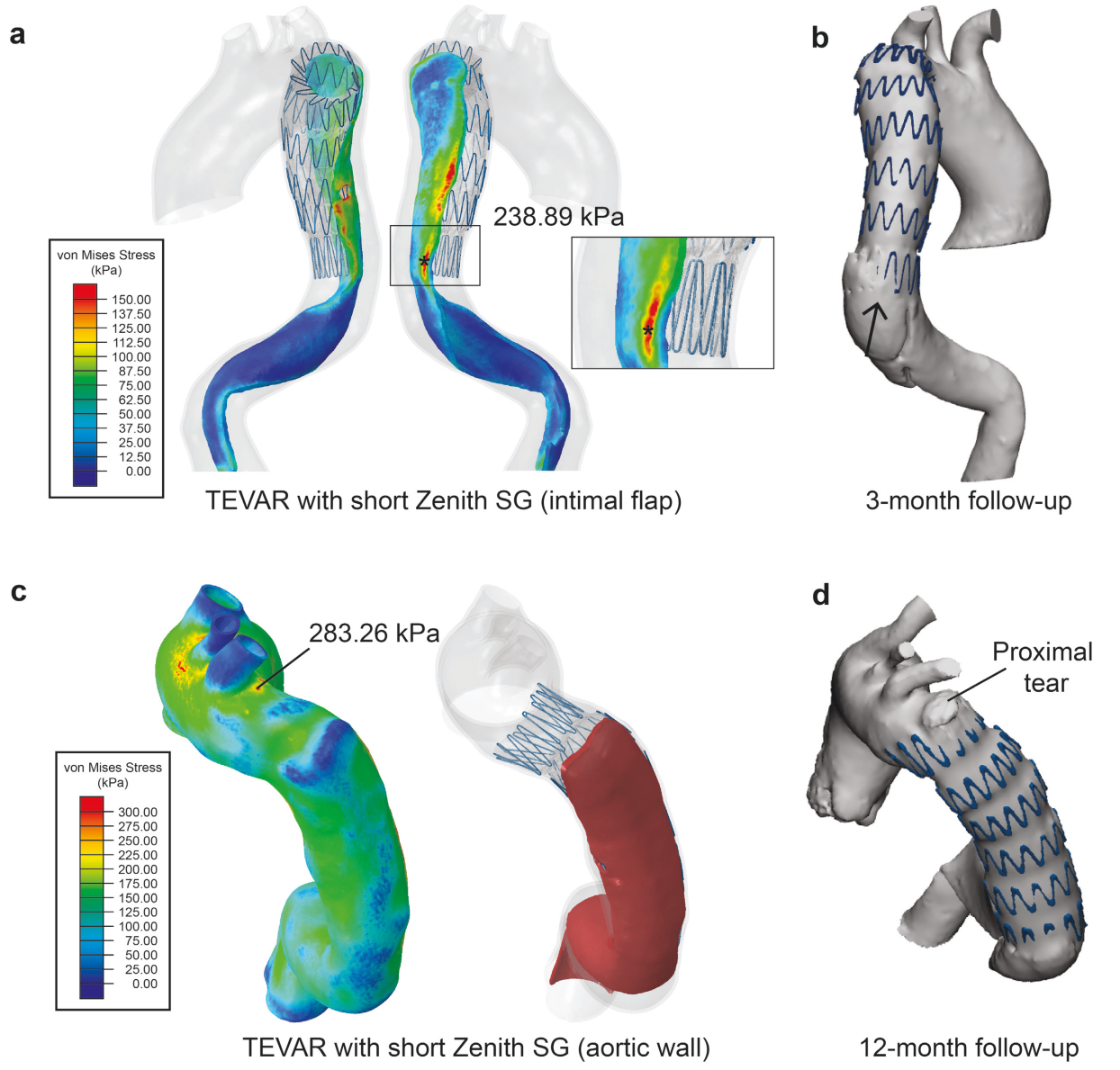


Figure 7.6 Stress distribution with Cook Zenith 42-38-150 mm stent-graft and reconstructions from clinical follow-ups. a. von Mises stress maps on the intimal flap. The distal landing zone was zoomed in to show the local stress distribution, b. 3-month follow-up geometry from the same view angle. The distal SINE is pointed by the black arrow, c. Distribution of von Mises stress on the aortic wall. High stress of 283.26 kPa was found at the location where a proximal tear was found at 12-month follow-up (d).

7.3.3 Impact of stent-graft lengths

Increasing the SG length resulted in changes in the stress pattern and the maximum value on the intimal flap. Due to that the proximal landing position of the medium length SG and long SG were fixed as the same position as the short SG scenario, no difference of the stress distribution was observed at the proximal landing zone.

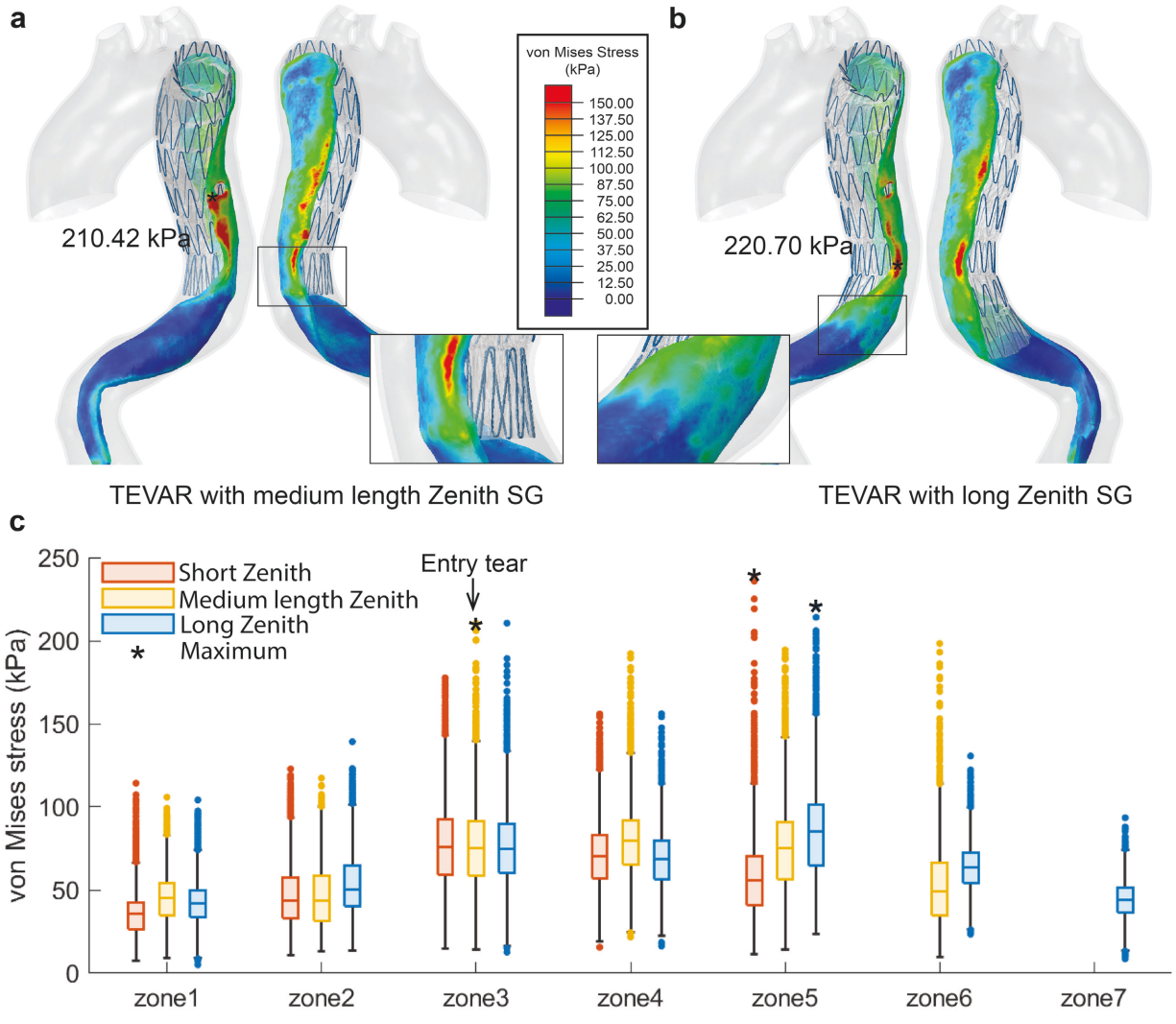


Figure 7.7 a. von Mises stress maps on the intimal flap with the medium-length Zenith SG, b. von Mises stress maps on the intimal flap with the long Zenith SG. The distal landing zones of the two scenarios were zoomed in to show the local stress distribution and c. comparison of the stress distribution in the landing zones.

With the medium-length (183 mm) Zenith SG, the maximum stress on the intimal flap was in the proximal entry tear region (zone 3) with a value of 210.42 kPa (Figure 7.7.a). In the distal landing zone (zone 6), elevated stress (>150 kPa) was found at the spot where the proximal end of strut 7 landed on rather than at the distal boarder of the SG. The maximum stress in the zone 6 was reduced to 198.32 kPa (Figure 7.7.c). With the long Zenith SG (208 mm), the maximum stress was 220.70 kPa which occurred at zone 5 where the strut 6 landed on (Figure 7.7.b), while the maximum stress in the distal landing zone (zone 7) was reduced to 96.69 kPa (Figure 7.7.c).

7.3.4 Impact of stent-graft designs

Changing the SG products resulted in changes in the stress pattern and the maximum value. Although the proximal landing position of the Valiant SG and C-TAG SG was assumed to be identical to that with the short Zenith SG, differences in the stress distribution were observed at the proximal landing zone when compared to the short Zenith SG. The simulation result with the Valiant SG revealed a high stress spot with a maximum value of 263.97 kPa in the aortic wall at the proximal landing zone (Figure 7.8.a) where a high stress was also found in the simulation result for the short Zenith SG (Figure 7.6.c). Similar high stress spot was also found in the simulation result for C-TAG SG, but the peak stress was much lower at 196.56 kPa (Figure 7.8.b).

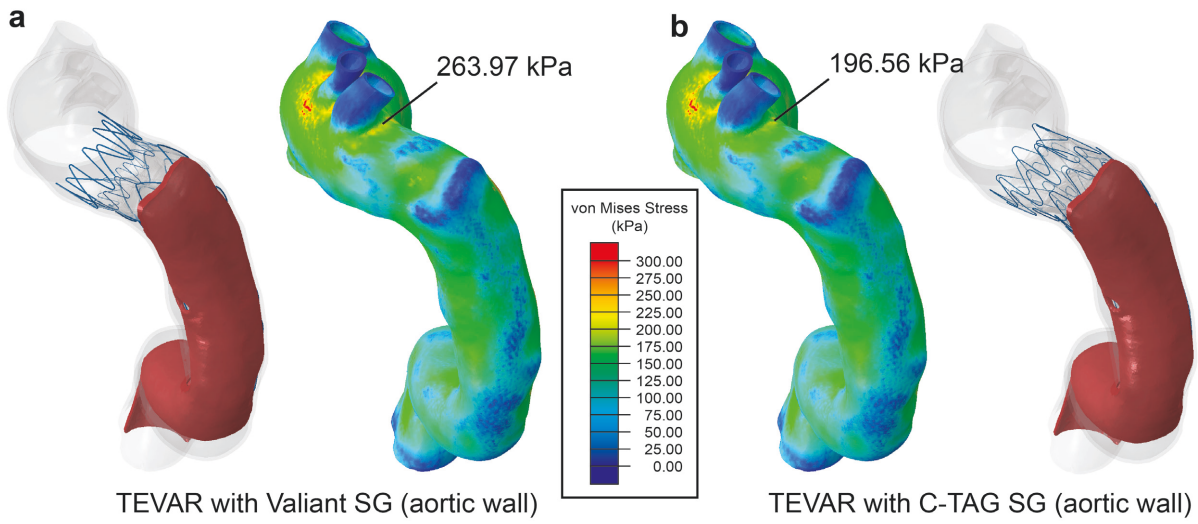


Figure 7.8 a. Distribution of von Mises stress on the aortic wall after deploying Valiant SG virtually into the aorta. High stress of 263.97 kPa was found at the proximal landing zone, b. Distribution of von Mises stress on the aortic wall after deploying C-TAG SG virtually into the aorta. High stress of 196.56 kPa was found at the proximal landing zone.

Both Valiant SG and C-TAG SG produced maximum values of stress on the intimal flap at the left posterior side of the distal landing zone (zone 5) where the maximum stress was found with the short Zenith SG. But the peak von Mises stress was reduced to 201.85 kPa with the Valiant SG and 206.16 kPa with C-TAG SG (Figure 7.9), both were lower than the peak von Mises stress found at the same location with the short Zenith SG.

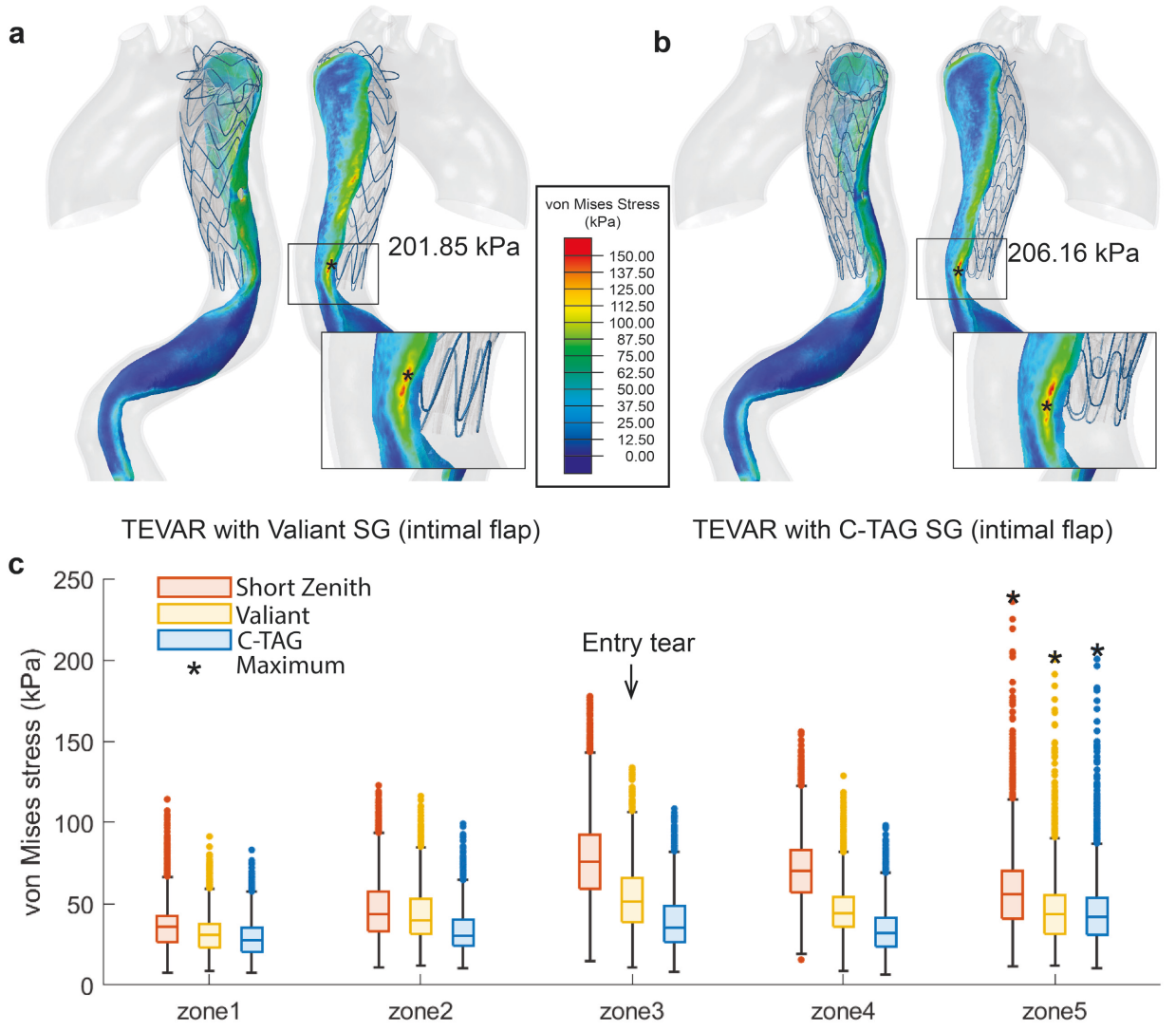


Figure 7.9 a. von Mises stress maps on the intimal flap with Valiant SG, b. von Mises stress maps on the intimal flap with Valiant SG. The distal landing zones of the two scenarios were zoomed in to show the local stress distribution and c. Comparison of the stress distribution in the landing zones.

7.4 Discussion

Short SG has been flagged up as a risk factor for distal SINE in recent clinical studies (Li et al., 2015, Ma et al., 2017). For the clinical case presented in this study (TEVAR with 158 mm length Zenith SG), the risk assessment outcome can be contradictory based on different clinical recommendations (high risk with SG <145 mm in Li et al.'s study and <165 mm in Ma et al.'s study). Moreover, longer SG can cover larger segment of the descending aorta,

potentially affecting spinal cord circulation and increasing the risk for paraplegia (Nienaber et al., 2007). Unfortunately, very limited study has been published so far to establish a third-party benchmark evaluation system for commercial SGs, nor patient-specific study of virtual deployment of different SGs in type B aortic dissection. Further insights into the impact of SG length and design on post-TEVAR wall stress will be valuable for understanding the factors responsible for the formation of SINE, thereby aiding pre-surgical planning in the future.

In this chapter, a FEM-based simulation method for SG deployment in a patient-specific type B aortic dissection reconstructed from pre-TEVAR CTA scan was presented. Previous FEM-based studies attempted to investigate the role of dissection geometry and wall stress in the occurrence of SINE (Menichini et al., 2018, Tan et al., 2021), but these studies relied on post-TEVAR CTA or magnetic resonance scans to reconstruct patient-specific geometry and assumed the SG as an additional wall layer without explicit description of the SG design. As mentioned in Chapter 4, other studies have investigated the solid-solid interaction between SG and aorta in type B aortic dissection by adopting virtual SG deployment approach, but the pre-stress conditions were ignored (Ma et al., 2018, Meng et al., 2020). By incorporating the pre-stress conditions and virtual SG deployment, the virtual stent-graft deployment model presented in this chapter is a step closer towards simulating the in vivo post-TEVAR biomechanical environment. This is important for accurate prediction of SG configuration and stress distribution.

The simulation results were verified by comparing the deployed SG configuration with the post-TEVAR CTA scan. Ideally, imaging acquired during the TEVAR procedure or immediately after should be used for validation purpose. Unfortunately, such information was not available for this retrospective study and the earliest follow-up scan was performed at 3-month post-TEVAR. Therefore, this limitation must be factored in when evaluating the difference in SG configuration between the model prediction and CTA scan. For SG positioning, the longitudinal and transverse deviations were 1.62 ± 1.10 mm and 3.53 ± 2.09 mm (Figure 7.5), respectively, which are comparable to those reported by Derycke et al. with their FEM-based virtual deployment of a complex double-branched SG in a patient-specific aortic arch aneurysm (Derycke et al., 2019). However, the model produced larger deviations

in the SG opening diameter, especially for the distal struts with deviations up to 25%. Since the patient was found to have developed a distal SINE at 3-month follow-up, the distal end of the SG had already expanded and partially pushed into the FL side. This might explain why the predicted SG diameter at the distal end was much smaller than the 3-month follow-up configuration.

Analysis of wall stress distributions on the intimal flap and outer wall revealed that with the short Zenith SG deployed in the TEVAR procedure, the maximum von Mises stress on the intimal flap (238.89 kPa) colocalised with the region where the distal SINE occurred at 3-month follow-up (Figure 7.6.a-b). Furthermore, high von Mises stress was observed at the proximal landing zone on the aortic wall, coinciding with the spot where a proximal new tear was identified at 12-month follow-up (Figure 7.6.c-d). These focal high stress regions have shown a strong spatial correlation with the locations where the distal SINE and proximal new tear occurred. The potential link between stress concentration at the distal landing zone and distal SINE is consistent with the findings reported in patient-specific studies using a simplified finite element model (Menichini et al., 2018). By employing a virtual stenting algorithm based on simplex deformable mesh method, Chen et al. identified a correlation between large stent-induced deformation and distal SINE (Chen et al., 2018). Stress concentration at the proximal landing zone and its potential correlation with proximal new tears have also been reported in previous studies (Ma et al., 2018, Meng et al., 2020).

In the most recent study reported by Tan et al., the effect of SG length on wall stress distribution was examined as part of a sensitivity analysis using an idealised geometric model (Tan et al., 2021). It was found that the distal SG landing position was an important factor in determining the magnitude of maximum wall stress, where landing in a straight portion of the aorta had the lowest maximum von Mises stress. However, the simplifications and assumptions made in their study meant that the complex SG design and the interactions between stent struts and intimal flap were not captured. To the best of the author's knowledge, no previous virtual SG deployment study has focused on the impact of SG length and design on aortic wall stress distribution and its correlation with SINE in type B aortic dissection.

The simulation results for the Zenith SG showed that increasing the SG length altered the wall stress pattern, the magnitude of maximum von Mise stress and its location. With the medium-length SG, the maximum stress was found at the entry tear which was sealed by the SG. At the distal landing zone, which is vulnerable to rupture due to material mismatch, wall stress was reduced by 17% compared to the short SG. Interestingly, the simulation results for long SG showed a further reduction of wall stress in the distal landing zone by ~60% compared to the short SG. Moreover, the maximum stress on the intimal flap was found in a region fully covered by the SG (Figure 7.7.b). Further to the findings in the study by Tan et al. (Tan et al., 2021), the stress level on the intimal flap also influenced by the occurrence of the entry tear in a straight portion (zone 3). High median value of von Mise stress was observed at the zone 3 after the virtual deployment of three difference lengths SGs with values of 75.64 kPa, 75.45 kPa and 74.82 kPa for the short, medium length and long SGs respectively (Figure 7.7).

The simulation results for different SG designs showed that compared to the short Zenith SG the maximum von Mises stress at the proximal landing zone was reduced by 7% with the Valiant SG and 31% by the C-TAG SG. Among the three SG products, C-TAG SG produced the lowest level of stress on the intimal flap, while the Zenith SG produced the highest level of stress (Figure 7.9.c). At the distal landing zone, the 42-38-150 mm tapered Valiant SG produced the lowest peak von Mises stress which showed a 16% reduction compared to the short Zenith SG. The C-TAG SG reduced the peak von Mises stress by 14% compared to the short Zenith SG. It should be noted that, due to the limited availability of SG configuration in real products, the C-TAG SG was the only straight SG with dimension of 42-42-150 mm which induced higher oversizing ratio than the tapered Valiant and Zenith SG. This might explain why the C-TAG SG produced slightly higher peak von Mises stress than the Valiant SG. However, the intimal flap exposed to high stress concentration was not fully covered by the SG, which still represents a risk for distal SINE.

In the clinical practice of TEVAR, SG length and design are usually selected based on anatomic features of the aortic dissection. With the raising awareness of post-TEVAR complications, newer generations of SGs of tapered configuration and longer length are becoming available, which offer improved sealing effect while minimising SG-induced injury. Through detailed

analysis of the biomechanical interactions between SG and the dissected aorta, computational simulations as shown in this study will not only improve our ability to predict post-TEVAR complications, but also assist in the development of future endograft designs and treatment planning.

7.5 Summary

In this chapter, virtual SG deployment simulations were performed to investigate the impact of SG length and design on post-TEVAR wall stress distribution. The short Zenith SG generated high von Mises stress at both the proximal landing zone and distal landing zone where a proximal new entry tear and distal SINE were identified on follow-up scans. Using the medium-length Zenith SG reduced the wall stress in the distal landing zone by 17%, whereas a more dramatic reduction of 60% was achieved with the long Zenith SG which may potentially reduce the risk of distal SINE. By switching to different SG designs of similar length to the short Zenith SG, the C-TAG SG produced the lowest level of stress on the intimal flap and reduced the peak von Mises stress by 31% and 14% at the proximal and distal ends, respectively, while the Valiant SG achieved a 7% reduction in peak von Mises stress at the proximal end and 16% reduction at the distal end. However, the high stress concentration spot on the intimal flap was not fully covered by the short length SGs. This chapter demonstrates the potential of using the virtual SG deployment model as a pre-surgical planning tool to help select the most appropriate SG length and design for individual patients.

Chapter 8

Conclusion and future work

Aortic dissection is a catastrophic aortic disease with a high mortality rate. In addition to medical therapies, TEVAR has been successful in managing type B aortic dissections and considered as an optional treatment procedure for selected type A aortic dissections. Although its less invasive nature is a great advantage over conventional open surgery, post-TEVAR complications such as stent-graft migration, SINE and RTAD cannot be ignored. Current clinical guidelines are mainly based on pre-TEVAR CTA scans and anatomical measurements, without giving adequate consideration of the complex biomechanical interactions between SG and the aorta.

This thesis presents a novel computational simulation framework for virtual SG deployment in patient-specific aortic dissections that is able to predict post-TEVAR SG configuration and biomechanical stresses in the aortic wall. The ultimate goal of this study is to provide a pre-surgical planning tool that will allow clinicians to choose an optimal SG and its landing position for individual patient in the future.

Starting with a complicated type B aortic dissection case with an extremely narrowed true lumen, the finite element-based simulation model demonstrated its feasibility in tackling the nonlinear contact problem associated with SG deployment and complex geometry. The finite element model accounts for detailed design features and material properties of SG, mechanical behaviour of dissected aorta, pre-stress in the aortic wall and the action of intraluminal blood pressure. Numerical simulations were performed with different model settings and material properties to determine their influences on the predicted SG

configuration. Comparisons with the real SG configuration obtained from the post-TEVAR CTA scan allowed for evaluation of the accuracy of the simulation model.

Having demonstrated its feasibility and accuracy for application in a type B aortic dissection, the virtual SG deployment model was tested for its ability to reproduce the immediate outcome of TEVAR as observed in a clinical case of type A aortic dissection. The simulation model was further personalised by incorporating patient-specific aortic root motion and material parameters corresponding to the patient's own ascending aortic tissues.

The patient-specific virtual SG deployment model was then applied to four additional type B aortic dissection patients, with a focus on analysing post-TEVAR biomechanical stresses in the repaired aortas. Higher wall stress was found in the distal landing zone of the SINE patients, indicating a potential link between high wall stress and SINE.

Finally, the impact of SG design and length on post-TEVAR biomechanical conditions was evaluated in a patient-specific type B aortic dissection. The virtual SG deployment model demonstrated its potential to serve as a pre-surgical planning tool by providing quantitative information on post-TEVAR SG configuration and biomechanical changes introduced by SG.

8.1 Summary of main contributions

A summary of the main contributions of this study is given below, followed by a discussion of limitations, future directions and clinical implications.

- A novel computational framework for virtual SG deployment in aortic dissection was developed and presented (Chapter 3). The model has the following novelties compared to previously published methods:
    1. By using a purpose-built segmentation approach, the intimal flap can be defined as a different material from the aortic wall and have non-uniform thickness (Chapter 3, 4 &7).
    2. The parametric models created for SG offer wider choices of SG design and size. The mechanical properties of different SG materials are also incorporated (Chapter 7).

3. By adopting nodal specific displacement on the virtual sheath in the SG deployment simulation, local anatomical complexities in aortic dissections can be handled with relative ease (Chapter 4). It also enables precise control of the virtual deployment procedure, allowing quick assessment of SG landing position and the immediate outcome of SG deployment (Chapter 5).
4. The model accounts for aortic wall pre-stress and the action of blood pressure on graft internal surface (Chapter 3 & 4).

- Model validation was performed on a type B aortic dissection by comparing the predicted SG configuration with the post-TEVAR CTA scan, demonstrating a good match with the real SG configuration. Simulation results also showed the importance of accounting for aortic wall pre-stress and blood pressure on the graft internal surface in the SG deployment simulation model (Chapter 4).
- When applied to a clinical case of failed TEVAR for a type A aortic dissection, the model successfully reproduced the immediate outcome of TEVAR as observed in vivo. Remarkable agreement was observed between the simulation result and the clinical outcome, which provided further validation of the model. The model not only helped to understand why the original TEVAR procedure failed in this patient, but also predicted a scenario where the risk of stent-graft migration could be mitigated by changing the SG landing position (Chapter 5).
- An initial attempt was made to identify differences in post-TEVAR biomechanical environment between SINE and non-SINE patients by performing virtual SG deployment simulations on four type B aortic dissections. The two SINE cases were found to have higher VMS, MPS and MSS than the two non-SINE cases, especially in the distal landing zone where SINE occurred. This preliminary finding highlighted the potential importance of biomechanical factors in predicting SINE and the need for examining a larger patient cohort (Chapter 6).
- The potential of using the virtual SG deployment model as a pre-surgical planning tool was demonstrated for the first time. Based on a pre-TEVAR CTA scan, it was possible to assess the biomechanical consequences of changing SG design and length in a patient-specific type B aortic dissection. (Chapter 7).

Furthermore, the finite element SG deployment model is not limited to the cases presented in this thesis. It is readily applicable to any aortic dissection geometries. It can also simulate SG deployment in acute or chronic dissections by changing the intimal flap mechanical properties and thickness. In addition, the motion of aortic root can be accounted for, which is a new feature and has not been reported in previous simulation studies of SG deployment in the aorta.

It is hoped that the virtual SG deployment simulation framework presented in this thesis can be further refined and developed to improve its robustness and computational efficiency. This will extend its application to a large patient cohort, which is necessary for elucidating the role of biomechanical factors in TEVAR-related complications. Having a robust and quick solution will also pave the way towards its future adoption as a pre-surgical planning tool, allowing clinicians to select the most appropriate SG landing position, length and design for individual patient. The finite element method-based model is also expected to help bioengineers to optimise the design of SG and develop new SG devices.

8.2 Limitations and future directions

The present study involves several limitations which should be addressed. Main limitations of this work are discussed below along with future directions.

8.2.1 Interaction with blood flow

In this thesis, blood flow and its interactions with the aortic wall and SG were not modelled directly, and a constant and uniform pressure loading was applied at the graft internal surface instead, which neglected the pulsatile nature of blood flow and haemodynamic changes after TEVAR. In all the simulations presented in this thesis, the internal blood pressure was assumed to be 80 mmHg which was uniformly distributed throughout the modelled aorta. This is a major limitation. Clinical studies have suggested that blood flow and its interactions with aortic wall and SG play a crucial role in evaluating the prognosis of aortic dissection after TEVAR (Nienaber and Clough, 2015). Following the deployment of SG, blood flow in the false lumen is reduced which causes thrombus formation and change in blood pressure within the false lumen (Xu et al., 2021). TEVAR-induced false lumen

thrombosis and change in blood pressure were not considered in the virtual SG deployment simulation model presented in this thesis.

With advances in medical imaging techniques, dynamic information such as blood flow velocities in the true and false lumens can be measured by means of echocardiography or 4D-flow MRI (Nienaber and Clough, 2015). By combining patient-specific MRI data with computational fluid dynamics simulations, distributions of blood pressure in the treated aorta can be obtained (Pirola et al., 2019). This pressure distribution is more realistic and may be applied at the internal surface for pre-stress calculation in the future. In addition, it is also possible to predict thrombosis of the false lumen (Menichini et al., 2016, Armour et al., 2020), which could potentially be integrated into the virtual SG deployment model in the future.

Fluid-structure interaction (FSI) simulation which incorporates dynamic interactions among blood flow, aortic wall and the SG, should be set as a future goal of this virtual simulation work. By combining FSI with the thrombosis model, it would push the model closer towards predicting the progression of aortic dissection following TEVAR.

8.2.2 Material property and thickness of aortic tissue

In this study, the aortic wall was assumed to have a uniform thickness with isotropic hyperelastic behaviour, although it would be more accurate to treat it as an anisotropic fibre-reinforced material (Roy et al., 2014). The stress-strain response of aortic wall is highly nonlinear, with a typical rapid stiffening under pressure arising from recruitment of collagen fibrils which exhibit significant anisotropic behaviour in circumferential and axial directions (Vorp, 2007). The anisotropic HGO material model discussed in Chapter 2 would be a good choice for the virtual SG deployment model presented in this thesis, which should be implemented in the future. It is also worth considering the use of a multi-level constitutive model which accounts for the growth and degradation of elastin and fibrous tissue. This will allow simulation of the growth-remodelling process after TEVAR (Grytsan et al., 2015).

Mechanical properties of the aorta vary with age, gender and the occurrence of disease (Humphrey and Holzapfel, 2012). Ideally, these factors should be taken into account when defining the material parameters in the simulation model. Due to the wide acceptance of

TEVAR for type B aortic dissection, very few open surgeries are performed for type B aortic dissections, thereby limiting the access to dissection tissue samples. However, there is still a need for comprehensive mechanical testing on dissected aortic tissues and intimal flap in the future. Furthermore, the aortic wall should have different material properties in the true lumen and false lumen side due to splitting of the wall layers. The influence of different material models and parameters for the aortic wall should be further investigated through a comprehensive sensitivity analysis. As mentioned in the previous section, the purpose-built segmentation approach developed in this thesis treats the intima flap as a separate material, so that changes in pathological state and mechanical behaviour of the intimal flap from acute to chronic phase can be accounted for in the simulation model.

Moreover, the aortic wall at the true lumen side and the false lumen side should have different wall thickness. However, direct measurement of wall thickness from CTA images was not reliable due to limited spatial resolution and the inability to distinguish between the wall and its surrounding tissues. Cine-MRI has been shown to provide valid and reliable measurement of aortic wall thickness which could potentially be adopted to acquire patient-specific aortic wall thickness for more accurate personalised simulations (Mensel et al., 2014).

8.2.3 Motion of the aorta

The aortic root motion was neglected in all simulations for type B aortic dissections but was included in the simulation of type A aortic dissection in Chapter 5. However, only the in-plane motion of the aortic root was incorporated, since the motion data was obtained by using 2D DSA image.

Dynamic imaging techniques, including dynamic CT and Cine-MRI, can provide reliable 3D motion information which can be used in the simulation model. There are examples in the literature where aortic root model derived from cine phase-contrast MRI has been used as input for finite element modelling of the aorta (Singh et al., 2016).

8.2.4 Cohort size

In Chapter 4, only one patient-specific case was used to demonstrate the proof of concept of the method, and for initial model validation and sensitivity test. Multiple cases will be needed for a more rigours validation.

The case study presented in Chapter 5 was also based on a single type A aortic dissection patient. TEVAR has only been introduced to selective type A aortic dissection cases in recent years (Nienaber et al., 2017). Patients may qualify for TEVAR in scenarios of prohibitive surgical risk so the number eligible patients is very limited, and failed TEVAR caused by immediate stent-graft migration in type A aortic dissection is even rare. Future studies will include more type A aortic dissection cases treated by TEVAR in order to further test the capability of the virtual SG deployment model in predicting immediate TEVAR outcomes.

Small cohort size is also a main limitation of the pilot study presented in Chapter 6. Although simulation results on the four cases showed colocation of higher VMS, MPS and MSS in the distal landing zone and the site when SINE occurred, this preliminary finding does not have any statistical power and must be validated using a larger cohort.

8.3 Clinical implications

The patient-specific virtual SG deployment simulation framework presented in this thesis has several potential implications for clinical research, device design and clinical application. After the preliminary study presented in Chapter 6, the simulation framework should be applied to a larger cohort of SINE and non-SNE patients. This will allow an in-depth biomechanical analysis of the key biomechanical factors associated with SINE formation. The results may be used to formulate a risk grading system for personalised assessment of the risk for post-TEVAR SINE and RTAD.

The virtual SG deployment simulation framework has a great potential to serve as a tool to assist the design and optimisation of SG. Current SG devices are primarily designed for treating type B aortic dissections and has been introduced to treat selective type A aortic dissections. By using the virtual SG deployment simulation with realistic aortic root motion

data, there are opportunities for further refinement of the SG design and for developing innovative SG devices specially tailored for type A aortic dissections.

The main potential application of the virtual SG deployment model is to assist clinicians to choose the most appropriate SG size, design and landing position at pre-surgical planning stage. Based on current clinical guidelines, TEVAR is usually performed in the subacute phase for complicated type B aortic dissections which allows 4-6 days between patient admission and TEVAR (Bozinovski and Coselli, 2008, Nienaber et al., 2016). Current estimate of the time required for a complete virtual SG deployment simulation is 49 hours on a workstation with Duo Intel Xeon E5-2630 central processing units (40 cores in total) (Figure 8.1). Taking advantage of the latest development in artificial intelligence and machine learning methods for medical image processing, it is possible to significantly accelerate the processing of CTA image and mesh generation (Lyu et al., 2021). Simulations of different SGs and deployment positions can be performed in parallel on high performance computing clusters. It is hoped that the virtual SG deployment simulation framework presented in this thesis will serve as a pre-surgical planning tool to assist clinicians in the future.

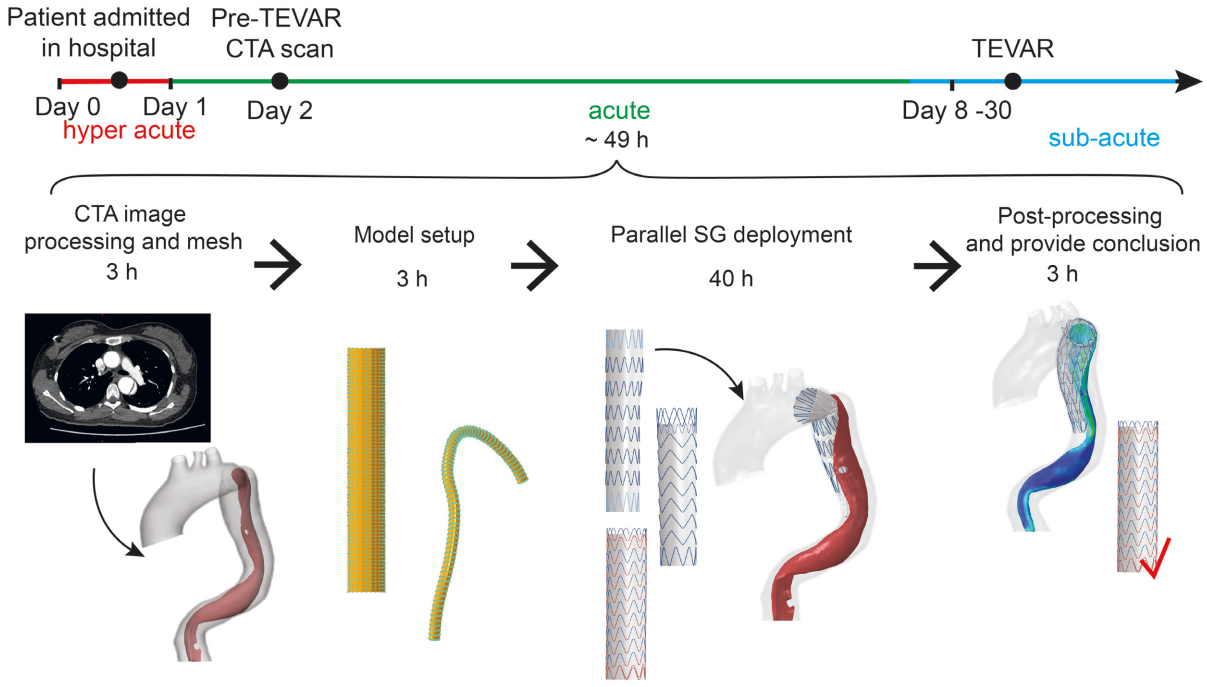


Figure 8.1 Possible timeline for management of type B aortic dissection with the virtual stent-graft deployment model serving as a pre-surgical planning tool.

Bibliography

ABAD, E. M. K., PASINI, D. & CECERE, R. 2012. Shape optimization of stress concentration-free lattice for self-expandable Nitinol stent-grafts. *Journal of biomechanics,* 45**,** 1028-1035.

ABAQUS USER'S MANUAL 2019. *Abaqus User's Manual 2019*.

ALTNJI, H. E., BOU-SAID, B. & WALTER-LE BERRE, H. 2015. Morphological and stent design risk factors to prevent migration phenomena for a thoracic aneurysm: a numerical analysis. *Med Eng Phys,* 37**,** 23-33.

AMABILI, M., ARENA, G. O., BALASUBRAMANIAN, P., BRESLAVSKY, I. D., CARTIER, R., FERRARI, G., HOLZAPFEL, G. A., KASSAB, A. & MONGRAIN, R. 2020. Biomechanical characterization of a chronic type a dissected human aorta. *Journal of Biomechanics,* 110**,** 109978.

AMABILI, M., BALASUBRAMANIAN, P., BOZZO, I., BRESLAVSKY, I. D. & FERRARI, G. 2019. Layer-specific hyperelastic and viscoelastic characterization of human descending thoracic aortas. *J Mech Behav Biomed Mater,* 99**,** 27-46.

ARMOUR, C. H., MENICHINI, C., MILINIS, K., GIBBS, R. G. & XU, X. Y. 2020. Location of reentry tears affects false lumen thrombosis in aortic dissection following TEVAR. *Journal of Endovascular Therapy,* 27**,** 396-404.

AURICCHIO, F., CONTI, M., MARCONI, S., REALI, A., TOLENAAR, J. L. & TRIMARCHI, S. 2013. Patient-specific aortic endografting simulation: from diagnosis to prediction. *Comput Biol Med,* 43**,** 386-94.

BAGUET, J.-P., CHAVANON, O., SESSA, C., THONY, F., LANTELME, P., BARONE-ROCHETTE, G. & MALLION, J.-M. 2012. European Society of Hypertension scientific newsletter: hypertension and aortic diseases. *Journal of hypertension,* 30**,** 440-443.

BAUMLER, K., VEDULA, V., SAILER, A. M., SEO, J., CHIU, P., MISTELBAUER, G., CHAN, F. P., FISCHBEIN, M. P., MARSDEN, A. L. & FLEISCHMANN, D. 2020. Fluid-structure interaction simulations of patient-specific aortic dissection. *Biomech Model Mechanobiol,* 19**,** 1607-1628.

BÖCKLER, D., BISCHOFF, M. S., KRONSTEINER, D., SKRYPNIK, D. & MEISENBACHER, K. 2021. Outcome analysis of the Gore Conformable Thoracic Stent Graft with active control system for the treatment of arch and descending thoracic aortic disease. *European Journal of Cardio-Thoracic Surgery*.

BOOHER, A. M., ISSELBACHER, E. M., NIENABER, C. A., TRIMARCHI, S., EVANGELISTA, A., MONTGOMERY, D. G., FROEHLICH, J. B., EHRLICH, M. P., OH, J. K. & JANUZZI, J. L. 2013. The IRAD classification system for characterizing survival after aortic dissection. *The American journal of medicine,* 126**,** 730. e19-730. e24.

BOZINOVSKI, J. & COSELLI, J. S. 2008. Outcomes and survival in surgical treatment of descending thoracic aorta with acute dissection. *The Annals of thoracic surgery,* 85**,** 965-971.

BUSTOS, C. A., GARCÍA-HERRERA, C. M. & CELENTANO, D. J. 2016. Mechanical characterisation of Dacron graft: Experiments and numerical simulation. *Journal of biomechanics,* 49**,** 13-18.

CAIMI, A., PASQUALI, M., STURLA, F., PLUCHINOTTA, F. R., GIUGNO, L., CARMINATI, M., REDAELLI, A. & VOTTA, E. 2020. Prediction of post-stenting biomechanics in coarcted aortas: A pilot finite element study. *J Biomech,* 105**,** 109796.

CANAUD, L., GANDET, T., SFEIR, J., OZDEMIR, B. A., SOLOVEI, L. & ALRIC, P. 2019. Risk factors for distal stent graft-induced new entry tear after endovascular repair of thoracic aortic dissection. *J Vasc Surg,* 69**,** 1610-1614.

CANAUD, L., OZDEMIR, B. A., PATTERSON, B. O., HOLT, P. J., LOFTUS, I. M. & THOMPSON, M. M. 2014. Retrograde aortic dissection after thoracic endovascular aortic repair. *Ann Surg,* 260**,** 389-95.

CANCHI, T., SAXENA, A., NG, E., PWEE, E. C. & NARAYANAN, S. 2018. Application of fluid–structure interaction methods to estimate the mechanics of rupture in asian abdominal aortic aneurysms. *Bionanoscience,* 8**,** 1035-1044.

CANTRILL, S. V., BROWN, M. D., BURTON, J. H., DIERCKS, D. B., GEMME, S. R., GERARDO, C. J., GODWIN, S. A., HAHN, S. A., HAUKOOS, J. S. & HUFF, J. S. 2015. Clinical policy: critical issues in the evaluation and management of adult patients with suspected acute nontraumatic thoracic aortic dissection. *Annals of Emergency Medicine,* 65**,** 32-42. e12.

CARDAMONE, L., VALENTIN, A., EBERTH, J. F. & HUMPHREY, J. D. 2009. Origin of axial prestretch and residual stress in arteries. *Biomech Model Mechanobiol,* 8**,** 431-46.

CHAGNON, G., REBOUAH, M. & FAVIER, D. 2015. Hyperelastic energy densities for soft biological tissues: a review. *Journal of Elasticity,* 120**,** 129-160.

CHEN, D., WEI, J., DENG, Y., XU, H., LI, Z., MENG, H., HAN, X., WANG, Y., WAN, J., YAN, T., XIONG, J. & TANG, X. 2018. Virtual stenting with simplex mesh and mechanical contact analysis for real-time planning of thoracic endovascular aortic repair. *Theranostics,* 8**,** 5758-5771.

CLEVELAND CLINIC. 2019. *Aorta Anatomy* [Online]. Available: https://my.clevelandclinic.org/health/articles/17058-aorta-anatomy [Accessed 01 February 2022].

CLOUSE, W. D., HALLETT, J. W., SCHAFF, H. V., SPITTELL, P. C., ROWLAND, C. M., ILSTRUP, D. M. & MELTON III, L. J. Acute aortic dissection: population-based incidence compared with degenerative aortic aneurysm rupture. Mayo Clinic Proceedings, 2004. Elsevier, 176-180.

COOK MEDICAL. 2019. *Zenith Dissection Graft Specifications and Components* [Online]. Available: https://www.cookmedical.com/data/resources/AI-D46657-EN-F_M3_1548273377837.pdf [Accessed April 21 2021].

COOK MEDICAL. 2021a. *Zenith Dissection* [Online]. Available: https://aortic.cookmedical.com/thoracic/ [Accessed 01 August 2021].

COOK MEDICAL. 2021b. *Zenith® TX2® Dissection Endovascular Graft* [Online]. Available: https://www.cookmedical.com/products/70594969-b346-46d6-aafe-4deb173e7ccd/ [Accessed 01 August 2021].

CZERNY, M., EGGEBRECHT, H., ROUSSEAU, H., MOUROZ, P. R., JANOSI, R.-A., LESCAN, M., SCHLENSAK, C., BÖCKLER, D., ANTE, M. & VDR WEIJDE, E. 2020. Distal stent graft–induced new entry after TEVAR or FET: insights into a new disease from EuREC. *The Annals of Thoracic Surgery,* 110**,** 1494-1500.

DAKE, M., THOMPSON, M., VAN SAMBEEK, M., VERMASSEN, F. & MORALES, J. 2013. DISSECT: a new mnemonic-based approach to the categorization of aortic dissection. *European Journal of Vascular and Endovascular Surgery,* 46**,** 175-190.

DAKE, M. D., KATO, N., MITCHELL, R. S., SEMBA, C. P., RAZAVI, M. K., SHIMONO, T., HIRANO, T., TAKEDA, K., YADA, I. & MILLER, D. C. 1999. Endovascular stent–graft placement for the treatment of acute aortic dissection. *New England Journal of Medicine,* 340**,** 1546-1552.

DE BOCK, S., IANNACCONE, F., DE SANTIS, G., DE BEULE, M., VAN LOO, D., DEVOS, D., VERMASSEN, F., SEGERS, P. & VERHEGGHE, B. 2012. Virtual evaluation of stent graft deployment: a validated modeling and simulation study. *J Mech Behav Biomed Mater,* 13**,** 129-39.

DELFINO, A., STERGIOPULOS, N., MOORE JR, J. & MEISTER, J.-J. 1997. Residual strain effects on the stress field in a thick wall finite element model of the human carotid bifurcation. *Journal of biomechanics,* 30**,** 777-786.

DEMANGET, N., AVRIL, S., BADEL, P., ORGEAS, L., GEINDREAU, C., ALBERTINI, J. N. & FAVRE, J. P. 2012. Computational comparison of the bending behavior of aortic stent-grafts. *J Mech Behav Biomed Mater,* 5**,** 272-82.

DEMANGET, N., DUPREY, A., BADEL, P., ORGÉAS, L., AVRIL, S., GEINDREAU, C., ALBERTINI, J.-N. & FAVRE, J.-P. 2013. Finite element analysis of the mechanical performances of 8 marketed aortic stent-grafts. *Journal of endovascular therapy,* 20**,** 523-535.

DEPLANO, V., BOUFI, M., GARIBOLDI, V., LOUNDOU, A. D., D'JOURNO, X. B., CAUTELA, J., DJEMLI, A. & ALIMI, Y. S. 2019. Mechanical characterisation of human ascending aorta dissection. *J Biomech,* 94**,** 138-146.

DERYCKE, L., PERRIN, D., COCHENNEC, F., ALBERTINI, J. N. & AVRIL, S. 2019. Predictive Numerical Simulations of Double Branch Stent-Graft Deployment in an Aortic Arch Aneurysm. *Ann Biomed Eng,* 47**,** 1051-1062.

DERYCKE, L., SENEMAUD, J., PERRIN, D., AVRIL, S., DESGRANGES, P., ALBERTINI, J. N., COCHENNEC, F. & HAULON, S. 2020. Patient Specific Computer Modelling for Automated Sizing of Fenestrated Stent Grafts. *Eur J Vasc Endovasc Surg,* 59**,** 237-246.

DESYATOVA, A., MACTAGGART, J. & KAMENSKIY, A. 2020. Effects of longitudinal pre-stretch on the mechanics of human aorta before and after thoracic endovascular aortic repair (TEVAR) in trauma patients. *Biomech Model Mechanobiol,* 19**,** 401-413.

DOBRIN, P., CANFIELD, T. & SINHA, S. 1975. Development of longitudina retraction of carotid arteries in neonatal dogs. *Experientia,* 31**,** 1295-1296.

DOBRIN, P. B., SCHWARCZ, T. H. & MRKVICKA, R. 1990. Longitudinal retractive force in pressurized dog and human arteries. *Journal of Surgical Research,* 48**,** 116-120.

DONG, Z., FU, W., WANG, Y., WANG, C., YAN, Z., GUO, D., XU, X. & CHEN, B. 2010. Stent graft-induced new entry after endovascular repair for Stanford type B aortic dissection. *J Vasc Surg,* 52**,** 1450-7.

DONG, Z. H., FU, W. G., WANG, Y. Q., GUO, D. Q., XU, X., JI, Y., CHEN, B., JIANG, J. H., YANG, J., SHI, Z. Y., ZHU, T. & SHI, Y. 2009. Retrograde type A aortic dissection after endovascular stent graft placement for treatment of type B dissection. *Circulation,* 119**,** 735-41.

DUERIG, T., PELTON, A. & STÖCKEL, D. 1999. An overview of nitinol medical applications. *Materials Science and Engineering: A,* 273**,** 149-160.

FARBER, M. A., GIGLIA, J. S., STARNES, B. W., STEVENS, S. L., HOLLEMAN, J., CHAER, R., MATSUMURA, J. S. & INVESTIGATORS, T.-C. T. 2013. Evaluation of the redesigned conformable GORE TAG thoracic endoprosthesis for traumatic aortic transection. *Journal of vascular surgery,* 58**,** 651-658.

FATTORI, R., MONTGOMERY, D., LOVATO, L., KISCHE, S., DI EUSANIO, M., INCE, H., EAGLE, K. A., ISSELBACHER, E. M. & NIENABER, C. A. 2013. Survival after endovascular therapy in patients with type B aortic dissection: a report from the International Registry of Acute Aortic Dissection (IRAD). *JACC Cardiovasc Interv,* 6**,** 876-82.

FUNG, Y.-C. 1993. *Mechanical properties of living tissues*, Springer.

FUNG, Y. 1984. What principle governs the stress distribution in living organs? *Biomechanics in China, Japan and USA***,** 1-13.

FUNG, Y. & LIU, S. 1989. Change of residual strains in arteries due to hypertrophy caused by aortic constriction. *Circulation research,* 65**,** 1340-1349.

FUNG, Y. C. 1991. What are the residual stresses doing in our blood vessels? *Annals of biomedical engineering,* 19**,** 237-249.

GARCIA-HERRERA, C. M., CELENTANO, D. J., CRUCHAGA, M. A., ROJO, F. J., ATIENZA, J. M., GUINEA, G. V. & GOICOLEA, J. M. 2012. Mechanical characterisation of the human thoracic descending aorta: experiments and modelling. *Comput Methods Biomech Biomed Engin,* 15**,** 185-93.

GEE, M. W., FÖRSTER, C. & WALL, W. A. 2010. A computational strategy for prestressing patient-specific biomechanical problems under finite deformation. *International Journal for Numerical Methods in Biomedical Engineering,* 26**,** 52-72.

GEE, M. W., REEPS, C., ECKSTEIN, H. H. & WALL, W. A. 2009. Prestressing in finite deformation abdominal aortic aneurysm simulation. *J Biomech,* 42**,** 1732-9.

GHRIALLAIS, R. N. & BRUZZI, M. 2014. Self-expanding stent modelling and radial force accuracy. *Computer methods in biomechanics and biomedical engineering,* 17**,** 318-333.

GOLLEDGE, J. & EAGLE, K. A. 2008. Acute aortic dissection. *The Lancet,* 372**,** 55-66.

GORE MEDICAL. 2021. *GORE® TAG® Conformable Thoracic Stent Graft with ACTIVE CONTROL System* [Online]. Available: https://www.goremedical.com/eu/products/ctagac [Accessed 01 August 2021].

GROENINK, M., LANGERAK, S. E., VANBAVEL, E., VAN DER WALL, E. E., MULDER, B. J., VAN DER WAL, A. C. & SPAAN, J. A. 1999. The influence of aging and aortic stiffness on permanent dilation and breaking stress of the thoracic descending aorta. *Cardiovascular research,* 43**,** 471-480.

GRYTSAN, A., WATTON, P. N. & HOLZAPFEL, G. A. 2015. A thick-walled fluid–solid-growth model of abdominal aortic aneurysm evolution: application to a patient-specific geometry. *Journal of biomechanical engineering,* 137**,** 031008.

GUINEA, G. V., ATIENZA, J. M., ROJO, F. J., GARCÍA-HERRERA, C. M., YIQUN, L., CLAES, E., GOICOLEA, J. M., GARCÍA-MONTERO, C., BURGOS, R. L. & GOICOLEA, F. J. 2010. Factors influencing the mechanical behaviour of healthy human descending thoracic aorta. *Physiological measurement,* 31**,** 1553.

HAGAN, P. G., NIENABER, C. A., ISSELBACHER, E. M., BRUCKMAN, D., KARAVITE, D. J., RUSSMAN, P. L., EVANGELISTA, A., FATTORI, R., SUZUKI, T. & OH, J. K. 2000. The

International Registry of Acute Aortic Dissection (IRAD): new insights into an old disease. *Jama,* 283**,** 897-903.

HAGER, A., KAEMMERER, H., RAPP-BERNHARDT, U., BLÜCHER, S., RAPP, K., BERNHARDT, T. M., GALANSKI, M. & HESS, J. 2002. Diameters of the thoracic aorta throughout life as measured with helical computed tomography. *The Journal of thoracic and cardiovascular surgery,* 123**,** 1060-1066.

HEMMLER, A., LUTZ, B., KALENDER, G., REEPS, C. & GEE, M. W. 2019a. Patient-specific in silico endovascular repair of abdominal aortic aneurysms: application and validation. *Biomech Model Mechanobiol,* 18**,** 983-1004.

HEMMLER, A., LUTZ, B., REEPS, C. & GEE, M. W. 2019b. In silico study of vessel and stent-graft parameters on the potential success of endovascular aneurysm repair. *Int J Numer Method Biomed Eng,* 35**,** e3237.

HOLZAPFEL, A. G. 2000. Nonlinear Solid Mechanics II.

HOLZAPFEL, G. A. 2006. Determination of material models for arterial walls from uniaxial extension tests and histological structure. *J Theor Biol,* 238**,** 290-302.

HOLZAPFEL, G. A., GASSER, T. C. & OGDEN, R. W. 2000. A new constitutive framework for arterial wall mechanics and a comparative study of material models. *Journal of elasticity and the physical science of solids,* 61**,** 1-48.

HOLZAPFEL, G. A. & OGDEN, R. W. 2015. On the tension–compression switch in soft fibrous solids. *European Journal of Mechanics-A/Solids,* 49**,** 561-569.

HOLZAPFEL, G. A., OGDEN, R. W. & SHERIFOVA, S. 2019. On fibre dispersion modelling of soft biological tissues: a review. *Proceedings of the Royal Society A,* 475**,** 20180736.

HOLZAPFEL, G. A., SOMMER, G., AUER, M., REGITNIG, P. & OGDEN, R. W. 2007. Layer-specific 3D residual deformations of human aortas with non-atherosclerotic intimal thickening. *Ann Biomed Eng,* 35**,** 530-45.

HOWARD, D. P., BANERJEE, A., FAIRHEAD, J. F., PERKINS, J., SILVER, L. E., ROTHWELL, P. M. & OXFORD VASCULAR, S. 2013. Population-based study of incidence and outcome of acute aortic dissection and premorbid risk factor control: 10-year results from the Oxford Vascular Study. *Circulation,* 127**,** 2031-7.

HUANG, C.-Y., HSU, H.-L., CHEN, P.-L., CHEN, I.-M., HSU, C.-P. & SHIH, C.-C. 2018. The impact of distal stent graft–induced new entry on aortic remodeling of chronic type B dissection. *The Annals of thoracic surgery,* 105**,** 785-793.

HUGHES, G. C. 2015. Management of acute type B aortic dissection; ADSORB trial. *The Journal of thoracic and cardiovascular surgery,* 149**,** S158-S162.

HUMPHREY, J. D. 1995. Mechanics of the arterial wall: review and directions. *Critical Reviews™ in Biomedical Engineering,* 23.

HUMPHREY, J. D., EBERTH, J. F., DYE, W. W. & GLEASON, R. L. 2009. Fundamental role of axial stress in compensatory adaptations by arteries. *J Biomech,* 42**,** 1-8.

HUMPHREY, J. D. & HOLZAPFEL, G. A. 2012. Mechanics, mechanobiology, and modeling of human abdominal aorta and aneurysms. *Journal of biomechanics,* 45**,** 805-814.

INSTITUTE FOR QUALITY AND EFFICIENCY IN HEALTH CARE. 2019. *'How does the blood circulatory system work?'* [Online]. Available: https://www.ncbi.nlm.nih.gov/books/NBK279250/ [Accessed 01 February 2022].

JANG, H., KIM, M. D., KIM, G. M., WON, J. Y., KO, Y. G., CHOI, D., JOO, H. C. & LEE, D. Y. 2017. Risk factors for stent graft-induced new entry after thoracic endovascular aortic repair for Stanford type B aortic dissection. *J Vasc Surg,* 65**,** 676-685.

JOHNS HOPKINS MEDICINE. 2021. *Aortic Dissection Repair* [Online]. Available: https://www.hopkinsmedicine.org/health/treatment-tests-and-therapies/-/media/ksw-images/pcardio20140403v0006300x300.ashx [Accessed 01 August 2021].

KAS'YANOV, V. 1974. A nisotropic nonlinear-elastic model of the large human blood vessels. *Polymer Mechanics,* 10**,** 756-764.

KLEINSTREUER, C., LI, Z., BASCIANO, C., SEELECKE, S. & FARBER, M. 2008. Computational mechanics of Nitinol stent grafts. *Journal of biomechanics,* 41**,** 2370-2378.

LAENNEC, R. T. H. 1819. *De l'auscultation médiate: ou traité du diagnostic des maladies des poumons et du coeur*, Brosson et Chaudé.

LI, Q., MA, W.-G., ZHENG, J., XU, S.-D., CHEN, Y., LIU, Y.-M., ZHU, J.-M., HUANG, L.-J. & SUN, L.-Z. 2019. Distal stent graft-induced new entry after TEVAR of type B aortic dissection: experience in 15 years. *The Annals of Thoracic Surgery,* 107**,** 718-724.

LI, Q., WANG, L. F., MA, W. G., XU, S. D., ZHENG, J., XING, X. Y., HUANG, L. J. & SUN, L. Z. 2015. Risk factors for distal stent graft-induced new entry following endovascular repair of type B aortic dissection. *J Thorac Dis,* 7**,** 1907-16.

LU, J., ZHOU, X. & RAGHAVAN, M. L. 2007. Inverse elastostatic stress analysis in pre-deformed biological structures: Demonstration using abdominal aortic aneurysms. *J Biomech,* 40**,** 693-6.

LU, Q., FENG, J., ZHOU, J., ZHAO, Z., BAO, J., FENG, R., YUAN, L., FENG, X., QU, L. & PEI, Y. 2013. Endovascular repair of ascending aortic dissection: a novel treatment option for patients judged unfit for direct surgical repair. *Journal of the American College of Cardiology,* 61**,** 1917-1924.

LYU, T., YANG, G., ZHAO, X., SHU, H., LUO, L., CHEN, D., XIONG, J., YANG, J., LI, S. & COATRIEUX, J.-L. 2021. Dissected aorta segmentation using convolutional neural networks. *Computer Methods and Programs in Biomedicine,* 211**,** 106417.

MA, T., DONG, Z. H., FU, W. G., GUO, D. Q., XU, X., CHEN, B., JIANG, J. H., YANG, J., SHI, Z. Y., ZHU, T., SHI, Y., JIANG, B. H. & XU, X. Y. 2017. Incidence and risk factors for retrograde type A dissection and stent graft-induced new entry after thoracic endovascular aortic repair. *J Vasc Surg*.

MA, T., DONG, Z. H., WANG, S., MENG, Z. Y., CHEN, Y. Y. & FU, W. G. 2018. Computational investigation of interaction between stent graft and aorta in retrograde type A dissection after thoracic endovascular aortic repair for type B aortic dissection. *J Vasc Surg,* 68**,** 14S-21S e2.

MEDTRONIC. 2021. *Medtronic Valiant Thoracic Stent Graft with the Captivia Delivery System* [Online]. Available: https://europe.medtronic.com/xd-en/healthcare-professionals/products/cardiovascular/aortic-stent-grafts/valiant-thoracic-stent-graft-with-captivia-delivery-system.html [Accessed 01 August 2021].

MENG, Z., MA, T., CAI, Y., LIU, X., WANG, S., DONG, Z. & FU, W. 2020. Numerical modeling and simulations of type B aortic dissection treated by stent-grafts with different oversizing ratios. *Artif Organs*.

MENICHINI, C., CHENG, Z., GIBBS, R. G. & XU, X. Y. 2016. Predicting false lumen thrombosis in patient-specific models of aortic dissection. *Journal of The Royal Society Interface,* 13**,** 20160759.

MENICHINI, C., PIROLA, S., GUO, B., FU, W., DONG, Z. & XU, X. Y. 2018. High Wall Stress May Predict the Formation of Stent-Graft-Induced New Entries After Thoracic Endovascular Aortic Repair. *J Endovasc Ther,* 25**,** 571-577.

MENSEL, B., QUADRAT, A., SCHNEIDER, T., KÜHN, J.-P., DÖRR, M., VÖLZKE, H., LIEB, W., HEGENSCHEID, K. & LORBEER, R. 2014. MRI-based determination of reference values of thoracic aortic wall thickness in a general population. *European radiology,* 24**,** 2038-2044.

MILLER, D. C., STINSON, E. B., OYER, P. E., ROSSITER, S. J., REITZ, B. A., GRIEPP, R. B. & SHUMWAY, N. E. 1979. Operative treatment of aortic dissections: experience with 125 patients over a sixteen-year period. *The Journal of thoracic and cardiovascular surgery,* 78**,** 365-382.

MOHAN, D. & MELVIN, J. W. 1982. Failure properties of passive human aortic tissue. I—uniaxial tension tests. *Journal of biomechanics,* 15**,** 887-902.

MOONEY, M. 1940. A theory of large elastic deformation. *Journal of applied physics,* 11**,** 582-592.

MORGAGNI, G. 1761. *De sedibus et causis morborum*.

NAUTA, F. J., CONTI, M., KAMMAN, A. V., VAN BOGERIJEN, G. H., TOLENAAR, J. L., AURICCHIO, F., FIGUEROA, C. A., VAN HERWAARDEN, J. A., MOLL, F. L. & TRIMARCHI, S. 2015. Biomechanical Changes After Thoracic Endovascular Aortic Repair in Type B Dissection: A Systematic Review. *J Endovasc Ther,* 22**,** 918-33.

NICHOLLS, F. & PARKER, G. 1761. LI. Observations concerning the body of his late Majesty, October 26, 1760. *Philosophical Transactions of the Royal Society of London***,** 265-275.

NIENABER, C. A. & CLOUGH, R. E. 2015. Management of acute aortic dissection. *The Lancet,* 385**,** 800-811.

NIENABER, C. A., CLOUGH, R. E., SAKALIHASAN, N., SUZUKI, T., GIBBS, R., MUSSA, F., JENKINS, M. P., THOMPSON, M. M., EVANGELISTA, A. & YEH, J. S. 2016. Aortic dissection. *Nature Reviews Disease Primers,* 2**,** 16053.

NIENABER, C. A., FATTORI, R., LUND, G., DIECKMANN, C., WOLF, W., VON KODOLITSCH, Y., NICOLAS, V. & PIERANGELI, A. 1999. Nonsurgical reconstruction of thoracic aortic dissection by stent–graft placement. *New England Journal of Medicine,* 340**,** 1539-1545.

NIENABER, C. A., KISCHE, S. & INCE, H. 2007. Thoracic aortic stent-graft devices: problems, failure modes, and applicability. *Semin Vasc Surg,* 20**,** 81-9.

NIENABER, C. A., KISCHE, S., ROUSSEAU, H., EGGEBRECHT, H., REHDERS, T. C., KUNDT, G., GLASS, A., SCHEINERT, D., CZERNY, M., KLEINFELDT, T., ZIPFEL, B., LABROUSSE, L., FATTORI, R., INCE, H. & TRIAL, I.-X. 2013. Endovascular repair of type B aortic dissection: long-term results of the randomized investigation of stent grafts in aortic dissection trial. *Circ Cardiovasc Interv,* 6**,** 407-16.

NIENABER, C. A., ROUSSEAU, H., EGGEBRECHT, H., KISCHE, S., FATTORI, R., REHDERS, T. C., KUNDT, G. N., SCHEINERT, D., CZERNY, M. & KLEINFELDT, T. 2009. Randomized comparison of strategies for type B aortic dissection: the INvestigation of STEnt Grafts in Aortic Dissection (INSTEAD) trial. *Circulation,* 120**,** 2519-2528.

NIENABER, C. A., SAKALIHASAN, N., CLOUGH, R. E., ABOUKOURA, M., MANCUSO, E., YEH, J. S., DEFRAIGNE, J. O., CHESHIRE, N., ROSENDAHL, U. P., QUARTO, C. & PEPPER, J. 2017. Thoracic endovascular aortic repair (TEVAR) in proximal (type A) aortic dissection: Ready for a broader application? *J Thorac Cardiovasc Surg,* 153**,** S3-S11.

NIENABER, C. A., ZANNETTI, S., BARBIERI, B., KISCHE, S., SCHARECK, W. & REHDERS, T. C. 2005. INvestigation of STEnt grafts in patients with type B Aortic Dissection: design of the INSTEAD trial—a prospective, multicenter, European randomized trial. *American heart journal,* 149**,** 592-599.

OGDEN, R. W. 1972. Large deformation isotropic elasticity–on the correlation of theory and experiment for incompressible rubberlike solids. *Proc. R. Soc. Lond. A,* 326**,** 565-584.

OLSSON, C., THELIN, S., STAHLE, E., EKBOM, A. & GRANATH, F. 2006. Thoracic aortic aneurysm and dissection: increasing prevalence and improved outcomes reported in a nationwide population-based study of more than 14,000 cases from 1987 to 2002. *Circulation,* 114**,** 2611-8.

PAPE, L. A., AWAIS, M., WOZNICKI, E. M., SUZUKI, T., TRIMARCHI, S., EVANGELISTA, A., MYRMEL, T., LARSEN, M., HARRIS, K. M., GREASON, K., DI EUSANIO, M., BOSSONE, E., MONTGOMERY, D. G., EAGLE, K. A., NIENABER, C. A., ISSELBACHER, E. M. & O'GARA, P. 2015. Presentation, Diagnosis, and Outcomes of Acute Aortic Dissection: 17-Year Trends From the International Registry of Acute Aortic Dissection. *J Am Coll Cardiol,* 66**,** 350-8.

PELTON, A., SCHROEDER, V., MITCHELL, M., GONG, X.-Y., BARNEY, M. & ROBERTSON, S. 2008. Fatigue and durability of Nitinol stents. *Journal of the mechanical behavior of biomedical materials,* 1**,** 153-164.

PEREJDA, A. J., ABRAHAM, P., CARNES, W. H., COULSON, W. F. & UITTO, J. 1985. Marfan's syndrome: structural, biochemical, and mechanical studies of the aortic media. *The Journal of laboratory and clinical medicine,* 106**,** 369-375.

PERRIN, D., BADEL, P., ORGEAS, L., GEINDREAU, C., DU ROSCOAT, S. R., ALBERTINI, J. N. & AVRIL, S. 2016. Patient-specific simulation of endovascular repair surgery with tortuous aneurysms requiring flexible stent-grafts. *J Mech Behav Biomed Mater,* 63**,** 86-99.

PERRIN, D., BADEL, P., ORGEAS, L., GEINDREAU, C., DUMENIL, A., ALBERTINI, J. N. & AVRIL, S. 2015a. Patient-specific numerical simulation of stent-graft deployment: Validation on three clinical cases. *J Biomech,* 48**,** 1868-75.

PERRIN, D., DEMANGET, N., BADEL, P., AVRIL, S., ORGEAS, L., GEINDREAU, C. & ALBERTINI, J. N. 2015b. Deployment of stent grafts in curved aneurysmal arteries: toward a predictive numerical tool. *Int J Numer Method Biomed Eng,* 31**,** e02698.

PETERSS, S., MANSOUR, A. M., ROSS, J. A., VAITKEVICIUTE, I., CHARILAOU, P., DUMFARTH, J., FANG, H., ZIGANSHIN, B. A., RIZZO, J. A., ADENIRAN, A. J. & ELEFTERIADES, J. A. 2016. Changing Pathology of the Thoracic Aorta From Acute to Chronic Dissection: Literature Review and Insights. *J Am Coll Cardiol,* 68**,** 1054-65.

PIROLA, S., GUO, B., MENICHINI, C., SAITTA, S., FU, W., DONG, Z. & XU, X. Y. 2019. 4-D flow MRI-based computational analysis of blood flow in patient-specific aortic dissection. *IEEE Transactions on Biomedical Engineering,* 66**,** 3411-3419.

RAGHAVAN, M. & VORP, D. A. 2000. Toward a biomechanical tool to evaluate rupture potential of abdominal aortic aneurysm: identification of a finite strain constitutive model and evaluation of its applicability. *Journal of biomechanics,* 33**,** 475-482.

RHODIN, J. A. 1980. Architecture of the vessel wall. *Vascular smooth muscle***,** 1-31.

RICHENS, D., KOTIDIS, K., NEALE, M., OAKLEY, C. & FAILS, A. 2003. Rupture of the aorta following road traffic accidents in the United Kingdom 1992–1999. The results of the

co-operative crash injury study. *European journal of cardio-thoracic surgery,* 23**,** 143-148.

RIVLIN, R. S. 1948. Large elastic deformations of isotropic materials IV. Further developments of the general theory. *Philosophical Transactions of the Royal Society of London. Series A, Mathematical and Physical Sciences,* 241**,** 379-397.

ROMAROWSKI, R. M., CONTI, M., MORGANTI, S., GRASSI, V., MARROCCO-TRISCHITTA, M. M., TRIMARCHI, S. & AURICCHIO, F. 2018. Computational simulation of TEVAR in the ascending aorta for optimal endograft selection: A patient-specific case study. *Comput Biol Med,* 103**,** 140-147.

ROMAROWSKI, R. M., FAGGIANO, E., CONTI, M., REALI, A., MORGANTI, S. & AURICCHIO, F. 2019. A novel computational framework to predict patient-specific hemodynamics after TEVAR: Integration of structural and fluid-dynamics analysis by image elaboration. *Computers & Fluids,* 179**,** 806-819.

ROY, D., HOLZAPFEL, G. A., KAUFFMANN, C. & SOULEZ, G. 2014. Finite element analysis of abdominal aortic aneurysms: geometrical and structural reconstruction with application of an anisotropic material model. *IMA Journal of Applied Mathematics,* 79**,** 1011-1026.

SALMASI, M. Y., PIROLA, S., SASIDHARAN, S., FISICHELLA, S. M., REDAELLI, A., JARRAL, O. A., O'REGAN, D. P., OO, A. Y., MOORE, J. E., XU, X. Y. & ATHANASIOU, T. 2021. High Wall Shear Stress can Predict Wall Degradation in Ascending Aortic Aneurysms: An Integrated Biomechanics Study. *Frontiers in Bioengineering and Biotechnology,* 9.

SASSANI, S. G., KAKISIS, J., TSANGARIS, S. & SOKOLIS, D. P. 2015a. Layer-dependent wall properties of abdominal aortic aneurysms: Experimental study and material characterization. *J Mech Behav Biomed Mater,* 49**,** 141-61.

SASSANI, S. G., TSANGARIS, S. & SOKOLIS, D. P. 2015b. Layer- and region-specific material characterization of ascending thoracic aortic aneurysms by microstructure-based models. *J Biomech,* 48**,** 3757-65.

SCHIELD, R. T. 1967. Inverse deformation results in finite elasticity. *Zeitschrift für angewandte Mathematik und Physik ZAMP,* 18**,** 490-500.

SCHLATMANN, T. J. & BECKER, A. E. 1977. Histologic changes in the normal aging aorta: implications for dissecting aortic aneurysm. *The American journal of cardiology,* 39**,** 13-20.

SCHRIEFL, A. J., ZEINDLINGER, G., PIERCE, D. M., REGITNIG, P. & HOLZAPFEL, G. A. 2012. Determination of the layer-specific distributed collagen fibre orientations in human thoracic and abdominal aortas and common iliac arteries. *J R Soc Interface,* 9**,** 1275-86.

SINGH, S., XU, X., PEPPER, J., IZGI, C., TREASURE, T. & MOHIADDIN, R. 2016. Effects of aortic root motion on wall stress in the Marfan aorta before and after personalised aortic root support (PEARS) surgery. *Journal of biomechanics,* 49**,** 2076-2084.

SOKOLIS, D. P., KRITHARIS, E. P., GIAGINI, A. T., LAMPROPOULOS, K. M., PAPADODIMA, S. A. & ILIOPOULOS, D. C. 2012a. Biomechanical response of ascending thoracic aortic aneurysms: association with structural remodelling. *Comput Methods Biomech Biomed Engin,* 15**,** 231-48.

SOKOLIS, D. P., KRITHARIS, E. P. & ILIOPOULOS, D. C. 2012b. Effect of layer heterogeneity on the biomechanical properties of ascending thoracic aortic aneurysms. *Medical & biological engineering & computing,* 50**,** 1227-1237.

SOMMER, G., SHERIFOVA, S., OBERWALDER, P. J., DAPUNT, O. E., URSOMANNO, P. A., DEANDA, A., GRIFFITH, B. E. & HOLZAPFEL, G. A. 2016. Mechanical strength of aneurysmatic and dissected human thoracic aortas at different shear loading modes. *Journal of biomechanics,* 49**,** 2374-2382.

SULEJMANI, F., POKUTTA-PASKALEVA, A., ZIGANSHIN, B., LESHNOWER, B., IANNUCCI, G., ELEFTERIADES, J. & SUN, W. 2017. Biomechanical properties of the thoracic aorta in Marfan patients. *Annals of cardiothoracic surgery,* 6**,** 610.

TABER, L. A. & HUMPHREY, J. D. 2001. Stress-modulated growth, residual stress, and vascular heterogeneity. *J. Biomech. Eng.,* 123**,** 528-535.

TAN, W. T., LIEW, Y. M., MOHAMED MOKHTARUDIN, M. J., PIROLA, S., WAN AB NAIM, W. N., AMRY HASHIM, S., XU, X. Y. & LIM, E. 2021. Effect of Vessel Tortuosity on Stress Concentration at The Distal Stent-Vessel Interface: Possible Link With New Entry Formation Through Biomechanical Simulation. *J Biomech Eng*.

TENG, Z., FENG, J., ZHANG, Y., HUANG, Y., SUTCLIFFE, M. P., BROWN, A. J., JING, Z., GILLARD, J. H. & LU, Q. 2015. Layer-and direction-specific material properties, extreme extensibility and ultimate material strength of human abdominal aorta and aneurysm: a uniaxial extension study. *Annals of biomedical engineering,* 43**,** 2745-2759.

TICKNER, E. G. & SACKS, A. H. 1967. A theory for the static elastic behavior of blood vessels. *Biorheology,* 4**,** 151-168.

TONG, J., CHENG, Y. & HOLZAPFEL, G. A. 2016. Mechanical assessment of arterial dissection in health and disease: Advancements and challenges. *J Biomech,* 49**,** 2366-73.

TONG, J., SCHRIEFL, A. J., COHNERT, T. & HOLZAPFEL, G. A. 2013. Gender differences in biomechanical properties, thrombus age, mass fraction and clinical factors of abdominal aortic aneurysms. *European Journal of Vascular and Endovascular Surgery,* 45**,** 364-372.

TRELOAR, L. 1943. The elasticity of a network of long-chain molecules—II. *Transactions of the Faraday Society,* 39**,** 241-246.

TSAMIS, A., KRAWIEC, J. T. & VORP, D. A. 2013. Elastin and collagen fibre microstructure of the human aorta in ageing and disease: a review. *Journal of the Royal Society Interface,* 10**,** 20121004.

UEDA, T., FLEISCHMANN, D., DAKE, M. D., RUBIN, G. D. & SZE, D. Y. 2010. Incomplete endograft apposition to the aortic arch: bird-beak configuration increases risk of endoleak formation after thoracic endovascular aortic repair. *Radiology,* 255**,** 645-652.

VAD, S., ESKINAZI, A., CORBETT, T., MCGLOUGHLIN, T. & VANDE GEEST, J. P. 2010. Determination of coefficient of friction for self-expanding stent-grafts. *J Biomech Eng,* 132**,** 121007.

VANDE GEEST, J. P., DILLAVOU, E. D., DI MARTINO, E. S., OBERDIER, M., BOHRA, A., MAKAROUN, M. S. & VORP, D. A. 2006. Gender-Related Differences in the Tensile Strength of Abdominal Aortic Aneurysm. *Annals of the New York Academy of Sciences,* 1085**,** 400-402.

VORP, D. A. 2007. Biomechanics of abdominal aortic aneurysm. *J Biomech,* 40**,** 1887-902.

VORP, D. A., SCHIRO, B. J., EHRLICH, M. P., JUVONEN, T. S., ERGIN, M. A. & GRIFFITH, B. P. 2003. Effect of aneurysm on the tensile strength and biomechanical behavior of the ascending thoracic aorta. *The Annals of Thoracic Surgery,* 75**,** 1210-1214.

VOTTA, E., PRESICCE, M., DELLA CORTE, A., DELLEGROTTAGLIE, S., BANCONE, C., STURLA, F. & REDAELLI, A. 2017. A novel approach to the quantification of aortic root in vivo structural mechanics. *Int J Numer Method Biomed Eng,* 33.

WANG, S., TOKGOZ, A., HUANG, Y., ZHANG, Y., FENG, J., SASTRY, P., SUN, C., FIGG, N., LU, Q. & SUTCLIFFE, M. P. 2019. Bayesian Inference-Based Estimation of Normal Aortic, Aneurysmal and Atherosclerotic Tissue Mechanical Properties: From Material Testing, Modeling and Histology. *IEEE Transactions on Biomedical Engineering,* 66**,** 2269-2278.

WEISBECKER, H., PIERCE, D. M., REGITNIG, P. & HOLZAPFEL, G. A. 2012. Layer-specific damage experiments and modeling of human thoracic and abdominal aortas with non-atherosclerotic intimal thickening. *J Mech Behav Biomed Mater,* 12**,** 93-106.

XIANG, D., KAN, X., LIANG, H., XIONG, B., LIANG, B., WANG, L. & ZHENG, C. 2019. Comparison of mid-term outcomes of endovascular repair and medical management in patients with acute uncomplicated type B aortic dissection. *The Journal of thoracic and cardiovascular surgery*.

XU, H., XIONG, J., HAN, X., MEI, Y., SHI, Y., WANG, D., ZHANG, M. & CHEN, D. 2021. Computed tomography-based hemodynamic index for aortic dissection. *The Journal of thoracic and cardiovascular surgery,* 162**,** e165-e176.

YEOH, O. H. 1993. Some forms of the strain energy function for rubber. *Rubber Chemistry and technology,* 66**,** 754-771.

YUAN, X., KAN, X., XU, X. Y. & NIENABER, C. 2021a. IDENTIFYING AND QUANTIFYING THE 4D MOTION OF AORTIC ROOT. *Journal of the American College of Cardiology,* 77**,** 1832-1832.

YUAN, X., MITSIS, A., MOZALBAT, D. & NIENABER, C. A. 2021b. Alternative management of proximal aortic dissection: concept and application. *Indian Journal of Thoracic and Cardiovascular Surgery***,** 1-10.

ZHOU, X.-C., YANG, F., GONG, X.-Y., ZHAO, M., ZHENG, Y.-F. & SUN, Z.-L. 2019. New nitinol endovascular stent-graft system for abdominal aortic aneurysm with finite element analysis and experimental verification. *Rare Metals,* 38**,** 495-502.

Apendix A

Analysis of inter-observer error in image segmentation

As described in Chapter 3, the segmentation of pre- and post-TEVAR CTA images involves manual operations to adjust the raw segmentation masks. Pre- and post-TEVAR CTA scans from one complicated type B aortic dissection patient who underwent TEVAR were analysed by two independent observers. Both observers followed the same segmentation protocol, including threshold setting, mask cropping, mask splitting and region growing. Manual adjustment of the masks was performed independently. Inter-observer errors were assessed by making slice-by-slice comparisons of the segmentation masks obtained by the two observers. Inter-observer differences were calculated based on the segmentation area on each slice:

$$Difference^i = \left| \frac{S_{ob1}^i - S_{ob2}^i}{S_{ob1}^i} \right| \times 100\%$$

where S_{ob1}^i is the segmentation area of the i th slice by observer 1, while S_{ob2}^i is the segmentation area of the ith slice by observer 2. The results for inter-observer errors are shown in Figure A.1, where the difference between two observers was 1.92 ± 1.26% for pre-TEVAR segmentation and 0.93 ± 1.31% for post-TEVAR segmentation based on one patient.

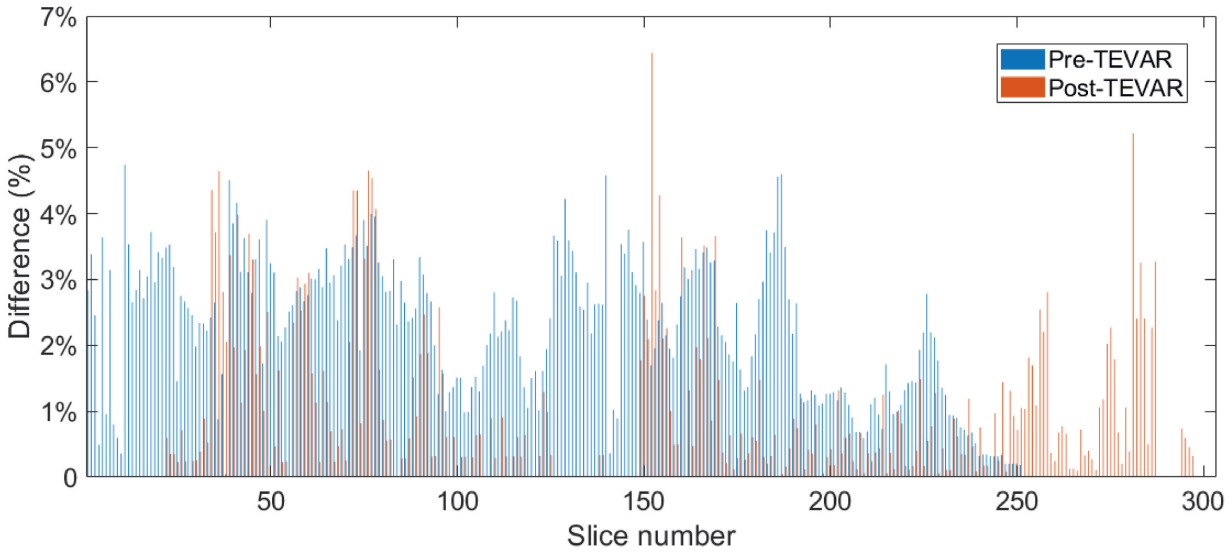


Figure A.1 Inter-observer error in the segmentation on each slice of pre- and post-TEVAR CTA images from one type B aortic dissection patient.

Apendix B

Mesh Sensitivity Test

B.1 Finite element mesh for the aortic wall

Five sets of finite element meshes (M1-M5) with the maximum mesh element size varying between 0.6 mm to 1.5 mm were generated for each patient-specific aortic dissection geometry. The same maximum element size was set for both the aortic wall and intimal flap, and these two parts were combined, so the total element number included both the aortic wall and intimal flap mesh. Table B.1 provides information on the five meshes generated for the patient-specific type B aortic dissection geometry presented in Chapter 4. Similar to the pre-stress procedure described in Chapter 3 (Section 3.8.1), finite element simulations were performed with a uniform internal pressure (gradually increased from 0 to 80 mmHg) normal to the internal surface of the aorta. The mean and maximum values of von Mises stress (VMS) and maximum principal logarithmic strain (MLE) obtained with the five meshes are summarised in Table B.2. Quantitative comparisons of the mean and maximum values of VMS and MLE between M1/M2, M2/M3, M3/M4 and M4/M5 are summarised in Table B.3. Mesh M4 was chosen for the aortic dissection geometry presented in this thesis.

Table B.1 Maximum element size and total element number for the five patient-specific type B aortic dissection meshes (M1-M5).

	Maximum element size (mm)	Total element number
M1	1.5	205,942
M2	1.25	403,558
M3	1.0	633,797
M4	0.75	1,128,804
M5	0.6	1,715,417

Table B.2 Maximum and mean values of von Mises stress (VMS) and the maximum principal logarithmic strain (MLE) obtained with the five aortic dissection meshes (M1-M5).

	Max VMS (KPa)	Mean VMS (KPa)	Max MLE	Mean MLE
M1	474.33	114.09	0.494	0.239
M2	422.33	116.14	0.509	0.242
M3	432.95	114.87	0.596	0.240
M4	442.10	115.36	0.609	0.242
M5	449.88	113.98	0.617	0.244

Table B.3 Quantitative comparison of the maximum and mean von Mises stress (VMS) and the maximum principal logarithmic strain (MLE) between M1/M2, M2/M3, M3/M4 and M4/M5.

	Max VMS difference (%)	Mean VMS difference (%)	Max MLE difference (%)	Mean MLE difference (%)
M1/M2	11.0%	1.8%	3.0%	1.3%
M2/M3	2.5%	1.1%	17.1%	0.8%
M3/M4	2.1%	0.4%	2.2%	0.8%
M4/M5	1.8%	1.2%	1.3%	0.8%

B.2 Finite element mesh for the stent-graft

Five sets of finite element meshes (M1-M5) with the maximum element size varying between 1 mm and 3 mm were created for Medtronic Valiant 28-28-150 mm stent-graft (SG) (Table B.4). Finite element simulations of SG crimping (from a stress-free state to a crimped state by using a virtual sheath) were performed on each mesh. The mean and maximum values of von Mises stress (VMS) and maximum principal logarithmic strain (MLE) obtained with the five meshes are summarised in Table B.5. Differences in the mean and maximum values of VMS and MLE between M1/M2, M2/M3, M3/M4 and M4/M5 are summarised in Table B.6. Mesh M4 was chosen for the SG model used in this thesis.

Table B.4 Maximum element size and total element number for the five stent-graft (SG) meshes (M1-M5).

	Maximum element size (mm)	Total element number
M1	3.0	221,088
M2	2.5	245,704
M3	2.0	327,072
M4	1.5	425,756
M5	1.0	509,172

Table B.5 Maximum and mean values of von Mises stress (VMS) and the maximum principal logarithmic strain (MLE) obtained with the five stent-graft (SG) meshes (M1-M5).

	Max VMS (MPa)	Mean VMS (MPa)	Max MLE	Mean MLE
M1	840.68	210.76	0.019	0.003
M2	806.66	213.86	0.02	0.003
M3	1009.81	249.14	0.026	0.004
M4	1015.16	247.7	0.027	0.004
M5	1018.58	251.3	0.027	0.004

Table B.6 Quantitative comparison of the maximum and mean von Mises stress (VMS) and the maximum principal logarithmic strain (MLE) between M1/M2, M2/M3, M3/M4 and M4/M5.

	Max VMS difference (%)	Mean VMS difference (%)	Max MLE difference (%)	Mean MLE difference (%)
M1/M2	4.2%	1.4%	1.9%	1.4%
M2/M3	20.1%	14.2%	22.8%	18.9%
M3/M4	0.5%	0.6%	3.7%	1.0%
M4/M5	0.3%	1.4%	1.4%	0.6%

Apendix C

Publications and Conferences

C.1 Peer-Reviewed Publications

Kan, X., Ma, T., Lin, J., Wang, L., Dong, Z. and Xu, X.Y., 2021. Patient-specific simulation of stent-graft deployment in type B aortic dissection: Model development and validation. *Biomechanics and Modeling in Mechanobiology*, *20*(6), pp.2247-2258.

Kan, X., Ma, T., Dong, Z. and Xu, X.Y., 2021. Patient-Specific Virtual Stent-Graft Deployment for Type B Aortic Dissection: A Pilot Study of the Impact of Stent-Graft Length. *Frontiers in Physiology*, p.1171.

Yuan, X.*, **Kan, X.***, Xu, X.Y. and Nienaber, C.A., 2020. Finite element modeling to predict procedural success of thoracic endovascular aortic repair in type A aortic dissection. *JTCVS Techniques*, 4, pp.40-47.

C.2 Conference abstracts

Kan, X., Yuan, X., Salmasi, M.Y., Moore, J., Sasidharan, S., Athanasiou, A., Xu, X.Y. and Nienaber, C.A., 2021. Comprehensive Mechanical Modelling of Thoracic Endovascular Aortic Repair in Type A Aortic Dissection. *Circulation,* 144(Suppl_1), pp.A10478-A10478.

Yuan, X., **Kan, X.**, Xu, X.Y. and Nienaber, C., 2021. Identifying and quantifying the 4D motion of aortic root. *Journal of the American College of Cardiology*, 77(18_Supplement_1), pp.1832-1832.

C.3 Presentations

Kan, X., Yuan, X., Salmasi, M.Y., Moore, J., Sasidharan, S., Athanasiou, A., Xu, X.Y. and Nienaber, C.A. Comprehensive Mechanical Modelling of Thoracic Endovascular Aortic Repair in Type A Aortic Dissection. *AHA Scientific Session 2021*, 13th-15th November 2021, Virtual - Poster Presentation.

Yuan, X., **Kan, X.**, Xu, XY. and Nienaber, CA., Identifying and quantifying the 4D motion of aortic root. *ACC 2021*, 15th-17th May 2021, Atlanta (US) - Poster Presentation.

Kan, X., Ma, T., Dong, Z. and Xu, X.Y. A Patient-specific Virtual Stent-graft Deployment in Type B Aortic Dissection. *UK-China Researcher Links Workshop,* 10th-12th September 2019, Shanghai (China) - Oral presentation.

Kan, X., Ma, T., Dong, Z. and Xu, X.Y. A Patient-specific Biomechanical Simulation for Virtual Stent-graft Deployment in Type B Aortic Dissection: A Retrospective Study of Stent-graft Induced New Entry Cases. *International Conference on Stents Materials, Mechanics and Manufacturing*, 15th-17th July 2019, London (UK) - Oral Presentation.

Kan, X., Ma, T., Dong, Z. and Xu, X.Y. Biomechanical Simulation of Thoracic Aortic Endovascular Repair (TEVAR) with Virtual Stent-graft Deployment for Type B Aortic Dissection. *World Congress of Biomechanics*, 8th-12th July 2018, Dublin (Ireland) - Poster Presentation.

Apendix D

Copyright Permissions

Permission has been requested to reproduce figures protected by copyright. License numbers are presented in Table D.1. For online images, Open Access journals and figures published elsewhere under a Creative Common License, license numbers have been listed as "Not Available" (N/A).

Permission to adapt the author's own work is as follows:

- Work presented in Chapter 4 is adapted from Kan, X., Ma, T., Lin, J., Wang, L., Dong, Z. and Xu, X.Y., 2021. Patient-specific simulation of stent-graft deployment in type B aortic dissection: Model development and validation. *Biomechanics and Modeling in Mechanobiology*, *20*(6), pp.2247-2258, published under a Creative Commons Attribibution (CC BY) license (https://creativecommons.org/licenses/by/4.0/legalcode).
- Work presented in Chapter 5 is adapted from Yuan, X., **Kan, X.,** Xu, X.Y. and Nienaber, C.A., 2020. Finite element modeling to predict procedural success of thoracic endovascular aortic repair in type A aortic dissection. *JTCVS Techniques*, 4, pp.40-47, published under a Creative Commons Attribution NonCommercial NoDerivatives (CC-BY-NC-ND) license

(https://creativecommons.org/licenses/by-nc-nd/4.0/legalcode).

- Work presented in Chapter 7 is adapted from Kan, X., Ma, T., Dong, Z. and Xu, X.Y., 2021. Patient-Specific Virtual Stent-Graft Deployment for Type B Aortic Dissection: A Pilot Study of the Impact of Stent-Graft Length. *Frontiers in Physiology*, p.1171, published under a Creative Commons Attribibution (CC BY) license (https://creativecommons.org/licenses/by/4.0/legalcode).

Table D.1 Figure copyright permissions.

Figure No.	Source	Copyright Holder	License Number
Figure 2.1	Institute for Quality and Efficiency in Health Care, 2019	Institute for Quality and Efficiency in Health Care	N/A
Figure 2.2	Cleveland Clinic, 2019	Cleveland Clinic	N/A
Figure 2.3	Holzapfel et al., 2000	Springer Nature	5251860681795
Figure 2.4	Nienaber et al., 2016	Springer Nature	5251870147444
Figure 2.5	Nienaber and Clough, 2015	Elsevier	5251870322491
Figure 2.8	Johns Hopkins Medicine, 2021 and Cook Medical, 2021a	Johns Hopkins Medicine and Cook Medical	N/A
Figure 2.9	Medtronic, 2021, Gore Medical, 2021 and Cook Medical, 2021b	Medtronic Vascular, W.L.Gore & Associates, Inc. and Cook Medical	N/A
Figure 2.10	Ma et al., 2017	Elsevier	5251870549978